

Dissertation  
submitted to the  
Combined Faculties for the Natural Sciences and for  
Mathematics  
of the Ruperto-Carola University of Heidelberg, Germany

for the degree of  
Doctor of Natural Sciences

presented by  
Dipl.-Phys. **Marcel Mudrich**  
born in Strasbourg  
Oral examination: 12th February, 2003



**Interactions in an optically trapped mixture  
of ultracold lithium and cesium atoms:  
Thermalization, spin-exchange collisions and  
photoassociation**

Referees:

Priv.-Doz. Dr. Matthias Weidemüller

Prof. Dr. Jörg Schmiedmayer



**Zusammenfassung:**

Ein kaltes Gas aus zwei verschiedenen atomaren Spezies gefangen in einem konservativen Potential ist ein spannendes System zur Untersuchung von Atom-Atom Wechselwirkungen und der mit ihnen verknüpften Thermodynamik. In der vorliegenden Arbeit wird die effiziente sympathetische Kühlung von optisch gespeicherten  $^7\text{Li}$ -Atomen durch elastische Stöße mit lasergekühlten  $^{133}\text{Cs}$ -Atomen beschrieben. Damit wird erstmals eine nahezu verlustfreie Kühlmethode demonstriert, mit der Temperaturen erreicht werden, die unterhalb der durch optische Kühlung erreichbaren liegen. Innerhalb von 5 s werden  $5 \times 10^4$  Li Atome von anfangs  $\sim 150 \mu\text{K}$  bis auf  $30 \mu\text{K}$  heruntergekühlt. Aus der Zeitskala der Thermalisierung leiten wir den zuvor unbekanntem Wirkungsquerschnitt für elastische Li-Cs Stöße ab,  $\sigma_{\text{LiCs}} = 8 \times 10^{-12} \text{ cm}^2$ . In einer zweiten Reihe von Experimenten werden Ratenkonstanten von Spin-Austausch-Prozessen in einem kalten Gas von Cs-Atomen und in einem Gemisch aus Li und Cs-Atomen im Grundzustand gemessen. Der dritte Teil ist einer vergleichenden Untersuchung der Photoassoziation von  $\text{Cs}_2$ -Molekülen in einer magneto-optischen Falle (MOT) und in einer quasi-elektrostatischen Falle (QUEST) gewidmet. In einer theoretischen Machbarkeitsstudie wird die Photoassoziation von LiCs erforscht.

**Abstract:**

A cold gas of two different atomic species confined in a conservative potential is an intriguing system for studying atom-atom interactions and the related thermodynamics. This thesis presents efficient sympathetic cooling of optically trapped  $^7\text{Li}$  atoms through elastic collisions with lasercooled  $^{133}\text{Cs}$  atoms. This represents the first demonstration of a nearly loss-free cooling method to temperatures below the limit of optical cooling. Within 5 s,  $5 \times 10^4$  Li atoms are cooled from initially  $\sim 150 \mu\text{K}$  down to  $30 \mu\text{K}$ , which corresponds to an increase in phase-space density by a factor 100. From the time-scale of thermalization, we infer the previously unknown scattering cross-section for elastic Li-Cs collisions,  $\sigma_{\text{LiCs}} = 8 \times 10^{-12} \text{ cm}^2$ . In a second series of experiments, rate constants for spin-exchange collisions are measured in a cold gas of Cs atoms and in a mixture of Li and Cs atoms in the groundstate. The third part is devoted to a comparative study on photoassociation of  $\text{Cs}_2$  molecules in a magneto-optic trap (MOT) and in a quasi-electrostatic trap (QUEST). The feasibility of forming cold LiCs dimers through photoassociation is investigated theoretically.



Failure is only the opportunity  
to begin again more intelligently.

Henry Ford (1863-1947)



# Contents

<b>1</b>	<b>Introduction</b>	<b>1</b>
<b>2</b>	<b>Combined QUEST</b>	<b>5</b>
2.1	Lithium and Cesium . . . . .	5
2.2	Optical dipole traps . . . . .	7
2.3	Magneto-optic traps . . . . .	16
2.4	Experimental setup . . . . .	20
2.5	Loading the QUEST . . . . .	22
2.6	Diagnostics . . . . .	32
2.7	Trap characterization . . . . .	38
2.8	Conclusion . . . . .	47
<b>3</b>	<b>Elastic collisions</b>	<b>49</b>
3.1	Basic concepts . . . . .	50
3.2	Evaporative cooling . . . . .	52
3.3	Sympathetic cooling . . . . .	58
3.4	Sympathetic evaporation . . . . .	66
3.5	Conclusion and outlook . . . . .	70
<b>4</b>	<b>Inelastic collisions</b>	<b>71</b>
4.1	Introduction . . . . .	71
4.2	Inelastic scattering . . . . .	72
4.3	Inelastic collisions with trapped atoms . . . . .	78
4.4	Homonuclear spin-changing collisions . . . . .	81
4.5	Heteronuclear spin-changing collisions . . . . .	94
4.6	Conclusion . . . . .	103
<b>5</b>	<b>Towards molecule formation</b>	<b>105</b>
5.1	Motivation . . . . .	105
5.2	A feasibility study of LiCs . . . . .	111
5.3	Photoassociation of Cs <sub>2</sub> . . . . .	132

5.4	Conclusion and outlook . . . . .	141
<b>6</b>	<b>Conclusion and outlook</b>	<b>143</b>
6.1	Conclusion . . . . .	143
6.2	Outlook . . . . .	145
<b>A</b>	<b>Release-and-recapture thermometry</b>	<b>149</b>
<b>B</b>	<b>Vacuum and lasers</b>	<b>153</b>
<b>C</b>	<b>Calculated LiCs levels</b>	<b>159</b>

# Chapter 1

## Introduction

The physics of ultracold atomic gases has experienced a tremendous development in the past 10 years. Interaction processes in atomic gases close to the absolute zero-point of temperature are very much different from those at room temperature. Collisions between neutral atoms at temperatures well below one millikelvin represent a rich topic that reaches into various fields of modern atom physics [Burnett et al., 2002, Weiner et al., 1999].

Bose-Einstein condensates of interacting particles are closely linked to condensed matter physics [Gre, ]. Recent experiments with strongly correlated degenerate fermionic alkali atoms shade new light on the physics of superconductivity [Modugno et al., 2002, O'Hara et al., 2002]. Besides, ultracold collisions play an important role in metrology [Santarelli et al., 1999], in quantum information processing [Pinkse et al., 2000], and in chemical physics [Masnou-Seeuws and Pillet, 2001, Donley et al., 2002].

At temperatures in the microkelvin range as achieved by laser cooling [Metcalf and van der Straten, 1999] or evaporative cooling [Ketterle and van Druten, 1996], the deBroglie wavelength of colliding atomic wavepackets acquire macroscopic values on the micrometer scale, much larger than the typical range of the interaction potential between two atoms. Therefore, ultracold collisions are governed by the laws of quantum mechanics, revealing phenomena that defy our classical imagination. For instance, the cross-section for elastic collisions between spin-polarized Cs atoms becomes larger than the cross-section given by the charge radius by nearly 6 orders of magnitude [Arndt et al., 1997] ! The mean-field force acting between colliding  $^{87}\text{Rb}$  atoms is repulsive, although the long-range interaction potential is attractive [Burnett et al., 2002] !

At microkelvin temperatures the kinetic energy ranges below one neV, causing weak long-range forces to influence the interaction processes. Therefore, external electric and magnetic fields can critically influence the collision

properties. By changing the magnetic field by just a few Gauss close to the “Feshbach resonance” of Cs at 48 G one can make the collision cross-section of ultracold Cs atoms diverge, thereby coupling the atoms to quasibound Cs<sub>2</sub> molecules [Chin et al., 2003]. Due to their nearly vanishing velocity, typically in the range of cm/s, ultracold atoms can be manipulated almost at will by applying appropriate magnetic and electric fields. Comparatively weak forces acting on the atomic magnetic and induced electric dipole moment can be utilized to trap and store the atoms over many minutes, leaving plenty of time for observing interaction processes. The release of internal energy in an exoergic collision, for instance, leads to the escape of the colliding atom pair out of the trap in almost any case.

Typical collision times by far exceed the lifetime of optically excited states. Therefore, the collision dynamics is influenced by the presence of near resonant laser fields. By optically exciting bound molecular states during an ultracold collision it is possible to form ultracold molecules (photoassociation) [Masnou-Seeuws and Pillet, 2001]. In doing so, one has full control over the individual quantum states of the reactants, the pairs of colliding atoms, as well as of the products, the associated molecules.

Only recently, research in the field of ultracold interactions between neutral atoms has been extended to mixtures of different atomic species, opening the way to a variety of new perspectives, three of which will be discussed in the work.

Thermalization in a two-component mixture as a consequence of elastic collisions leads to the exchange of heat between the two gas components. In a closed system, heat-exchange results in cooling of the hot ensemble (sympathetic cooling). By supplying a large reservoir of cold atoms, a second ensemble of atoms or molecules can be cooled without particle loss. Thus, sympathetic cooling represents a loss-free alternative to evaporative cooling. In magnetically trapped mixtures of different species, sympathetic cooling has been successfully applied for reaching quantum degeneracy of bosonic potassium [Modugno et al., 2001], of fermionic potassium [Roati et al., 2002], as well as of fermionic lithium [Hadzibabic et al., 2002]. In these experiments, the cooling agent was cooled by evaporation, so that the achievable temperature was finally limited by the loss of the cooling agent.

This limitation can be overcome by choosing a coolant gas that can be optically cooled to very low temperatures. The situation is particularly promising, if the cooled gas has small mass so that the critical temperature for reaching the quantum degenerate regime is rather high. In this respect, the choice of cesium (Cs) as the cooling agent and lithium (Li) as the gas to be cooled, appears very favorable, since Li is the lightest and Cs the heaviest stable alkali atom. In the frame of this work, efficient sympathetic cooling of Li

by lasercooled Cs was demonstrated for the first time in a quasi-electrostatic trap (QUEST) [Mudrich et al., 2002]. The QUEST is particularly suited for experiments involving different atomic species since any polarizable particle including molecules can be trapped [Takekoshi et al., 1998]. In addition, off-resonant scattering of trapping light is completely negligible, leading to very long storage times [Engler et al., 2000].

An optically trapped atomic sample is well suited as a probe for exoergic collision processes. Since any hyperfine or magnetic states of the ground-state are equally confined by the conservative potential of the QUEST, different inelastic collisions channels can be studied. Changes in the phase-space distribution of the atomic sample as a result of exoergic collisions can be observed without the perturbations due to near-resonant light or strong magnetic fields. The inelastic rate-coefficients supply information about the interaction potentials complementary to the elastic scattering properties. In this work, we have performed detailed measurements on spin-exchange collisions in a sample of unpolarized Cs atoms and, for the first time, in a mixture of Li and Cs atoms [Mosk et al., 2001b].

The third perspective arising from the possibility of simultaneously storing different atomic species is the formation of heteronuclear molecules through photoassociation. Thus far, all photoassociation work has been performed with single-species samples of ultracold alkali atoms, with hydrogen, helium and calcium [Masnou-Seeuws and Pillet, 2001]. Recently, PA spectra of heteronuclear  ${}^6\text{Li}{}^7\text{Li}$  molecules were observed [Schlöder et al., 2001]. However, PA of two different atomic species has been demonstrated only once with NaCs by two-step excitation to an autoionizing state [Shaffer et al., 1999]. Trapping of  $\text{Cs}_2$  molecules in the groundstate was observed in a QUEST [Takekoshi et al., 1998] and in a mixed atomic and molecular trap [Vanhaecke et al., 2002]. The interests in forming and trapping ultracold heteronuclear molecules range from precision spectroscopy, atom molecule interactions, long-range interactions between polar molecules, tests of fundamental theories.

In this work, we present photoassociation spectra of  $\text{Cs}_2$  recorded both in the magneto-optical trap and in the QUEST. Furthermore, we theoretically explore photoassociation of heteronuclear LiCs dimers. Groundstate LiCs dimers are particularly interesting due to their extremely large electric dipole moment [Igel-Mann et al., 1986]. Polar molecules can be efficiently manipulated using electric fields [Rost et al., 1992]. The dipole-dipole interaction between LiCs dimers is expected to cause interesting ordering effects [Santos et al., 2000]. Moreover, due to its large dipole moment, LiCs is a candidate for precision measurements of the electric dipole moment of the electron (EDM) [Hudson et al., 2002].

The present work is organized as follows: Chapter 2 gives an overview over the experimental setup of the combined QUEST for Li and Cs. The optimal scheme for simultaneous transfer of Li and Cs into the QUEST is described as well as the characterization of the trapping potential. In Chapter 3, we present experimental results on evaporative cooling of Cs, sympathetic cooling of Li by Cs and sympathetic evaporation of Li induced by thermalization with Cs. Chapter 4 is devoted to inelastic collisions between Cs atoms and in a mixture of Li and Cs atoms. In the case of spin-exchange collisions of Cs, precise rate coefficients are determined and compared to theoretical predictions. In Chapter 5, we study the feasibility of the formation of heteronuclear LiCs dimers by photoassociation. In the second part, we present experimental results on photoassociation of Cs<sub>2</sub> both in a magneto-optical trap and in the QUEST.

# Chapter 2

## Combined quasi-electrostatic trap for lithium and cesium atoms

This Chapter is dedicated to the experimental prerequisites for performing experiments with simultaneously stored Li and Cs atoms in a quasi-electrostatic trap (QUEST). After reviewing the basic principles of laser cooling and trapping we briefly describe our experimental setup. Optimized strategies for loading and characterizing the QUEST are detailed in the last part.

### 2.1 Lithium and Cesium

The experiments presented in this work are performed with the lightest alkali-metal atom, lithium (Li) and the heaviest stable alkali-metal atom, cesium (Cs). In this Section, the relevant spectroscopic properties of both atoms are presented.

#### 2.1.1 Lithium

Two stable lithium isotopes are found in nature:  ${}^7\text{Li}$  with a natural abundance of 92.5% and  ${}^6\text{Li}$  with a natural abundance of 7.5%.  ${}^7\text{Li}$  has a nuclear spin  $I = \frac{3}{2}$  while the nuclear spin of  ${}^6\text{Li}$  is  $I = 1$ . Since there is only one unpaired electron, the electron spin is  $S = \frac{1}{2}$ . Therefore,  ${}^7\text{Li}$  obeys bosonic quantum statistics while  ${}^6\text{Li}$  constitutes a compound fermion. The experiments described here are performed exclusively with the bosonic isotope, and in the following Li denotes the  ${}^7\text{Li}$  isotope.

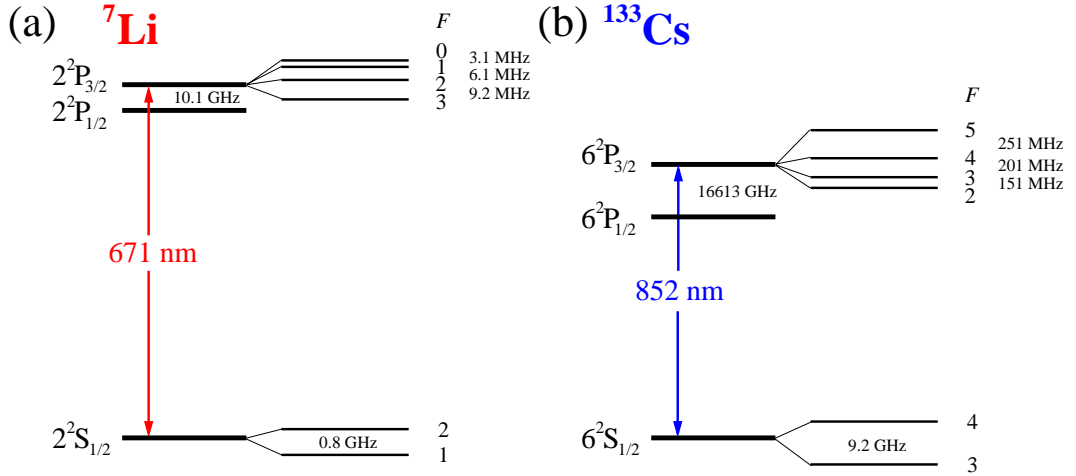


Figure 2.1: Level scheme of the ground and first excited states for (a) lithium and (b) cesium.

The level scheme of the ground and first excited state of lithium is depicted in Fig. 2.1(a). The ground state is  $2^2S_{1/2}$  in spectroscopic notation. The state is split into two hyperfine states with total angular momentum  $F = 1$  and  $F = 2$  with a hyperfine splitting of 803 MHz. The first excited state at an energy of 1.85 eV corresponding to a wavelength  $\lambda_{\text{Li}} = 670.78$  nm has a lifetime of 30 ns. It is split into a fine-structure doublet of  $2^2P_{1/2}$  and  $2^2P_{3/2}$  with an energy difference of 10.1 GHz. The two resonances from the ground state to the  $2^2P_{1/2}$  and  $2^2P_{3/2}$  states are called  $D1$  and  $D2$  lines, respectively. The main spectroscopic interest for our experiments is concentrated on the  $D2$  line since it represents the stronger transition.

The  $2^2P_{3/2}$  state is split into a hyperfine multiplet of four states with  $F' = 0 \dots 3$ . Note the inverted order of the excited hyperfine states. The transitions  $2^2S_{1/2}(F = 2) \leftrightarrow 2^2P_{3/2}(F' = 3)$  and  $2^2S_{1/2}(F = 1) \leftrightarrow 2^2P_{3/2}(F' = 0)$  are closed in the sense that the dipole selection rules only allow spontaneous decay of the excited state back into the initial ground state. Many photons can be scattered by driving such a closed transition with a laser field. However, in the case of lithium the splitting of these states is on the order of the natural linewidth  $\Gamma_{\text{Li}}/2\pi = 5.9$  MHz and can therefore not be resolved by ordinary spectroscopical means. Therefore, the  $D2$  line of Li effectively represents an three-level system consisting of the two hyperfine ground states and the unresolved excited state hyperfine multiplet.

	$A$	$I$	$\lambda_{D2}$ (nm)	$\Gamma/2\pi$ (MHz)	$\Delta_{HFS}$ (GHz)	$\Delta_{HFS}^*$ (MHz)	$T_{Doppler}$ ( $\mu\text{K}$ )	$T_{rec}$ ( $\mu\text{K}$ )	$\alpha_{stat}$ ( $\text{A}\text{sm}^2/\text{V}$ )
<b>Li</b>	7	3/2	671	5.9	0.8	$\sim 8$	140	3	$2.7 \times 10^{-39}$
<b>Cs</b>	133	7/2	852	5.3	9.2	$\sim 200$	130	0.1	$6.63 \times 10^{-39}$

Table 2.1: Important parameters for cooling and trapping Li and Cs:  $A$  atomic mass,  $I$  nuclear spin,  $\lambda_{D2}$  wave length of  $D2$ -transition,  $\Gamma/2\pi$  natural linewidth of the excited state,  $\Delta_{HFS}$  hyperfine splitting of the ground-state,  $\Delta_{HFS}^*$  average hyperfine splitting of the excited state,  $T_{Doppler} = \hbar\Gamma/k_B$  ‘‘Doppler limit’’,  $T_{rec} = (\hbar k)^2/(2k_B)$  ‘‘recoil limit’’,  $\alpha_{stat}$  static polarizability.

### 2.1.2 Cesium

The structure of the cesium level scheme shown in Fig. 2.1(b) is quite similar to the one of lithium, but with important quantitative differences. Only one stable isotope exists:  $^{133}\text{Cs}$  with a nuclear spin  $I = \frac{7}{2}$ . The ground state  $6^2S_{1/2}$  is split by 9.2 GHz, which is the well-known frequency defining the time standard. The cesium  $D2$  transition  $6^2S_{1/2} \leftrightarrow 6^2P_{3/2}$  is at a wavelength  $\lambda_{\text{Cs}} = 852.11$  nm corresponding to an energy difference of 1.46 eV. The fine-structure splitting of the  $D1$  and  $D2$  lines is 16.6 THz, or, expressed in wavelength difference,  $\Delta\lambda_{D1-D2,\text{Cs}} = 42.23$  nm. The natural linewidth of the excited state  $\Gamma_{\text{Cs}}/2\pi = 5.3$  MHz is much smaller than hyperfine splitting so that all lines of the excited state hyperfine multiplet  $F' = 2 \dots 5$  can be spectroscopically resolved. In particular, the closed transitions  $6^2S_{1/2}(F=4) \leftrightarrow 6^2P_{3/2}(F'=5)$  and  $6^2S_{1/2}(F=3) \leftrightarrow 6^2P_{3/2}(F'=2)$  constitute effective two-level systems. The two-level transitions can only be depopulated by off-resonant excitation of another excited hyperfine state. This state might then decay into the hyperfine ground state which is decoupled from the driving field. If large photon scattering rates are required, as for laser cooling and trapping, a second laser field is needed to recycle atoms from the other hyperfine ground state.

## 2.2 Optical dipole traps

Optical dipole traps rely on the electric dipole interaction with far-detuned light. The dipole force arises from the interaction of the induced atomic dipole with the driving optical field. Typical trap depths are in the range below one millikelvin. Atomic gases have to be precooled by appropriate

methods in order to be efficiently transferred into an optical dipole trap. The optical excitation can be kept extremely low, so that such a trap is not limited by the light-induced mechanisms present in radiation-pressure traps like the magneto-optical trap. Under appropriate conditions, the trapping mechanism is independent of the particular sub-level of the electronic ground state, in contrast to magnetic traps [Hess et al., 1987]. The internal ground-state dynamics can thus be fully exploited for experiments, which is possible on a time scale of many seconds. In this Section we will discuss the basic concepts of trapping in optical dipole potentials that result from the interaction with *far-detuned* light. For a general overview over the many different concepts and applications of optical dipole traps, the reader is referred to [Grimm et al., 2000].

### 2.2.1 Dipole force and scattering rate

When an atom is placed into laser light, the electric field  $\mathbf{E}$  induces an atomic dipole moment  $\mathbf{p}$  that oscillates at the driving frequency  $\omega$ . The amplitude  $p$  of the dipole moment is simply related to the field amplitude  $E$  by

$$p = \alpha E. \quad (2.1)$$

Here,  $\alpha$  is the complex polarizability which we assume to be scalar.

The *interaction potential* of the induced dipole moment  $\mathbf{p}$  in the driving field  $\mathbf{E}$  is given by

$$U_{\text{dip}} = -\frac{1}{2} \langle \mathbf{p} \cdot \mathbf{E} \rangle = -\frac{1}{2\epsilon_0 c} \text{Re}(\alpha) I, \quad (2.2)$$

where the angular brackets denote the time average over the rapid oscillating terms, the field intensity is  $I = 2\epsilon_0 c |E|^2$ , and the factor  $\frac{1}{2}$  takes into account that the dipole moment is an induced, not a permanent one. The potential energy of the atom in the field is thus proportional to the intensity  $I$  and to the real part of the polarizability  $\alpha$  which describes the in-phase component of the dipole oscillation being responsible for the dispersive properties of the interaction, like e.g. the refractive index. The *dipole force* results from the gradient of the interaction potential

$$\mathbf{F}_{\text{dip}}(\mathbf{r}) = -\nabla U_{\text{dip}}(\mathbf{r}) = \frac{1}{2\epsilon_0 c} \text{Re}(\alpha) \nabla I(\mathbf{r}). \quad (2.3)$$

It is thus a conservative force, proportional to the intensity gradient of the driving field.

The power absorbed by the oscillator from the driving field (and re-emitted as dipole radiation) is given by

$$P_{\text{abs}} = \langle \dot{\mathbf{p}} \cdot \mathbf{E} \rangle = 2\omega \text{Im}(pE^*) = \text{Im}(\alpha) \frac{I}{\epsilon_0 c} \omega. \quad (2.4)$$

The absorption results from the imaginary part of the polarizability, which describes the out-of-phase component of the dipole oscillation. Considering the light as a stream of photons  $\hbar\omega$ , the absorption can be interpreted in terms of photon scattering in cycles of absorption and subsequent spontaneous re-emission processes. The corresponding *scattering rate* is

$$\Gamma_{\text{sc}}(\mathbf{r}) = \frac{P_{\text{abs}}}{\hbar\omega} = \frac{1}{\hbar\epsilon_0 c} \text{Im}(\alpha) I(\mathbf{r}). \quad (2.5)$$

Thus, we have expressed the two main quantities of interest for dipole traps, the interaction potential and the scattered radiation power, in terms of the position-dependent field intensity  $I(\mathbf{r})$  and the polarizability  $\alpha(\omega)$ . These expressions are valid for any polarizable neutral particle in an oscillating electric field. This can be an atom in a near-resonant or far off-resonant laser field, or even a molecule in an optical or microwave field.

For dipole trapping, however, we are interested in the far-detuned case with very low saturation and thus very low scattering rates ( $\Gamma_{\text{sc}} \ll \Gamma$ ). In this regime, the polarizability  $\alpha$  is very well approximated by the polarizability of the classical harmonic oscillator subject to the classical radiation field. Then, we obtain the following expressions for the dipole potential  $U_{\text{dip}}$  and the scattering rate  $\Gamma_{\text{sc}}$

$$\begin{aligned} U_{\text{dip}}(\mathbf{r}) &= -\frac{3\pi c^2}{2\omega_0^3} \left( \frac{\Gamma}{\omega_0 - \omega} + \frac{\Gamma}{\omega_0 + \omega} \right) I(\mathbf{r}) \\ \Gamma_{\text{sc}}(\mathbf{r}) &= \frac{3\pi c^2}{2\hbar\omega_0^3} \left( \frac{\omega}{\omega_0} \right)^3 \left( \frac{\Gamma}{\omega_0 - \omega} + \frac{\Gamma}{\omega_0 + \omega} \right)^2 I(\mathbf{r}). \end{aligned} \quad (2.6)$$

Here,  $\omega$  and  $\omega_0$  stand for the laser frequency and the resonance frequency of the classical oscillator, respectively. The damping rate  $\Gamma = \omega_0^3 / (3\pi\epsilon_0\hbar c^3) |\langle e|\mathbf{p}|g \rangle|^2$  is determined by the dipole matrix element between ground and excited state. For the  $D$  lines of alkali atoms, this expression agrees with the classical damping rate due to radiative energy loss  $\Gamma = e^2\omega_0^2 / (6\pi\epsilon_0 m_e c^3)$  within a few percent.

The general expressions (2.6) are valid for any driving frequency  $\omega$  and show two resonant contributions: Besides the usually considered resonance at  $\omega \simeq \omega_0$  (first term in equations (2.6)), there is also the so-called counter-

rotating term (second term in equations (2.6)). When the laser field is detuned far below resonance ( $\omega \ll \omega_0$ ), as in the particular case of a quasi-electrostatic trap, both terms contribute by equal amounts. In the quasi-electrostatic approximation the expressions simplify to

$$\begin{aligned} U_{\text{dip}}(\mathbf{r}) &= -\frac{3\pi c^2}{\omega_0^3} \frac{\Gamma}{\omega_0} I(\mathbf{r}), \\ \Gamma_{\text{sc}}(\mathbf{r}) &= \frac{6\pi c^2}{\hbar\omega_0^3} \left(\frac{\omega}{\omega_0}\right)^3 \left(\frac{\Gamma}{\omega_0}\right)^2 I(\mathbf{r}). \end{aligned} \quad (2.7)$$

This expression is a very good approximation to the dipole potential of quasi-electrostatic traps,

$$U_{\text{dip}}(\mathbf{r}) = -\alpha_{\text{stat}} \frac{I(\mathbf{r})}{2\varepsilon_0 c}, \quad (2.8)$$

first proposed and realized by [Takekoshi et al., 1995, Takekoshi and Knize, 1996]. The static polarizabilities for Li and Cs are given in table 2.1. The light-shift potential both of the ground and excited state is attractive since the polarizability is generally positive. Atoms can therefore be trapped in all internal states by the same light field. Since the trap depth in Eq. (2.8) does not depend on the detuning from a specific resonance line as in the case of a far-off-resonance trap [Grimm et al., 2000], different atomic species or even molecules may be trapped in the same trapping volume.

However, trapping forces, even if generated by intense focused lasers, are rather feeble. E.g. the resulting trap depth in our setup (effective power in the chamber  $P \approx 100$  W, beam radius in the focus  $w_0 \approx 90 \mu\text{m}$ ) is only about  $1 \text{ mK} \times k_B$ . Therefore, high power lasers in the far-infrared spectral range have to be employed to create sufficiently deep traps. The  $\text{CO}_2$ -laser at  $10.6 \mu\text{m}$  which is commercially available with cw powers up to some kilowatts is particularly well suited for the realization of a QUEST [Takekoshi and Knize, 1996].

An important feature of the QUEST is the practical absence of photon scattering. The scattering rate in our setup is  $\lesssim 2$  photons/hour, showing that the QUEST represents an ideal realization of a purely conservative trap. Due to the extremely small scattering rate and the small recoil energy of the  $\text{CO}_2$ -laser photons at a wavelength of  $10.6 \mu\text{m}$ , heating by trap light photons can be completely neglected in a quasi-electrostatic trap.

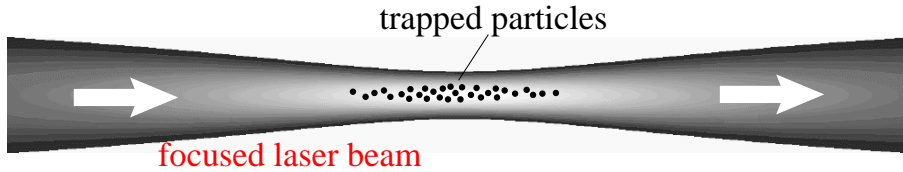


Figure 2.2: Optical dipole trap formed by the focus of a laser beam. When the laser frequency is detuned far below any electronic resonance, the optical dipole potential for the atomic ground state becomes quasi-electrostatic.

### 2.2.2 Focused-beam dipole trap

The dipole force points towards increasing intensity if the light field is tuned below the atomic transition frequency (*red detuning*). Therefore, already the focus of a laser beam constitutes a stable dipole trap for atoms, as first proposed by [Ashkin, 1978]. A focused Gaussian laser beam tuned far below the atomic resonance frequency represents the simplest way to create a dipole trap providing three-dimensional confinement. This situation is sketched in Fig. 2.2. The spatial intensity distribution of a focused Gaussian beam with power  $P$  propagating along the  $z$ -axis is described by

$$I(r, z) = \frac{2P}{\pi w^2(z)} \exp\left(-2\frac{r^2}{w^2(z)}\right) \quad (2.9)$$

where  $r$  denotes the radial coordinate. The  $1/e^2$ -radius  $w(z)$  depends on the axial coordinate  $z$  via

$$w(z) = w_0 \sqrt{1 + \left(\frac{z}{z_R}\right)^2} \quad (2.10)$$

where the minimum radius  $w_0$  is called the beam waist and  $z_R = \pi w_0^2/\lambda$  denotes the *Rayleigh length*. From the intensity distribution one can derive the optical potential  $U(r, z) \propto I(r, z)$  using Eq. (2.8). The trap depth is given by  $U_0 \equiv |U(r=0, z=0)| = \alpha_{stat} P / (\pi \varepsilon_0 c w_0^2)$ .

The Rayleigh length  $z_R$  is larger than the beam waist by a factor of  $z_R = \pi w_0^2/\lambda$ . Therefore the potential in the radial direction is much steeper than in the axial direction. To provide stable trapping one has to ensure that the gravitational force does not exceed the confining dipole force. Focused-beam traps are therefore mostly aligned along the horizontal axis. In this case, the strong radial force  $\sim U_0/w_0$  minimizes the perturbing effects of gravity.

If the thermal energy per particle  $k_B T$  of an atomic ensemble is much smaller than the potential depth  $U_0$ , the extension of the atomic sample is

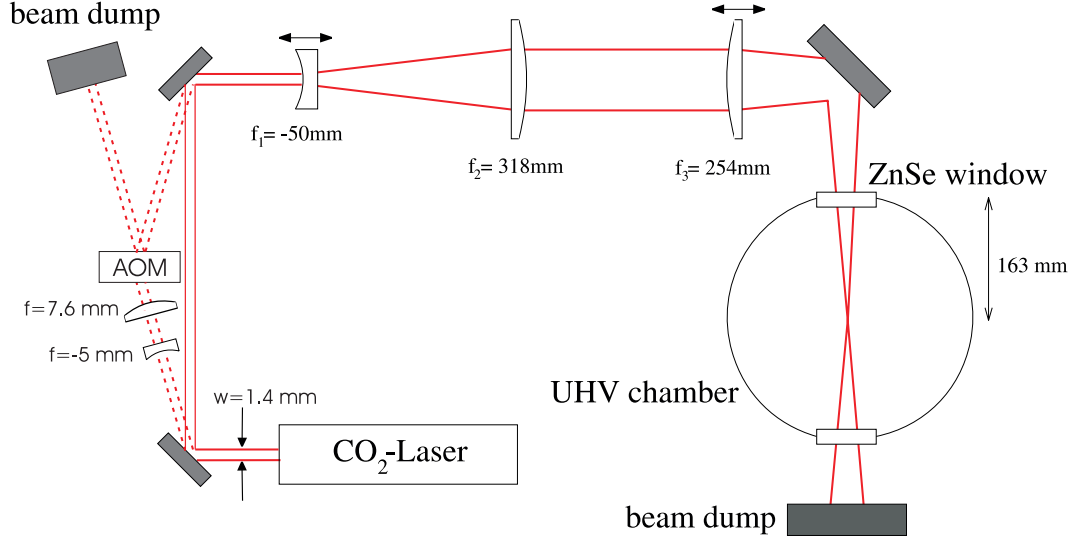


Figure 2.3: CO<sub>2</sub>-laser optics. The dashed red lines indicate the beam path of the CO<sub>2</sub>-laser when an acousto-optic modulator (AOM) is installed for intensity modulation.

radially small compared to the beam waist and axially small compared to the Rayleigh range. In this case, the optical potential can be well approximated by a simple cylindrically symmetric harmonic oscillator

$$U(r, z) \simeq -U_0 \left( 1 - 2 \frac{r^2}{w_0^2} - \frac{z^2}{z_R^2} \right). \quad (2.11)$$

The oscillation frequencies of a trapped atom in the radial and axial direction are then given by  $\omega_{rad} = (4U_0/mw_0^2)^{1/2}$  and  $\omega_{ax} = (2U_0/mz_R^2)^{1/2}$ , respectively.

### 2.2.3 CO<sub>2</sub>-laser optics

The central part of the experiment is the dipole trap laser. We use an industrial grade CO<sub>2</sub>-laser with an effective cw output power of 130 W (Model Evolution 100 by Synrad). This laser is pumped by a radio-frequency (RF) induced discharge inside a sealed-off discharge tube. A total RF-power of  $2 \times 600$  W at 40.68 MHz is fed from the water-cooled RF-power supply to the water-cooled laser-head. The duty-cycle of laser operation is controlled by a TTL-signal in the range of 1-100%, however, at 100% duty-cycle the laser power cannot be adjusted continuously. Since the chopped mode leads to heating of the trapped atoms in the QUEST by parametric excitation, the

laser has to be operated at 100% duty-cycle during the storage time of atoms in the QUEST. According to the laser specifications, the output beam has a small contribution of higher transversal modes to the zero-order Gaussian mode  $\text{TEM}_{00}$ . This contribution is quantified by the quantity  $M^2$ , which is listed with  $< 1.2$ .

**Beam characterization** The  $1/e^2$ -beam radius at the laser output was measured to be 1.4 mm. Using the optical setup that is described in detail in [Engler, 2000], we have measured the  $1/e^2$ -beam waist of the focus to be  $w_0^{\text{TEM}_{00}} = (72 \pm 3) \mu\text{m}$ , assuming a pure Gaussian  $\text{TEM}_{00}$  mode. Taking into account the  $M^2$  factor, we obtain the real beam waist,  $w_0 = M^2 \times w_0^{\text{TEM}_{00}} = (86 \pm 4) \mu\text{m}$ . Owing to favorable circumstances, this value matches the one estimated for attaining maximum transfer of Li [Wohlleben, 2000]. From power measurements in front of and behind the main vacuum chamber we infer the power in the trapping region,  $P = 108 \text{ W}$ . We calculate the depths of the trapping potentials for Li and Cs to be  $U_0^{\text{Li}} = 0.34 \text{ mK} \times k_B$  and  $U_0^{\text{Cs}} = 0.84 \text{ mK} \times k_B$ , respectively. This trap configuration was used for the experiments presented in Sec. 2.5.3, Sec. 3.3, and Sec. 3.4.

**Thermal effects** When the  $\text{CO}_2$ -laser was first put into operation, we observed a rapid rise in pressure in the main chamber from  $5 \times 10^{-11}$  to  $5 \times 10^{-10}$  mbar. We attribute this effect to heating of the ZnSe view-ports as a consequence of absorption. We found a remedy by gluing water-cooled copper cylinders onto the window flanges. Furthermore, we observe a slow drift of the focus position of several hundred  $\mu\text{m}$  on a minute-timescale after switching on the  $\text{CO}_2$ -laser. To keep the laser focus constant, the  $\text{CO}_2$ -laser has to be constantly operated at a duty-cycle between 70 and 100%. Typically, we set the duty-cycle to 100% when storing the atoms in the QUEST, and to 80% during the MOT loading stages, to prevent the laser from damage. After switching on the laser, it takes about 30 min. until constant trapping conditions are achieved.

**Acousto-optic modulator** One disadvantage of our  $\text{CO}_2$ -laser system is the fact that output power cannot be changed in continuous operation. In order to explore the possibility of modulating the laser intensity and thereby the trap depth, we have installed an acousto-optic modulator (model AGM-408BB1 with driver model GE-4050, both from IntraAction Corp.). The AOM basically consists of a single crystal optical germanium (Ge) block with anti-reflection coating at  $10.6 \mu\text{m}$  wavelength. The active aperture is  $8 \times 8 \text{ mm}$ . The AOM is water-cooled, whereas the driver is air-cooled. At

the maximum RF-driving power of 50 W (at 40 MHz) we observe a deflection efficiency into the first order of 86% with respect to the zero order when the RF-driver is off. The deflection efficiency is strongly dependent on polarization of the laser light, which has to be parallel to the basis of the AOM. The dependence of deflection efficiency as a function of RF-power is nearly linear, with a slight hysteresis effect. Power absorption in the Ge crystal is about 17%, e.g. we are left with 90 W in the 1st order. Behind all optics and the vacuum chamber we measure a power of 50 W. In order to prevent the Ge crystal from damage, we expand the laser beam by a factor 1.5 before passing through the AOM using the telescope shown in Fig. 2.3. The measured  $1/e^2$ -beam radius in front of the AOM is 2.7 mm.

By using the same optical elements as before to form the QUEST focus (lenses  $f_1$ ,  $f_2$ , and  $f_3$  in Fig. 2.3), we measure a horizontal and vertical waist of  $w_0^{horiz} = 68 \mu\text{m}$  and  $w_0^{vert} = 56 \mu\text{m}$ , respectively. If we assume a power of 60 W in the vacuum chamber, we calculate the trap depth for Li and Cs of 0.4 and 1.0  $\text{mK} \times k_B$ , respectively, which is still sufficient for trapping a large number of atoms. Due to thermal lensing effects inside the Ge crystal as a function of laser power, we observe beam-steering with increasing laser power in vertical direction with respect to the AOM, i.e. in horizontal direction with respect to the vacuum chamber. We measure a total horizontal shift at the input window of 4 mm. This power-dependent beam shift is very annoying when trying to adjust the optical path, since the adjustment is done at low power. In addition, the focus position is shifted by about 10 mm away from the input window. This shift was compensated by translating the last focusing lens  $f_3$  in Fig. 2.3. The radial shift of the focus position as a function of RF-power was found to be on the order of 100  $\mu\text{m}$ . The AOM was installed in the experiments presented in sections 2.7.2, 3.2, and 4.5. In order to keep explanations short, we will speak of AOM QUEST whenever the AOM is installed.

**Switching times** For fast detection of the  $\text{CO}_2$ -laser light, we use a photovoltaic detector with a matched preamplifier (model PD-10.6-3 ( $3 \times 3$  mm), preamp 481-5, both from Boston Electronics Corp.). The detector has maximum spectral response close the 10.6  $\mu\text{m}$  wavelength of the  $\text{CO}_2$ -laser and a low  $1/f$  noise level. It is specified for a maximum cw intensity of 1  $\text{W}/\text{mm}^2$ . The preamplifier is designed for the frequency band DC-5 MHz.

In Fig. 2.4, we compare the switching times of  $\text{CO}_2$ -laser power. When the AOM is used for switching on the laser power (a), full power is reached after 6  $\mu\text{s}$ . However, when the RF-power supply of the  $\text{CO}_2$  is used for switching, it takes about 1 ms until laser operation has reached steady-state conditions.

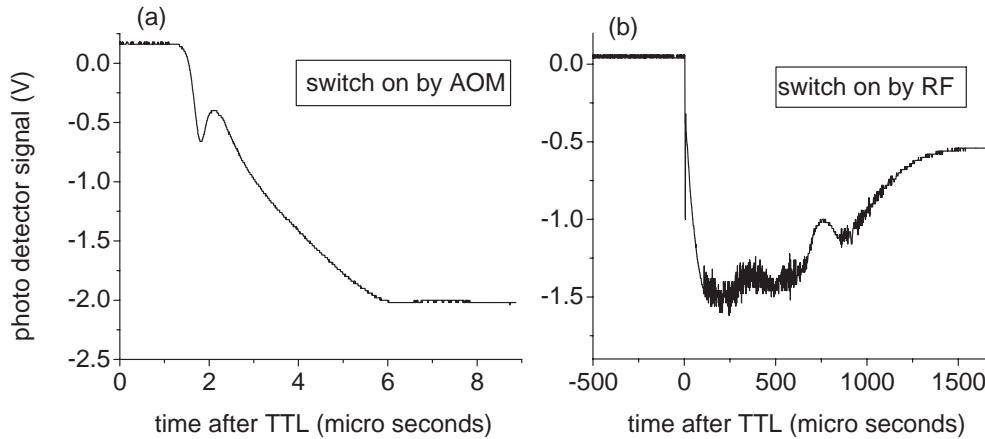


Figure 2.4: Comparison of the switching times when the  $\text{CO}_2$ -laser power is switched on by means of the AOM (a) and by switching the RF-power supply of the laser.

Fig. 2.5 displays the same curves for switching the laser power off. This case is more important for our purposes, since our Cs temperature measurements rely on recording the expanding cloud after switching off the  $\text{CO}_2$ -laser beam. In the case of switching the AOM, it takes about  $2.3 \mu\text{s}$  until laser power is off, whereas it takes about  $300 \mu\text{s}$  in the case of extinguishing the RF-power of the laser itself. The slower response of the laser output when switching the RF-power supply is probably due to both slow rise time of the RF-power level and slow degradation of the excitation in the laser gas [Wittman, 1987]. The influence of this switching behavior on the temperature measurements is discussed in Sec. 2.6.3.

**Coherence length** Using the fast detector for  $\text{CO}_2$  radiation, we have recorded the interference of two beams from the  $\text{CO}_2$ -laser, propagating along different distances. For this purpose, we set up an interferometer in Michelson geometry, using an optical grade salt (NaCl) plate as a 10:90 beam splitter. One of the back reflecting mirrors was mounted on a z-translation stage to be able to change the optical path in that branch with micrometer precision. The difference in path lengths was changed by up to 2 m. Finally, we were limited by the dimensions of the optical table. Fig. 2.6 shows the interferogram recorded for the length of the two branches differing by about 2 m. The moveable mirror was displaced by about  $80 \mu\text{m}$ . We detect in-

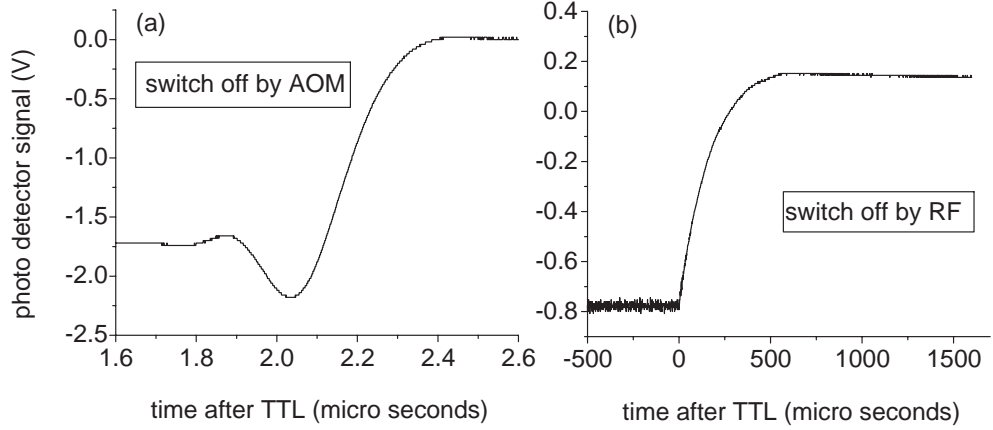


Figure 2.5: Comparison of the extinguishing times of CO<sub>2</sub>-laser power.

interference fringes with nearly 100% visibility. Kinks in the photodetector signal, as the one close to the displacement of 1 arbitrary unit, are due to mode hops of the CO<sub>2</sub>-laser induced by feedback from the mirrors of the interferometer. From the coherence length  $L_c \gtrsim 2$  m we can estimate an upper bound for the spectral width of the laser radiation, using the relation  $\Delta\nu = c/L_c$ . We find  $\Delta\nu \approx 150$  MHz. The free spectral range, which denotes the spacing between laser resonator modes, is of the same order of magnitude,  $\nu_{FSR} = c/(2L) \approx c/(2 \times 2.4 \text{ m}) = 63$  MHz. Since the spacings between vibrational lines and between rotational lines of the <sup>12</sup>C<sup>16</sup>O<sub>2</sub> molecule are much larger than 150 MHz [Wittman, 1987], we conclude that our CO<sub>2</sub>-laser most probably operates on one single longitudinal mode. However, we cannot exclude mode hops between longitudinal modes on a long time scale.

## 2.3 Magneto-optic traps

The magneto-optical trap (MOT) has developed into a work-horse in atomic physics, whenever cold ( $T < 1$  mK) and dense ( $n > 10^{10}$  atoms/cm<sup>3</sup>) atomic samples are needed. In the experiments described below, the MOT is used for accumulating atoms from atomic beams, to cool and compress them. Thus, the MOT represents the starting point for further experiments with ultracold atoms transferred from the MOT into the QUEST. In this section, we will outline the basic functionality of the MOT as far as our experiments

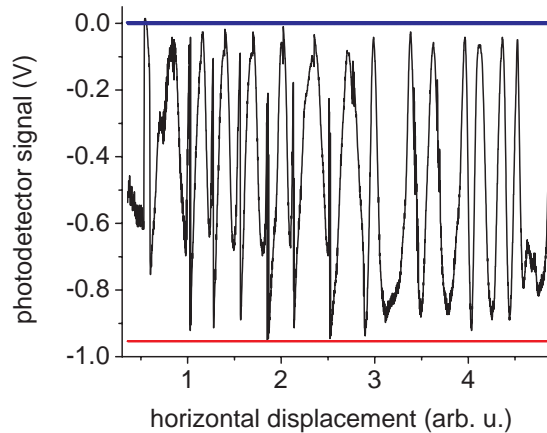


Figure 2.6: Interferogram recorded with a Michelson setup. The difference in path lengths is about 2 m.

are concerned. The physics of magneto-optic trapping has been nicely presented in [Weidemüller, 2000], a comprehensive descriptions of the magneto-optical trap can be found in the monograph on laser cooling and trapping [Metcalf and van der Straten, 1999].

### 2.3.1 Radiation pressure force

The principle of the MOT is based on the radiation pressure force acting on an atom as it interacts with near-resonant light. For a simple two-level system, consisting of a single ground state  $g$  and a single excited state  $e$ , one finds the following semiclassical expression for the radiation pressure force [Cohen-Tannoudji et al., 1988]:

$$\mathbf{F}_{\text{rad}} = \hbar \mathbf{k} \Gamma \frac{1}{2} \frac{I/I_S}{1 + I/I_S + 4(\delta/\Gamma)^2} \quad (2.12)$$

where  $\delta = \omega - \omega_0$  is the detuning from resonance and  $I_S = \hbar \Gamma \omega_0^3 / 12 \pi c^2$  denotes the saturation intensity.

Eq. (2.12) can be interpreted in a very intuitive way:  $\hbar \mathbf{k}$  is the momentum of a photon from the laser wave. This momentum is absorbed by the atom when absorbing the photon. Subsequently, a photon is emitted by spontaneous emission, but on average no momentum is transferred to the atom because  $\langle \hbar \mathbf{k}' \rangle = 0$  with  $\hbar \mathbf{k}'$  denoting the momentum of the spontaneously emitted photon. Therefore, the force of the atom is the momentum transfer

times the photon scattering rate  $\Gamma_{\text{sc}}$ . The scattering rate is the product of the spontaneous emission rate  $\Gamma$  and the population of the excited state  $\Pi_e$  which, for a two-level atom, is given by the last term in Eq. (2.12). Although the momentum transfer by absorption of one single photon is rather small, the acceleration due to the radiation pressure reaches very high values of  $10^6 - 10^7 g$  because of the large scattering rate  $\Gamma_{\text{sc}} \sim 10^7 \text{ s}^{-1}$ .

From Eq. (2.12) follows that the radiation pressure force critically depends on the detuning of the laser light from resonance. An atom moving with a velocity  $v$  “sees” a laser frequency that is shifted by an amount  $\Delta\omega = \pm kv$  due to the Doppler effect. The effective detuning of the laser from resonance is therefore given by

$$\delta_{\text{Doppler}} = \omega - \omega_0 \mp \mathbf{k} \cdot \mathbf{v}. \quad (2.13)$$

If an atom moves towards the laser beam, the laser frequency is shifted towards higher frequencies. Consequently, when the laser is detuned below the atomic resonance, a counter-moving atom will be shifted towards resonance and thus experience a stronger force. If an atom is exposed to laser radiation from opposite directions at a frequency below the atomic resonance, the atom will always absorb more photons from the counter-propagating laser field than from the co-propagating one which gives rise to a friction force according to Eq. (2.13). The motion of an atom which is illuminated with laser beams from all six spatial directions is thus strongly damped. The term *optical molasses* has been coined for pairs of counter-propagating laser beams detuned below the atomic resonance, in which the atoms are cooled by the friction force exerted by the radiation pressure.

### 2.3.2 Magneto-optical force

This friction force only provides compression in velocity space. To additionally confine the atoms to a small volume one needs a spatially dependent force. Such a force can be created by a combination of magnetic quadrupole field with appropriate polarization of the light fields, as indicated in Fig. 2.7(a). Due to the Zeeman effect in the inhomogeneous field  $B(\mathbf{r})$ , the detuning becomes a function of position

$$\delta_{\text{Zeeman}} = \omega - \omega_0 \pm \mu' B(\mathbf{r}) \quad (2.14)$$

with  $\mu' = (g_e m_e - g_g m_g) \mu_B$  being the effective magnetic moment of the transition used ( $g_{g,e}$  = g-factor the the ground and excited state,  $m_{g,e}$  = magnetic quantum number,  $\mu_B$  = Bohr’s magneton). The laser frequency is chosen below the atomic resonance, and the polarizations are adjusted such that an atom away from the center always absorbs more photons from

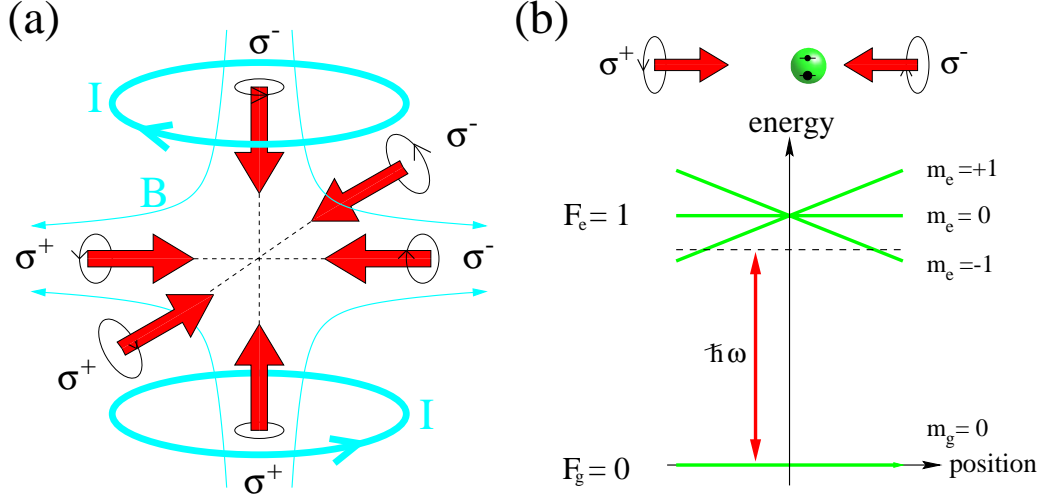


Figure 2.7: Magneto-optical trap. (a) Schematic drawing of the setup. The currents  $I \sim 30$  A induce an axially symmetric quadrupole magnetic field  $B$ . The laser beams are circularly polarized. (b) Energy level diagram for a ground state with total angular momentum  $F_g=0$  and an excited state with  $F_e=1$  in a quadrupole magnetic field. The laser frequency  $\omega$  is tuned below the atomic resonance frequency at zero field. At positions right from the center, the laser beam driving the  $\sigma^-$  transition is tuned closer to resonance by the Zeeman effect. The atom therefore absorbs more photons from the  $\sigma^-$  beam than from the  $\sigma^+$  beam. The atom is thus being pushed towards the center which represents the point of stable equilibrium for the radiation pressure of all beams.

the wave pushing it towards the center than from the opposite wave, as schematically shown in Fig. 2.7(b). Thus, the atoms experience a spatially-dependent restoring force and the point of zero magnetic field constitutes the center of the trap.

In this way, the magneto-optical trap provides two nice things at the same time: cooling through the Doppler effect and confinement via the Zeeman effect [Raab et al., 1987]. When both Zeeman and Doppler shift are small compared to the laser detuning  $\omega - \omega_0$ , the force can be expanded in velocity and position:

$$\mathbf{F}_{\text{MOT}} \simeq -\beta_{\text{fric}} \mathbf{v} - \kappa_{\text{conf}} \mathbf{r}. \quad (2.15)$$

Thus, the atomic ensemble is cooled and compressed into the center of the magnetic quadrupole field.

Cooling in the MOT is even more effective due to the presence of

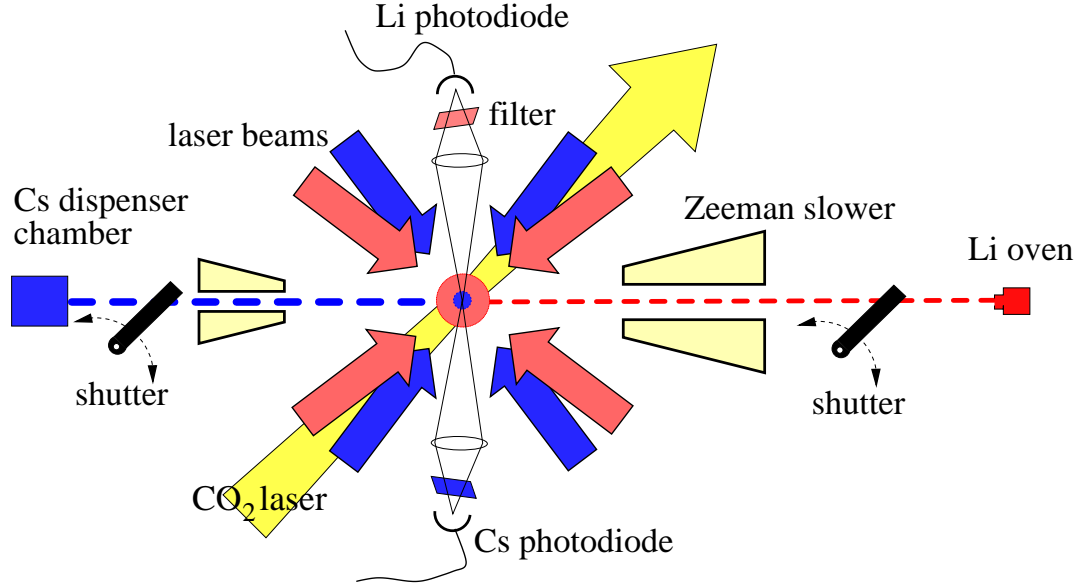


Figure 2.8: Schematic illustration of the experimental setup.

polarization-gradient cooling mechanisms which rely on selective optical pumping between Zeeman sublevels of the ground state in fields with spatially varying polarizations [Dalibard and Cohen-Tannoudji, 1989]. The final velocity of the trapped atoms corresponds to only a few photon recoils  $\hbar k/m$ , the natural limit of laser cooling (“recoil limit”). The two atoms of interest in our work, Li and Cs, differ strongly in the achievable temperatures. Cs, on the one hand, with its closed transition  $6^2S_{1/2}(F=4) \rightarrow 6^2P_{3/2}(F'=5)$  (see Section 2.1.2) is perfectly suited for the application of polarization-gradient cooling mechanisms. Achievable temperatures are around  $10 \mu\text{K}$ . Lithium, on the other hand, provides no closed two-level system because of the unresolved hyperfine structure of the excited state (see Section 2.1.1), and optical pumping among magnetic ground-state sublevels is strongly perturbed. However, due to the small lithium mass, the achievable temperatures in a MOT are around  $300 \mu\text{K}$ , which also corresponds to only a few photon momentum recoils.

## 2.4 Experimental setup

Figure 2.8 shows a schematic view of our experimental setup. For details on the vacuum system and the laser setup, the reader is referred to appendix B. The MOT for Li and Cs atoms consists of three mutually orthogonal pairs of counter-propagating laser beams for each species with opposite circular

polarization, intersecting at the center of an axially symmetric magnetic quadrupole field. Field gradients are 14 G/cm along the vertical axis, and 7 G/cm along the horizontal directions.

**Lasers** The light field of the Li-MOT is formed by retro-reflected beams with a  $1/e^2$ -radius of 7 mm. The Cs-MOT configuration was changed during this work from retro-reflected beams with  $1/e^2$ -radius of 4 mm to the “5 beams” configuration with 6 mm radius. The latter geometry consists of one retro-reflected beam along the axis of symmetry of the magnetic field ( $z$ -direction) and 4 single beams in the  $x - y$ -plane. The larger beams have lead to an increase in the steady state number of loaded atoms by one order of magnitude. The “5 beams” configuration has lead to a reduction of the effect of a shifting MOT-cloud while loading as a consequence of unbalanced radiation pressure as the atoms cloud becomes opaque. All measurements presented in this Chapter and in Chapter 3 were performed using 3 retro-reflected beams. The measurements of Chapters 4 and 5 were done using the “5 beams” configuration.

Due to the hyperfine doublet in the groundstate of alkali-atoms, two laser fields with a frequency difference equal to the hyperfine splitting are required to prevent optical pumping into a state which is decoupled from the laser field. Total laser power is about 26 mW for the Cs-MOT at 852 nm and 27 mW for the Li-MOT at 671 nm. Completely separated optics is used for the two wavelengths. The same windows are used for each trapping laser beam at 852 nm and 671 nm. The light is coupled into the vacuum chamber with a small angle between the 671 nm-beam and the 852 nm-beam.

The laser beams are provided exclusively by diode lasers. For the trapping of Cs, a distributed-Bragg-reflection (DBR) diode laser is operated close to the  $6^2S_{1/2}(F = 4) \rightarrow 6^2P_{3/2}(F' = 5)$  cycling transition of the cesium  $D2$  line at 852 nm. To avoid optical pumping into the other hyperfine ground state, a second laser beam from a DBR diode laser resonant with the  $6S_{1/2}(F = 3) \rightarrow 6P_{3/2}(F = 4)$  transition is superimposed with the trapping beam. Trapping of Li is accomplished with diode lasers in a master-slave injection-locking scheme as described in [Schünemann et al., 1998]. The Li and Cs laser systems are discussed in detail in appendix B.

**MOT loading** Both MOTs are loaded from Zeeman slowed effusive atomic beams which can be interrupted by mechanical shutters. This ensures very low background pressure in the main chamber of about  $5 \times 10^{-12}$  mbar. The Cs oven at a temperature of typically 110 °C is continuously filled during operation by running a current of  $\sim 3$  A through a set of nine Cs dispensers.

The Cs-MOT accumulates atoms from the slow velocity tail ( $v \leq 10$  m/s) of the Maxwell distribution. Typically, close to  $10^8$  atoms (at a detuning  $\delta_{\text{Cs}} = -1.5 \Gamma_{\text{Cs}}$ ) are trapped with a loading time constant of several seconds. Li has to be evaporated at much higher temperatures. The small mass of Li results in much higher atom velocities. Atoms with velocity  $v \leq 600$  m/s are decelerated in a compact Zeeman slower by an additional laser beam at 671 nm [Engler, 2000]. At a Li oven temperature of 420 °C, loading rates are around  $10^7$  atoms/s, yielding up to  $10^8$  trapped Li atoms. Densities for the Cs and the Li-MOT range between  $10^9$  and  $10^{10}$  atoms/cm<sup>3</sup>.

The Li atomic beam shines through the main chamber directly onto a sapphire window, used for input coupling the counter-propagating Zeeman slower beam. Deposition of Li on the window has created a thin layer, which absorbs part of the intensity of the Zeeman slower beam. This has led to a continuously decreasing loading rate of the Li-MOT. We found a remedy to the problem by regularly irradiating the Zeeman slower window with a halogen lamp of 20 W power. Care was taken not to heat up the window further than 100 °C.

## 2.5 Loading the QUEST

The trapping potential of the QUEST is a shallow conservative potential. In order to load atoms into the QUEST, the atoms have to be cooled during the transfer to extract the gained potential energy. This is done by superimposing the MOT onto the focus of our trapping laser. The transfer efficiency from the MOT into the QUEST can be estimated using an analytical model described in [Engler, 2000]. For further cooling and compression, different optimized schemes have been worked out for Li and Cs. In order to achieve as reproduceable transfer conditions as possible, both transfer cycles for Li and Cs are triggered to a fixed fluorescence level of the MOT, measured with photodiodes. After all magnetic fields are switched off and the MOT light is extinguished, it is very important to shield the dipole trap from any resonant stray light, in particular if long storage times ( $\gtrsim 10$  s) are to be reached. This is accomplished by extinguishing all near-resonant light beams using fast mechanical shutters [Singer et al., 2002]. The timing control of the experiment is realized by a digital and analog I/O card for PC (AdWin Light from Jäger Messtechnik), controlled by an independent timing processor TL400. The timing sequence is compiled using sophisticated software based on LabView that was developed in our group [Wohlleben, 2000].

### 2.5.1 Cesium transfer

The temperature of the Cs cloud after molasses cooling falls far below the depth of the trapping potential. Therefore, the transfer efficiency is mainly determined by the spatial overlap of the atomic cloud with the QUEST potential. The spatial overlap of the Cs-MOT with the focus of our CO<sub>2</sub>-laser beam is optimized by carefully adjusting the laser focus onto the center of the MOT. The relative position is monitored by successively imaging both the atom cloud in the MOT and the cigar-shaped distribution of atoms in the QUEST after sufficient equilibration time ( $\sim 1$  s). In [Kuppens et al., 2000], the transfer efficiency into a far-off resonance trap was reported to be maximum when the center of the MOT was slightly misaligned in axial direction. However, in our experiments, no such dependence was observed [Wohlleben, 2000]. On the contrary, perfect overlap is crucial for achieving low temperatures since the atoms pick up potential energy when loaded away from the potential minimum.

The Cs atom is very well suited for molasses cooling, as discussed in Sec. 2.3.2. In our experiment we realize molasses cooling by simply changing the detuning of the MOT laser normally operated slightly red-detuned from the transition  $F = 4 \rightarrow F' = 5$  after switching off the MOT magnetic field. When molasses cooling is applied on the atoms right after switching off the MOT without dipole trap, we achieve temperatures of  $\lesssim 5 \mu\text{K}$  at a detuning of  $\delta \approx 20 \Gamma$ . Apparently, the molasses cooling dynamics is modified by the presence of the optical potential of the QUEST.

Fig. 2.9 displays the number (a) and temperature (b) of transferred Cs atoms as a function of frequency detuning of the molasses laser with respect to the transition  $F = 4 \rightarrow F' = 5$ . The different symbols stand for the different MOT configurations discussed in Section 2.4. In either case, the maximum transfer efficiency is reached at a laser frequency of 2-3  $\Gamma$  blue detuned from the transition  $F = 4 \rightarrow F' = 4$ . Moreover, the lowest temperatures are reached at the same detuning. We attribute the observed cooling behavior to a combined effect of blue detuned Sisyphus cooling [Boiron et al., 1998] and of an effective dark MOT [Ketterle et al., 1993] at the trap center induced by the ac Stark shift due to the QUEST laser beam [Barrett et al., 2001]. By changing the MOT geometry to 5 beams, we have obviously gained roughly a factor of 3 in the number of transferred atoms. However, the temperature is systematically higher at these detunings by almost a factor of 2. The dependence on the duration of the molasses pulse is weak within 5-50 ms. The number of transferred atoms is further increased by about a factor of 2 by changing the laser frequency to about 20  $\Gamma$  to the red of the transition  $F = 4 \rightarrow F' = 5$  about 5 ms prior to switching off the MOT magnetic field.

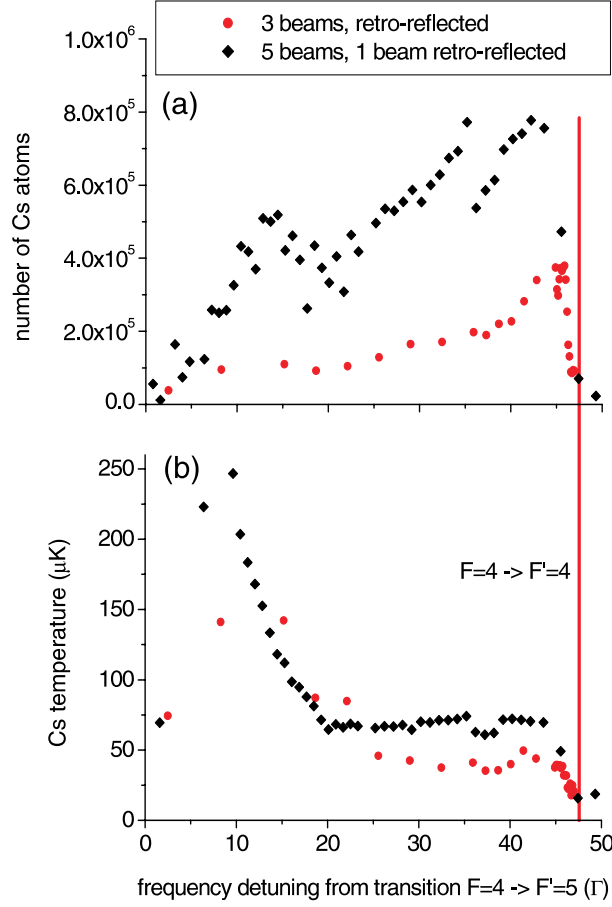


Figure 2.9: Number (a) and temperature (b) of transferred Cs atoms into the QUEST as a function of laser detuning in units of the natural linewidth  $\Gamma$  with respect to the transition  $F = 4 \rightarrow F' = 5$ . The vertical line indicates the transition  $F = 4 \rightarrow F' = 4$ .

By applying an additional cooling pulse at blue molasses detuning 0.5 s after transfer we achieve a temperature of  $\gtrsim 25 \mu\text{K}$  with 3 beam geometry and  $\gtrsim 35 \mu\text{K}$  in 5 beam configuration.

Fig. 2.10 displays the achievable Cs temperature in the QUEST depending on density. The measurements were performed in the AOM QUEST (see Sec. 2.2.3) for two values of the depth of the trapping potential,  $U_0 = 510$  and  $125 \mu\text{K} \times k_B$ . For comparison, the triangle displays the typical Cs temperature achieved in the expanding cloud in the absence of the QUEST laser. For a fixed trap depth  $U_0$ , the density is varied by triggering the transfer timing sequence onto different fluorescence levels of the MOT. Thus, the number of transferred atoms is changed over about one order of magnitude.

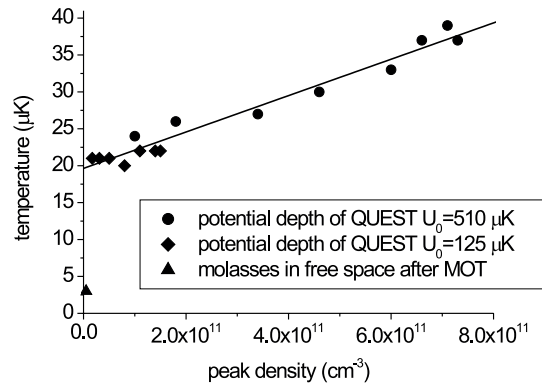


Figure 2.10: Density dependence of the achievable Cs temperature in the QUEST. For comparison, the triangle depicts the temperature achieved in the absence of the QUEST laser.

For each value of the fluorescence level, the molasses detuning is optimized. The measured temperature values seem to be linearly correlated with density. This density dependence is probably caused by photon reabsorption [Boiron et al., 1998]. However, there must be another factor limiting the cooling efficiency in the QUEST to the extrapolated temperature value of  $\sim 20 \mu\text{K}$ . We assume that the spatially varying potential of the QUEST modifies the optical potential of the molasses laser such that Sisyphus mechanisms are perturbed.

### 2.5.2 Lithium transfer

The Li cloud released from the MOT has a higher temperature than the depth of the QUEST potential for Li atoms by about a factor of 10. Since the Li-MOT is larger than the CO<sub>2</sub>-laser focus by roughly a factor of 10, the transfer efficiency is mainly determined by the overlap in momentum space of the Li cloud and the QUEST phase-space volume.

**Trap alignment** The adjustment of the CO<sub>2</sub>-laser focus is determined by the position of the Cs-MOT. Therefore, the overlap of QUEST and Li-MOT is optimized by shifting the Li-MOT using three independent homogeneous magnetic fields along the  $x$ ,  $y$ , and  $z$ -spacial directions. These positioning fields are generated by additional coils placed outside the main vacuum chamber. Fast switching is provided for by TTL-controlled circuits based on the FET BUK 100 50 GL. Since transfer efficiency for Li is much weaker than for

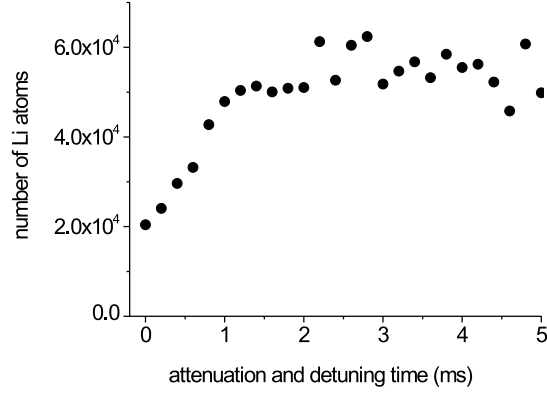


Figure 2.11: Number of transferred Li atoms into the QUEST as a function of duration of the detuning and attenuation phase.

Cs (see below), the size of the CO<sub>2</sub>-laser focus is adjusted to reach maximum transfer efficiency of Li. This is done by shifting the first telescope lens  $F_1$  in Fig. 2.3 and thereby changing the expansion ratio of the telescope  $F_1$  and  $F_2$ . The resulting shift in position of the focus is compensated by translating the last focusing lens  $f_3$ . The transfer efficiency is measured by recording the fluorescence signal of the transferred Li atoms after recapture in the MOT.

**MOT compression** Since sub-doppler cooling mechanisms are inefficient with Li atoms (see Sec. 2.3.2), the transfer scheme differs significantly from the one of Cs. The maximum transfer rates are achieved by shifting the frequencies of both MOT lasers close to the resonance frequencies and by simultaneously attenuating the laser intensities. The laser frequencies are shifted to a detuning of 8.8 MHz ( $1.5\Gamma$ ) to the red of the transition  $F = 1 \rightarrow F'$  and 3.3 MHz ( $0.6\Gamma$ ) to the red of the transition  $F = 2 \rightarrow F'$ , respectively. The intensities in both MOT beams is typically reduced to 20% using electro-optic modulators (EOM). By shifting the laser frequencies close to resonance the atomic cloud is compressed, whereas intensity attenuation produces an effective dark MOT, as observed in [Ketterle et al., 1993]. The resulting temperature and density of the atomic cloud is  $T_{\text{Li}}=0.3\text{-}1$  mK and  $n_{\text{Li}} \sim 10^{10} \text{ cm}^{-3}$ . We have tried to obtain lower temperatures in the Li-MOT by introducing pin-holes in the MOT laser beams as spacial filters. The beam profiles adopted nearly perfect Gaussian shape on the expense of laser intensity. However, the temperature of the compressed atomic cloud remained unchanged.

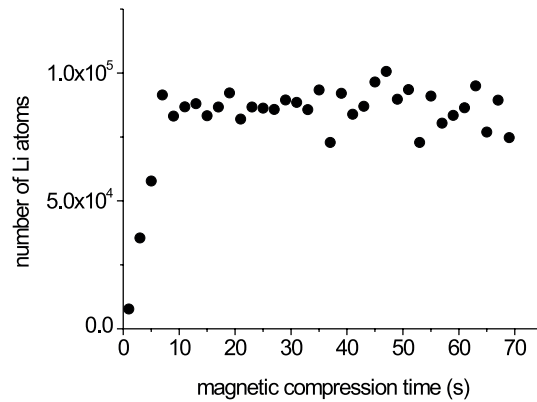


Figure 2.12: Number of transferred Li atoms as a function of the magnetic compression time. The maximum magnetic field gradient is reached after about 10 ms.

Fig. 2.11 displays the Li transfer efficiency as a function of the length of the detuning and attenuation phase. Typically 1 ms is sufficient for increasing the number of transferred atoms by about a factor of 3. Constant transfer conditions are ensured by triggering the transfer timing sequence to a fixed fluorescence level of the Li-MOT. It is important to note, that both MOT lasers must be extinguished before switching off the MOT magnetic field. Otherwise, transient magneto-optic forces lead to loss of atoms from the QUEST.

The transfer conditions are greatly improved by magnetically compressing the Li-MOT a few milliseconds before switching of the MOT lasers and the MOT magnetic field [Petrich et al., 1994a]. This is realized by ramping up the MOT quadrupole field from 13 to 37 G/A within about 10 ms. The resulting number of transferred atoms is depicted in Fig. 2.12. The maximum magnetic field gradient is reached 10 ms after increasing the control voltage of the power supply. During this ramping time, the transfer efficiency rises continuously and saturates as soon as the maximum field gradient is reached. The overall gain in transfer efficiency is a factor of 3.

**Saturation of transfer** Fig. 2.13 shows the dependence of transfer efficiency on the size of the Li-MOT. When loading  $\gtrsim 10^7$  Li atoms into the Li-MOT, the MOT enters the density limited regime and temperature rises. The positive effect of slightly increased spacial overlap is derogated by the reduced overlap in momentum space. Thus, we observe saturation of the

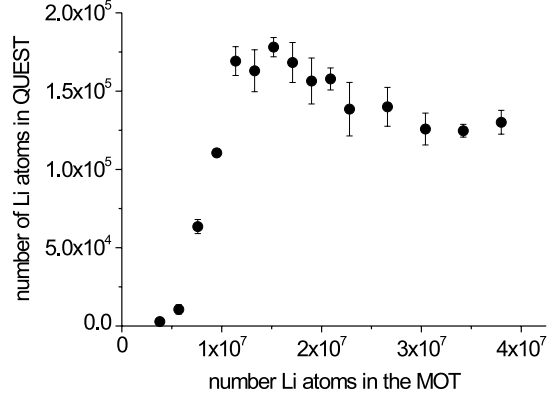


Figure 2.13: Transfer of Li atoms into the QUEST as a function of the number of atoms loaded into the MOT.

transfer efficiency Li atoms at about  $10^7$  Li atoms loaded into the MOT. The maximum number of transferred atoms amounts to  $2 \times 10^5$ . The temperature of the trapped Li sample cannot be directly measured since the density is too low for absorption imaging (see Sec. 2.6.2). In addition, due to the low initial density, the scattering cross-section of Li is very small, preventing the Li sample to thermalize within the observation times (see Sec. 3.2). Therefore, the energy distribution of the Li sample in the QUEST reflects the projection of the (thermal) distribution of Li atoms released from the MOT onto the density of states of the QUEST potential. This distribution is non-thermal since preferentially high-energetic states close to the edge of the trapping potential are populated. Strictly speaking, the temperature is undefined, therefore we specify the mean kinetic energy which is on the order of  $150 \mu\text{K} \times k_B$ .

### 2.5.3 Combined transfer

There are different possible timing schemes for combining both transfer of Li and Cs in one experimental cycle. The easiest way would be to load both Li and Cs-MOTs at the same time and to transfer both species simultaneously into the QUEST. However, there are two reasons why this procedure is unfavorable. First, light-assisted, exoergic collisions in the overlap region of the two MOTs dramatically reduce the steady-state number of atoms of both kinds [Schlöder et al., 1999]. Second, due to slight imbalance of the radiation pressure, the centers of the two MOTs do not exactly coincide. Therefore,

the Li-MOT has to be repositioned using homogeneous magnetic offset-fields, as discussed in Sec. 2.5.2. This, however, is only possible if the Li transfer is separated in time from the Cs transfer. Now the question arises, which order is best, first transfer of Li and then Cs or vice versa ?!

**Light-assisted collisions** The answer appears obvious, when considering the long-range interaction potentials of groundstate Li and excited state Cs\* and vice versa (see Sec. 5.2). The long-range Van-der-Waals interaction between Cs\* and Li is exclusively attractive, whereas the Van-der-Waals potential of Cs interacting with Li\* always leads to repulsion. In the case of attractive interaction, Cs\* and Li are accelerated towards each other during the collision which enhances the probability of an exoergic collision (“flux enhancement” [Weiner et al., 1999]). In this case, both atoms escape out of the MOT. In the case of repulsive interaction, Cs and Li\* repel each other, thereby suppressing exoergic collisions (“optical shielding”). Hence, it appears advantageous to first accumulate and transfer Cs, and then load and transfer Li while Cs is already optically stored in its groundstate. In order to further minimize light-induced heating and loss processes, the Li-MOT is loaded spatially displaced from the stored Cs sample in the QUEST. The latter scheme we will call “combined transfer”, the reversed timing we will speak of as “reversed transfer”.

However, there is also elastic interaction in addition to exoergic collisions. Since in both Li and Cs-MOTs the temperature is higher than the trap depth of the other species, we also expect heating and trap loss from elastic collisions. Moreover, we may expect perturbations from the atomic beams that propagate through the QUEST region during MOT loading. Even the MOT lasers and the switching of the MOT magnetic field may cause heating and trap loss of the trapped species. Here, we present the experimental investigation of the two transfer schemes.

**Superimposed traps** Figures 2.14 display the number of Li and Cs atoms remaining in the QUEST after 0.5 s simultaneous storage time as a function of MOT loading time. When we load the Cs-MOT first up to a fixed fluorescence level and we then load the Li-MOT during a variable time interval, we obtain plot (a) (combined transfer). The Li transfer clearly saturates after a MOT loading time of about 1.5 s. The number of already transferred Cs atoms is apparently affected by the Li-MOT, in spite of optical shielding due to the repulsive long-range interaction potential. Exponential fitting of the data yields a time constant of 3.3 s. However, Cs loss during the typical Li-MOT loading time of 1.5 s is only about 30%. Fig. 2.14 (b) shows the

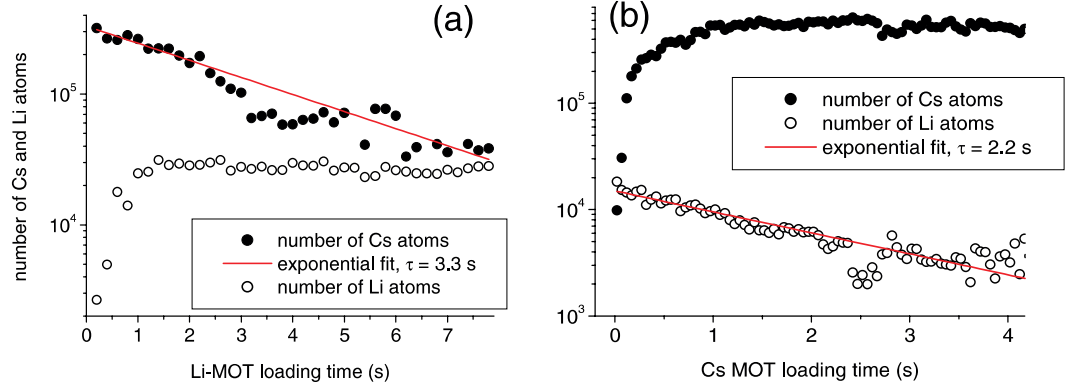


Figure 2.14: Number of Li and Cs atoms remaining in the QUEST as a function of loading time of the Li-MOT (a) and Cs-MOT (b).

experimental results for reversed transfer. The Li-MOT is loaded first up to a fixed fluorescence level before transferring into the QUEST. Then the Cs-MOT is loaded during a variable time interval, before transferring Cs into the QUEST. Apparently, the Cs transfer saturates as quickly as the Li transfer, however, on a much higher level. The number of Li atoms surviving the Cs-MOT is well fitted by an exponential function. The decay constant of 2.2s is indeed smaller than the one measured in case (a), as expected from the behavior of the long-range interactions.

In Fig. 2.15 (a), we record the loss of Li and Cs from the QUEST as a result of shining in the Li atomic beam for a variable length of time after combined transfer. The Li oven was operated at a temperature of 440 °C. Clearly, the atomic beam has only little influence on the optically trapped Cs and no effect on Li. If we additionally switch on the Li-MOT lasers, the number of stored Cs atoms decays with a time constant of 7.7 s. However, the effect of the Li lasers without atomic beam was found to have no influence at all. From these observations we deduce that perturbations are mainly caused by collisions with optically excited Li atoms.

**Shifted MOTs** Fig. 2.16 displays the transfer efficiencies for combined and reversed transfer as a function of the magnetic offset field which is used for displacing the second MOT. The offset field is applied along the symmetry axis of the MOT quadrupole field. Thus, 1 G corresponds to about  $1/14 \text{ cm} \approx 0.7 \text{ mm}$  of displacement. In the case of combined transfer (a), we see no effect on the stored Cs when the Li-MOT is loaded at different positions during 1 s. However, in the reversed transfer scheme, the Li atoms in the QUEST are noticeably affected by the 2 s Cs-MOT loading phase. Interestingly, from

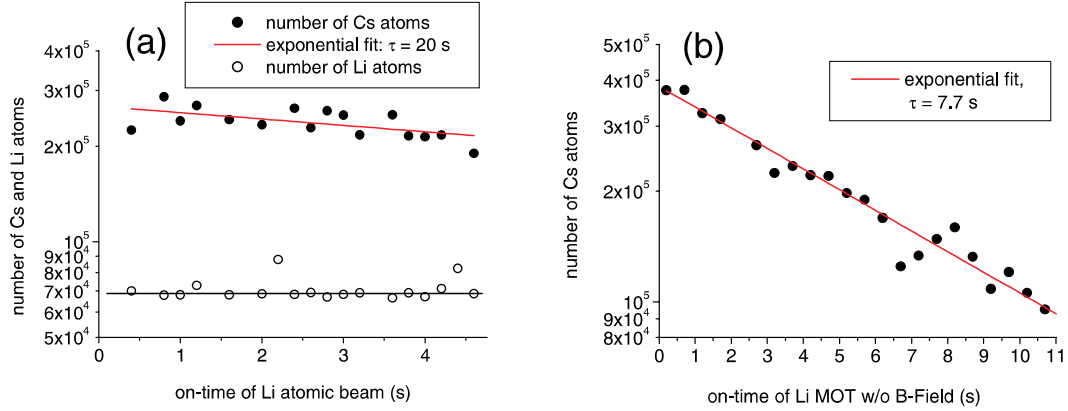


Figure 2.15: Number of Li and Cs atoms remaining in the QUEST as a function of illumination time by the Li atomic beam (a) and by the Li atomic beam plus Li-MOT lasers (b).

the width of the minimum in recaptured Li atoms we can infer an effective width of the Cs-MOT of roughly 0.6 mm, which matches the observed width using absorption imaging quite well.

Figures 2.14 and 2.16 clearly show that the combined transfer scheme is more advantageous compared with the reversed one, in particular since the number of Li atoms initially transferred into the QUEST stays far behind the number of transferred Cs atoms for reasons discussed in sections 2.5.2 and 2.5.1. All measurements involving simultaneously stored Li and Cs in the QUEST are performed using the combined transfer scheme. The detailed timing scheme is sketched in Fig. 2.17. In table 2.2 we summarize the most important parameters characterizing single-species and combined transfer.

**Cooling in the QUEST** Finally, we analyze the influence of the additional molasses pulse applied to the Cs sample after both Cs and Li have been transferred into the QUEST. Fig. 2.18 displays the number of recaptured Li and Cs atoms as a function of the duration of the cooling pulse. The frequency is set to  $3 \Gamma$  blue detuned with respect to the transition  $F = 4 \rightarrow F' = 4$ . Clearly, the molasses pulse has a stronger influence on the Cs than on the Li sample. The slow Li loss with increasing molasses duration is caused by exoergic collisions with excited Cs atoms. However, during the typical pulse length of 5 ms the Li remains nearly unaffected. This result is very encouraging, since it opens the way to repeated optical cooling of Cs in order to extract the gained heat from thermalization with Li (see Sec. 3.3).

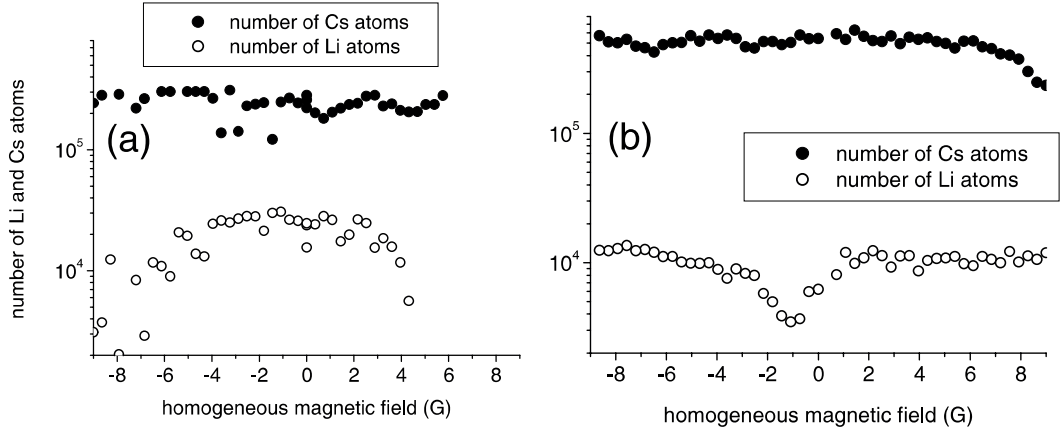


Figure 2.16: Number of recaptured Li and Cs atoms as a function of the magnetic displacement field. (a) First Cs transfer, then Li-MOT loading during 1 s. (b) First Li transfer, then Cs-MOT during 2 s.

## 2.6 Diagnostics

The most important parameters that we measure in our experiments are: number of atoms, temperature, spatial dimensions of the atomic sample and density. These parameters are measured using two methods, imaging of the fluorescence and imaging of the absorption of the atomic cloud.

### 2.6.1 Fluorescence imaging

The simplest way of detecting the atomic sample is to record the light spontaneously scattered by the atoms when illuminated by near resonant light. In most cases, one simply detects the fluorescence light emitted by the atoms trapped in the MOT. Since the atoms remain trapped in the MOT for a long time, one can choose very long exposure times. Thus, it is possible to detect down to 100 atoms using our experimental setup. However, due to the light pressure acting on the atoms when illuminated by near resonant light, information about the shape and density of the atomic distribution is mostly lost when taking a fluorescence picture.

In our experiment, the fluorescence light is measured using photodiodes and a CCD camera. In addition, we use two video cameras mounted at an angle of  $90^\circ$  between each other to monitor the shapes and relative positions of the MOT clouds. The photodiode signals are mainly used for monitoring the loading curve of the MOT and thereby providing a trigger signal for starting the experimental cycle, as discussed in Sec. 2.4. Due to the low density of the

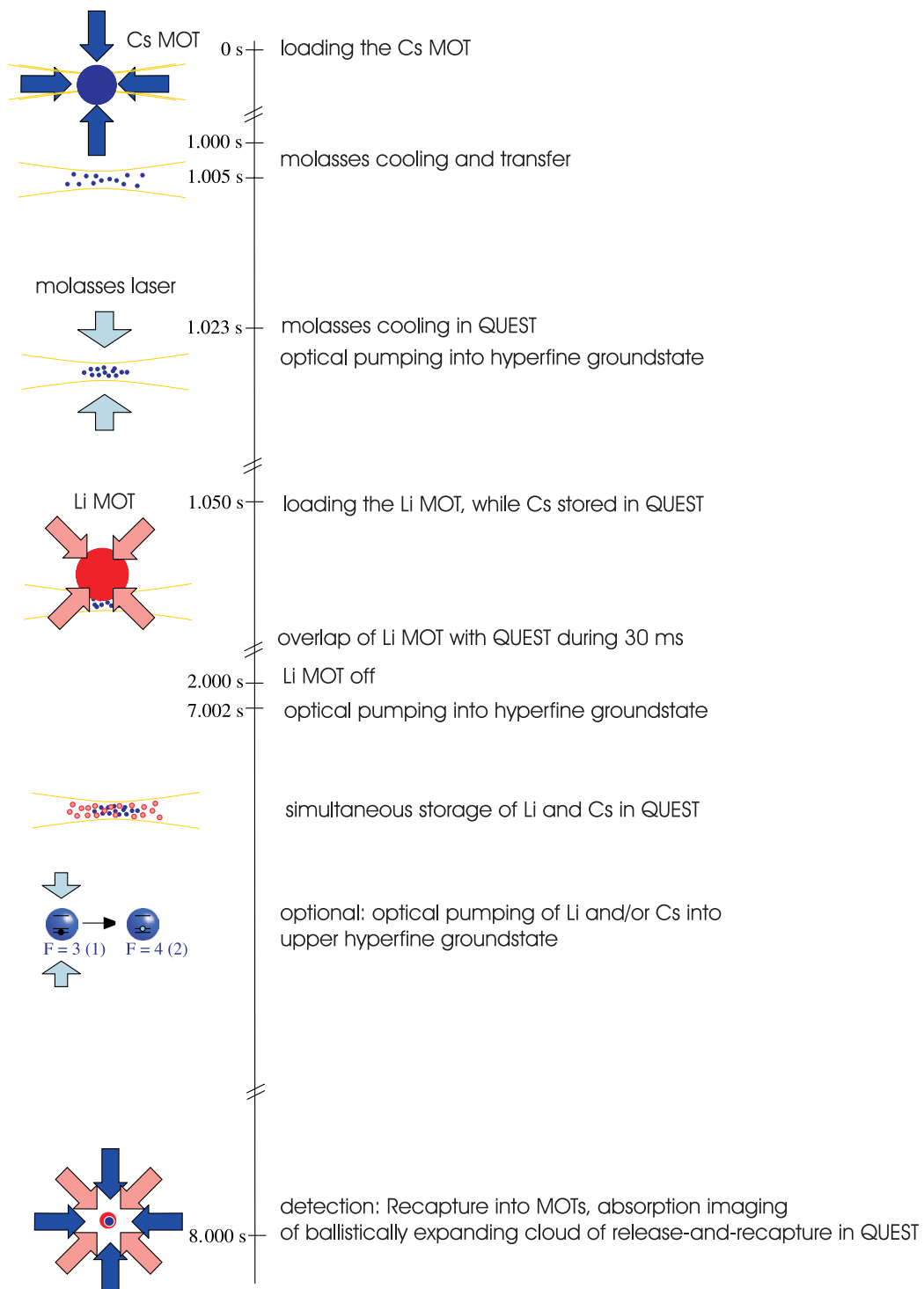


Figure 2.17: Loading sequence for simultaneous storage of Li and Cs in the QUEST.

	Lithium	Cesium
# of stored atoms	$1 \times 10^5$ ( $5 \times 10^5$ )	$1 \times 10^6$ ( $2 \times 10^6$ )
temperature	30 ( $\sim 150$ ) $\mu\text{K}$	30 (25) $\mu\text{K}$
density	$5 \times 10^{10}$ ( $\sim 5 \times 10^9$ ) $\text{cm}^{-3}$	$1 \times 10^{12}$ ( $3 \times 10^{12}$ ) $\text{cm}^{-3}$
radial/axial frequencies	$2\pi \times (2100/42)$ Hz	$2\pi \times (740/15)$ Hz
radial/axial extension	27/1300 (15/720) $\mu\text{m}$	8.5/420 (9.3/460) $\mu\text{m}$
potential depth	$300 \times k_B$ $\mu\text{K}$	$740 \times k_B$ $\mu\text{K}$

Table 2.2: Parameters for Li and Cs atoms simultaneously stored in the QUEST. The numbers in parentheses give the parameters for one single species in the trap showing the positive effect of sympathetic cooling on the Li parameters.

Li sample in the QUEST, fluorescence imaging is the only detection method used in all experiments involving Li. The number of Li atoms is inferred from the fluorescence signal by accounting for the laser frequency, sensitivity of the photodiode, electronic gain, and solid angle [Schlöder, 1998]. The effective temperature of the Li sample can be inferred from releasing-and-recapture measurements as outlined in appendix A.

Fluorescence imaging of the Cs sample is used in those measurements, when only information about the number of trapped atoms is required. Since we determine the number of Cs atoms from absorption images quite precisely, we calibrate the fluorescence signal to the absorption signal. Thus, the Cs fluorescence images provide the atom number with nearly equal reliability as absorption images.

### 2.6.2 Absorption imaging

For detection of the atom number, density and temperature of the trapped Cs sample, we use absorption imaging. This method consists of imaging the shadow imprinted into a resonant laser beam by the atomic cloud. The intensity of the laser beam must be much smaller than the saturation intensity of the atoms ( $I_{sat}=1.1 \text{ mW/cm}^2$  for Cs) so that induced photon emission is suppressed. Besides, the absorption pulse must be short compared with the time scale the dynamics of the atomic sample happens on. Due to low intensity and short illumination times, the atomic distribution remains nearly unaffected by the detection pulse. Thus, we obtain information about the

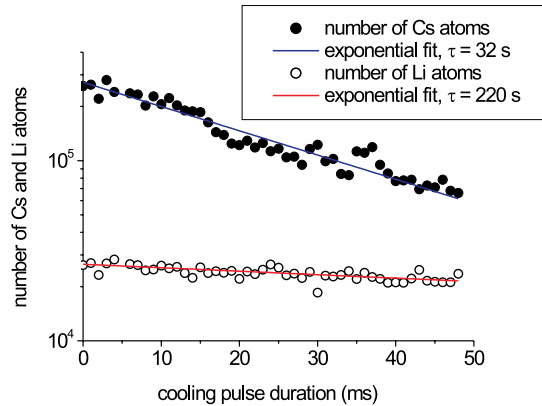


Figure 2.18: Influence of the addition Cs cooling pulse on the simultaneously trapped Li and Cs sample.

density distribution and the spatial dimensions of the atomic sample. For further details, the reader is referred to [Engler, 2000].

**Experimental implementation** In the experiments presented below, the absorption pulse is applied during 0.1-0.3 ms on resonance with the transition  $|F = 4\rangle \rightarrow |F' = 5\rangle$  at an intensity of  $30 \mu\text{W}/\text{cm}^2$ . For this purpose, we have set up a grating-stabilized diode laser, which is frequency stabilized to a Doppler-free spectroscopy signal, as described in appendix B. The laser was checked to have a spectral width much smaller than the natural line width  $\Gamma = 2 \times 5.3 \text{ MHz}$ . Before flashing the absorption pulse, the Cs atoms are optically pumped into the doubly polarized state  $|F = 4, m_F = 4\rangle$  by shining in both MOT repumper and a 0.1 ms polarizing pulse of the same light as the absorption pulse. Since the absorption beam is  $\sigma_+$ -polarized, the transition is closed, e.g. the on-resonance absorption cross-section is given by  $\sigma = 3\lambda^2/(2\pi)$ . In order to obtain the integrated absorption profile along the optical axis,  $A(x, y)$ , the absorption image of the cloud is divided by an image taken without atoms a few seconds after the absorption image. Thus, the intensity profile of the absorption beam is eliminated. Before the division, the stray-light background in the absence of absorption light is subtracted from each image.

Under the assumption of thermal equilibrium and a harmonic trapping potential, the atomic cloud has a Gaussian spatial distribution with cylindrical symmetry. Therefore, we integrate the logarithm of the absorption profile,  $\ln(A(x, y))$ , along the radial and axial coordinate with respect to the

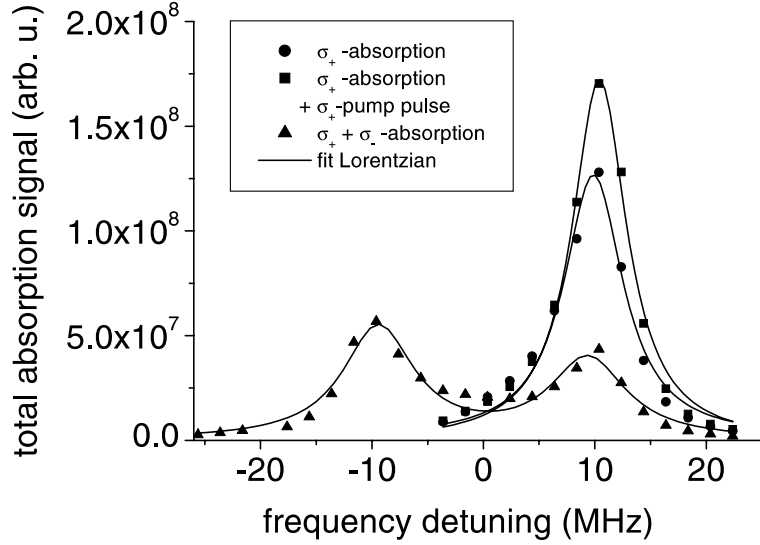


Figure 2.19: Absorption signal of the expanding Cs cloud as a function of detuning of the absorption laser with respect to the transition  $F = 4 \rightarrow F' = 5$ .

trapping laser beam and fit both one-dimensional profiles by Gaussian functions. From the fitted radial and axial Gaussian widths  $\sigma_{rad,ax}$ , we obtain the total number of atoms  $N = -2\pi\sigma_{rad}\sigma_{ax} \ln(1 - \hat{A})/s$ . Here,  $\hat{A}$  denotes the peak absorption. The average density of the atomic sample is determined by  $\bar{n} = \int n(\mathbf{r})^2 d^3r / \int n(\mathbf{r}) d^3r = N / ((4\pi)^{3/2} \sigma_{rad}^2 \sigma_{ax})$ . We estimate the systematic error of the determination of the atom number and density to be of the order of 20 %, mainly due to uncertainties in the absorption cross-section. Since this type of measurement is destructive, the procedure is repeated for the same initial conditions and various relaxation times. Shot-to-shot fluctuations of the atom number, density and temperature are in the range of 5 %.

**Preparation pulse** Fig. 2.19 displays the integral absorption signal of the expanding Cs cloud 60 ms after extinguishing the MOT lasers as a function of the frequency detuning of the absorption laser with respect to the transition  $F = 4 \rightarrow F' = 5$ . The length of the absorption pulse is 0.1 ms. During the entire experimental cycle we have applied a magnetic offset field of 7.2 G. The filled circles represent the measurement, in which the absorption pulse is  $\sigma^+$ -polarized. We observe a pronounced absorption peak at about 10 MHz detuning, which corresponds to the expected Zeeman-shift of the magnetic sub-level  $F = 4$ ,  $m_F = 4$ . This result can be explained by a combination of

optical pumping into the doubly polarized state induced by the absorption pulse and by the fact that the transition amplitude for the transition  $F = m_F = 4 \rightarrow F' = m'_F = 5$  is the strongest [Steck, 1998].

The filled squares depict the same measurement, except for an additional  $\sigma_+$ -polarized pumping pulse embedded in a repumping pulse which is applied 10 ms before the absorption pulse. Clearly, the absorption peak has increased. This results from the fact that the atoms are prepared in the doubly polarized state by the additional pumping pulse so that the absorption pulse couples more efficiently to the atoms. It was checked experimentally, that 0.1 ms is enough to maximally polarize the atoms with this scheme. However, this type of measurements does not provide independent detection of the population of Zeeman levels, since the detection process itself alters the level population. In the near future, we will implement a double-resonance scheme to be able to determine the population of magnetic sub-levels. For comparison, the triangles in Fig. 2.19 represent the same measurement as above, except that polarization of the absorption beam is linear resulting in a  $\sigma_+ - \sigma_-$  linear combination in the frame of the atoms. Clearly, both the doubly-polarized and the stretched states,  $F = m_F = 4$  and  $F = 4, m_F = -4$ , respectively, contribute strongest to the absorption signal.

### 2.6.3 Ballistic expansion thermometry

The Cs temperature is measured by absorption imaging in two different ways: The temperature in radial direction,  $T_{rad}$ , is obtained from the ballistically expanding Cs cloud after extinguishing the CO<sub>2</sub>-laser beam. The increasing radial width  $\sigma_{rad}$  as a function of the expansion time  $t_{exp}$  is fitted using the relation

$$\sigma_{rad}(t_{exp}) = \sqrt{\sigma_{rad}^2(0) + \frac{k_B T_{rad}}{m} t_{exp}^2} \quad (2.16)$$

Fig. 2.20 shows typical absorption images of the expanding Cs cloud 0.1 ms (a), 1.5 ms (b), and 3 ms (c) after switching of the CO<sub>2</sub>-laser. The radial width increases roughly linearly, whereas the axial width is totally dominated by the constant initial value  $\sigma_{ax}(0)$ .

Fig. 2.21 compares two measurements of radial widths as a function of the expansion time after extinguishing the CO<sub>2</sub>-laser. The initial conditions in both measurements were identical. In the measurement represented by the open squares, the laser beam is extinguished using the AOM; in the one depicted by (filled circles), the CO<sub>2</sub> RF-power is switched off. The solid lines represent results of fitting the data points with Eq. (2.16). Apparently,

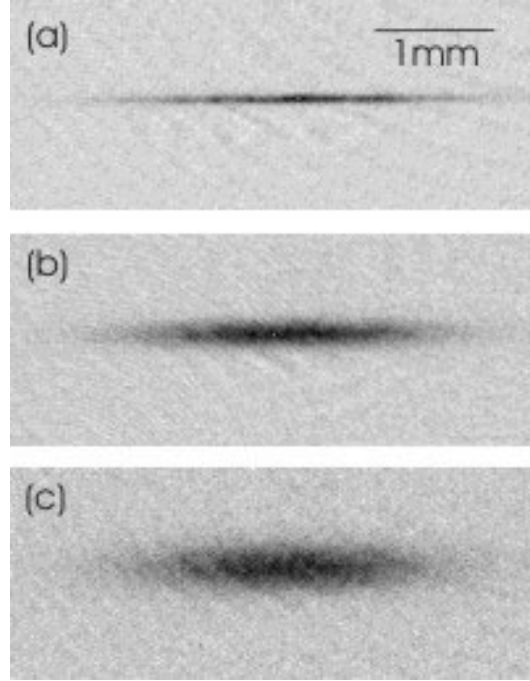


Figure 2.20: Absorption images of the expanding Cs cloud taken 0.1 ms (a), 1.5 ms (b), and 3 ms (c) after switching off the CO<sub>2</sub>-laser.

two different values for the temperature are measured. This effect can be attributed to adiabatic cooling of the atomic sample in the case of switching off the RF-power, since the switching time  $\tau \approx 150 \mu\text{s}$  is comparable to a quarter of the trap oscillation period in radial direction,  $\pi/(2\omega_{rad}) \approx 350 \mu\text{s}$  (see Sec. 3.2). To correct for this effect, all temperature measurement performed by switching of the RF-power supply are multiplied by a factor 1.28.

The axial temperature,  $T_{ax}$ , is inferred from the axial width of the Cs sample,  $\sigma_{ax}$ , using the relation  $m\omega_{ax}^2\sigma_{ax}^2 = k_B T_{ax}$ . Here,  $m$  denotes the mass of the Cs atom.  $T_{ax}$  and  $T_{rad}$  are in agreement within the uncertainty of the trap frequencies. We denote by  $T = (2T_{rad} + T_{ax})/3$  the average temperature.

## 2.7 Trap characterization

The exact knowledge of the parameters characterizing the trapping potential is crucial for understanding the loading behavior and the thermodynamics related to atom-atom interactions. We use two independent methods for determining the anisotropy and the maximum depth of the trapping potential: Measuring the oscillation frequency of trapped atoms in radial and axial

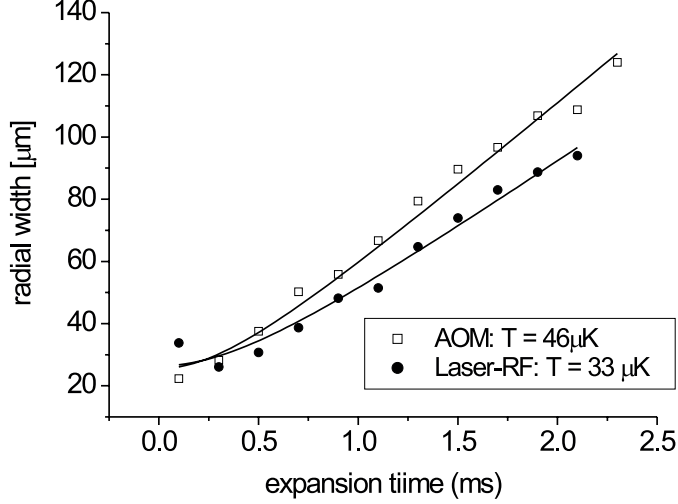


Figure 2.21: Comparison of the radial expansion curves when CO<sub>2</sub>-laser beam is extinguished using the AOM (open squares) and when the RF-power supply of the CO<sub>2</sub>-laser is switched off (filled circles).

directions gives information about the stiffness of the potential in these directions. By scanning the shift of the atomic resonance frequency due to the AC-Stark effect we directly measure the depth of the trapping potential  $U_0$ .

### 2.7.1 Trap oscillations

If the temperature of the trapped atoms is small compared with the depth of the trapping potential,  $T \ll U_0/k_B$ , then the atoms are preferentially localized close to the center of the trap. In this case, the trapping potential can be approximated by a simple cylindrically symmetric harmonic oscillator,

$$U(r, z) \approx -U_0 \left( 1 - 2\frac{r^2}{w_0^2} - \frac{z^2}{z_R^2} \right). \quad (2.17)$$

The radial and axial trap frequencies are given by

$$\omega_{rad} = \sqrt{\frac{4U_0}{mw_0^2}}, \quad \omega_{ax} = \sqrt{\frac{2U_0}{mz_R^2}}. \quad (2.18)$$

In our experiment, we observe damped harmonic oscillations in both radial and axial directions. The exponential damping originates from the fact

that the trapping potential is not a pure harmonic potential. Since the trapped atomic cloud has a finite extension, those atoms with large oscillation amplitudes are affected by the non-harmonic part of the potential. Their oscillation frequency is decreased with respect to the pure harmonic oscillation. This leads to diffusion of the initially coherent oscillation of every atom. The oscillation of the atomic ensemble appears to be damped, even though each atom continues to oscillate. As a second consequence of the non-harmonicity of the trapping potential, the radial and axial degrees of freedom are coupled. A pure axial oscillation eventually evolves into a radial one, and vice versa. Third, we only expect a harmonic oscillation of an ensemble of atoms, if the ensemble is thermal. Due to the comparatively fast thermalization dynamics, this condition is well fulfilled in the case of Cs (see Sec. 3.2).

**Axial oscillations** Fig. 2.22 shows two series of absorption images of the Cs cloud containing  $5 \times 10^5$  atoms at a temperature of  $35 \mu\text{K}$ . Since the measurement is destructive, each picture results from repeating the experimental cycle with increased storage time. Each picture is taken 3 ms after extinguishing the  $\text{CO}_2$ -laser. In series (a), an axial oscillation of the center-of-mass of the atomic distribution is induced by loading the QUEST from a Cs-MOT, which is shifted by 1 mm with respect to the center of the QUEST. First, the atomic cloud moves left until it reaches the left turning point after about 25 ms, then it oscillates back.

**Radial oscillations** Fig. 2.22 (b) shows the oscillation of the radial width of the atomic distribution after 3 ms of ballistic expansion. The oscillation is excited by switching off the  $\text{CO}_2$ -laser during 1 ms and subsequently recapturing the atoms in the QUEST at  $t = 0$ . The second storage phase before releasing the atoms to take the absorption picture is increased in steps of 0.1 ms. The timing scheme is illustrated in Fig. 2.23. One clearly sees that the distribution first becomes broader until about 0.4 ms recapture time, then it narrows down again.

During the off-time of 1 ms, the atomic cloud expands by only about  $50 \mu\text{m}$ , compared to the waist of the  $\text{CO}_2$ -laser of  $w_0 = 84 \mu\text{m}$ . Therefore, practically all atoms are recaptured into the QUEST. The oscillation is induced by the fact that the expanding atoms are recaptured at a larger distance  $r$  from the center of the trap. The gained potential energy is subsequently periodically transformed into kinetic energy in the course of the oscillation. Since the oscillation mode has cylindric symmetry, the observed frequency amounts to twice the actual radial trap frequency. Of course, the

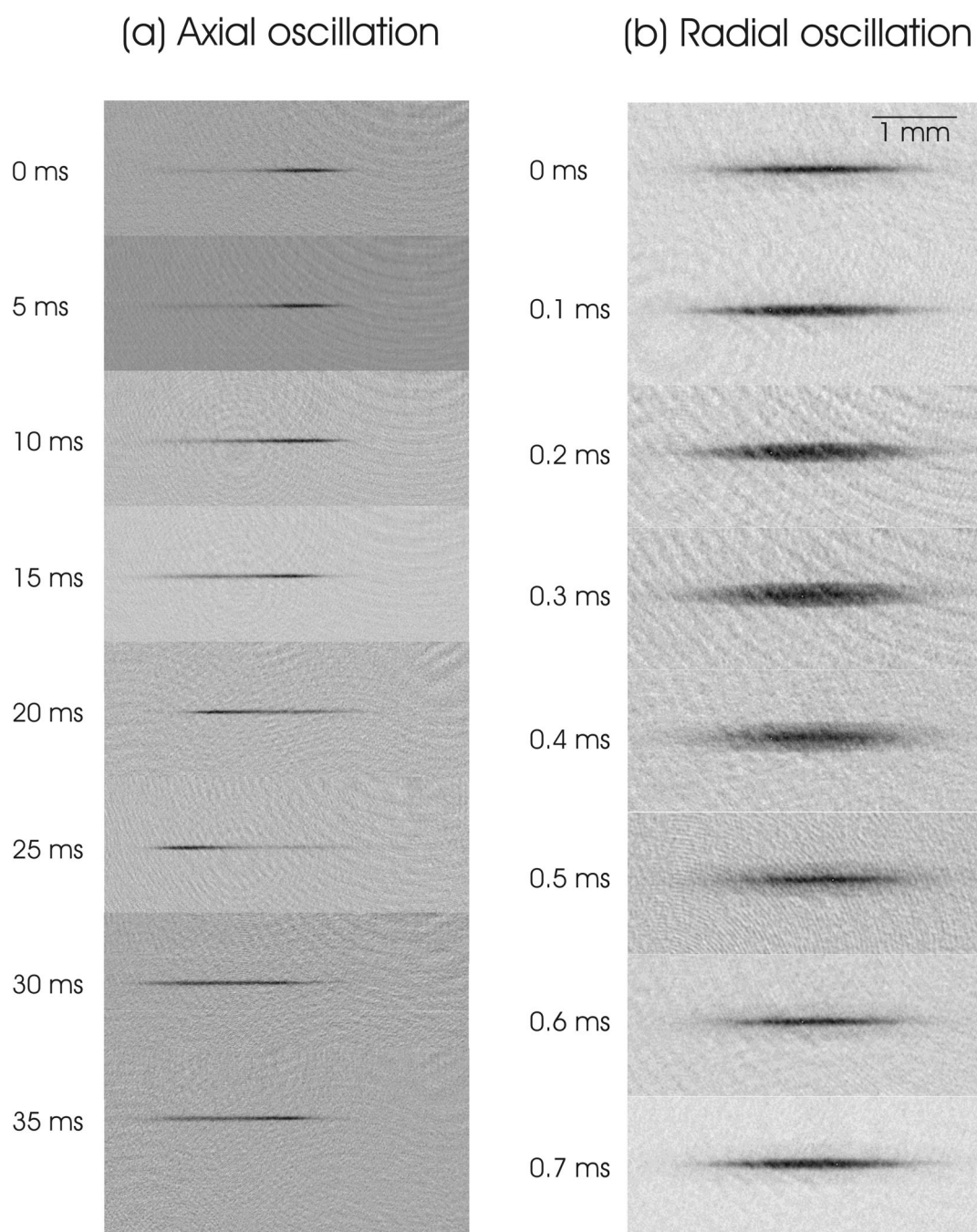


Figure 2.22: Absorption images of the trapped Cs cloud after 3 ms of ballistic expansion. (a) By loading the QUEST 1 mm shifted from the center of the trap, an oscillation in axial direction is excited. (b) Radial oscillation of the width of the atomic cloud.

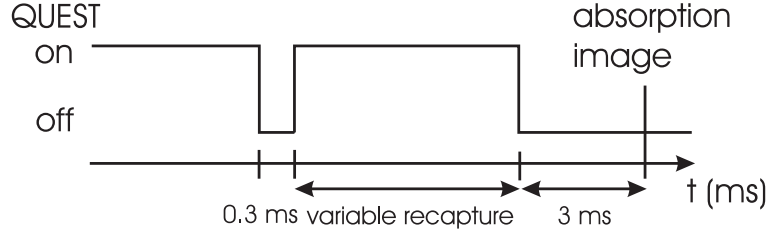


Figure 2.23: Excitation of radial trap oscillations. The  $\text{CO}_2$ -laser is switched off during 1 ms. After switching the laser on again, the atoms oscillate coherently in radial direction. This second storage phase has variable duration. The atomic distribution is detected by absorption imaging after 3 ms of ballistic expansion.

same happens in the axial direction, however, the gain in potential energy is negligible due to the weak axial confinement. Since the measured width of the distribution after 3 ms of free expansion is much larger than the initial width ( $\sim 10 \mu\text{m}$ ), the images in Fig. 2.22 (b) actually reflect the momentum distribution and the observed oscillation represents an oscillations in momentum space (the second term on the right-hand side of Eq. (2.16) dominates over the first one).

The peak positions and the radial widths of the Cs cloud are plotted in Fig. 2.24 (a) and (b), respectively, as a function of storage time after excitation of an axial and radial trap oscillation. The solid lines represent least-square fits of an exponentially damped sine-function. We obtain the radial and axial trap frequencies of  $\omega_{rad} = 2\pi \times (740 \pm 20)$  Hz and  $\omega_{ax} = 2\pi \times (15 \pm 1)$  Hz. With the AOM QUEST we measure  $\omega_{rad} = 2\pi \times (600 \pm 20)$  Hz and  $\omega_{ax} = 2\pi \times (12 \pm 1)$  Hz. It is important to note that the amplitude of the oscillation must be kept as small as possible to suppress the influence of the non-harmonic part of the trapping potential.

With the present trap configuration we measure the maximum trap depth to be  $U_0 = 740 \mu\text{K}$  (see Sec. 2.7.2). From the equations (2.18) we obtain the values  $w_0 = 92 \mu\text{m}$  and  $z_R = 3.2$  mm. These two value are not compatible with the intensity profile of a pure Gaussian beam, described by expression (2.9), with  $z_R = \pi w_0^2 / \lambda$ . From the latter expression we would expect a Rayleigh range of  $z_R = 2.5$  mm, which is a factor 1.3 smaller than the actually measured one. We attribute this discrepancy to spherical aberration of the  $\text{CO}_2$ -laser optics, resulting from the fact that all three lenses are spherical. In order to account for this effect, we describe the trapping potential by a three-dimensional Gaussian function with cylindrical symmetry

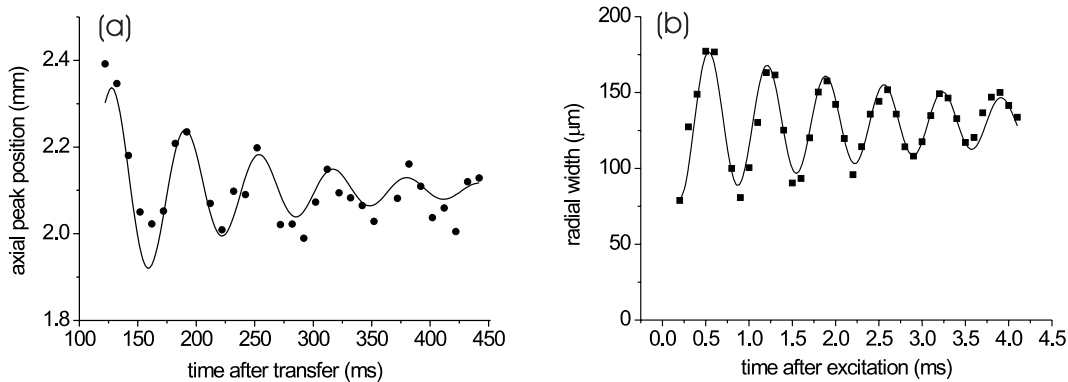


Figure 2.24: (a) Peak position of the axial absorption profile, which is fitted by a Gaussian function. The oscillation is excited by transferring the Cs atoms axially shifted by 0.5 mm from the center of the QUEST. (b) Width of the Gaussian fit to the radial profile of the atomic cloud after 3 ms of free expansion. The recapture time after excitation of the radial oscillation is varied.

with independent radial and axial widths,

$$U(r, z) = -U_0 \exp\left(-\frac{2r^2}{w_{rad}^2} - \frac{2z^2}{w_{ax}^2}\right). \quad (2.19)$$

Note that in the harmonic approximation this expression coincides with the previously derived one, Eq. (2.17), for  $w_{ax} = \sqrt{2}z_R$ .

**Parametric excitation** In order to cross-check the discussed method of measuring the radial trap frequency, we have performed the following experiment. Cs atoms are stored during 5 s in the AOM QUEST and then recaptured in the MOT to measure the number of remaining atoms. During the entire storage time, the intensity of the trapping beam is intensity modulated at a modulation depth of 8%. Fig. 2.25 displays the number of recaptured atoms as a function of the modulation frequency. We observe a minimum in the number of recaptured atoms at the modulation frequency of about 1.2 kHz, which exactly matches twice the radial trap frequency measured by the release-and-recapture method. When the trap depth is modulated at twice the trap frequency, the atoms are parametrically excited to perform oscillations. Eventually, they are ejected out of the trap, which leads to the observed trap-loss. The asymmetry of the minimum can be explained by the fact that those atoms that oscillate with a large amplitude are sensitive to smaller frequencies due to the non-harmonicity of the trapping potential.

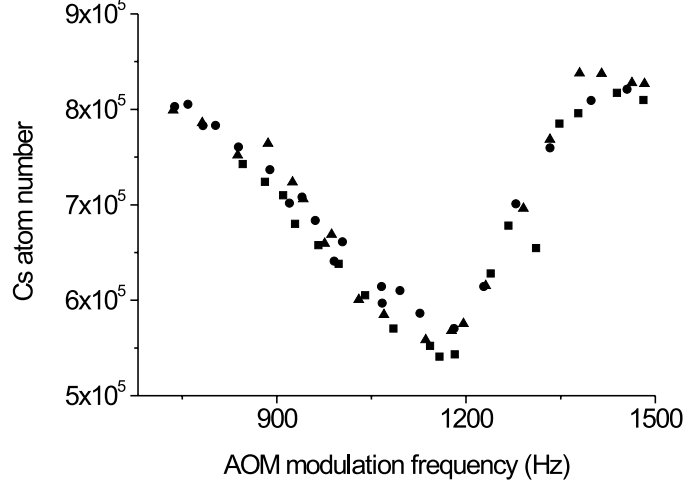


Figure 2.25: Trap-loss of Cs after 5 s storage time induced by parametric excitation. The intensity of the CO<sub>2</sub> trapping laser beam is intensity modulated with a modulation depth of 8% and variable frequency.

However, there are no higher frequencies involved in the system than the harmonic frequencies.

### 2.7.2 Light shift measurement

In the preceding section we have discussed the determination of trapping frequencies, which give information about the stiffness and anisotropy of the trapping potential. In this section, we present an experimental method how to measure the absolute depth of the trapping potential independently from the trap oscillations. The main idea is to record the shift of the resonance frequency of the trapped Cs atoms due to the AC-Stark shift. This frequency shift is proportional to the local depth of the trapping potential. Thus, by measuring the maximum shift in resonance frequency we obtain the value for the trap depth  $U_0$ .

Experimentally, we measure the absorption of the trapped Cs atoms as a function of the detuning of the absorption laser from the atomic resonance frequency  $\omega_0$ . In order to model the measured absorption curve we have to take into account the exact shape of the potential, the distribution of trapped atoms and the line width of the absorption laser. The latter is negligible in our case, due to the improved laser-lock described in appendix B.

Assuming a classical gas in thermal equilibrium, the distribution of the

trapped atoms at temperature  $T$  (in units of  $U_0/k_B$ ) as a function of their total energy  $\varepsilon$  is given by

$$\zeta(\varepsilon, T) = \rho(\varepsilon) e^{-\varepsilon/T}. \quad (2.20)$$

The energy density of states  $\rho(\varepsilon)$  contains all relevant information about the trapping potential  $U(\mathbf{r})$ . It is defined by [Luiten et al., 1996]

$$\rho(\varepsilon) \equiv (2\pi\hbar)^{-3} \int d^3r d^3p \delta(\varepsilon - U(\mathbf{r}) - p^2/2m), \quad (2.21)$$

such that  $\rho(\varepsilon)d\varepsilon$  is equal to the number of single-particle eigenstates in the trapping potential having energies between  $\varepsilon$  and  $\varepsilon + d\varepsilon$ . After integration over momenta  $\mathbf{p}$  we obtain

$$\rho(\varepsilon) = \frac{2\pi(2m)^{3/2}}{(2\pi\hbar)^3} \int_{U(\mathbf{r}) \leq \varepsilon} d^3r \sqrt{\varepsilon - U(\mathbf{r})}. \quad (2.22)$$

As discussed in Section 2.7.1, the trapping potential is assumed to be of Gaussian shape with cylindrical symmetry. For the sake of simple expressions we rescale the potential energy and coordinates to unit-less parameters

$$U'(\mathbf{r}) = U(\mathbf{r})/U_0; \quad x' = x/(\sqrt{2}\sigma_{ax}) \quad y' = y/(\sqrt{2}\sigma_{rad}) \quad z' = z/(\sqrt{2}\sigma_{rad}). \quad (2.23)$$

Now the trapping potential can be written as

$$U'(\mathbf{r}) = 1 - e^{-r'^2}. \quad (2.24)$$

The expression for the density of states 2.22 takes the form

$$\rho(\varepsilon) \propto \int_0^{-\ln(1-\varepsilon)} du \sqrt{u(\varepsilon - 1 + e^{-u})}, \quad (2.25)$$

where  $u = r'^2$ . By substituting this expression into equation (2.20) we obtain the energy distribution of the trapped atoms. Finally, we have to include into the calculation the fact that the energy distribution is probed with finite resolution due to the Lorentzian absorption profile of the Cs atoms

$$L(\delta) = \frac{2}{\pi(1 + 4\delta^2)}. \quad (2.26)$$

Here, the frequency detuning  $\delta$  is given in units of the natural linewidth  $\Gamma \approx 2\pi \times 5.3$  MHz for Cs atoms. The distribution function of the absorption laser detunings  $A(\delta, T)$  is obtained by convolution

$$A(\delta, T) = \int_0^C d\delta' \zeta(1 - \delta'/C, T) L(\delta - \delta'), \quad (2.27)$$

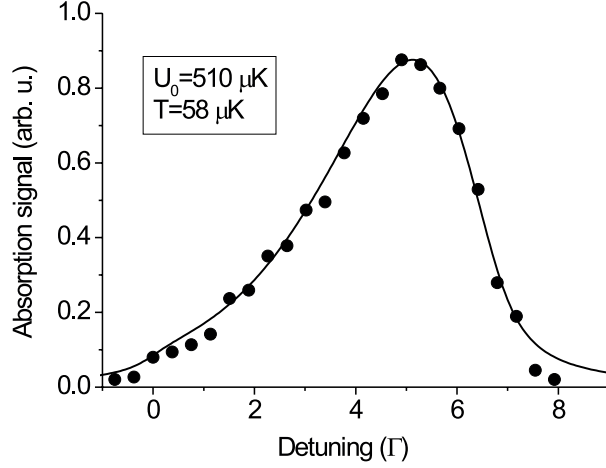


Figure 2.26: Integrated absorption signal of the trapped Cs cloud at  $T = 58 \mu\text{K}$  as a function of absorption laser detuning.

where  $C = (\alpha_{exc}/\alpha - 1) U_0/(\hbar\Gamma)$  is the conversion factor from energies  $\varepsilon$  (in units of  $U_0$ ) to detunings  $\delta$  (in units of  $\Gamma$ ).

Figure 2.26 displays the integral absorption signal of the Cs atomic cloud trapped in the AOM QUEST as a function of the detuning of the absorption laser. The model curve (solid line) results from fitting Eq. (2.27) to the experimental data points. The free parameters are the temperature, which becomes manifest in the width of the distribution, and the potential depth  $U_0$  determined by the position of the falling edge at large detunings. We obtain  $T = 58 \mu\text{K}$  and  $U_0 = 510 \mu\text{K} \times k_B$ .

The value for the temperature  $T$  coincides with the one measured by ballistic expansion (Sec. 2.6.2) within 10 % uncertainty. From the value of the trap depth  $U_0$  together with the measured trapping frequencies of  $\omega_{rad} = (600 \pm 20) \text{ Hz}$  one can calculate back the effective beam waist  $w_{eff} = \sqrt{4U_0/(m\omega_{rad}^2)} = 95 \mu\text{m}$  and laser power in the vacuum chamber  $P = \pi\varepsilon_0 c U_0 w_{eff}^2 / \alpha_{stat} = 79,5 \text{ W}$ . The latter is in agreement with the previously measured one  $P_{exp} = (70 \pm 10) \text{ W}$ . The value for the waist is somewhat larger than the measured ones in vertical and horizontal direction with respect to the AOM,  $w_{vert} = (68 \pm 10) \mu\text{m}$  and  $w_{horiz} = (56 \pm 10) \mu\text{m}$ , respectively 2.2.3. The reason for the discrepancy is the fact that waist measurements were done on a test assembly with slightly tighter focusing. From simulation of the beam path this difference is expected to be in the range of 20 %.

## 2.8 Conclusion

The quasi-electrostatic trap (QUEST) constitutes a universal optical trap suited for storing simultaneously both Li and Cs atoms in any internal state. The negligible photon scattering rate leads to complete suppression of optical excitation of the stored atoms, resulting in very long storage times of about 1 min. The QUEST is realized by a focused laser beam provided by a robust industrial-grade CO<sub>2</sub>-laser. An optimum strategy for combined loading of Li and Cs into the QUEST out of two individual MOTs is worked out, resulting in initially  $10^5$  and  $10^6$  trapped Li and Cs atoms in the QUEST, at temperatures of  $\sim 150$  and  $30 \mu\text{K}$ , respectively. Full information on the phase-space distribution of the trapped Cs sample is obtained from absorption images of the ballistically expanding atomic cloud. The number of Li atoms is determined from fluorescence images, and the Li temperature is inferred using release-and-recapture measurements. The trapping potential of the QUEST is characterized using two independent methods. Recording the radial and axial trap frequencies gives information about the stiffness of the potential, from measuring the light shift of trapped atoms we deduce the depth of the trapping potential. The resulting trap parameters are in good agreement with the measured parameters characterizing the CO<sub>2</sub>-laser beam.



# Chapter 3

## Elastic collisions

Elastic scattering constitutes the basis of thermodynamics. The exchange of energy and momentum between elastically colliding microscopic particles leads to thermal equilibrium of the ensemble. Understanding elastic collisions is crucial when studying the physics of mixed ultracold atomic gases in atom traps such as the QUEST.

When speaking of collisions in atom traps, we mean *ultracold* collisions, in which the relative velocity between the colliding atoms is  $\lesssim 1$  m/s. However, the physics of ultracold collisions is not just an extension of thermal collision processes to very small energies. A variety of new phenomena appears in the ultracold regime, which are invisible at usual temperatures. Since the kinetic energy of the colliding atoms is much smaller than the interaction energy, weak long-range interactions become important ( $\lesssim 1$   $\mu\text{m}$ ). Therefore, external electric and magnetic fields can critically influence the collision properties. At very low temperatures, the colliding atoms reveal their matter wave nature and the de Broglie wavelengths becomes larger than the typical range of the interaction potential. Therefore, ultracold collisions are governed by the laws of quantum mechanics. In particular, only partial scattering waves with zero angular momentum (*s*-waves) contribute to the total scattering amplitude. As the collision energy tends to zero, the collisional properties of the system reduce to one parameter, the scattering length  $a$ .

In this Chapter, we investigate the thermodynamics mediated by elastic collisions in ultracold samples containing Li atoms, Cs atoms and mixtures of Li and Cs. After a brief discussion of the basic concepts, we present experimental results on evaporative cooling of ultracold Cs. Then, we report on the first demonstration of sympathetic cooling in a mixture of optically trapped gases. We discuss particular experimental conditions, in which we observe a surprising effect we called “sympathetic evaporation”.

### 3.1 Basic concepts

In this section, we summarize the most important expressions derived from quantum mechanical scattering theory. For a detailed discussion, we recommend [Landau and Lifshitz, 1977, Heinzen, 1999, Pethick and Smith, 2002]. The total cross-section for elastic scattering of two distinguishable particles is given by the sum over all partial scattering cross-sections

$$\sigma_l = \frac{4\pi}{k^2}(2l + 1) \sin^2 \delta_l, \quad (3.1)$$

where  $\hbar k$  denotes the relative momentum and  $\delta_l$  represents the scattering phase for each angular momentum  $l$ . The scattering phase can be seen as the shift in phase of the scattered radial wave function with respect to the incoming resulting from the interaction. Obviously, the scattering cross-section  $\sigma_l$  cannot exceed the so called “unitary limit”,

$$\sigma_{l,max} = \frac{4\pi}{k^2}(2l + 1). \quad (3.2)$$

At very low collision energies ( $kr_0 \ll 1$ , where  $r_0$  is the characteristic range of the interaction potential), only partial waves with zero angular momentum ( $l = 0$ ) contribute to the scattering process, since the scattering cross-section for higher partial waves scales as  $\sigma_l \sim k^{4l}$ . The so-called *s*-wave scattering approximation is well fulfilled in our experiments with  $T \lesssim 100 \mu\text{K}$ . At very low energies, the elastic scattering cross-section tends to the finite constant value

$$\sigma = 4\pi a^2 = \text{const}, \quad (3.3)$$

if the interaction potential  $U(r)$  vanishes faster than  $r^{-3}$ . This condition is fulfilled for groundstate atoms considered here, which interact via the  $r^{-6}$ -Van der Waals potential. In Eq. (3.3),  $a = \lim_{k \rightarrow 0} \delta_0/k$  denotes the important quantity called scattering length. For two colliding alkali atoms, there are two different scattering states, characterized by singlet (spins anti-parallel) and triplet (spins parallel) symmetry. Therefore, one distinguishes between the singlet and triplet scattering lengths  $a_S$  and  $a_T$ , respectively. The triplet scattering length applies to the collisions of doubly-spin-polarized atoms, since their collisions proceed purely on the triplet potential. However, most other collisions involve an admixture of singlet and triplet states, and there is no case in which alkali atoms collide on their singlet potential.

For  ${}^7\text{Li}$ , the scattering lengths are  $a_T = (40.9 \pm 0.2) a_0$  and  $a_S = (-20 \pm 10) a_0$  [Abraham et al., 1997, Schreck et al., 2001b]. Due to the small mass of  ${}^7\text{Li}$ , the condition  $kr_0 \ll 1$  is well fulfilled in our experiments. Thus, we can

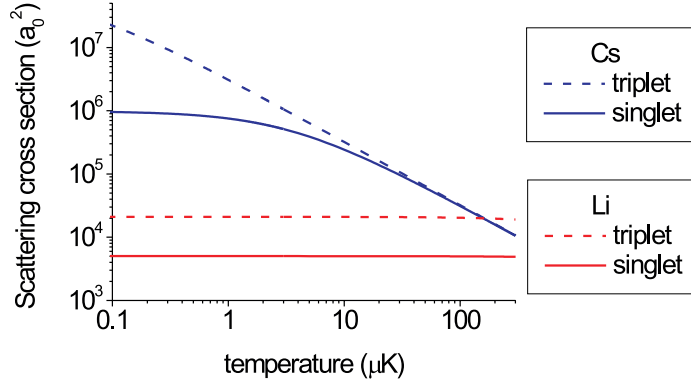


Figure 3.1: Cross-sections for elastic scattering between Cs atoms (blue lines) and between Li atoms (red lines).

calculate the temperature independent cross-section for collisions between Li atoms using formula 3.3. The resulting cross-sections are plotted in Fig. 3.1 as two horizontal lines.

If the interaction potential supports a weakly bound state of zero angular momentum ( $l = 0$ ) with a very small binding energy  $\varepsilon \ll U(r_0)$ , we speak of resonant scattering at low energies. Here,  $U(r_0)$  stands for the potential energy at the characteristic distance  $r_0$ . In this case, the scattering cross-section varies with momentum as

$$\sigma = \frac{4\pi a^2}{1 + k^2 a^2}. \quad (3.4)$$

This situation is true for collisions between  $^{133}\text{Cs}$  atoms [Arndt et al., 1997]. The singlet and triplet scattering lengths are quoted as  $a_S = 280 a_0$  and  $a_T = 2400 a_0$  in [Leo et al., 2000]. The triplet scattering length shows a pronounced dependence on the magnetic field  $B$  [Kerman et al., 2001, Weber et al., 2002]. It varies from a large negative value at zero field ( $-3000 a_0$  at 0 G) to large positive values at higher fields ( $1000 a_0$  at 55 G), going through zero at 17 G. This smooth variation over a wide magnetic field range can be interpreted as a result of a broad Feshbach resonance at about -8 G; here the negative field corresponds to a resonance position of +8 G [Leo et al., 2000] in the state with  $m_F = -3$ . In addition to this broad one, several narrow Feshbach resonances occur, with the most prominent one at 48 G [Weber et al., 2002].

Fig. 3.1 shows the corresponding cross-sections as a function of temperature  $T = \pi(\hbar k)^2/(16m_{\text{Cs}}k_B)$  for the singlet and triplet channel (blue lines).

For the achievable temperatures in our experiments (10 – 100  $\mu\text{K}$ ) the Cs cross-section is clearly determined by the unitary limit (Eq. (3.2)). At higher temperature ( $\gtrsim 200 \mu\text{K}$ ), the Cs cross-section falls below the one for Li in the triplet channel (red dashed line). It is important to note that in the case of bosonic particles in the same internal state, the scattering cross-sections discussed above are twice as large as the ones for distinguishable particles.

In order to establish the link between the microscopic collisional physics and macroscopic observables we have to perform averaging over the ensemble. We consider a binary mixture of interacting particles (1) and (2), each distributed in phase-space according to  $f_{1,2}(\mathbf{r}, \mathbf{p}_{1,2})$ . Here,  $\mathbf{r}$  and  $\mathbf{p}_{1,2}$  denote the position and momentum coordinates of atoms (1) and (2). The total number of collisions per unit time in a two-component gas is linked to the microscopic scattering cross-section  $\sigma$  by

$$\Gamma_{\text{coll}} = \langle \sigma(v_r)v_r \rangle_{r,v_r} \quad (3.5)$$

$$= \int d^3r \int \frac{d^3p_1}{(2\pi\hbar)^3} \int \frac{d^3p_2}{(2\pi\hbar)^3} F_1(\mathbf{r}, \mathbf{p}_1) F_2(\mathbf{r}, \mathbf{p}_2) \sigma \left( \left| \frac{\mathbf{p}_1}{m_1} - \frac{\mathbf{p}_2}{m_2} \right| \right) \left| \frac{\mathbf{p}_1}{m_1} - \frac{\mathbf{p}_2}{m_2} \right|. \quad (3.6)$$

The indices  $r, v_r$  in Eq. (3.5) indicate the spatial and momentum integration. In the approximation of isotropic  $s$ -wave collisions the cross-section  $\sigma_{12}$  can only depend on the relative velocity of the colliding particles,  $v_r = |\mathbf{p}_1/m_1 - \mathbf{p}_2/m_2|$ .

If each component gas is in thermal equilibrium, the phase-space distributions factorize into the spatial and momentum distributions,  $f(\mathbf{r}, \mathbf{p}) = f_{\mathbf{r}}(\mathbf{r}) \times f_{\mathbf{p}}(\mathbf{p})$ . The coefficient determining the inelastic collision rate per atom per unit volume  $G$  is obtained by the momentum integral [Pethick and Smith, 2002]

$$G = \langle \sigma(v_r)v_r \rangle_{v_r}. \quad (3.7)$$

## 3.2 Evaporative cooling

Evaporative cooling of trapped neutral atoms is an efficient cooling technique that has led to the coldest temperatures ever observed in the universe: submicro-Kelvin temperatures. It has been the key technique to achieve Bose-Einstein condensation in almost all the experiments so far [Ketterle and van Druten, 1996]. Originally demonstrated with magnetically trapped hydrogen [Hess et al., 1987], evaporative cooling was extended to alkali atoms by combining it with laser cooling [Petrich et al., 1994b]. Evaporative cooling in an optical dipole trap was

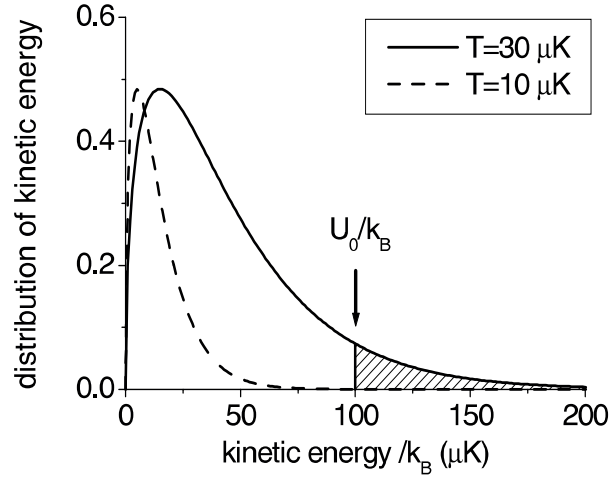


Figure 3.2: Distribution functions of kinetic energy at two evaporation steps. The initial temperature is  $T = 30 \mu\text{K}$  (solid line). The high-energy tail of the distribution is depleted due to the finite trap depth  $U_0 = 100 \mu\text{K}$  (hatched area). Thermalization of the truncated distribution results in lower temperature  $T = 10 \mu\text{K}$  and smaller atom number (dashed line).

first observed by [Adams et al., 1995]. Very recently, both Bose-Einstein and Fermi degeneracy were attained by evaporative cooling of alkali atoms trapped in quasi-electrostatic  $\text{CO}_2$ -laser traps (QUEST) [Barrett et al., 2001, Granade et al., 2002].

**Principle** Evaporation describes the process of selective removal of particles from a system with finite binding energy. The basic idea is sketched in Fig. 3.2. The thermal distribution with initial temperature  $T = 30 \mu\text{K}$  (solid line) is truncated due to the finite depth  $U_0 = 100 \mu\text{K}$  of the trapping potential. Since the evaporating particles (hatched area) carry away more than their share of thermal energy, the temperature of the system decreases. Thermalization due to elastic collisions makes evaporation proceed continuously until it eventually slows down to reach a state of quasi-equilibrium (dashed line). This type of evaporation in a constant trapping potential is called *plain evaporation*. If the system is modified during the evaporation process in such a way that less energetic particles can escape from the system we speak of *forced evaporation*. In this case, the goal is to efficiently convert a large number of atoms  $N$  into low temperature  $T$  by optimally controlling the potential parameters of the trap (usually the depth  $U_0$ ) or the elastic scattering cross-section  $\sigma_{el}$  of atoms.

Obviously, the precondition for evaporative cooling is the suppression of

exoergic collisions which lead to trap loss and even heating (see Chapter 4) instead of cooling. Thus, the elastic scattering rate per atom  $\gamma_{el} = \Gamma_{el}/N$  must exceed the inelastic rate  $\gamma_{inel} \ll \gamma_{el}$ . For the sake of simplicity, we substitute the phase-space integral (Eq. (3.6)) by  $\gamma_{el} = \sigma_{el}\bar{n}\bar{v}$ . The mean relative velocity  $\bar{v}$  is given by  $\bar{v} = 4\sqrt{k_B T/(\pi m)}$  and  $\bar{n}$  denotes the mean density. In the ideal case, the increase in density and/or scattering cross-section  $\sigma_{el}$  compensates for the loss of atoms so that  $\gamma_{el}$  rises during evaporation. This regime is called “runaway evaporation” and it allows for an increase in phase-space density  $n\Lambda^3$  by up to a factor  $10^6$  while reducing the number of trapped atoms by factor  $10^3$  [Mewes et al., 1996]. The critical value for Bose-Einstein condensation of a free gas is  $n\Lambda^3 \geq 2.612$ , where  $\Lambda$  stands for the thermal de Broglie wave length  $\Lambda = h/\sqrt{2\pi m k_B T}$ . The time scale we expect the evaporation dynamics to happen on is determined by the thermalization time  $\tau_{th}$ . It is related to the elastic scattering rate by  $\tau_{th} \approx 10/\gamma_{el}$  for a harmonic trap [Arndt et al., 1997]. Thus, it takes on average 10 collisions per atom for the entire sample to reach equilibrium.

**Evaporative cooling of Cs in the QUEST** In this section, we present experimental results on evaporative cooling of Cs atoms in the AOM QUEST [Engler et al., 2000]. The experiments were performed in the course of exploring improved conditions for laser cooling and evaporative cooling of Cs in a QUEST of variable trap depth. We use the simple focused-beam geometry described in Section 2.2.3. The laser intensity and therefore the depth of the trapping potential is controlled by means of an AOM inserted in the optical path. The trap depth and trap frequencies at full power are  $U_0 = (510 \pm 20) \mu\text{K} \times k_B$ ,  $\omega_{rad} = 2\pi \times (600 \pm 40) \text{ Hz}$  and  $\omega_{ax} = 2\pi \times (12 \pm 1) \text{ Hz}$  (see Section 2.7). Using this configuration we are able to load up to  $10^6$  Cs atoms into the QUEST at an initial temperature of  $(37 \pm 2) \mu\text{K}$ . We induce evaporation by linearly ramping down the intensity of the trapping beam during 1 s to  $U_0 = 160 \mu\text{K} \times k_B$ . The new trap frequencies are measured to be  $\omega_{rad} = 2\pi \times 330 \text{ Hz}$  and  $\omega_{ax} = 2\pi \times 6.5 \text{ Hz}$ . Subsequently, the temperature and number of the remaining atoms is measured using absorption imaging (see Section (2.6.2)).

Figure 3.3 shows the elastic scattering rate per atom

$$\gamma_{el} = \frac{2a_{S,T}^2}{\pi + \frac{4mk_B T}{\hbar^2} a_{S,T}^2} \frac{m}{k_B T} N \omega_{rad}^2 \omega_{ax} \quad (3.8)$$

expected for our experimental parameters. Here, we have substituted expression (3.4) for  $\sigma_{el}(T)$ . Since we are dealing with unpolarized atoms, we expect the effective scattering length to lie in between  $a_S$  and  $a_T$ . Thus, we

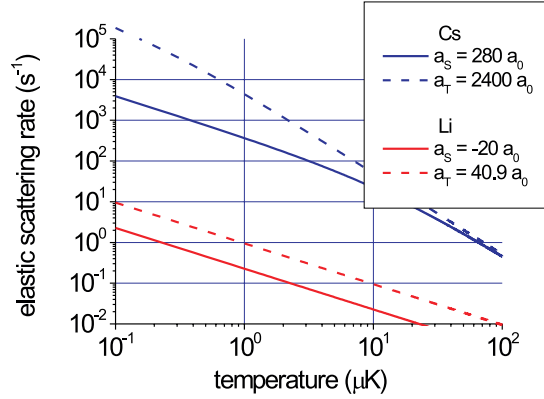


Figure 3.3: Calculated elastic scattering rate per atom  $\gamma_{el} = \sigma_{el}\bar{n}\bar{v}$  for the experimental parameters  $N_{Cs} = 10^6$ ,  $\omega_{rad} = 2\pi \times 330$  Hz,  $\omega_{ax} = 2\pi \times 6.5$  Hz for Cs (blue lines). The Cs singlet and triplet scattering lengths are  $a_S = 280 a_0$  and  $a_T = 2400 a_0$ , respectively [Leo et al., 2000]. For comparison, the red lines depict the expected scattering rate for Li.

expect initial collision rates of about  $5 \text{ s}^{-1}$  which implies a thermalization time  $\tau$  on the order of 5 s, much less than the storage time (10 – 100 s). For comparison, we have plotted the elastic scattering rate per atom expected in a thermal sample of  $10^5$  Li atoms for the same trap geometry. Obviously, the thermalization time for Li ( $10/\gamma_{el}^{Li} \gtrsim 1000$  s) exceeds the storage time in our trap. Therefore, we do not expect the Li cloud to thermalize in experiments involving only Li.

Figure 3.4 displays the time evolution of the number of atoms (a) and temperature (b) after adiabatically ramping down the intensity to the trap depth  $U_0 = 160 \text{ } \mu\text{K}$  in 1 s. During the first 10 s we observe a fast drop in the number of atoms compared to the exponential decay curve for a time constant  $\tau = 32$  s (dashed line). Simultaneously, the temperature decreases significantly from  $21 \text{ } \mu\text{K}$  down to  $16 \text{ } \mu\text{K}$ . We observe a thermalization time on the order of 5 s, as expected.

**Model** The solid lines in Figure 3.4 are the result of the numerical model described in [Weidemüller, 2000]. Briefly, the model is based on a kinetic equation for the evolution of the phase-space distribution, which is substituted by a Boltzmann distribution truncated at the trap depth [Luiten et al., 1996]. One finally arrives at two coupled rate equations for

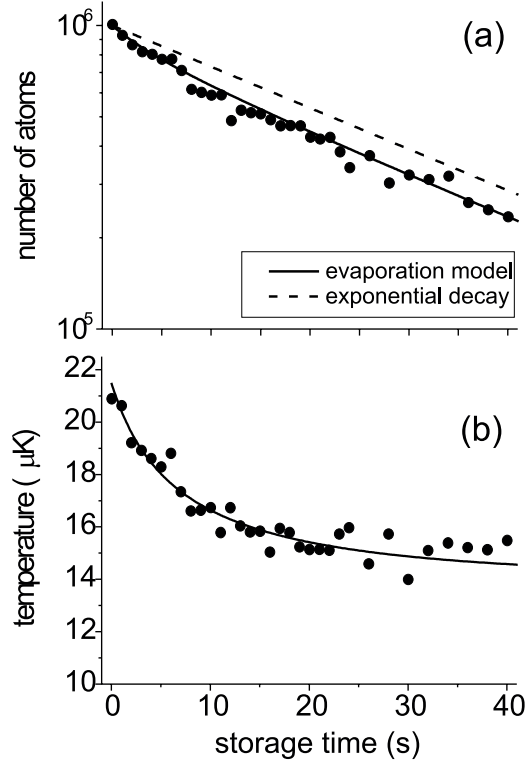


Figure 3.4: Measured loss of atoms (a) and drop in temperature (b) as a result of plain evaporation. At  $t = 0$  the depth of the trapping potential was reduced by ramping down the trapping beam intensity.

the number of atoms and temperature

$$\dot{N}(t) = -\sigma_{el}\beta_{evap}(T(t))N(t)^2 - \alpha_{bg}N(t) \quad (3.9)$$

$$\dot{T}(t) = -\sigma_{el}\xi_{evap}(T(t))N(t). \quad (3.10)$$

The first term on the right hand side of equation (3.9) describes the loss of atoms due to evaporation through elastic binary collisions, characterized by the cross-section  $\sigma_{el}$  and the temperature-dependent rate coefficient  $\beta_{evap}$ . The second term in Eq. (3.9) accounts for particle loss due to collisions with the hot background gas. The rate of change in temperature (Eq. (3.10)) resulting from evaporation is also proportional to  $\sigma_{el}$ , since elastic collisions promote atoms to energies higher than the evaporation threshold. The effect of gravity and the temperature dependence of the collision cross-section are not contained in the model. Due to gravity, evaporation predominantly takes place in only one spatial dimension thereby slowing down the cooling process. Therefore, the model prediction might overestimate the cooling rate.

Neglecting the temperature dependence of  $\sigma_{el}$ , however, is not expected to significantly affect the result since the change in temperature due to evaporation is small.

In order to fit the experimental data, we have varied both  $\sigma_{el}$  and  $\alpha_{bg}$ . The experimental data points in Fig. 3.4 nicely match the model curves (solid lines) despite the approximations in the model. The cross-section  $\sigma_{el}$ , which is assumed to be temperature independent, amounts to  $550 a_0$ . This value is in agreement within 10% with the calculated one,  $\sim 500 a_0$ , for a temperature of  $20 \mu\text{K}$  (see Section 3.1). The rate constant for background gas collisions  $\alpha_{bg}$  is determined by the exponential drop of  $N(t)$  after long storage times and takes the value  $\alpha_{bg} = 35 \text{ s}$ . This value is about half as large as the one measured at full laser power. The origin of the deviation is not fully understood.

**Forced evaporation** Besides the investigation of plain evaporation in a constant trapping potential we have performed experiments on forced evaporation by continuously ramping down the intensity of the trapping laser beam. In contrast to the standard RF-techniques for forced evaporation in magnetic traps [Mewes et al., 1996], both the depth and the curvature of the trapping potential are reduced in our case. Since the change of the potential is slow compared with the trap frequencies, we expect an additional cooling effect due to adiabatic expansion [O'Hara et al., 2001]. This effect can be estimated using the fact that the phase-space density  $\mu \propto \omega_{rad}^2 \omega_{ax} / T^3$  remains unchanged in adiabatic processes. By changing the depth of the trapping potential by a factor  $a = U'_0 / U_0$  we change the trap frequencies by  $\sqrt{a} = \omega'_{rad,ax} / \omega_{rad,ax}$ . Thus, we obtain the scaling law for temperature associated with adiabatic expansion,  $T' = \sqrt{a}T$ . However, adiabatic expansion also leads to decreasing density according to the scaling law  $n' = a^{3/4}n$ . Since the elastic scattering rate  $\gamma_{el}$  scales linearly with density, the evaporation rate goes down at the same rate as  $n$ .

Starting with the same experimental conditions as outlined above, we have applied a linear intensity ramp during 10 s down to 15% of the initial trapping beam intensity. The resulting parameters are  $T = 7 \mu\text{K}$  and  $N = 1.5 \times 10^5$  atoms at an average density of  $\bar{n} = 2 \times 10^{10} \text{ cm}^{-3}$ . Pure adiabatic expansion would have lead to  $T = 14 \mu\text{K}$  and  $\bar{n} = 5 \times 10^{10} \text{ cm}^{-3}$ . This confirms that evaporative cooling has actually taken place. However, due to the density decrease, the estimated elastic collision rate went down from  $20 \text{ s}^{-1}$  to  $5 \text{ s}^{-1}$ , which implies a thermalization time of 2 s.

Obviously, this approach will not lead to success, in particular if we have in mind sympathetic cooling of lithium to quantum degeneracy. One pos-

sible improvement could be the optimization of the shape of the intensity ramp as discussed in [O'Hara et al., 2001]. The more promising perspective, however, is improving the starting conditions, in particular the temperature. Therefore, in the near future we will implement Raman sideband cooling [Kerman et al., 2000] that should provide us with initial temperatures of  $\lesssim 1 \mu\text{K}$  at a density of  $\sim 10^{12} \text{ cm}^{-3}$ .

### 3.3 Sympathetic cooling

Cooling an ensemble of particles by exchanging heat through thermal contact with a colder one is the most obvious and fundamental cooling method. It is the only possibility to cool a gas that cannot be cooled directly, as it is the case for bosonic atoms with small elastic scattering cross-section [Bloch et al., 2001, Modugno et al., 2001] and for fermions at low temperature [Truscott et al., 2001, Schreck et al., 2001b, Roati et al., 2002, Hadzibabic et al., 2002]. Sympathetic cooling is particularly useful if the heat absorbed by the cooling agent can be extracted in an efficient and direct way, e.g., by laser cooling. In contrast to evaporative cooling, sympathetic cooling represents a loss-free approach which may be important for instance when the trapping configuration only allows for small particle numbers or when working with a rare species.

#### 3.3.1 Motivation

Sympathetic cooling has first been demonstrated with charged particles which thermalize through the long-range Coulomb interaction [Larson et al., 1986]. For neutral atoms and molecules one can use helium gas as a cooling agent which can be cooled cryogenically to well below 1 K [deCarvalho et al., 1999]. Only recently, sympathetic cooling has been successfully extended to the ultra-cold regime [Myatt et al., 1997, Truscott et al., 2001, Schreck et al., 2001b, Bloch et al., 2001, Modugno et al., 2001]. Quantum degeneracy of bosons and fermions was obtained by thermalization between atoms of the same species in different internal states [Myatt et al., 1997], between two isotopes of the same species [Truscott et al., 2001, Schreck et al., 2001a] and, as a recent highlight, between atoms of different species [Modugno et al., 2001, Hadzibabic et al., 2002]. The degree of quantum degeneracy obtained in those experiments was finally limited by two important loss processes: exoergic collisions between magnetically trapped atoms (see Chapter 4), and evaporation, which decreases the heat capacity of the cooling agent.

Li can neither be efficiently cooled using standard laser cooling techniques (see Sec. 2.5.2), nor can we cool it using evaporative cooling in our trap configuration (see Sec. 3.2). However, sympathetic cooling of Li through thermal contact with Cs seems to be a very promising approach. On the one hand, Cs is easily cooled down to a few micro-Kelvin in free space (see Sec. 2.5.1) using laser cooling techniques [Boiron et al., 1998, Vuletić et al., 1998]. On the other hand, we expect the onset of quantum degeneracy of Li at such low temperatures, as a consequence of the small Li mass (see Fig. 6.2). The prospect of extending our studies to a mixture of degenerate bosonic Cs and fermionic  ${}^6\text{Li}$  is particularly tempting [Modugno et al., 2002, O'Hara et al., 2002]. However, the cross-section for inter-species Li-Cs collisions mediating the heat exchange had been unknown thus far [Mosk et al., 2001b]. Precise measurements of inter-species scattering properties have only been performed with mixtures  ${}^6\text{Li}$  -  ${}^7\text{Li}$  [Truscott et al., 2001, Schreck et al., 2001b],  ${}^{87}\text{Rb}$  -  ${}^{41}\text{K}$  and  ${}^{87}\text{Rb}$  -  ${}^{40}\text{K}$  [Ferrari et al., 2002, Modugno et al., 2001].

### 3.3.2 Experiment

The experiments on sympathetic cooling were performed in the QUEST formed by  $\text{CO}_2$ -laser light of power 108 W focused to a waist  $w_0 = 86 \mu\text{m}$  [Kraft, 2001]. The resulting trap depth for Cs and Li is  $U_0^{\text{Cs}}/k_B = 0.85 \text{ mK}$  and  $U_0^{\text{Li}}/k_B = 0.34 \text{ mK}$ , respectively, with an experimental uncertainty of 10%. The radial and axial oscillation frequencies of trapped Cs (Li) atoms are  $\omega_{x,y}/2\pi = 0.85 \text{ kHz}$  (2.4 kHz) and  $\omega_z/2\pi = 18 \text{ Hz}$  (50 Hz). Atoms are transferred into the dipole trap from magneto-optical traps (MOT) for Li and Cs which are superimposed on the focus of the  $\text{CO}_2$ -laser beam. When loaded separately, we obtain  $5 \times 10^5$  Cs atoms in the QUEST, which we cool by polarization gradient cooling to  $20 \mu\text{K}$ . The Cs is optically pumped into the lowest hyperfine state ( $F = 3$ ), and since we compensate the magnetic field, the atoms are distributed evenly over the degenerate  $m_F$ -states. The peak density of Cs atoms in the QUEST is  $\sim 2 \times 10^{11} \text{ cm}^{-3}$ . From Eq. (3.8) we infer the collision rate to be approximately  $7 \text{ s}^{-1}$ , and thermalization through Cs-Cs collisions is estimated to take  $\sim 2 \text{ s}$ .

Since the Li temperature in the MOT exceeds the depth of the trapping potential  $U_0^{\text{Li}}/k_B$ , we only load up to  $10^5$  Li atoms into the QUEST without magnetic compression. Numerical simulations indicate that these atoms occupy a truncated thermal distribution with an internal energy of  $\sim 3k_B \times 75 \mu\text{K}$ , which only very weakly depends on the MOT temperature. The lithium atoms are optically pumped into the  $F = 1$  hyperfine state, and in the absence of a magnetic guiding field distribute themselves over the degenerate  $m_F$ -states.

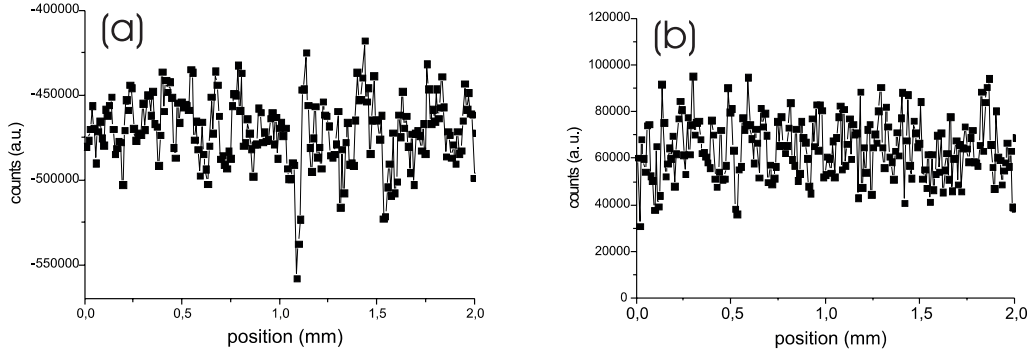


Figure 3.5: Radial projections of absorption images of the Li cloud before (b) and after 10 s of simultaneous storage with Cs (a).

In order to simultaneously trap the two species, a Cs-MOT is loaded and the atoms are transferred into the QUEST in optical molasses. Subsequently, a Li-MOT is loaded at a slightly different position, to minimize light-induced atom loss in a two-species. Once it reaches the desired density, the Li-MOT is compressed and overlapped with the QUEST for a few ms to optimize transfer of Li atoms. We can simultaneously trap typically  $4 \times 10^4$  Li atoms with up to  $10^5$  Cs atoms (see Sec. 2.5.3). After a variable interaction time in the QUEST, usually a few seconds, we analyze the gas sample. The temperature and atom number of Cs are determined by absorption imaging and time-of-flight velocimetry (see Sec. 2.6.2). The Li sample in our trap is too dilute to resolve its spacial dimensions using absorption imaging.

Fig. 3.5 displays projections onto the radial axis of Li absorption images taken after 10 s of storage time. When no Cs is loaded, the integrated absorption profile shows nothing but noise (b). However, when Cs is simultaneously stored together with Li, the Li cloud becomes visible on a signal-to-noise level of 1.6 (a). The increase in optical density can be attributed to an increase in spacial density as a result of sympathetic cooling.

For a more quantitative analysis, we determine the temperature of the Li gas using the release-recapture method, described in appendix A. Fig. 3.6 shows two such release-recapture measurements: one for a pure Li ensemble and one for a Li ensemble that has been trapped simultaneously with cold Cs. The pure Li gas is seen to be lost from the trap in  $\sim 0.4$  ms, while the ensemble of Li that has been in thermal contact with cold Cs is seen to contain many more slow atoms, which indicates cooling. From the fit of these release-recapture curves using the model discussed in appendix A, we infer the temperature of the Li cloud.

The thermalization time is measured by taking a series of temperature

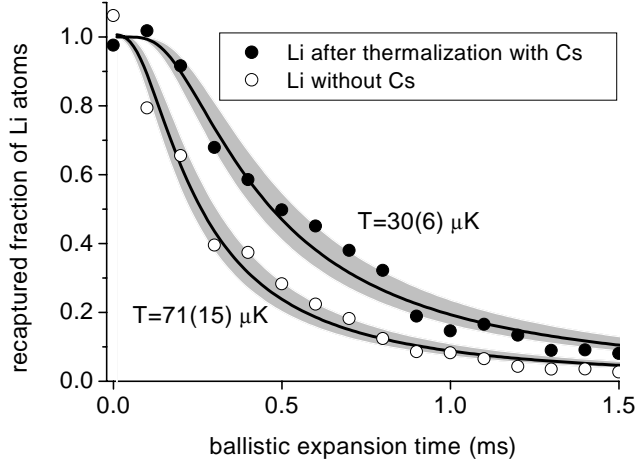


Figure 3.6: Release-recapture thermometry for Li atoms. The atoms are recaptured into the optical dipole trap after a variable time of free expansion. Open circles: Li without Cs. Closed circles: Li thermalized with Cs for 5 s. Solid lines: Fit curve. The gray area depicts a 20% variation in the temperature.

measurements for both components, as seen in Fig. 3.7. The Cs and Li temperatures converge to the same value  $\bar{T} = 33 \mu\text{K}$ . The measured atom numbers show that no significant loss of either Li or Cs occurs during thermalization. The thermalization time is  $1.6(2)$  s, indeed much shorter than the rest-gas induced decay time of the trapped gas.

### 3.3.3 Model

In order to deduce the Li-Cs scattering properties, an analytical model for the thermalization dynamics in trapped gas mixtures was developed [Mosk, 2000a, Mosk et al., 2001b, Mudrich et al., 2002]. An analytical formula for the evolution of the temperatures in a mixture of equal mass atoms has already been derived in [Delannoy et al., 2001]. The latter approach was extended to atoms with different mass, however, the dependence of the cooling efficiency on the mass ratio was derived under the assumption of equal trap frequencies. This assumption corresponds to an implicit mass dependence of the trap potential, which is not present for realistic traps and which leads to a strongly overestimated reduction of the cooling efficiency at a large mass ratio. In [Mosk, 2000a], the approach of [Delannoy et al., 2001] was adapted by assuming an explicit trap potential, so that our results remain

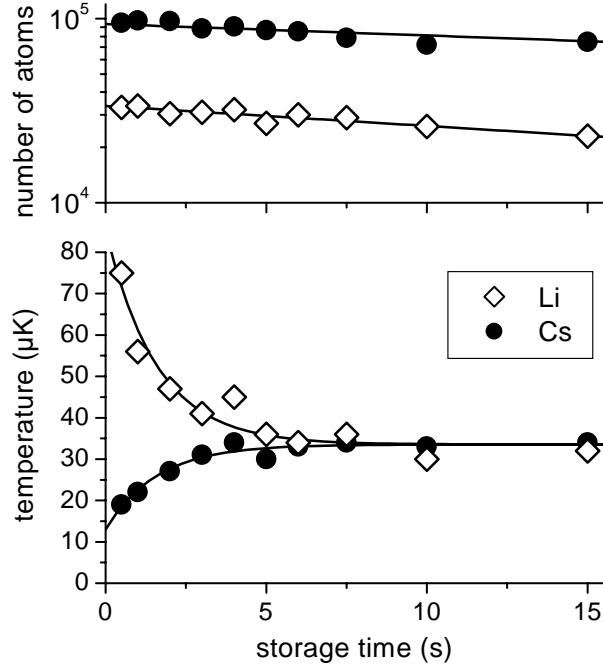


Figure 3.7: Evolution of Cs and Li temperatures (lower graph) and atom numbers (upper graph) during simultaneous storage. The temperatures exponentially approach equilibrium with a thermalization time constant of 1.6(2) s (solid lines in lower graph). The decay constant of the number of trapped atoms is 70 s for Cs and 40 s for Li.

valid for large mass ratios as it is the case for Li-Cs. Here, we summarize the basic assumptions and main results.

We consider a binary mixture of particles (1) and (2) trapped in a harmonic potential with cylindrical symmetry  $U_{1,2} = \frac{1}{2}m_{1,2}(\omega_{rad,1,2}^2(x^2 + y^2) + \omega_{ax,1,2}^2 z^2)$ . The depth of the potential for each particle is related to its static polarizabilities  $\alpha_{1,2}$  as  $U_1/U_2 = \alpha_1/\alpha_2$ . Each single component gas is assumed to be in thermal equilibrium. Thus, the phase-space density is given by

$$f(\mathbf{r}, \mathbf{p}) = n_0 \Lambda^3 \exp\left(-\frac{p^2}{2mk_B T}\right) \exp\left(-\frac{U(\mathbf{r})}{k_B T}\right) \quad (3.11)$$

where  $\Lambda = \sqrt{2\pi\hbar^2/mk_B T}$ . The local density is obtained from the integration

$$n(\mathbf{r}) = \int \frac{d^3 p}{(2\pi\hbar)^3} f(\mathbf{r}, \mathbf{p}).$$

We denote by  $n_0 = n(0) = (m/(2\pi k_B T))^{3/2} \omega_{rad}^2 \omega_{ax}$  the peak density. We

assume  $n_0\Lambda^3 \ll 1$ , e.g., both gases obey classical Boltzmann statistics. The total number of collisions per unit time in a two-component gas  $\Gamma_{\text{coll}}$  is obtained from the phase-space integral (3.6). The momentum integration is carried out by transforming into center-of-mass coordinates,

$$\begin{pmatrix} m_1 \mathbf{v}_1 \\ m_2 \mathbf{v}_2 \end{pmatrix} \rightarrow \begin{pmatrix} M (\mathbf{v}_1 + \mathbf{v}_2) \\ \mu (\mathbf{v}_1 - \mathbf{v}_2) \end{pmatrix}$$

where  $M = m_1 + m_2$  denotes the total mass and  $\mu = m_1 \times m_2 / M$  is called the reduced mass. We find

$$\begin{aligned} \Gamma_{\text{coll}} &= \sigma_{12} \frac{N_1 N_2}{V_{12}} \sqrt{\frac{8k_B}{\pi} \left( \frac{T_1}{m_1} + \frac{T_2}{m_2} \right)} \\ &\equiv \frac{N_1 N_2}{V_{12}} \sigma_{12} \bar{v} \end{aligned} \quad (3.12)$$

Here, we define the effective volume for binary collisions as a measure of the spatial overlap of the two clouds

$$\begin{aligned} V_{12} &= N_1 N_2 \left( \int d^3r n_1(\mathbf{r}) n_2(\mathbf{r}) \right)^{-1} \\ &= \left( \frac{2\pi k_B (T_1 + T_2 \frac{\alpha_1}{\alpha_2})}{m_1} \right)^{\frac{3}{2}} \frac{1}{\omega_{rad,1}^2 \omega_{ax,1}} \end{aligned} \quad (3.13)$$

Then, the collision rate takes the form

$$\Gamma_{\text{coll}} = \frac{\sigma_{12} N_1 N_2 \omega_{rad,1}^2 \omega_{ax,1}}{k_B \pi^2} \cdot \frac{m_1^{3/2} \sqrt{\frac{T_1}{m_1} + \frac{T_2}{m_2}}}{\left( T_1 + \frac{\alpha_1}{\alpha_2} T_2 \right)^{3/2}} \quad (3.14)$$

Next, we derive an expression for the average energy transfer per unit time. The energy of particle (1) is given by

$$\begin{aligned} E_1 &= \frac{p_1^2}{2m_1} \\ &= \frac{m_1}{2} \left( \mathbf{V} + \frac{\mu}{m_1} \mathbf{v} \right)^2 = \frac{1}{2} \left( m_1 V^2 + 2\mu V v \cos \theta + \frac{\mu^2}{m_1} v^2 \right) \end{aligned} \quad (3.15)$$

In an elastic collision, the absolute values of  $\mathbf{v}$  and  $\mathbf{V}$  cannot change, only  $\cos \theta$  can be different. After an isotropic (*s*-wave) collision,  $\cos \theta$  averages to zero. Thus, the mean energy lost in a collision with incoming  $v, V, \theta$  is

$\Delta E_1 = -\mu V v \cos \theta$ . The energy transfer rate follows from multiplying the integrand in expression (3.6) by this factor. By performing the integration in analogy to the derivation of expression (3.6) we obtain

$$\dot{E}_1 = \Gamma_{\text{coll}} \xi k_B (T_2 - T_1), \quad (3.16)$$

where  $\xi = 4m_1 m_2 / (m_1 + m_2)^2$ . Thus, the energy transfer is reduced by the factor  $\xi$  with respect to collisions between atoms with equal mass. For equal-mass atoms in a harmonic trap, approximately 3 collisions per atom are needed for thermalization [Arndt et al., 1997]. For  $^{133}\text{Cs}$  and  $^7\text{Li}$ , we need  $3/\xi \approx 15$  collisions per atom to thermalize.

If we assume an energy dependent scattering cross-section according to the unitary limit (3.2),

$$\sigma_{12} = \frac{4\pi}{k^2},$$

with  $k = \mu v / \hbar$ , we find in complete analogy with the energy-independent case

$$\dot{E}_1 = \frac{1}{2} \Gamma_{\text{coll}} \xi k_B (T_2 - T_1), \quad (3.17)$$

i.e. the energy transfer per collision is on average a factor 2 smaller for resonant collisions.

Numerically, the thermalization process can be studied by simulating collisions between two thermal distributions [Mosk, 2000b]. In the case studied in the analytical theory here, both gases stay Maxwell-Boltzmann distributed throughout the heat exchange process. This can be simulated for untrapped gases in the following way: An atom is selected at random from both distributions. The relative velocity is calculated, and a collision is simulated with a probability that is proportional to the relative velocity multiplied by the cross-section. If a collision takes place, the direction of the relative velocity is randomized.

In case both gases remain Maxwell-Boltzmann distributed, the result of the numerical simulation reproduces the analytically calculated thermalization time of  $\tau_{\text{therm}} = 3\tau_{\text{coll}}/2\xi$  for constant cross-section and  $\tau_{\text{therm}} = 3\tau_{\text{coll}}/4\xi$  for unitary cross-section. This is to be compared to a factor  $\sim 4$  in thermalization efficiency between constant cross-section and resonant collisions, found numerically in [Arndt et al., 1997] for collisional damping of deformation mode in a one component gas. We also simulated the case where only one distribution is assumed to remain thermal and the other distribution may evolve freely (although it is thermal both in the initial and final state). In this case, the thermalization is slightly slower, although the deviation is relatively small, on the order of 20%.

The change in temperature of the two component gases is given by

$$\begin{aligned}\dot{T}_1 &= \frac{\dot{E}_1}{C_1} \\ \dot{T}_2 &= -\frac{\dot{E}_1}{C_2},\end{aligned}\tag{3.18}$$

where  $C_{1,2} = 3N_{1,2}k_B$  are the heat capacities of ensembles in a harmonic potential. The time scale of thermalization  $\tau$  is related to the temperature difference  $\Delta T = T_1 - T_2$  as

$$\tau^{-1} = \frac{d(\Delta T)}{\Delta T dt} = \frac{\Gamma_{\text{Coll}}\xi}{3} \cdot \frac{N_1 + N_2}{N_1 N_2}.\tag{3.19}$$

For equal masses and trap frequencies we reproduce the result of [Delannoy et al., 2001].

For the initial conditions of our experiment we obtain an approximate initial cooling time constant, when we neglect the influence of the Cs temperature since there are more Cs atoms which are colder and more tightly confined than Li atoms,

$$\tau_{\text{initial}}^{-1} \approx \frac{\sigma_{\text{LiCs}}\omega_{\text{rad,Li}}^2\omega_{\text{ax,Li}}m_{\text{Li}}\xi}{\pi^2} \cdot \frac{N_{\text{Li}} + N_{\text{Cs}}}{3k_B T_{\text{Li}}}.\tag{3.20}$$

In the final stage of sympathetic cooling the final temperature  $\bar{T} = (N_1 T_1 + N_2 T_2)/(N_1 + N_2)$  is approached exponentially, with a time constant

$$\tau_{\text{final}}^{-1} \approx \frac{2\sigma_{\text{LiCs}}\omega_{\text{rad,Li}}^2\omega_{\text{ax,Li}}}{\pi^2} \left(1 + \frac{\alpha_{\text{Li}}}{\alpha_{\text{Cs}}}\right)^{-3/2} \sqrt{\frac{m_{\text{Li}}^3 \xi}{m_{\text{Li}} + m_{\text{Cs}}}} \cdot \frac{N_{\text{Li}} + N_{\text{Cs}}}{3k_B T_{\text{Li}}}\tag{3.21}$$

The effect of the mass difference on the thermalization time is a factor  $\xi^{-1/2} \approx 2.3$  in the time constant. With a large mass difference, the thermalization efficiency per collision is reduced by the factor  $\xi$ , but the collision frequency depends on  $\bar{v}$ , which is proportional to  $\xi^{-1/2}$ .

The thermalization curves shown in Fig. 3.7 are fitted simultaneously by exponential functions with identical time constant. Using expression (3.21), we infer the cross-section for Li-Cs collisions,

$$\sigma_{\text{LiCs}} = 8(4) \times 10^{-12} \text{ cm}^2.\tag{3.22}$$

Here, the main limitation of the accuracy is the determination of the absolute densities. This value stays behind the unitary cross-section  $4\pi/k_{\text{LiCs}}$  by a

factor 5. Assuming  $s$ -wave scattering dominates, we find an effective  $s$ -wave scattering length  $|a_{\text{LiCs}}| = (\sigma_{\text{LiCs}}/4\pi)^{1/2} = 180_{-50}^{+40}a_0$ .

It is interesting to compare the inter-species Li-Cs collision rate per Li atom  $\gamma_{\text{Li}}^{\text{final}} = (\tau_{\text{final}}N_{\text{Li}})^{-1}$  to the homonuclear Cs-Cs collision rate per Cs atom  $\gamma_{\text{Cs}}$  given by expression (3.8). For the approximation  $T_{\text{Li}} = T_{\text{Cs}} = \bar{T}$  and assuming the unitary scattering cross-section for Cs collisions,  $\sigma_{\text{Cs}} = 4\pi/k^2$ , we obtain

$$\frac{\gamma_{\text{Li}}^{\text{final}}}{\gamma_{\text{Cs}}} = 2 \frac{\sigma_{\text{LiCs}}}{\sigma_{\text{Cs}}} \sqrt{\frac{m_{\text{Li}} + m_{\text{Cs}}}{m_{\text{Li}}}} \left(1 + \frac{\alpha_{\text{Cs}}}{\alpha_{\text{Li}}}\right)^{3/2}. \quad (3.23)$$

At a temperature  $\bar{T} = 30 \mu\text{K}$  we find  $\gamma_{\text{Li}}^{\text{final}}/\gamma_{\text{Cs}} = 3.7$ . Thus, the Li atoms have roughly as high a collision rate with Cs as the Cs atoms themselves, even though the Cs-Cs collisions have the maximum  $s$ -wave cross-section. The explanation for this lies in the small unitary cross-section and the low thermal velocity for Cs, both a result of the high mass. The collision-enhancing effects of the low Li mass compensate the loss of thermalization efficiency that is caused by the mass ratio factor  $\xi$ .

### 3.4 Sympathetic evaporation

In a trap of finite depth, thermalizing collisions lead to evaporation of particles (see Sec. 3.2). This evaporation is practically absent in two cases: if the temperature is much lower than the trap depth (as it is the case for pure Cs samples in our trap) or if the collision rate is extremely small (as it is the case for pure Li samples in our trap). The thermalizing Li-Cs collisions enable, besides cooling, evaporation of the Li from the trap. The Li evaporates even under conditions where the Cs evaporation is negligible, as the trap depth for Li is significantly smaller than for Cs. Assuming energy-independent cross-sections, the evaporation probability per collision in an ensemble where the Cs and Li are thermalized is  $P_{\text{evap}} \sim \eta \exp(-\eta)$ , where  $\eta = U_0^{\text{Li}}/k_B T$ .

The numerical model described above was adapted for simulating sympathetic evaporation in a mixture of gases confined in trapping potentials of finite depth [Mosk, 2000b]. Due to the numerous simplifying assumptions, the model is mainly intended to give a qualitative understanding of the thermalization process in an open system.

An atom undergoing an elastic collision is considered to be lost from the trap if its kinetic energy exceeds its potential one,  $E_{\text{kin}}^{\text{Li}} > E_{\text{pot}}^{\text{Li}}$ . Fig. 3.8 shows the calculated energy distributions for the trapped Li and Cs atoms as a function of discrete collision times. The initial Cs distribution is thermal as a consequence of the short Cs thermalization time  $\tau \approx 0.5$  s. The initial Li distribution is represented by a Maxwell-Boltzmann distribution truncated

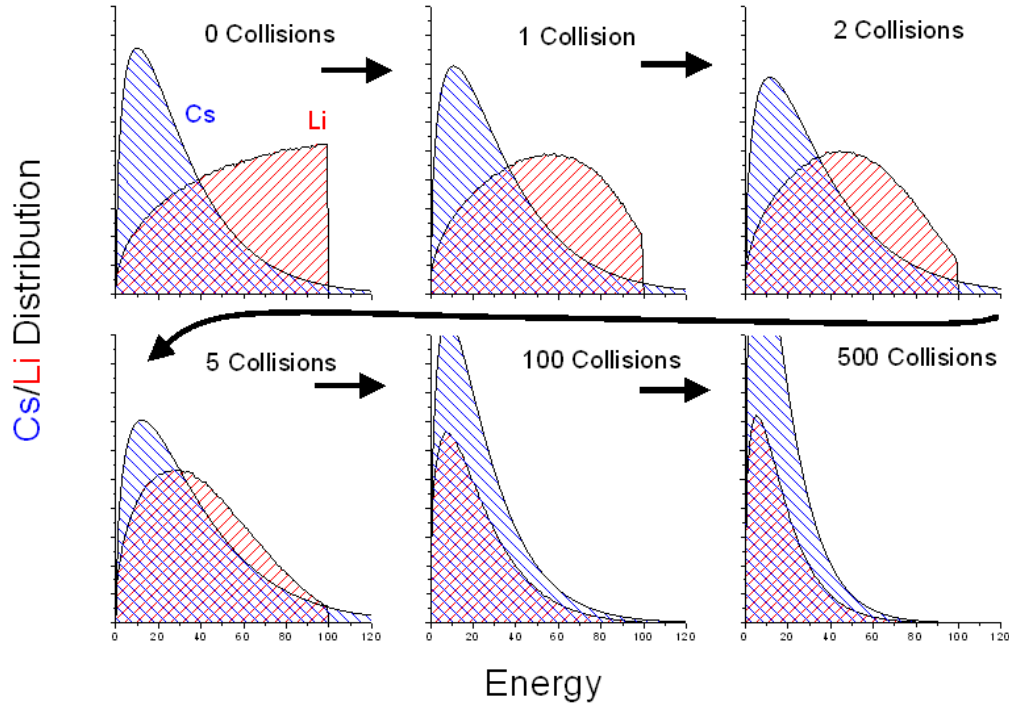


Figure 3.8: Numerical simulation of the evolution of Li and Cs energy distributions for various Li-Cs collision times. The initial Cs distribution is thermal whereas the one for Li is a Maxwell-Boltzmann distribution truncated at the depth of the trapping potential. As the two ensembles thermalize via elastic collisions the width of the Li distribution decreases drastically (sympathetic cooling). Surprisingly, the width of the final Cs distribution is also reduced (sympathetic evaporation).

at the potential depth of the trap. The thermalization process is simulated by evaluating the energy distributions after discrete collision times. As expected, the width of the Li distribution is drastically reduced during the first collision times, reflecting sympathetic cooling of Li. Correspondingly, the Cs distribution is broadened, indicating heating. For longer thermalization times, however, both the Li and Cs distributions become continuously narrower, as a result of sympathetic evaporation. Surprisingly, the final width of the Cs distribution falls below the initial one for the chosen initial parameters. Thus, we may expect to observe an overall cooling effect on Cs on the timescale of evaporation of Li, which appears paradox. However, this merely reflects the fact that the evaporating Li atoms carry away energy extracted

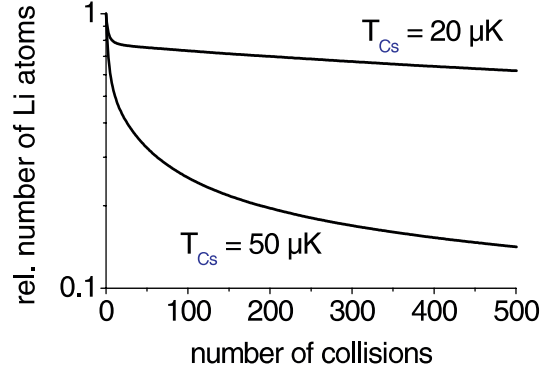


Figure 3.9: Simulated evaporation of Li atoms through Li-Cs collisions. At low initial Cs temperature  $T = 20 \mu\text{K} < U_0^{\text{Li}}/(10k_B)$ , only a small Li loss occurs during the first thermalization time. For higher Cs temperature  $T = 50 \mu\text{K} > U_0^{\text{Li}}/(10k_B)$ , continuous sympathetic evaporation takes place.

both out of the Li and the Cs distribution. For the relevant mass ratio and range of  $\eta$ , we find an atom loss rate  $\gamma_{\text{evap}} \simeq 0.5 \eta e^{-\eta} \gamma_{\text{Li}}$ . In particular, the simulations confirm that  $P_{\text{evap}}$  is almost independent of the mass ratio as long as  $\eta > 2/\xi$ .

By counting the number of Li atoms remaining trapped as a function of the collision times, we obtain the curves shown in Fig. 3.9. Apparently, the fast initial cooling process of Li is accompanied by loss of Li atoms. In the case of low initial Cs temperature  $T = 20 \mu\text{K} < U_0^{\text{Li}}/(10k_B)$ , Li evaporation is negligible. For higher Cs temperature  $T = 50 \mu\text{K} > U_0^{\text{Li}}/(10k_B)$ , however, Li atoms continuously escape out of the trap as a result of sympathetic evaporation.

Fig. 3.10 shows the experimentally observed evolution of the number of trapped Li atoms in thermal contact with a Cs gas at a temperature of  $37 \mu\text{K}$ . The inset shows the evaporation rate  $\gamma_{\text{evap}}$  as a function of temperature. We fit the numerical model to the data, with  $\gamma_{\text{Li}}$  as the only free parameter, and obtain a fit at  $\gamma_{\text{Li}} \sim 30 \text{ s}^{-1}$ , which results in an effective cross-section for evaporation of about  $3 \times 10^{-11} \text{ cm}^2$ . Due to simplifying assumptions in the numerical model and due to the experimental uncertainties mainly in the determination of the temperature, we estimate an uncertainty of a factor of 3 for this value of the cross-section. The cross-section is thus consistent with the more precise cross-section determined from thermalization.

According to the numerical model, the slow evaporation of Li may be accompanied by decreasing Cs temperature. When choosing the initial Cs particle number equal to the Li number and the initial Cs temperature  $T \approx U_0^{\text{Li}}/(10k_B)$ , we obtain the model curve displayed in Fig. 3.11 (a). Dur-

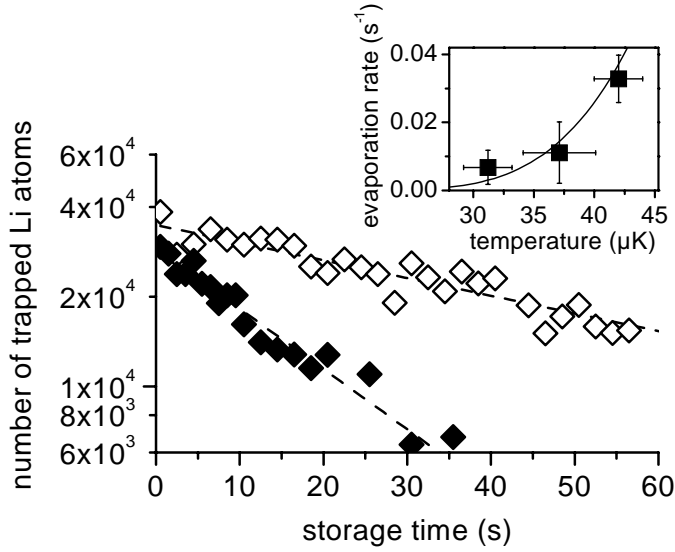


Figure 3.10: Evaporation of Li atoms. Main graph: Evolution of the number of stored Li atoms without Cs (open diamonds) and with Cs at a temperature  $\bar{T} = 37(2) \mu\text{K}$  (closed diamonds). Inset: Evaporation loss rate (corrected for rest-gas losses) versus temperature. The solid line is a model fit to the data (see text).

ing the first thermalization time the Cs sample is heated. The successive sympathetic evaporation of Li out of the trap results in decreasing Cs temperature. Indeed, we could observe this effect experimentally, as shown in Fig. 3.11 (b) (filled symbols). The open symbols illustrate the Cs temperature evolution measured for the same conditions but without Li. The solid lines are to guide the eye. Since residual heating was present in the experiment ( $\sim 50 \text{ nK/s}$ ), we could not observe the final Cs temperature to actually fall below the initial value, as predicted by the model.

Sympathetic evaporation poses a limit to thermalization in shallow traps: a considerable fraction of the atoms is lost during the first thermalization time for traps with  $U_0^{\text{Li}}/k_B\bar{T} < W(3/\xi)$  ( $\bar{T}$  is the average temperature,  $W$  is the product logarithm function). For the Li-Cs mass ratio, thermalization without significant loss is possible if  $\eta \gtrsim 4$ . In the initial few collisions, the Li distribution is far from thermal equilibrium with the Cs, and the evaporation loss cannot be estimated analytically. In numerical simulations, we see a small loss of Li atoms in the initial few collisions, which is  $< 10\%$  if  $k_B T_{\text{Cs}} < U_0^{\text{Li}}/10$ , in qualitative agreement with the experimental data in Fig. 3.10.

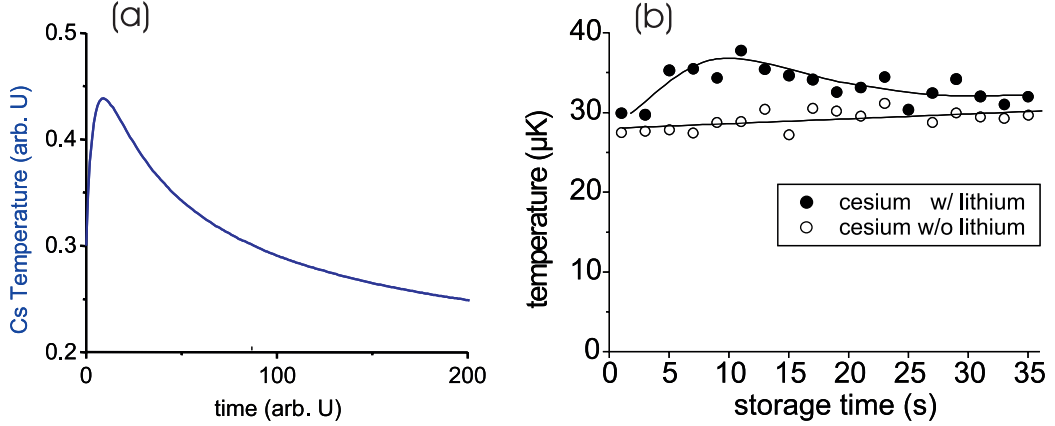


Figure 3.11: (a) Calculated Cs temperature evolution for equal initial number of Li and Cs particles and initial Cs temperature  $T \approx U_0^{\text{Li}}/(10k_{\text{B}})$ . (b) Experimental evidence of the cooling effect of Cs through sympathetic evaporation of Li (filled symbols). For comparison, the open symbols depict the Cs temperature without Li. The solid lines are to guide the eye.

### 3.5 Conclusion and outlook

The usefulness of sympathetic cooling depends strongly on the timescale of thermalization. To reach the quantum degenerate regime in our trap geometry, the temperature of the Li gas must be decreased by two orders of magnitude from the initial temperature after loading (see Fig. 6.2), which takes  $\sim 5$  thermalization times, assuming the Cs is optically cooled to be always much below the Li temperature. This means only an average number of  $\sim 50$  Li-Cs collisions are needed for sympathetic cooling, compared with more than 1000 Li-Li collisions for evaporative cooling of Li to BEC.

The heat which the Li transfers to the Cs can be removed by repeated pulsed optical cooling. This is more efficient than continuous cooling since the light-induced inelastic collisions can act only during the short (20 ms) cooling pulses, while thermalization continues over longer time. In this way, we have been able to reach Li temperatures down to  $25 \mu\text{K}$ . The main limitation for reaching lower temperatures is the base temperature of the Cs polarization-gradient cooling. Different optical cooling schemes such as Raman-sideband cooling [Kerman et al., 2000] may provide lower Cs temperatures and ultimately an evaporation-free route to quantum degeneracy of both the fermionic and bosonic lithium isotopes.

# Chapter 4

## Inelastic collisions

This Chapter is dedicated to the description and analysis of experiments on inelastic collisions between trapped Li and Cs atoms. After a short motivation of our experiments we present a few theoretical considerations on the two binary inelastic processes possible: Spin exchange and dipolar collisions. A simple thermodynamic model is derived that establishes the link between the microscopic collisional physics and macroscopic observables. Finally, experimental results both on homonuclear (Cs-Cs, Li-Li) and heteronuclear collisions (Li-Cs) are discussed.

### 4.1 Introduction

Inelastic collisions in the ultracold regime have been extensively studied since the early days of laser cooling [Weiner et al., 1999]. The primary concern has been the limitation of achievable density and storage time due to trap loss in magnetic traps [Legendijk et al., 1986]. Inelastic collisions in the groundstate have gained importance as a limiting factor for the stability of Bose-Einstein condensates [Guéry-Odelin et al., 1998]. On the other side, groundstate collisions allow for sensitive probing of the groundstate interaction potentials [Dulieu et al., 1994, Chin et al., 2000]. Recently, the investigation of spin-changing collisions in the presence of light has been extended to mixtures of alkali atoms [Schlöder et al., 1999, Telles et al., 2001b, Young et al., 2000].

The most common method of studying inelastic collisions is the measurement of the particle loss from the MOT. The observed sudden increase of the loss rate in the limit of small capture velocity of the MOT has generally been attributed to spin-exchange collisions. They are expected to be the dominant loss channel when the effective depth of the MOT is lowered below the groundstate hyperfine splitting  $\Delta E_{HFS}$  of the trapped atoms. In this case the

internal energy  $\Delta E_{HFS}$  or  $2\Delta E_{HFS}$  converted into kinetic energy in a binary spin-exchange collision exceeds the escape velocity and both atoms escape out of the trap. Recently, an alternative interpretation for the enhanced trap loss at low light intensity was proposed [Telles et al., 2001a]. It is based on light-assisted collisions in combination with strong variation of the escape velocity with laser intensity. This alternative approach was motivated by numerous inconsistencies: The trap loss rate at low intensities exhibits a strong intensity dependence contrary to the expectation for a pure groundstate collision process [Nesnidal and Walker, 2000]. Also, a dramatic enhancement of the hyperfine-changing collision rate in the presence of near resonant trapping light was observed by Gensemer *et al.* [Gensemer et al., 2000].

For this reason, traps that do not rely on resonant photon scattering are more suitable for investigating groundstate collisions. Indeed, spin-exchange measurements with sympathetically cooled  $^{87}\text{Rb}$  atoms in a magnetic trap have revealed a collision rate much smaller than previously inferred from trap-loss measurements in a MOT [Myatt et al., 1997]. On the other side, giant spin relaxation was observed with magnetically trapped Cs atoms [Söding et al., 1998] on the order of the spin-exchange collision rate previously observed in an unpolarized Cs sample trapped in an opto-electric trap (OET) [Lemonde et al., 1995]. Recently, Roati *et al.* have performed spin-exchange collision measurements with unpolarized  $^{40}\text{K}$  atoms in a FORT [Roati et al., 2001]. In the present work we report on measurements of the homonuclear spin-exchange collision rates in samples of ultracold Li and Cs atoms trapped in a quasi-electrostatic trap (QUEST). This type of trap is particularly suited for experiments on spin-exchange collisions because it provides a conservative potential which is independent of the hyperfine state and spin projection [Grimm et al., 2000]. In addition, we present measurements on inelastic inter-species collisions in an ultracold mixture of Li and Cs atoms.

## 4.2 Inelastic scattering

As in Chapter 3, we recommend [Landau and Lifshitz, 1977, Heinzen, 1999, Pethick and Smith, 2002] as an introduction to the field. In the presence of inelastic collision channels, quantum scattering theory provides us with the expressions for the elastic and inelastic partial scattering cross-sections, respectively,

$$\begin{aligned}\sigma_{el}^{(l)} &= \frac{\pi}{k^2}(2l+1)|1-S_l|^2, \\ \sigma_{in}^{(l)} &= \frac{\pi}{k^2}(2l+1)(1-|S_l|^2).\end{aligned}\tag{4.1}$$

Here, for each angular momentum  $l$ ,  $S_l$  is a complex number with absolute value smaller than unity. In the case of pure elastic collisions,  $S_l$  is related to the scattering phases  $\delta_l$  by  $S_l = e^{2i\delta_l}$  (see Sec. 3.1). For  $S_l = -1$  the elastic cross-section becomes equal to the unitarity limit for distinguishable particles and inelastic scattering is absent. If  $S_l = 1$ , there are no collisions at all. In the case of maximum inelastic cross-section ( $S_l = 0$ ) the elastic and inelastic cross-sections are equal:

$$\sigma_{el}^{(l)} = \sigma_{in}^{(l)} = \frac{\pi}{k^2}(2l+1)$$

From Eq. (4.1) follows the interesting fact, that elastic scattering exists without inelastic collisions ( $S_l = -1$ ), but if inelastic processes are involved then there are necessarily elastic collisions. For a given value of  $\sigma_{in}^{(l)}$ , the cross-section for elastic scattering must be in the interval

$$\sqrt{\sigma_0} - \sqrt{\sigma_0 - \sigma_{in}^{(l)}} \leq \sqrt{\sigma_{el}^{(l)}} \leq \sqrt{\sigma_0} + \sqrt{\sigma_0 + \sigma_{in}^{(l)}},$$

where  $\sigma_0 = (2l+1)\pi/k^2$ . This interval corresponds to the area between the lower and the upper curve in Fig. 4.1 for  $l = 0$ .

At low energy ( $kr_0 \ll 1$ , “s-wave regime”) the formalism of elastic scattering can be generalized to inelastic processes by allowing the scattering length  $a$  to be a complex number. Thus, one finds the cross-section for elastic and inelastic scattering, respectively,

$$\begin{aligned}\sigma_{el} &= 4\pi a^2, \\ \sigma_{in} &= \frac{4\pi}{k} \text{Im}(a).\end{aligned}\tag{4.2}$$

In contrast to the elastic cross-section the inelastic one is velocity dependent and proportional to  $1/v$  (“ $1/v$ -law”, H. A. Bethe, 1935). This means that inelastic processes become more important compared to the elastic ones as temperature is decreased.

### 4.2.1 Spin-exchange processes

Spin-exchange collisions can be qualitatively understood using the simple picture illustrated in Fig. 4.2 [Heinzen, 1999]. Two atoms enter the collision region in a particular combination of hyperfine and magnetic sub-levels

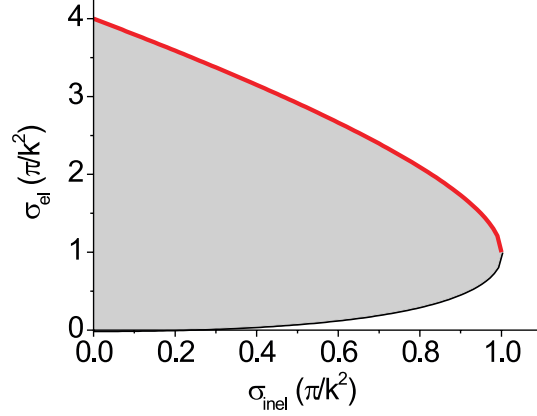


Figure 4.1: Lower and upper bound for the scattering cross-section for elastic collisions when inelastic processes are possible (solid and dashed line, respectively).

$|F_1, m_{F_1}\rangle |F_2, m_{F_2}\rangle$  (in Fig. 4.2,  $F_1 = 3, F_2 = 4$ ). They are accelerated through the spin recoupling region by the dispersive interaction. The spin states of the atoms project onto the singlet and triplet molecular states according to the relevant Clebsch-Gordan coefficients. The singlet and triplet waves propagate separately, reflect from the short-range barrier, and again pass through the recoupling region. Since the wave function phase shift is different for the singlet and triplet components due to the propagation, they do not reconstruct the original atomic hyperfine states, but rather produce a different superposition of hyperfine states. At zero magnetic field, in this type of collision the total magnetic spin quantum number  $M_F$  must be conserved.

The rate of the described process can be estimated using the leading term of the interaction potential [Pethick and Smith, 2002]

$$U_{ex} = \frac{4\pi\hbar^2(a_T - a_S)}{\mu} \mathbf{S}_1 \cdot \mathbf{S}_2 \delta(\mathbf{r}). \quad (4.3)$$

Here,  $\mathbf{S}_1$  and  $\mathbf{S}_2$  are the total electronic spins of the colliding atoms,  $\mu$  is the reduced mass and  $a_S$  and  $a_T$  are the singlet and triplet scattering lengths, respectively. In analogy to elastic scattering, the coefficient determining the inelastic collision rate per atom per unit volume is linked to the microscopic scattering cross-section  $\sigma_{F_1, F_2}^{F_1', F_2'}$  by Eq. (4.4)

$$G_{F_1, F_2}^{F_1', F_2'} = \left\langle \sigma_{F_1, F_2}^{F_1', F_2'}(v_r) v_r \right\rangle_{v_r}. \quad (4.4)$$

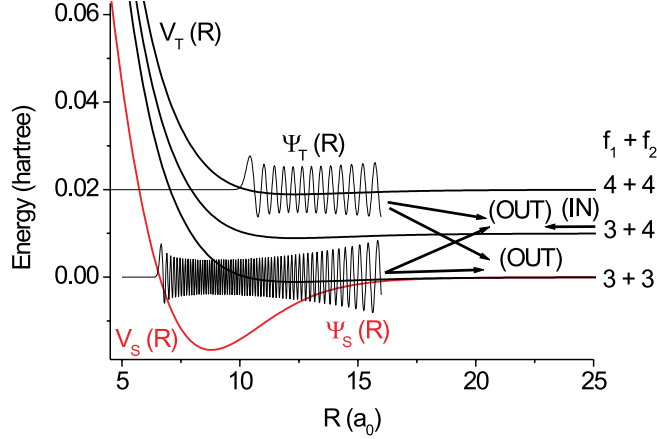


Figure 4.2: Schematic illustration of an exchange collision between one Cs atom in hyperfine state  $|F_1 = 3\rangle$  and one Cs atom in  $|F_2 = 4\rangle$ . Two atoms entering the collision region on the  $F_1 = 3$ ,  $F_2 = 4$ -asymptote are projected onto the singlet and triplet states. After separate propagation these states couple back to a different superposition of atomic states from the original ones. The hyperfine splitting is stretched by a factor  $10^4$ . The singlet potential curves connected to the hyperfine asymptotes other than  $F_1 = 3$ ,  $F_2 = 3$  are omitted.

Here, the initial and final hyperfine states of the scattering atoms are  $F_1, F_2$  and  $F'_1, F'_2$ , respectively. We denote by  $v_r$  the relative velocity between the colliding particles. In a trapped gas of inelastically interacting atoms of only one species, the rate of change of the local atom densities is given by

$$\dot{n}_{F_1} = \dot{n}_{F_2} = -G_{F_1, F_2}^{F'_1, F'_2} n_{F_1} n_{F_2}, \quad (4.5)$$

provided that every inelastic collision leads to the loss of both colliding atoms from the trap. The typical lifetime of an atom in state  $F_1$  is given by  $\tau_{F_1} = 1 / (G_{F_1, F_2}^{F'_1, F'_2} n_{F_2})$ . For two incoming atoms with nearly zero kinetic energy which interact by the potential given by Eq. (4.3) we obtain the rate coefficient

$$G_{F_1, F_2}^{F'_1, F'_2} = 4\pi(a_T - a_S)^2 v_r' |\langle F'_1, F'_2 | \mathbf{S}_1 \cdot \mathbf{S}_2 | F_1, F_2 \rangle|^2. \quad (4.6)$$

The fact that rates of spin-exchange processes vary as  $(a_T - a_S)^2$  makes it possible to deduce information about the scattering lengths from data on the

lifetimes of atoms in traps [Myatt et al., 1997]. For hydrogen, the difference of the scattering lengths is of the order of the Bohr radius  $a_0$ , and therefore for atoms in the upper hyperfine state, the rate coefficient is of order  $10^{-13} \text{ cm}^3\text{s}^{-1}$  if the spin matrix element is of order unity. For alkali atoms the corresponding values are of order  $10^{-11} \text{ cm}^3\text{s}^{-1}$  because of the larger scattering lengths. Since typical densities in the described experiments are of order  $10^{12} \text{ cm}^{-3}$ , the estimated rate coefficients indicate that atoms will be lost by exchange collisions in a fraction of a second. Hyperfine changing collisions of Cs were first observed by trap loss in a MOT when lowering the escape velocity below a threshold value [Sesko et al., 1989]. The value for the rate coefficient was found to range between  $10^{-11}$  and  $10^{-10} \text{ cm}^3/\text{s}$ . The spin exchange rate coefficient was remeasured in unpolarized Cs in an opto-electric trap (OET) at rather low density [Lemonde et al., 1995]. At  $10 \mu\text{K}$ , a rate coefficient of  $3(2) \times 10^{-11} \text{ cm}^3/\text{s}$  was found. This value was confirmed by an experiment using a far-off-resonance optical trap (FORT) [Vuletić et al., 1998]. To our knowledge, no measurements or theoretical predictions have been performed as far as spin exchange collisions between  $^7\text{Li}$  are concerned. For  $^6\text{Li}$ , a rate constant of the order of  $10^{-9} \text{ cm}^3/\text{s}$  was measured by trap loss from a resonator-enhanced optical dipole trap [Mosk et al., 2001a].

### 4.2.2 Dipolar processes

Some inelastic processes cannot occur via the central part of the interaction potential because of the angular momentum selection rule  $\Delta M_F = 0$ . For example, two atoms which are both in the doubly polarized state  $|F = I + 1/2, m_F = F\rangle$  cannot scatter to any other state with the same projection of the total spin angular momentum  $M_F$ . On the other side, two atoms both in the maximally stretched state  $|F = I - 1/2, m_F = -F\rangle$  could undergo a transition according to the selection rule  $\Delta M_F = 0$  to states that have  $F = I + 1/2$ . These states lie above the original states by the hyperfine energy splitting and therefore such collisions are also suppressed.

However, inelastic collisions involving the doubly polarized or maximally stretched states may occur via the magnetic dipole-dipole interaction. This interaction has no central symmetry, and the selection rules are  $\Delta l = 0, \pm 2$  and  $\Delta(m_l + M_F) = 0$ . For the decay of a doubly polarized gas, this leads to  $\sim T$  and  $\sim B$  independent rate coefficients  $G^{dipolar}$  of the order  $(a_0/|a_T - a_S|)^2 \sim 10^{-2}-10^{-4}$  times those for spin-exchange processes for alkali atoms [Pethick and Smith, 2002]. However, dipolar rates can be much greater or much less than these typical values because coupling between channels can give resonances, and also because of phase-space limitations. The latter are important for atoms initially in the lower hyperfine multiplet. The

phase space available is reflected in the factor  $v_r'$  in (4.6). In this case, the relative velocity in the final state is only due to Zeeman splitting as opposed to the hyperfine energy in spin exchange collisions. Since  $v_r' \propto \sqrt{B}$  for small fields, the dipolar rate vanishes in the limit of low magnetic fields. The rate coefficient for dipolar relaxation of  ${}^7\text{Li}$  in the  $|F = 2, m_F = 2\rangle$  hyperfine state was measured in a magnetic trap at 1000 G. The value of  $(1.1 \pm 0.1) \times 10^{-14} \text{ cm}^3/\text{s}$  [Gerton et al., 1999] is in agreement with the predicted one,  $(9.4 \pm 0.2) \times 10^{-15} \text{ cm}^3/\text{s}$  [Moerdijk and Verhaar, 1996].

In the heavier alkalis Rb and Cs, there is an additional inelastic loss mechanism. This second order spin-orbit interaction gives rise to transitions like the dipolar collisions. The sign of the interaction is opposite to that of the dipolar interaction. In Rb, this leads to a decreased inelastic rate coefficient for the doubly polarized and maximally stretched states compared with the result for the dipolar interaction alone. In the case of Cs, second order spin-orbit interaction overwhelms the dipolar contribution and results in an increased inelastic scattering rate of  $8 \times 10^{-12} \text{ cm}^3\text{s}^{-1}$  [Söding et al., 1998]. The experiment was carried out with Cs atoms in the doubly polarized state  $|F = 4, m_F = 4\rangle$  at  $8 \mu\text{K}$  in a magnetic field of about 100 G. Until very recently, these losses have thwarted attempts to achieve Bose-Einstein condensation of Cs atoms [Weber et al., 2002].

### 4.2.3 Three-body processes

Besides the discussed inelastic collisions involving two atoms, three-body recombination collisions can put limits on the achievable densities in traps. In a three-body collision, energy and momentum conservation allows two atoms to be scattered into a bound molecular state. The binding energy is released into kinetic energy shared between the formed molecule and the third atom. Consequently, the particles either escape from the trap or contribute to heating of the sample, depending of the amount of energy released versus the depth of the trapping potential.

The rate of this process is given by the equation

$$\dot{n} = -L_3 n^3,$$

where  $L_3$  is the corresponding rate coefficient and  $n$  is the density of atoms.  $L_3$  can be crudely estimated assuming that all processes occur via the central part interaction and forgetting about phase-space considerations. For a three-body collision to occur, three atoms must be within a volume  $r_0^3$ , where  $r_0$  is the distance out to which the two-body interaction plays a role. The probability of an atom being within a volume  $r_0^3$  is of order  $nr_0^3$ . Thus, the rate

of three-body processes compared with two-body collisions is roughly given by the same factor, that is  $L_3 \sim \langle \sigma_{el}(v)v \rangle r_0^3$ . Since for alkalis  $r_0 \sim 10^2 a_0$  and taking the elastic rate coefficient  $\langle \sigma_{el}(v)v \rangle \sim 10^{-11} \text{ cm}^3\text{s}^{-1}$ , we obtain the rough estimate for the three-body rate coefficient of order  $10^{-30} \text{ cm}^6\text{s}^{-1}$ . For  ${}^7\text{Li}$ ,  $L_3$  was calculated to be  $2.6 \times 10^{-28} \text{ cm}^6\text{s}^{-1}$  [Moerdijk and Verhaar, 1996].

In a three-body system with large scattering length, as it is the case with Cs,  $L_3$  is predicted to be linked to the scattering length  $a$  as  $L_3 = C\hbar a^4/m$ , where the constant  $C$  may take values between 10 and 200 [Bedaque et al., 2000]. Thus, taking  $a = -2400$  and  $C = 100$ , we calculate  $L_3 \approx 10^{-23} \text{ cm}^6\text{s}^{-1}$ . In recent experiments,  $L_3$  was found to amount to about  $10^{-24} \text{ cm}^6\text{s}^{-1}$  for Cs atoms in the  $|F = 3, m_F = 3\rangle$  state at  $\sim 100$  G magnetic field [Grimm, 2002]. At typical densities of about  $10^{12} \text{ cm}^{-3}$  in our experiments we therefore expect collision rates via three-body interaction of the order of  $0.1 \text{ s}^{-1}$ . Since the density decays within fractions of a second by two-body processes, we can safely neglect three-body collisions in our experiments.

### 4.3 Inelastic collisions with trapped atoms

In order to determine the exact value of the two-body rate coefficient  $G$  for a certain inelastic process from experimental observables, we have to carry out the averaging in expression (4.4). We consider a mixture of trapped atoms (1) and (2), which are in thermal equilibrium ( $T_1 = T_2 = T$ ). This assumption is based on the fact that elastic collisions are always present in a mixture of interacting particles (see Sec. 4.2). Besides, even in a mixture of two species with strongly differing masses as it is the case with Li and Cs, the elastic inter-species collision rate is still very high (see Sec. 3.1). However, in the case of trap loss collisions and quickly decreasing density, this approximation may not be valid at all times. Here, we assume the atoms to be distributed according to the thermal phase-space distribution (3.11) in Chapter 3. Furthermore, we take the inelastic scattering cross-section of the form as in Eq. (4.2) <sup>1</sup>,

$$\sigma_{in} = \frac{\beta}{k}. \quad (4.7)$$

Then, the momentum integration of Eq. (4.4) is trivial and we obtain  $G = \beta = \text{const}$ . The total inelastic scattering rate is calculated in analogy to the elastic one in Sec. 3.3. Again, we consider the trapping potential to

---

<sup>1</sup>For the more general case  $\sigma_{in} = \beta(v_r)/v_r \propto v^{-\mu-1}$ , the averaging procedure is carried out in complete analogy to the discussion presented here in [Guéry-Odelin, 1998]

be harmonic and of cylindrical symmetry. We obtain

$$\Gamma_{in} = G \frac{N_1 N_2}{V_{12}}, \quad (4.8)$$

where the effective volume is given by 3.13.

In this Chapter, we focus on spin exchange collisions, in which the hyperfine splitting energy  $\Delta E_{HFS}$  is released into kinetic energy. From energy and momentum conservation follows, that in a collision between particles (1) and (2) having masses  $m_1$  and  $m_2$ , particle (1) receives the energy share

$$\Delta E_1 = \frac{\Delta E_{HFS}}{1 + \frac{m_1}{m_2}}. \quad (4.9)$$

Thus, in collisions involving two particles of the same kind, the released internal energy is shared to equal parts between the two particles. In the case of collisions between  ${}^7\text{Li}$  and  ${}^{133}\text{Cs}$  atoms, 95% of the released energy is picked up by the Li and 5% by the Cs atom. In our experiments, the gain in kinetic energy for either colliding atomic species exceeds the depth of the trapping potential. Therefore, we can safely assume both colliding atoms to escape out of the trap. Thus, the total collision rate  $\gamma_{total}$  becomes observable as the rate of decrease of the number of atoms (1) and (2) remaining in the trap,

$$\dot{N}_1 = \dot{N}_2 = -G \frac{N_1 N_2}{V_{12}}. \quad (4.10)$$

However, this model is not yet suited for fully describing the evolution of a trapped atomic sample of two different species. The effective volume  $V_{12} = V_{12}(T)$  is a function of temperature, which is also altered by the inelastic processes.

### 4.3.1 Relaxation heating

Next, we are interested in the mean energy of a pair of atoms (1) and (2) that undergo a collision,

$$\langle E(1) + E(2) \rangle_{\text{Coll}} = \langle (E_{kin}(1) + E_{pot}(1) + E_{kin}(2) + E_{pot}(2)) \sigma v_r \rangle_{v_r, \mathbf{r}} / G. \quad (4.11)$$

This expression can be split into one velocity integration and one spatial integration. For the mean kinetic energy we obtain

$$\langle E_{kin}(1) + E_{kin}(2) \rangle_{\text{Coll}} = 3k_B T, \quad (4.12)$$

which is the mean kinetic energy in of a harmonically trapped gas.

The average potential energy  $E_{pot}(\mathbf{r}) = (\omega_{ax}^2 x^2 + \omega_{rad}^2 (y^2 + z^2)) m/2$  in harmonic approximation over the distributions of the colliding atoms  $f_{r,1}(\mathbf{r})$  and  $f_{r,2}(\mathbf{r})$  is determined from the spatial integral

$$\begin{aligned} \langle E_{pot}(1) + E_{pot}(2) \rangle_{\text{Coll}} &= \frac{\int d^3r (E_{pot,1}(\mathbf{r}) + E_{pot,2}(\mathbf{r})) f_{r,1}(\mathbf{r}) f_{r,2}(\mathbf{r})}{\int d^3r f_{r,1}(\mathbf{r}) f_{r,2}(\mathbf{r})} \\ &= \frac{3}{2} k_B T. \end{aligned} \quad (4.13)$$

Thus, the extracted potential energy by a collision in which two atoms escape from the trap amounts to just half of the mean potential energy of two atoms trapped in a harmonic potential,  $2 \times (3/2) k_B T$ .

The average total energy of the two colliding atoms is given by

$$\langle E_{total} \rangle_{\text{Coll}} = \frac{3}{4} 6 k_B T, \quad (4.14)$$

We define the reduction factor  $q = 3/4$  such that  $\langle E_{total} \rangle_{\text{Coll}} = 6q k_B T$ , where  $6k_B T$  is the mean energy of a pair of atoms in the trap. In other words, a pair of escaping atoms carries away a smaller amount of energy than average, which results in effective heating of the remaining atomic sample. The opposite effect is the well-known evaporation of atoms from the high-energy tail of the Maxwell distribution when the distribution is truncated due to the finite depth of the trapping potential 3.2. Continuous rethermalization then leads to cooling. For this reason, relaxation heating as a consequence of inelastic collisions is also called “anti-evaporation”. The situation is illustrated in Fig. 4.3. The mean potential energy of one atom from a thermal ensemble in units of  $k_B T$  is  $3/2$ . The mean potential energy per atom that undergoes a collision is  $3/4$ . This is the case if only the atoms from the shaded area were able to collide inelastically.

We now derive the rate of change in temperature due to anti-evaporation. It can be calculated from the total energy of the trapped atomic cloud  $E = 3N k_B T$ ,

$$\Delta T = \frac{\Delta E}{3k_B N} - \frac{E \Delta N}{3k_B N^2}. \quad (4.15)$$

Here,  $N = N_1 + N_2$  is the total number of atoms. One inelastic collision is determined by a change in atom number  $\Delta N = -2$  and a change in total energy  $\Delta E = -6q k_B T$ . By substituting these expressions in Eq. (4.15) we obtain the relation between change in temperature and atom number

$$\frac{\dot{T}}{T} = (q - 1) \frac{\dot{N}}{N} \quad (4.16)$$

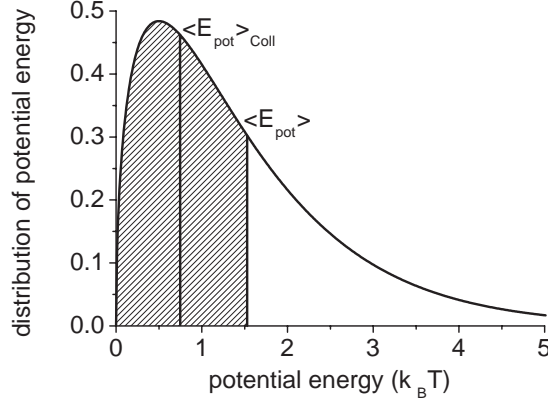


Figure 4.3: Schematic illustration of “anti-evaporation”. Trap-loss collisions occur preferentially in the low-energy part of the potential energy distribution (shaded area). Rethermalization leads to an effective broadening of distribution, i.e. relaxation heating.

By integrating over time from  $t_0$  to  $t$  we obtain

$$T = T_0 \left( \frac{N}{N_0} \right)^{q-1}, \quad (4.17)$$

where  $N_0$  and  $T_0$  are the initial values at  $t = t_0$ .

## 4.4 Homonuclear spin-changing collisions

In this Section we concentrate on measurements of spin-changing collisions between atoms of only one kind ((1)=(2)). Then, the two rate equations (4.10) can be added up to give

$$\dot{N} = -2GN^2/V(T). \quad (4.18)$$

It is important to note that in the homonuclear case each inelastic scattering event leads to trap loss of two atoms of the same kind. This fact is accounted for by the factor of two on the right side of Eq. (4.18). By substituting the relation between temperature and particle number, Eq. (4.17) into the rate equation (4.18) we obtain an expression of the simple form

$$\dot{N} = A_N N^{x_N}, \quad (4.19)$$

where the constants are defined as  $A_N = -2G\omega_{rad}^2\omega_{ax}(mN_0^{q-1}/(4\pi k_B T_0))^{3/2}$  and  $x_N = -3(q-1)/2 + 2$ . Equation (4.19) is easily solved,

$$N(t) = ((1-x_N)A_N t + N_0^{1-x_N})^{\frac{1}{1-x_N}}. \quad (4.20)$$

Since relative changes in atom number and temperature are proportional to each other according to Eq. (4.16), we obtain an expression for  $T(t)$  of identical form as Eq. (4.20),

$$\dot{T} = A_T T^{x_T}. \quad (4.21)$$

Here, the constants take the values  $A_T = 2G(1-q)\omega_{rad}^2\omega_{ax}(m/(4\pi k_B))^{3/2} \times N_0 T_0^{1/(1-q)}$  and  $x_T = 1/(q-1) - 1/2$ .

In principle we have to add an additional term  $-\alpha N$  on the right side of Eq. (4.19) to account for trap loss due to collisions with the residual background gas. However,  $\alpha \approx 0.01 \text{ s}^{-1} \ll GN/V(T)$  in the regime of high density and low temperature that we investigate. Therefore, this extra loss term is negligible. Equation (4.18) can be written in terms of the mean density  $\bar{n} = N/V(T)$ ,

$$\dot{N} = -2G\bar{n}N. \quad (4.22)$$

From the logarithmic derivative of the mean density,

$$\frac{\dot{\bar{n}}}{\bar{n}} = \frac{\dot{N}}{N} - \frac{3\dot{T}}{2T} \quad (4.23)$$

we obtain the rate equation for the mean density using Eq. (4.16),

$$\dot{\bar{n}} = -\tilde{G}\bar{n}^2, \quad (4.24)$$

where  $\tilde{G} = (1 - \frac{3}{2}(q-1))G$ . This equation is easily solved by

$$\bar{n}(t) = \frac{\bar{n}_0}{1 + 2\bar{n}_0\tilde{G}t}. \quad (4.25)$$

Thus, we have derived a simple analytic model describing the evolution of atom number, temperature and density under the influence of relaxation heating caused by trap loss collisions.

#### 4.4.1 Cs ( $F_1 = 4$ , $F_2 = 4$ )

In our experiments, the CO<sub>2</sub>-laser beam is focused to a beam radius  $w_{rad} \approx 93 \mu\text{m}$  and the focus is carefully aligned with the center of the Cs-MOT. The trapping potential of the QUEST is characterized using two

independent methods: The radial and axial trap frequencies of the Cs atoms  $\omega_{rad} = 2\pi \times (740 \pm 20)$  Hz and  $\omega_{ax} = 2\pi \times (15 \pm 1)$  Hz, respectively, are measured as described in Sec. 2.7.1. From recording the AC-Stark shift of the trapped distribution we infer the depth of the trapping potential  $U_0 = (740 \pm 20) \mu\text{K} \times k_B$  (see Section 2.7.2). The QUEST is loaded by switching off all magnetic fields and by applying a molasses cooling pulse during 10 ms. For this purpose the MOT lasers are detuned to 150 MHz to the blue from the transition  $|6s_{1/2}, F = 4\rangle \rightarrow |6p_{3/2} F' = 4\rangle$ . Thus, we are able to load up to  $10^6$  Cs atoms into the QUEST at a temperature of about 50  $\mu\text{K}$ . A further molasses pulse is applied when the atom distribution has reached equilibrium 0.5 s after transfer to set the initial temperature down to 30  $\mu\text{K}$ .

For detection of the atom number, density and temperature, we use absorption imaging, as described in Section 2.6.2. The absorption pulse is applied during 0.3 ms on resonance with the transition  $|F = 4\rangle \rightarrow |F' = 5\rangle$  at an intensity of 30  $\mu\text{W}/\text{cm}^2$ . Since this type of measurement is destructive, the procedure is repeated for the same initial conditions and various relaxation times. Shot-to-shot fluctuations of the atom number, density and temperature are in the range of 5%.

The Cs temperature is measured by absorption imaging in two different ways: The temperature in radial direction,  $T_{rad}$ , is obtained from the ballistically expanding Cs cloud after switching off the RF-source of the CO<sub>2</sub>-laser within about 150  $\mu\text{s}$ . The increasing radial width  $\sigma_{rad}$  as a function of the expansion time  $t_{exp}$  is fitted using the relation  $\sigma_{rad}^2(t_{exp}) - \sigma_{rad}^2(0) = t_{exp}^2 k_B T_{rad} / m$ , which gives  $T_{rad}$  (see Sec. 2.6.2). Adiabatic cooling effects during the switching time are taken into account by scaling the temperature to temperature measurements performed using an acousto-optic modulator (AOM) as a fast switch for the CO<sub>2</sub>-laser beam. The axial temperature,  $T_{ax}$ , is inferred from the axial width of the Cs sample,  $\sigma_{ax}$ , using the relation  $m\omega_{ax}^2 \sigma_{ax}^2 = k_B T_{ax}$ . Here,  $m$  denotes the mass of the Cs atom. The average temperature  $T$  is calculated according to  $T = (2T_{rad} + T_{ax})/3$ .

Spin-changing collisions between Cs atoms are detected by measuring the trap loss and temperature increase as a function of storage time after optically repumping the atoms into the upper hyperfine groundstate  $|F = 4\rangle$ . Since the hyperfine splitting of the Cs groundstate  $\Delta E_{HFS} = 9.2$  GHz exceeds by far the depth of the trapping potential for  $U_0$  we can safely assume two inelastically colliding atoms to be lost from the trap. The optical repumping pulse is provided by mechanically switching on the MOT repumping light ( $|F = 3\rangle \rightarrow |F' = 4\rangle$  transition) during 2 ms. The repumping efficiency is checked to be  $> 99\%$  using absorption imaging. Since the population of the  $m_f$ -states reflects the one in the MOT, we assume the Cs sample to be

unpolarized.

Fig. 4.4 shows typical data from a measurement of trap loss and relaxation heating as a function of time after optically pumping the Cs atoms into the upper hyperfine state  $|F = 4\rangle$  at  $t = 0$ . The evolution of the atom number  $N(t)$  and mean density  $\bar{n}(t)$  (filled symbols in Fig. 4.4 (a), (c)) clearly exhibit a non-exponential behavior which is a signature of a multibody decay. For comparison, we have plotted as open symbols the density, temperature and number for the case that all atoms remain in the lowest groundstate  $|F = 3\rangle$ . Clearly, the exponential decay due to rest-gas collisions in (a) and (c) is negligible on the relevant time scale. Simultaneously to the non-exponential density decay, we observe a pronounced rise in temperature  $T(t)$  ((b) filled symbols) as a consequence of relaxation heating. The small initial temperature increase in the case of Cs remaining in  $|F = 3\rangle$  (open symbols) is not fully understood. Residual parametric heating due to laser instabilities may be one explanation. Thermalization of the cold thermal cloud with a dilute cloud of weakly bound hot atoms may be another reason.

The solid line in Fig. 4.4 (a) displays the result of fitting expression (4.24) to the data. The free fit parameters are the initial density  $\bar{n}_0$  and the scaled two-body rate coefficient  $\tilde{G}_{(4,4)}$ . We obtain  $\tilde{G}_{(4,4)} = (1.9 \pm 0.2 \pm 0.3) \times 10^{-11} \text{cm}^3/\text{s}$  as a result of fitting three selected data sets. The first error reflects statistical fluctuations whereas the second error is an estimate of the systematic uncertainty. The latter is dominated by the uncertainty in the absorption cross-section and therefore in the absolute number of atoms. The solid lines in Fig. 4.4 (b) and (c) result from fitting the data using expressions (4.21) and (4.19). The rate coefficient  $\tilde{G}_{(4,4)}$  was held fixed and the free parameters were  $T_0, q$ , and  $N_0, q$ , respectively. The resulting values for  $q$  are in agreement to better than 10%. We obtain  $q = 0.50 \pm 0.05$ , which is surprisingly small compared to the expected value  $q = 3/4$ . In particular, from  $q = 0.5$  follows vanishing mean potential energy per colliding atom,  $\langle E_{pot} \rangle_{\text{Coll}} = 0$ . This result is not physical, since the number of atoms having vanishing potential energy tends to zero. Apparently, an additional heating mechanism leads to a faster increase in temperature than expected from relaxation heating. This heating process might originate from grazing collisions of the escaping atoms with cold trapped atoms [Beijerinck, 2000]. The mean free path  $l \approx (\sqrt{2}\bar{n}\sigma_{el})^{-1}$  is on the order of 1 mm for the initial conditions of our experiments. This is the same order of magnitude as the axial dimension of the trapped Cs cloud,  $\sigma_{ax} = \sqrt{k_B T / (m\omega_{ax}^2)} \approx 0.6$  mm. This possible explanation will be further investigated.

Besides, we have tried to fit the data using rate equations assuming a temperature dependent rate coefficient  $G_{(4,4)}(T) = G_0 T^{-\nu}$  as found in [Söding et al., 1998]. However, the value for  $\nu$  obtained from fitting the den-

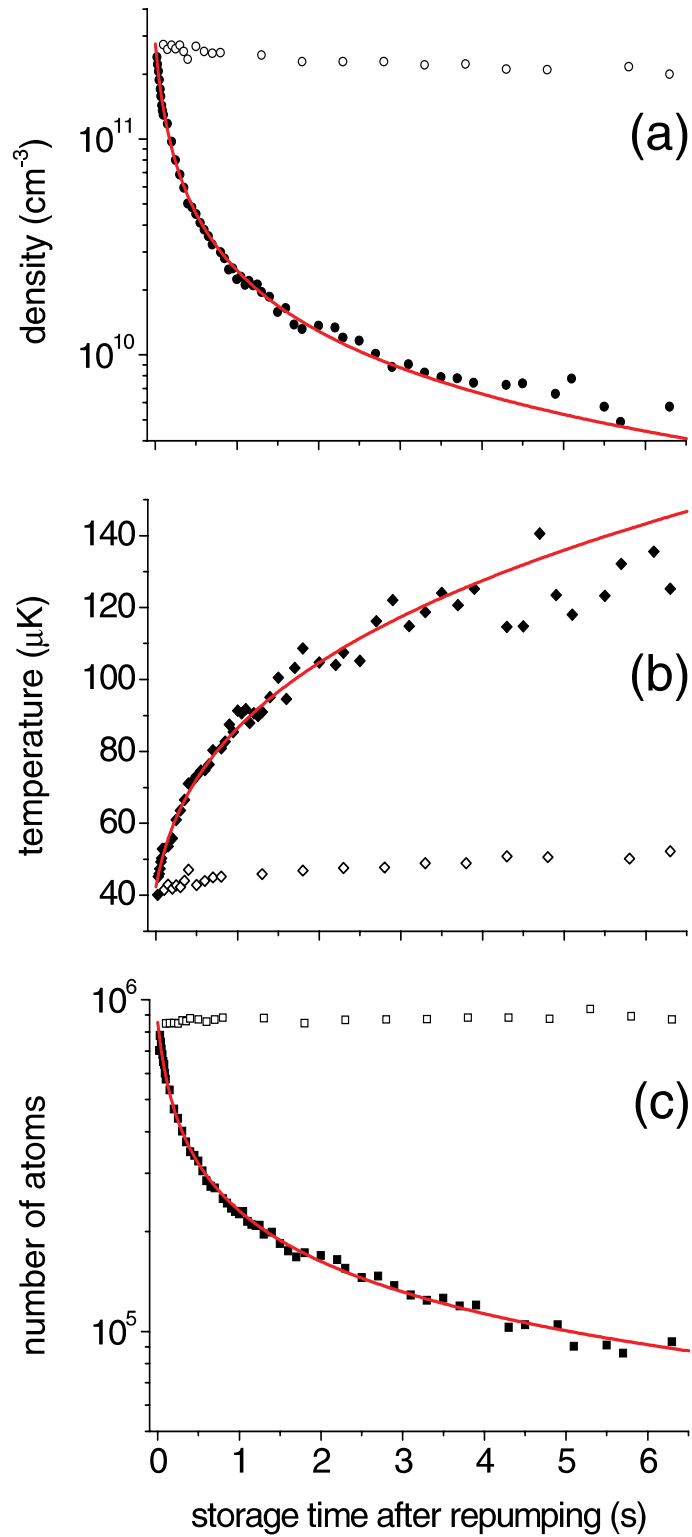


Figure 4.4: Trap loss and relaxation heating resulting from spin exchange collisions. (a) Nonexponential drop in the mean density of atoms in  $|F = 4\rangle$  (filled symbols) compared to negligible trap loss due to rest gas collisions of atoms in  $|F = 3\rangle$  (open symbols). (b) Temperature increase as a result of relaxation heating. (c) Nonexponential drop in the number of stored atoms.

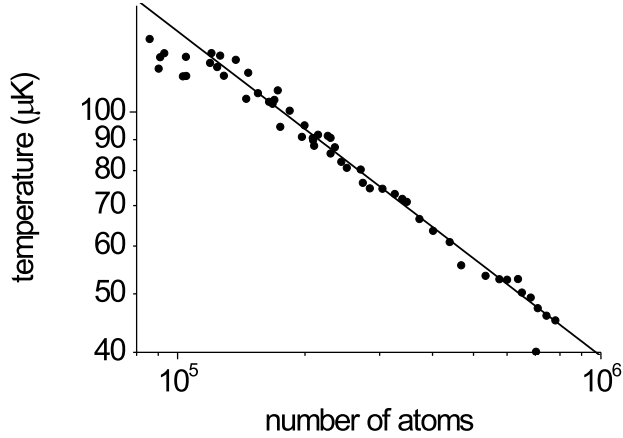


Figure 4.5: Same data as in Fig. 4.4 (a) and (b), plotted in log-log scale. The data nicely match the power law dependence of Eq. (4.17) (solid line). However, we infer a reduction factor  $q \approx 0.5$  from the slope of the straight line, in contradiction to the expected value  $q = 3/4$ .

sity decay was not consistent with the one for  $q$  inferred from fitting  $T(N)$  (see below). The influence of the non-harmonic part of the trapping potential on the relaxation dynamics cannot explain the large deviation, since the heat capacity is only modified by roughly 10% compared with the harmonic potential. Nor the breakdown of thermalization as a result of decaying density and rising temperature can explain our observations. Slowing thermalization would have the effect that the depleted region at the potential minimum was not refilled by atoms scattered to low energies. As a consequence, anti-evaporation would stop and the overall heating effect were diminished. This issue definitely merits further investigation.

Nevertheless, the approach of fitting the density evolution  $\bar{n}(t)$  to extract  $\tilde{G}_{(4,4)}$  as well as fitting  $T(t)$  and  $N(T)$  to determine the phenomenological parameter  $q$  is perfectly justified. Using  $q = 0.5$ , we obtain the final result for the two-body rate coefficient,

$$G_{(4,4)} = (1.1 \pm 0.1 \pm 0.2) 10^{-11} \text{cm}^3/\text{s}.$$

In Fig. 4.5, the same data as in Fig. 4.4 (a) and (b) are plotted in log-log scale. The data are well fitted by the power law dependence of Eq. (4.17) (solid line). Free fit parameters are the reduction factor  $q$  and the ratio of initial values  $T_0/N_0$ . Linear regression yields the value  $q \approx 0.5$ , in perfect agreement with the one deduced from fitting the time evolutions  $T(t)$  and

$N(t)$ .

#### 4.4.2 Cs ( $F_1 = 4$ , $F_2 = 3$ )

Similar measurements as described above were performed with Cs partially repumped into the upper hyperfine state  $|F = 4\rangle$ . This is realized by applying a short depumping pulse on the  $|F = 4\rangle \rightarrow |F' = 4\rangle$  transition 20 ms after all atoms were repumped into  $|F = 4\rangle$ . The total number of atoms and the temperature is measured as described above. In order to detect the fraction of atoms in  $|F = 4\rangle$ , an absorption image is taken without previously repumping and preparing the atoms in the doubly polarized state  $|F = 4, m_F = 4\rangle$ . In the latter case, the detection efficiency is weaker because the absorption cross-section is smaller for a non-cycling transition. The weaker detection efficiency of the  $|F = 4\rangle$ -population is corrected for by introducing a scaling factor. This factor is given by the ratio of absorption signals obtained by applying the two methods on the same Cs sample previously repumped into  $|F = 4\rangle$  but not spin-polarized.

Fig. 4.6 (a) shows decay curves of the average density for different initial populations of the hyperfine state  $|F = 4\rangle$ . The density decay is purely exponential with a time constant  $\tau = 40$  s if all atoms are depumped into the lowest groundstate  $|F = 3\rangle$ , as expected from the residual background gas pressure (open squares). From a linear fit of the corresponding temperature evolution (b) after initial equilibration we deduce a residual heating rate of 300 nK/s. The closed symbols display the evolution of the total density (a) and temperature (b) when 64%, 86% and 100% of the atoms are in  $|F = 4\rangle$  (from top to bottom). The depumping pulse lengths are 4.5  $\mu$ s, 15.4  $\mu$ s and 2 ms, respectively. The open symbols with corresponding shapes (a) represent the density curves for the  $|F = 4\rangle$ -fraction. The fact that the behavior of the latter fraction is almost unchanged with different population ratios provides an indication of the inelastic scattering rate coefficient for two atoms from the different fractions,  $G_{(3,4)}$ , being much smaller than the rate  $G_{(4,4)}$ . The temperature evolution both of the atom fraction in  $|F = 4\rangle$  and of the total ensemble is found to be identical within the fluctuations. This confirms the assumption of fast thermalization.

The decay curves are described by coupled differential equations for the total average density  $\bar{n}_{tot}$  and the density of the atom fraction in  $|F = 4\rangle$ ,  $\bar{n}_4$ ,

$$\begin{aligned}\dot{\bar{n}}_{tot} &= -\alpha\bar{n}_{tot} - 2\tilde{G}_{(3,4)}\bar{n}_4(\bar{n}_{tot} - \bar{n}_4) - \tilde{G}_{(4,4)}(T)\bar{n}_4, \\ \dot{\bar{n}}_4 &= -\alpha\bar{n}_4 - \tilde{G}_{(3,4)}\bar{n}_4(\bar{n}_{tot} - \bar{n}_4) - \tilde{G}_{(4,4)}(T)\bar{n}_4.\end{aligned}\tag{4.26}$$

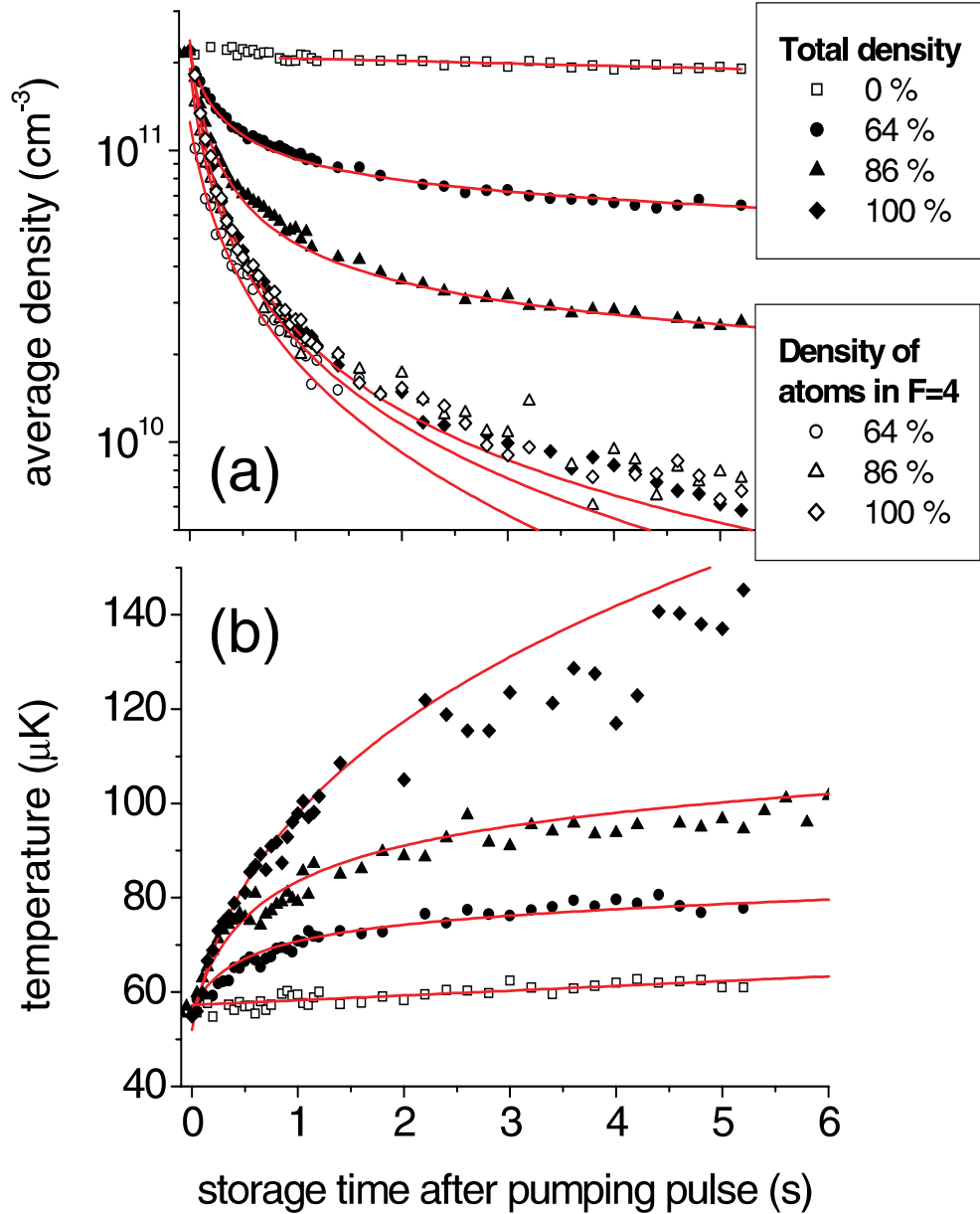


Figure 4.6: Inelastic collisions of Cs partially repumped into the upper hyperfine state  $|F = 4\rangle$ . Fig. (a) shows the density decay for various initial values for the population in  $|F = 4\rangle$ , Fig. (b) the corresponding temperature of the total density. The decay is exponential if only  $|F = 3\rangle$  is populated (open squares). The closed symbols display the evolution of the total density for 64%, 86% and 100% of the population in  $|F = 4\rangle$  (from top to bottom). The open symbols with corresponding shapes represent the  $|F = 4\rangle$ -fraction. The solid lines are best fits of the numerical solution of Eq. (4.26) to the data.

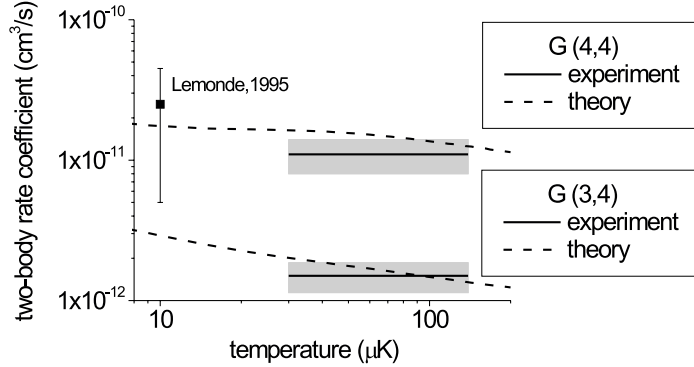


Figure 4.7: Comparison of experimental and theoretical results for the two-body rate coefficients  $G_{(4,4)}$  and  $G_{(3,4)}$  as a function of temperature.

The cross-coefficient  $\tilde{G}_{(3,4)}$  is assumed to be temperature independent as is  $G_{(4,4)}$ . We fit the numerical solution of these rate equations to both  $\bar{n}_{(4,4)}$  and  $\bar{n}_{(3,4)}$  curves simultaneously (solid lines in Fig. 4.6 (a)). Besides  $G_{(3,4)}$ , the free fit parameters are the initial values  $\bar{n}_{tot,0}$ ,  $\bar{n}_{4,0}$  and  $T_0$ . We obtain the value for the effective cross-coefficient  $\tilde{G}_{(3,4)} = (2.6 \pm 0.3 \pm 0.5) \times 10^{-12} \text{cm}^3 \text{s}^{-1}$ , which leads to

$$G_{(3,4)} = (1.5 \pm 0.2 \pm 0.3) 10^{-12} \text{cm}^3 \text{s}^{-1}.$$

The temperature curves (solid lines in Fig. 4.6 (b)) are calculated from the evolution of the total density according to

$$T(t) = T_0 \left( 1 + \bar{n}_0 \tilde{G} t \right)^{-2 \frac{q-1}{3q-5}}. \quad (4.27)$$

This expression follows from Eq. (4.23), (4.16) and (4.25).

Figure 4.7 compares the experimental and theoretical results for the coefficients  $G_{(4,4)}$  and  $G_{(3,4)}$  as a function of temperature. The experimental values are depicted as horizontal lines in the investigated temperature interval of 30 – 140  $\mu\text{K}$ . The uncertainty interval is indicated as shaded area. The value for  $G_{(3,4)}$  is about one order of magnitude smaller than the one for  $G_{(4,4)}$ . The same behavior was observed in similar measurements with optically trapped  $^{40}\text{K}$  [Roati et al., 2001]. The dashed curves represent theoretical predictions of [Tiesinga, 2002]. The rate coefficients are calculated in the approximation of pure  $s$ -wave scattering. The depicted lines result from averaging the rate coefficients over the thermal energy distribution at temperature  $T$ . The agreement of our experimental values with theory is

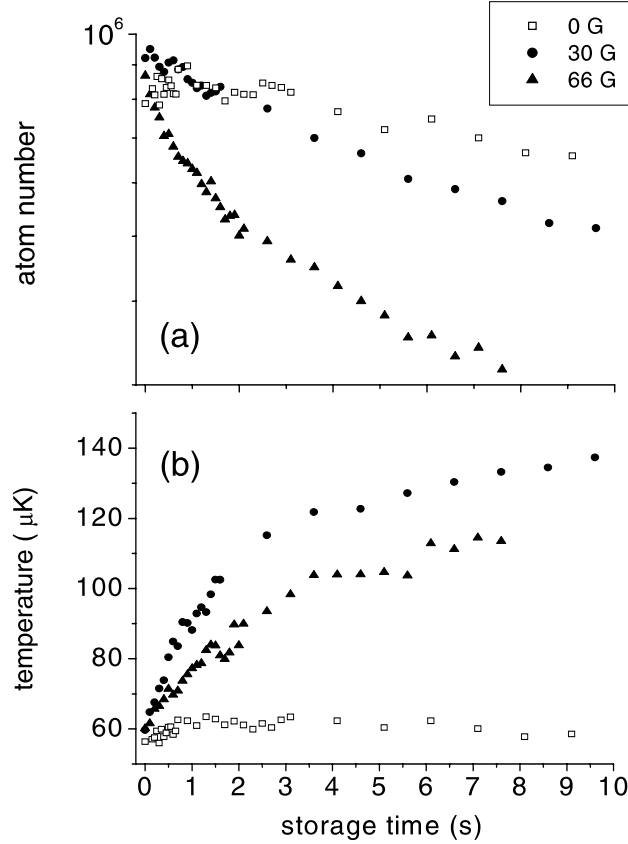


Figure 4.8: Influence of a homogeneous magnetic field on the number (a) and temperature (b) of trapped atoms in the lower hyperfine groundstate  $|F = 3\rangle$ . When a magnetic bias field is applied (filled symbols), we observe non-exponential trap loss and relaxation heating as a result of dipolar collisions.

excellent. Also, previous measurements match both theory and our results [Sesko et al., 1989, Lemonde et al., 1995].

#### 4.4.3 Cs ( $F_1 = 4$ , $F_2 = 4$ ) in a homogeneous magnetic field

Fig. 4.8 shows the influence of a homogeneous magnetic bias field on the trapped Cs atoms. In (a), the number of atoms initially prepared in the lowest hyperfine state  $|F = 3\rangle$  is depicted as a function of storage time for the magnetic field values 0 G (open squares), 30 G (solid circles), and 66 G (solid triangles). The corresponding temperature evolution is plotted in Fig. 4.8

(b). As in the case of spin exchange collisions we observe a non-exponential decrease in atom number accompanied by heating. Again, this behavior can be explained by inelastic collisions, namely dipolar relaxation between the Zeeman shifted magnetic sub-levels  $|F = 3, m_f\rangle$ . In this case, the Zeeman splitting  $\Delta E_{\text{Zeeman}} = g_f \mu_B B \approx 0.47 \text{ MHz/G}$  is converted into kinetic energy in every inelastic collision. The gain in kinetic energy is shared to equal parts between the two colliding atoms. In contrast to spin exchange collisions, this energy is not necessarily much larger than the depth of the trapping potential  $U_0$ . At 30 G, the gain in kinetic energy per atom released in an inelastic collision falls below the trap depth,  $\frac{1}{2}\Delta E_{\text{Zeeman}} < U_0$ . Therefore, the released Zeeman energy mainly leads to heating in addition to relaxation heating due to anti-evaporation. The observed atom number decay results both from inelastic collisions directly and from evaporation out of the trap due to the high temperature. At 66 G magnetic field, the gain in energy per atom  $\frac{1}{2}\Delta E_{\text{Zeeman}} \gtrsim U_0$ , such that inelastic collisions mainly lead to trap loss.

Fig. 4.8 shows the number of trapped atoms after a fixed storage time, in which a variable homogeneous magnetic field is applied. The storage time is 4 s when all atoms are prepared in  $|F = 3\rangle$  lowest groundstate (open symbols) and 0.4 s for the trap loss measurement of Cs in the  $|F = 4\rangle$  (filled symbols). Clearly, the number of atoms remaining in the trap continuously drops with magnetic field. This reflects the increasing Zeeman splitting released into kinetic energy in a dipolar collision. In addition, the collision rate is expected to increase as  $\sqrt{B}$  due to phase-space considerations (see Section 4.2.2). In contrast to dipolar collisions, the number of remaining atoms repumped into  $|F = 4\rangle$  after 0.4 s storage time shows no magnetic field dependence (closed symbols). This can be explained by the fact that the phase-space available in an inelastic collisions is entirely determined by the hyperfine energy splitting, which is independent of the magnetic field.

#### 4.4.4 Li ( $F_1 = 2, F_2 = 2$ )

The situation with Li is somewhat different from the one with Cs. Due to the small scattering cross-section and the low initial density of trapped atoms, we expect collision rates per atom on the order  $\gamma_{\text{Li}} \sim 0.01 - 0.1 \text{ s}^{-1}$ . Thus, thermalization happens on the time scale of storage time,  $\tau_{\text{therm}} \approx 10/\gamma_{\text{Li}} \gtrsim 100 \text{ s}$ . For this reason, we do not observe evaporation, although the mean kinetic energy is of the order of the Li trap depth,  $\langle E_{\text{kin}} \rangle \sim U_{0,\text{Li}}$  (see Sec. 3.2). However, these considerations also hold as far as relaxation heating due to inelastic trap loss is concerned. In the absence of elastic collisions, the depleted states at low energies are not refilled and the relaxation heating quickly stops. Strictly speaking, we cannot presume the atomic distribution

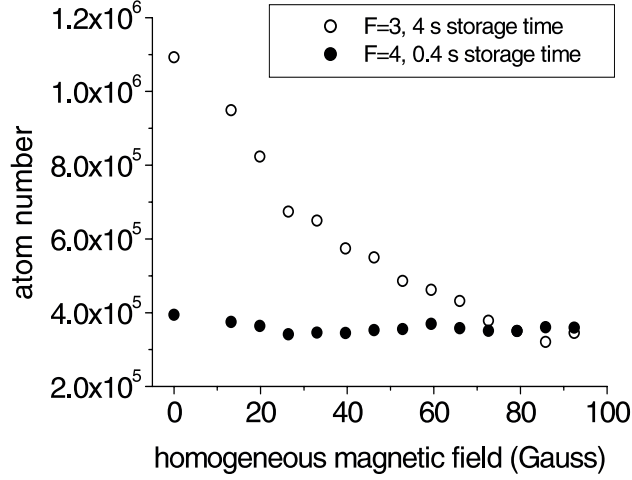


Figure 4.9: Number of remaining atoms after 0.4 s (4 s) of storage time at a homogeneous magnetic field of 66 G. The atoms are prepared in the  $F = 4$  ( $F = 3$ ) hyperfine state.

to be thermal. Nevertheless, we estimate the effective volume using Gaussian functions as spatial distributions.

Due to the low Li density, absorption imaging cannot be applied. Therefore, the measurement of atom numbers relies on imaging the fluorescence light onto a carefully calibrated photodiode or the CCD camera (see Sec. 2.6.1). The systematic error due to uncertainties of the detection efficiency is of the order of 50%. Using a release-and-recapture technique we roughly estimate the mean kinetic energy of the Li sample in the QUEST (see appendix A). Changes in  $\langle E_{kin} \rangle$  due to relaxation heating effects cannot be resolved. For the sake of feasibility, anti-evaporation is neglected and  $\langle E_{kin} \rangle$  is assumed to remain constant. Using the discussed simplifications, the rate equation modelling trap loss of Li takes the form

$$\dot{N}_{\text{Li}} = -\alpha_{bg} N_{\text{Li}} - 2G_{\text{Li}} \frac{N_{\text{Li}}^2}{V_{\text{Li}}}. \quad (4.28)$$

Here, we include a loss term  $\alpha_{bg} N_{\text{Li}}$  in order to account for trap-loss collisions with the background gas. The experiments on spin-exchange collisions of Li and on inter-species inelastic collisions (Sec. 4.5) were performed in the AOM QUEST (see Sec. 2.2.3). For Cs, the measured radial and axial trap frequencies in this geometry are  $\omega_{rad} = 2\pi \times (600 \pm 20)$  Hz and  $\omega_{ax} = 2\pi \times (12 \pm 1)$  Hz, respectively. By recording the AC Stark shift of the trapped atoms in the QUEST we infer the Cs trap depth  $U_0 = (510 \pm$

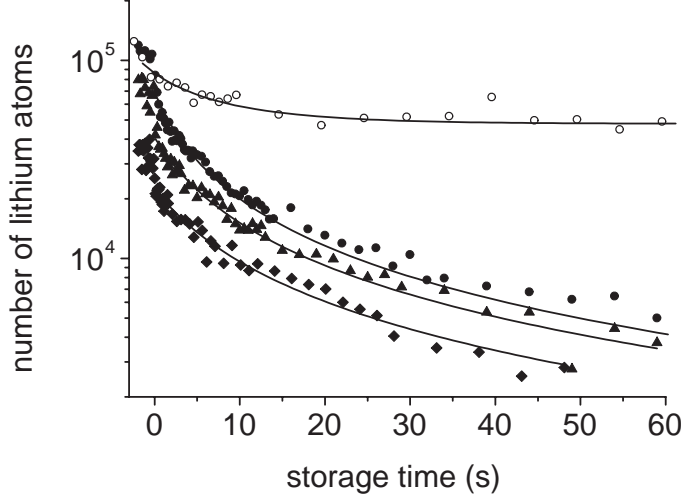


Figure 4.10: Trap loss measurement of Li atoms prepared in the upper hyperfine groundstate  $|F = 2\rangle$  at  $t = 0$  for three different values of the initial number of atoms (filled symbols). For comparison, the open symbols represent the time evolution of Li in the lowest hyperfine groundstate  $|F = 1\rangle$ .

$20)\mu\text{K} \times k_B$  (see Sec. 2.7.2). The trap depth for Li atoms differs from the one for Cs due to the different static polarizabilities for Cs and Li,  $\alpha_{\text{Cs}}$  and  $\alpha_{\text{Li}}$ , respectively. Thus we obtain  $U_0^{\text{Li}} = U_0^{\text{Cs}} \times \alpha_{\text{Li}}/\alpha_{\text{Cs}} = (210 \pm 20) \mu\text{K}$ . The Li trap frequencies can be calculated from the measured ones for Cs using  $\omega_{\text{Li}} = \omega_{\text{Cs}} \sqrt{U_0^{\text{Li}} m_{\text{Cs}} / (U_0^{\text{Cs}} m_{\text{Li}})} \approx 2.78 \omega_{\text{Cs}}$ . Thus, the effective volume is given by  $V_{\text{Li}} = (4\pi k_B T / m_{\text{Li}})^{3/2} / (\omega_{\text{rad}}^2 \omega_{\text{ax}})$ , which is assumed to be constant. In this case, equation (4.28) has the analytic solution

$$N_{\text{Li}}(t) = \frac{N_{\text{Li},0} e^{-\alpha_{\text{bg}} t}}{1 + 2 \frac{N_{\text{Li},0}}{V_{\text{Li}}} \frac{G_{\text{Li}}}{\alpha_{\text{bg}}} (1 - e^{-\alpha_{\text{Li}} t})}. \quad (4.29)$$

The transfer sequence for Li is described in Section 2.5.2. As in the Cs case, the atoms are repumped into the upper hyperfine state  $|F = 2\rangle$  by mechanically switching on the MOT repumping light during 2 ms on the transition  $|F = 1\rangle \rightarrow |F'\rangle$ . After a variable relaxation time, the number of remaining atoms of each species is measured. Shot-to-shot fluctuations of the Li atom number are in the range of 15%.

Figure 4.10 displays trap loss curves of Li after repumping into the  $|F = 2\rangle$  hyperfine state at  $t = 0$  (filled symbols). The three curves are recorded under identical experimental conditions for different values of the initial atom

number and temperature,  $N_{\text{Li},0} = 2.3 \times 10^4$  and  $T_0 = 60 \mu\text{K}$ ,  $N_{\text{Li},0} = 4.1 \times 10^4$ , and  $T_0 = 50 \mu\text{K}$ ,  $N_{\text{Li},0} = 6.9 \times 10^4$  and  $T_0 = 46 \mu\text{K}$ . These initial conditions are controlled by triggering the Li transfer sequence to a given Li-MOT fluorescence level. The initial Li temperature is inferred from release-and-recapture measurements and has an uncertainty of  $\pm 20\%$ . Interestingly, the loss rate at a given storage time is the same for the three curves, although the number of atoms is different. This reflects the fact that, apparently, the initial density is identical, no matter how many Li atoms are loaded. For comparison, the open symbols represent the evolution of the number of Li atoms in the lowest hyperfine groundstate  $|F = 1\rangle$ . The small non-exponential drop during the first 10 s may be due to evaporation, although we do not expect thermalization on this time scale. From fitting Eq. (4.28) to the data we obtain the parameter  $\alpha_{bg}$  associated with trap loss collisions with the hot background gas. Fitting the same equation to the inelastic loss curves yields the two-body rate coefficient

$$G^{\text{Li}} = (7 \pm 1 \pm 3) \times 10^{-11} \text{ cm}^3/\text{s}.$$

The first error results from statistical fluctuations whereas the second error is an estimate of the systematic uncertainty discussed above. This value is surprisingly large as compared to the rate coefficient for spin-changing collisions of Cs. However, it stays behind the rate constant of the order of  $10^{-9} \text{ cm}^3/\text{s}$  that was measured with  $^6\text{Li}$ .

## 4.5 Heteronuclear spin-changing collisions

The investigation of inelastic groundstate interactions has only recently been extended to mixtures of different atomic species [Schlöder et al., 1999, Young et al., 2000, Telles et al., 2001b]. The main interest is directed towards complementary information about heteronuclear groundstate interaction potentials, which are not yet precisely predicted. Also, the thermodynamics of trapped mixtures undergoing both elastic and inelastic collisions is an interesting issue. The understanding of multispecies groundstate interactions is a prerequisite for further work on mixtures of Bose-Einstein and Fermi degenerate gases [Modugno et al., 2001, Hadzibabic et al., 2002, Roati et al., 2002] and the formation of ultracold heteronuclear molecules [Bahns et al., 2000].

Spin-changing collisions between Li and Cs have briefly been studied in [Schlöder et al., 1999]. The rate coefficient for spin-exchange collisions in the heteronuclear system Na-K was measured to exceed the one for Na-Na by roughly one order of magnitude [Santos et al., 1999]. In [Young et al., 2000],

spin-exchange collisions between groundstate Rb and Na atoms were identified. All cited experiments were carried out in mixed-species MOTs, and the measured rate coefficients featured a strong dependence on the intensity of the near-resonant trapping light. In this section, we present first experimental results on ultracold inelastic collisions between two different atomic species in the electronic groundstate.

First, we briefly describe the combined Li and Cs transfer sequence into the QUEST (see Sec. 2.5.3). Since the two MOTs perturb each other when operated simultaneously [Schlöder et al., 1999], we first transfer Cs from the Cs-MOT. Then the Li-MOT is loaded slightly displaced from the optically stored Cs atoms to minimize inelastic collisions with hot Li-MOT atoms. A subsequent Cs molasses pulse sets the initial Cs temperature to about  $30 \mu\text{K}$ . In the last step the compressed Li-MOT is positioned onto the QUEST and all resonant laser beams and the magnetic fields are switched off. Both the number of Li and Cs atoms loaded into the QUEST are controlled by triggering the corresponding transfer sequences to fixed MOT fluorescence threshold values.

The Li and Cs atoms are initially optically pumped into the lowest hyperfine groundstate by switching off the MOT cooling lasers 1 ms later than the repumping laser. In order to prepare one or both atomic species in the upper hyperfine groundstate for the collisional studies presented below, an optical repumping pulse is applied 1 s after the combined loading of the QUEST. The repumping pulse is provided by mechanically switching on the MOT repumping light during 2 ms on the transition  $|F = 3\rangle \rightarrow |F' = 4\rangle$  for Cs and  $|F = 1\rangle \rightarrow |f'\rangle$  for Li.

Since the thermalization time between Li and Cs is on the order of 1 s, we assume the Li-Cs mixture to be thermally equilibrated when the inelastic interaction is launched. After a variable relaxation time, the number of remaining atoms of each species is measured. Since the population of the  $m_F$ -states reflects the one in the MOT, we assume both Li and Cs samples to be unpolarized. This type of measurement is destructive, therefore the procedure is repeated for the same initial conditions and various relaxation times. Shot-to-shot fluctuations of Li atom number are in the range of 20% in this combined transfer scheme.

In the experiments presented below, the Cs atom number is inferred from the integrated fluorescence image of the Cs cloud after recapture into the Cs-MOT. The latter method is carefully calibrated to the absorption imaging technique. The error resulting from the calibration is much smaller than the estimated systematic error in number determination using absorption imaging, which is of order 20%.

Before analyzing the heteronuclear collision experiments we check the

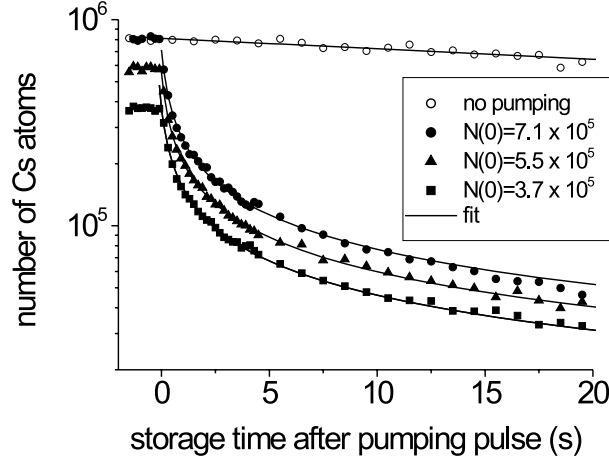


Figure 4.11: Cs trap loss due to spin-exchange collisions in the AOM QUEST. The number of remaining atoms  $N(t)$  are measured using fluorescence imaging of the recapture MOT.

validity of the analytic model presented in Sec. 4.4 for the inelastic Cs decay in the shallower AOM QUEST recorded by fluorescence imaging. Fig. 4.11 displays Cs loss curves for three different values of the initial number of atoms, controlled by triggering the Cs transfer sequence to different Cs-MOT fluorescence levels. As in the case of Li, the loss rate at a given storage time is unchanged for the three curves, although the number of atoms is different. Apparently, for the given MOT laser detuning and intensity, both Li and Cs transfer are density limited. By fitting equation (4.20) to the data with fixed values of  $q = 0.5$  and  $G = 1.1 \times 10^{-11} \text{cm}^3/\text{s}$  (solid lines) we obtain the initial temperature values. The latter values are in agreement within 10% with the ones measured using absorption imaging of the expanding cloud.

#### 4.5.1 Cs( $F=4$ ) Li( $F=1$ )

In a mixture of Cs in  $|F=4\rangle$  and Li in  $|F=1\rangle$  there are two collision channels. First, the Cs atoms can collide inelastically among each other. The associated rate coefficient has been discussed in Sec. 4.4.1. Second, inelastic inter-species collisions affect both Li and Cs atoms. In the latter case, the hyperfine energy  $\Delta E_{HFS,Cs} = 9.2 \text{ GHz} \times h = 440 \text{ mK} \times k_B$  is converted into kinetic energy of the colliding Li and Cs atoms. According to Eq. (4.9), 95% of the energy is absorbed by the Li and 5% by the Cs atom. Clearly, the

gain in kinetic energy exceeds by far the depth of the trapping potential for both Li and Cs,  $U_{0,\text{Cs}} = 510 \mu\text{K}$  and  $U_{0,\text{Li}} = 210 \mu\text{K}$ , leading to trap loss of both atoms.

Fig. 4.12 displays loss curves of Li and Cs atoms simultaneously stored in the QUEST in plots (a) and (b), respectively. Identical symbols in plots (a) and (b) correspond to one measurement. The open symbols depict trap loss curves for  $N_{\text{Cs},0} = 8 \times 10^5$  Cs atoms prepared in the lowest groundstate  $|F = 3\rangle$ . The three different filled symbols reflect inelastic trap loss curves for different values of the initial number and temperature of Cs atoms,  $N_{\text{Cs},0} = 7.2 \times 10^5$  and  $T_{\text{Cs},0} = 38 \mu\text{K}$  (diamonds),  $N_{\text{Cs},0} = 2.3 \times 10^5$  and  $T_{\text{Cs},0} = 28 \mu\text{K}$  (triangles),  $N_{\text{Cs},0} = 7.2 \times 10^4$  and  $T_{\text{Cs},0} = 26 \mu\text{K}$  (circles).

At  $t = 0$ , the Cs atoms are optically repumped into the upper hyperfine groundstate  $|F = 4\rangle$ , whereas the Li atoms remain in their lowest groundstate. The subsequent non-exponential decay of the number of Cs atoms (b) primarily results from homonuclear spin-exchange collisions as discussed in Sec. 4.4. This is due to the fact that in the measurements presented here, the initial number of Cs atoms exceeds the number of Li atoms initially loaded. However, in the case of loading as many Cs atoms as Li atoms (circles), the Cs decay curve falls off faster. This can be explained by the additional inter-species collision channel becoming observable at roughly equal initial atom numbers. Due to the much larger transfer efficiency for Cs than for Li (see Sec. 2.5.3), it was not possible to reverse the situation with our current setup. The presented experimental data are average values of three measurements each, performed under identical conditions.

The non-exponential drop in number of Li atoms (a) can entirely be attributed to inelastic inter-species collisions with Cs atoms in  $|F = 4\rangle$ . Therefore, the decay rate strongly depends on the number of Cs atoms present in the trap. The loss curve for the case of purely elastic Li-Cs interaction (open symbols) features an increased decay rate compared with single-species storage. This behavior reflects the effect of sympathetic evaporation discussed in Sec. 3.4. However, this loss curve is to be compared with the inelastic one for large Cs atom numbers (diamonds). Apparently, both trap loss collisions with rest gas atoms and sympathetic evaporation are negligible on the time scale of inelastic trap loss.

We model the trap loss dynamics using the coupled rate equations

$$\begin{aligned} \dot{N}_{\text{Cs}} &= -\alpha_{bg}^{\text{Cs}} N_{\text{Cs}} - G_{(4,4)} \frac{N_{\text{Cs}}^2}{V_{\text{Cs}}} - G_{(1,4)}^{\text{LiCs}} \frac{N_{\text{Li}} N_{\text{Cs}}}{V_{\text{LiCs}}}, \\ \dot{N}_{\text{Li}} &= -\alpha_{bg}^{\text{Li}} N_{\text{Li}} - G_{(1,4)}^{\text{LiCs}} \frac{N_{\text{Li}} N_{\text{Cs}}}{V_{\text{LiCs}}}. \end{aligned} \quad (4.30)$$

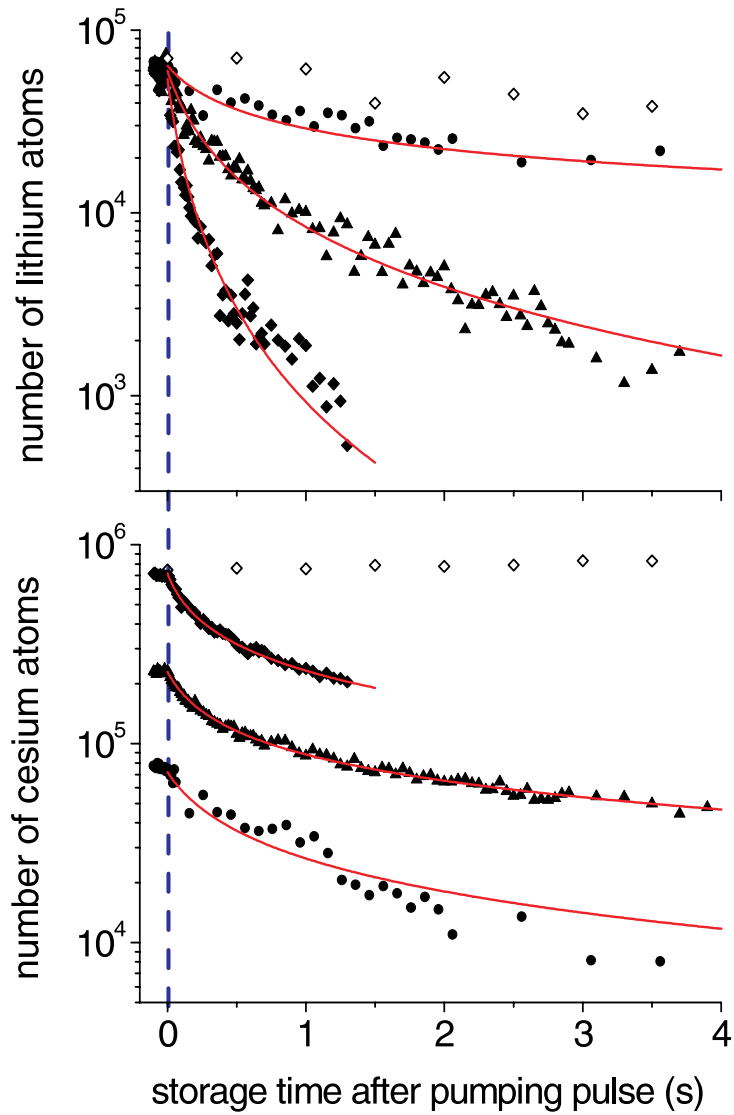


Figure 4.12: Li (a) and Cs (b) trap loss as a result of both single-species and inter-species spin-changing collisions in the combined QUEST. At  $t = 0$ , the Cs atoms are optically repumped into the upper hyperfine groundstate  $|F = 4\rangle$ . Identical symbols in plots (a) and (b) correspond to one measurement. The three different filled symbols reflect different values of the initial number and temperature of the Cs atoms. The open symbols depict loss curves for both Cs and Li prepared in their lowest groundstates  $|F = 3\rangle$  and  $|F = 1\rangle$ , respectively.

Here, the parameters  $\alpha_{bg}^{\text{Li}}$  and  $\alpha_{bg}^{\text{Cs}}$  roughly amount to  $1/100 \text{ s}^{-1}$  and can be neglected. The homonuclear rate coefficient  $G_{(4,4)} = 1.1 \times 10^{-11} \text{ cm}^3/\text{s}$  is held fixed and the Cs temperature evolution is determined using expression (4.17) with  $q = 0.5$ . The last term in Eq. (4.31) describes the escape out of the trap of equal numbers of Li and Cs atoms as a consequence of heteronuclear spin-changing collisions according to Eq. (4.10). The corresponding rate coefficient  $G_{(1,4)}^{\text{LiCs}}$  is assumed to be temperature independent. Relaxation heating as a result of heteronuclear trap loss collisions is neglected in the model. This can be justified by the fact that the temperature of the Li-Cs system is dominated by the Cs temperature due to the larger Cs particle number. For this reason we substitute the temperature dependence of the effective volumes  $V_{\text{Cs}}(T)$  and  $V_{\text{LiCs}}(T)$  (see Eq. (3.13)) by the dependence on  $T_{\text{Cs}}$ .

The rate equations are solved numerically and fitted to the experimental Li and Cs data simultaneously. As free parameters we vary  $G_{(1,4)}^{\text{LiCs}}$  and the boundary values  $N_{\text{Li},0}$  and  $N_{\text{Cs},0}$ . The resulting fit curves are represented by solid lines in Fig. 4.12. Clearly, the model reproduces the mixed trap loss dynamics quite well. We obtain the value for the interspecies rate coefficient

$$G_{(1,4)}^{\text{LiCs}} = (1.8 \pm 0.2 \pm 0.6) \times 10^{-10} \text{ cm}^3/\text{s}$$

The first error results from statistical fluctuations whereas the second error is an estimate of the systematic uncertainty, which is dominated by the determination of the number of Li atoms. This value is about half as large as the previously measured one,

$\gamma_{\text{LiCs}} = 5(1) \times 10^{-10} \text{ cm}^3/\text{s}$  [Schlöder et al., 1999]. The discrepancy may be attributed to the influence of near-resonant light present in the MOT measurement [Gensemer et al., 2000].

### 4.5.2 Cs(F=3) Li(F=2)

In spin-changing collisions involving Cs in  $|F = 3\rangle$  and Li in  $|F = 2\rangle$ , the released internal energy amounts to  $\Delta E_{\text{HFS,Li}} = 800 \text{ MHz} \times h = 38 \text{ mK} \times k_{\text{B}}$ . In this case, the Cs share of kinetic energy is only  $1.9 \text{ mK} \times k_{\text{B}}$ . However, this gain in kinetic energy still necessarily results in loss out of the trap.

Fig. 4.13 shows the observed trap loss curves for the reversed situation as described in the previous sections. Here, the Cs atoms are prepared in their lowest groundstate whereas the Li atoms are optically pumped to the upper hyperfine state  $|F = 2\rangle$ . We observe only little effect on the number of Cs atoms since it exceeds by far the Li atom number. The evolution of the number of Li atoms, however, features a rapid drop which again strongly

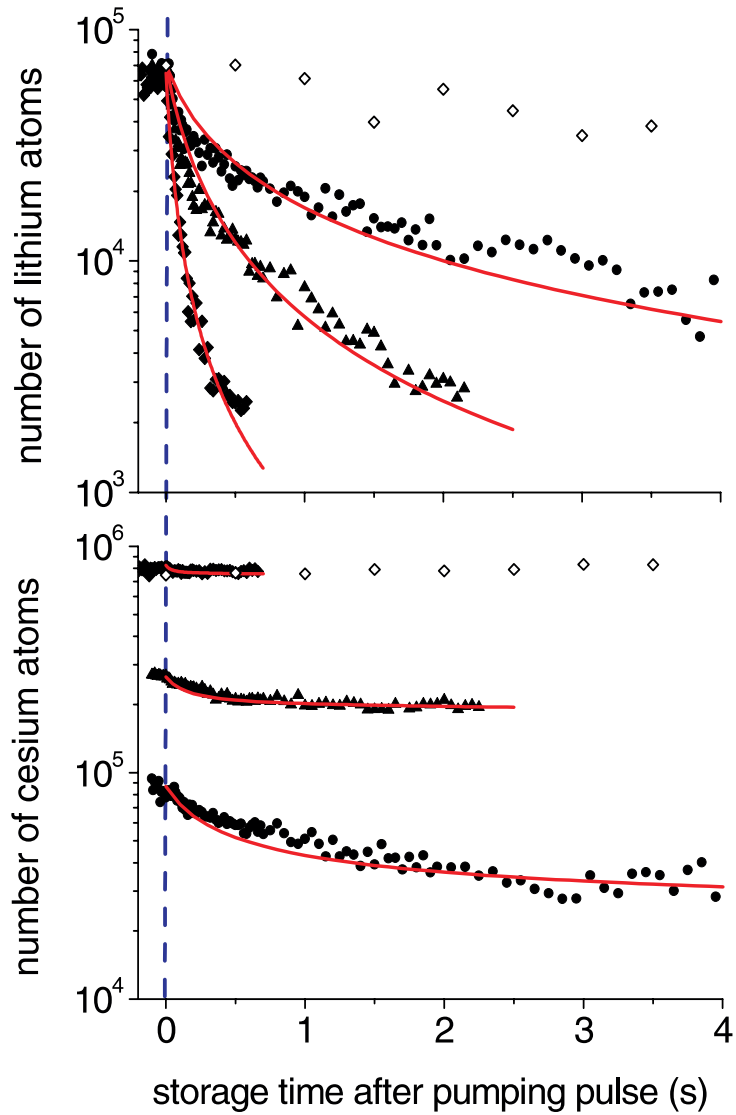


Figure 4.13: Inter-species trap loss collisions induced by Li atoms optically pumped into the upper hyperfine groundstate  $|F = 2\rangle$ . The three different filled symbols reflect different values of the initial number of Cs atoms. The open symbols depict loss curves for both Li and Cs prepared in their lowest groundstates.

depends on the number of simultaneously stored Cs atoms. The fact that for roughly equal atom numbers (filled circles) the Li decay is much faster than in the homonuclear case (Fig. 4.10), indicates that  $G_{(2,3)}^{\text{LiCs}} > G^{\text{Li}}$ . As in the previous section, each experimental curve results from averaging over three

individual measurements.

We describe the trap loss dynamics by the coupled rate equations

$$\begin{aligned}\dot{N}_{\text{Cs}} &= -\alpha_{\text{Cs}}N_{\text{Cs}} - G_{(2,3)}^{\text{LiCs}} \frac{N_{\text{Li}}N_{\text{Cs}}}{V_{\text{LiCs}}}, \\ \dot{N}_{\text{Li}} &= -\alpha_{\text{Li}}N_{\text{Li}} - G^{\text{Li}} \frac{N_{\text{Li}}^2}{V_{\text{Li}}} - G_{(2,3)}^{\text{LiCs}} \frac{N_{\text{Li}}N_{\text{Cs}}}{V_{\text{LiCs}}}.\end{aligned}\quad (4.31)$$

Since the number of Cs atoms is not significantly influenced by the inelastic trap loss collisions the Cs temperature is held constant over the entire simultaneous storage time. However, we have to allow for a rising temperature of Li as a result of anti-evaporation in order to reproduce the observed behavior. In other words, we can no longer presume thermal equilibrium between Li and Cs. Strictly speaking, we can neither suppose the Li distribution to be thermalized.

For the sake of simplicity, we still evaluate the effective volumes using Gaussian functions as spatial distributions according to Eq. (3.13) in Chapter 3. The Li temperature is calculated in analogy to Eq. (4.17),

$$T_{\text{Li}} = T_{\text{Li},0} \left( \frac{N_{\text{Li}}}{N_{\text{Li},0}} \right)^{q_{\text{Li}}-1}, \quad (4.32)$$

by setting  $T_{\text{Li},0} = T_{\text{Cs},0}$ . The reduction factor is fixed to  $q_{\text{Li}} = 0.5$  assuming identical relaxation dynamics for Li-Cs as for Cs-Cs trap loss collisions. However, if  $q_{\text{Li}}$  is varied as a free parameter in the fit of the experimental data, one finds roughly the same result. This model for  $T_{\text{Li}}(t)$  represents a crude simplification, since the Li and Cs clouds are confined in trapping potentials of different depth. Nevertheless, the additional uncertainty due to the variable Li temperature is limited, since  $G_{(2,3)}^{\text{LiCs}}$  is primarily determined by the initial slope of the decay curves, when  $T_{\text{Li}} \approx T_{\text{Cs}}$ . The rising Li temperature effectively slows down the decay rate at longer storage times, which contribute less to the fit accuracy. Free fit parameters are  $G_{(2,3)}^{\text{LiCs}}$  and the initial values  $N_{\text{Li},0}$  and  $N_{\text{Cs},0}$ .

The fit curves are plotted as solid lines in Fig. 4.13. The model reproduces the mixed trap loss dynamics reasonably well for the measurements when  $N_{\text{Cs},0} \gg N_{\text{Li},0}$ . When  $N_{\text{Cs},0} \approx N_{\text{Li},0}$ , the model curves overestimate the inelastic loss rate. This is due to the fact that relaxation heating of Cs from inelastic collisions with Li becomes significant at roughly equal atom numbers. As a consequence, the two-species effective volume increases and the collision rate goes down. However, this effect is not included in the model. We obtain the value for the interspecies rate coefficient

$$G_{(2,3)}^{\text{LiCs}} = (2.4 \pm 0.8 \pm 1.0) \times 10^{-10} \text{ cm}^3/\text{s}$$

Again, the first error results from statistical fluctuations and the second error is an estimate of the systematic uncertainty.

### 4.5.3 Cs(F=4) Li(F=2)

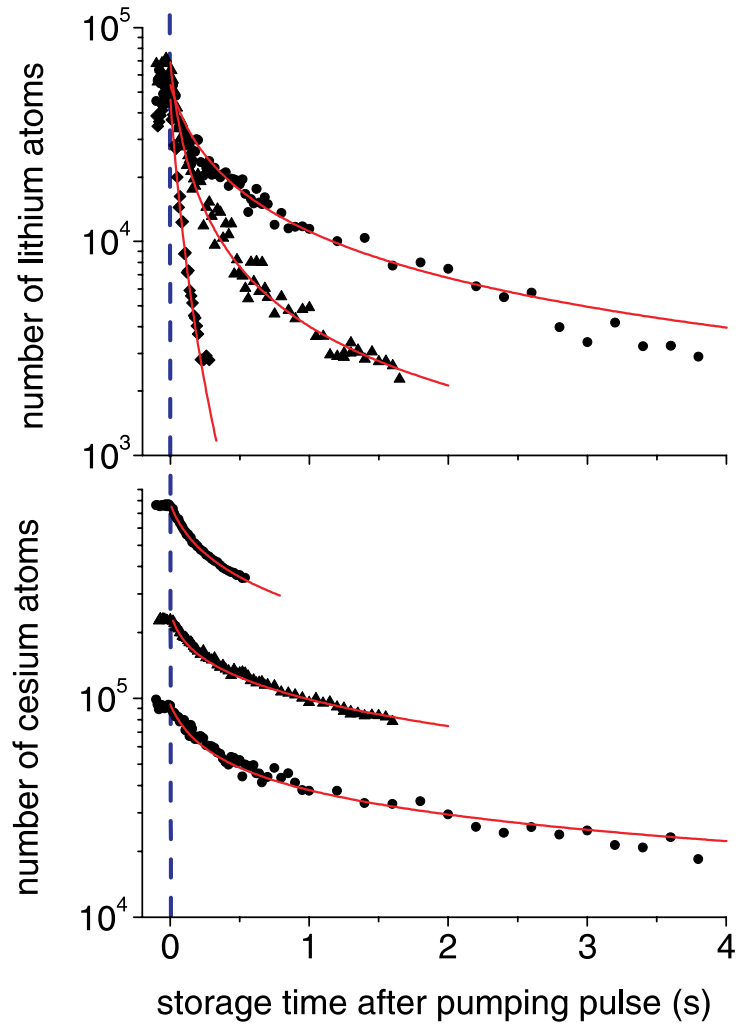


Figure 4.14: Trap loss curves as a result of both colliding Li and Cs atoms being prepared in their upper hyperfine groundstates.

Finally, Fig. 4.14 displays the trap loss curves recorded when both Li and Cs atoms are optically repumped into their upper hyperfine groundstates. As in Fig. 4.12, we observe fast trap loss of both Li and Cs atoms. Both

rate equations for Li and Cs now contain homonuclear and heteronuclear loss terms,

$$\begin{aligned}\dot{N}_{\text{Cs}} &= -\alpha_{\text{Cs}}N_{\text{Cs}} - G^{\text{Cs}}\frac{N_{\text{Cs}}^2}{V_{\text{Cs}}} - G_{(2,4)}^{\text{LiCs}}\frac{N_{\text{Li}}N_{\text{Cs}}}{V_{\text{LiCs}}}, \\ \dot{N}_{\text{Li}} &= -\alpha_{\text{Li}}N_{\text{Li}} - G^{\text{Li}}\frac{N_{\text{Li}}^2}{V_{\text{Li}}} - G_{(2,4)}^{\text{LiCs}}\frac{N_{\text{Li}}N_{\text{Cs}}}{V_{\text{LiCs}}}.\end{aligned}\tag{4.33}$$

As in the previous section, we allow for different temperatures of Li and Cs. The Cs temperature is assumed to behave according to anti-evaporation due to single-species collisions, as in Sec. 4.5.1. The Li temperature again changes according to Eq. (4.32), with a fixed value  $q_{\text{LiCs}} = 0.5$ . The fit results are

$$G_{(2,4)}^{\text{LiCs}} = (3.5 \pm 2.0 \pm 1.0) \times 10^{-10} \text{ cm}^3/\text{s}.$$

## 4.6 Conclusion

Trap loss measurements in optical dipole traps are a new approach to the investigation of ultracold inelastic collisions in the groundstate. Rate coefficients of inelastic processes provide complementary information about groundstate interaction potentials. The thermodynamics accompanying trap loss collisions are an important and interesting aspect. For the case of spin exchange collisions between Cs atoms in the  $|F = 4\rangle$  hyperfine state, we derive an analytic model describing the thermodynamics fairly well. However, the observed heating is stronger than expected from our model. This point requires further clarification. Nevertheless, we are able to infer reliable values for the rate coefficients  $G_{(4,4)}$  and  $G_{(3,4)}$ , which are in excellent agreement with theoretical predictions and with previous measurements. On the basis of the measured coefficient  $G_{(4,4)}$ , it was possible to deduce the cross-coefficient  $G_{(3,4)}$  from measurements with partially repumped Cs atoms. In future experiments, we will investigate inelastic collisions of doubly polarized Cs atoms in order to reproduce the dipolar relaxation rate studied in [Söding et al., 1998].

Inter-species spin-changing collisions between Cs  $|F = 4\rangle$  and Li  $|F = 1\rangle$  are well described by a simple rate equation model based on the assumption of thermal equilibrium between Li and Cs. The corresponding rate coefficient is in reasonable agreement with previous measurements. Trap loss collisions between Cs  $|F = 3\rangle$  and Li  $|F = 2\rangle$  and between Cs  $|F = 4\rangle$  and Li  $|F = 2\rangle$ , however, can only be modelled when allowing for diverging Li and Cs temperatures. This indicates that in the latter cases, the elastic scattering cross-section falls below the one in the case of Cs  $|F = 4\rangle$  colliding with

**Two-body rate coefficients ( $\text{cm}^3/\text{s}$ )**

System	This work	Prev. experiments	Theory ***
Cs (4,4)	$1.1(3) \times 10^{-11}$	$2.5(2) \times 10^{-11}$ *	$1.4 \times 10^{-11}$
Cs (3,4)	$1.5(4) \times 10^{-12}$	-	$1.6 \times 10^{-12}$
Li (2,2)	$7(3) \times 10^{-11}$	-	-
LiCs (1,4)	$1.8(8) \times 10^{-10}$	$5(1) \times 10^{-10}$ **	-
LiCs (2,3)	$2(1) \times 10^{-10}$	-	-
LiCs (2,4)	$4(2) \times 10^{-10}$	-	-

Table 4.1: Summary of the experimental results and comparison with literature. References: \* [Lemondé et al., 1995], \*\* [Schlöder et al., 1999], \*\*\* [Tiesinga, 2002].

Li  $|F = 1\rangle$ . The significant deviations of the data points from the model curves are mainly due to the fact that the Li ensemble is far from thermal equilibrium at low densities. In order to improve the accuracy of this kind of measurement, we will both improve our Li absorption imaging system and increase the pair density by reducing the Cs temperature and enhancing the Li transfer. Table 4.1 summarizes the experimental results and compares them with literature.

# Chapter 5

## Towards molecule formation

In this Chapter we present two approaches to the formation of ultracold groundstate molecules. After a brief introduction to the field, we study the feasibility of the formation of LiCs through photoassociation (PA) in the first part. Based on the potential curves taken from literature we calculate the expected PA-spectra and estimate the PA-rates. Molecular constants of groundstate LiCs can be predicted from the groundstate potentials. The ability of trapping groundstate LiCs in a QUEST is discussed. In the second part we present first experimental results on PA-spectroscopy of Cs<sub>2</sub>. The PA-spectra of Cs<sub>2</sub> are measured by recording the trap loss both from a magneto-optic trap and from the QUEST.

### 5.1 Motivation

**Spectroscopy in the ultracold** The interest in the formation of cold molecules is manifold. High-resolution spectroscopy was first proposed in 1987 [Thorsheim et al., 1987] and extensively reviewed [Stwalley and Wang, 1999, Masnou-Seeuws and Pillet, 2001]. The main advantage compared with classical molecular spectroscopy is the fact that at sub-mK temperatures line broadening due to the Doppler effect is virtually eliminated. Thus, free-bound absorption lines appear as sharp as ordinary naturally broadened bound-bound lines ( $\lesssim 10$  MHz). Since the probability for free-bound transitions is highest for large internuclear distances, PA-spectroscopy is ideally suited for observing "long-range states" at high vibrational excitation [Le Roy, 1973, Stwalley and Uang, 1978]. Besides, in ultracold photoassociative collisions partial waves with angular momentum greater than zero are nearly suppressed (see Sec. 3.1). Thus, only the lowest rotational states are generally populated in the photoassociated molecules,

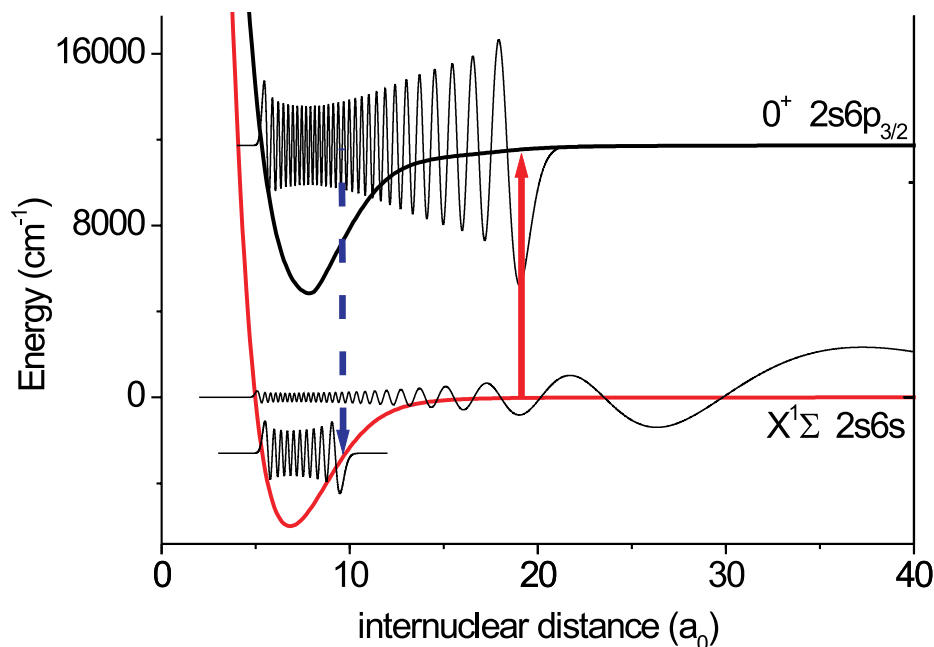


Figure 5.1: Schematic illustration of the photoassociation process of LiCs. Two colliding atoms are excited by absorbing a photoassociation photon toward a bound excited state (red arrow). Deexcitation proceeds by spontaneous or induced emission either back to a pair of free atoms or to a bound groundstate (blue arrow).

which simplifies the interpretation.

**Photoassociation** The principle idea of PA is illustrated in Fig. 5.1 for the LiCs case <sup>1</sup>. The colliding Li and Cs atoms approach each other at initially small kinetic energy due to the ultralow temperature. As they start to interact via the attractive singlet potential in the illustrated case, they are accelerated toward each other. This manifests in the initially large period of the collision wave function that oscillates faster inside the ground potential well. By absorption of a PA-laser photon, the collisional state is excited to a bound excited state (red arrow). According to the Franck-Condon principle the transition takes place at the internuclear distance where the wave

<sup>1</sup>The conversion factors for atomic units are  
 $1 \text{ cm}^{-1} = 1/219474 \text{ hartree} = 0.1240 \text{ meV} = 1.439 \text{ K} = 29.9792 \text{ GHz}$  and  $1 \text{ a}_0 = 0.529177 \text{ \AA}$

function overlap of the initial and final wave functions is maximum. The so called Condon point approximately coincides with the outer turning point of the classical vibration for highly excited vibrational states. Due to energy conservation the energy difference between free and bound state has to match the laser frequency. Thus, provided the spectral width of the laser falls below the energy width of the excited state, one can stimulate a free-bound transition state selectively. The deexcitation can proceed by spontaneous emission (blue arrow) or by induced emission through a second laser. The final state may either be a pair of free atoms or a bound state of the singlet or triplet groundstate. The rate of both absorption and emission are mainly determined by the overlap integral of the initial and final wave functions and by selection rules according to the symmetries of both states.

PA-spectroscopy on homonuclear systems has already been performed with all alkali atoms from Li to Cs, with hydrogen, helium and calcium [Masnou-Seeuws and Pillet, 2001]. Recently, PA-spectra of heteronuclear  ${}^6\text{Li}{}^7\text{Li}$  molecules have been observed [Schlöder et al., 2001]. However, PA of two different atomic species has been demonstrated only once with NaCs by two-step excitation to an autoionizing state [Shaffer et al., 1999]. The demonstration of PA of LiCs would be an important step towards the extension of PA-spectroscopy of heteronuclear molecules. PA has not only proved to be a complementary spectroscopic technique. Free-bound transitions induced by a laser field are indeed an efficient way to form cold molecules in excited electronic states. However, the lifetime of a photoassociated molecule is short, and after a few nanoseconds it decays by spontaneous emission, usually giving back a pair of atoms. The route to ultracold molecules in the groundstate depends on the occurrence of particular stabilization schemes in which spontaneous (or stimulated) emission also transfers population toward bound levels of the groundstate. Up to now ultracold groundstate molecules have only been observed for three homonuclear alkali dimers  $\text{Cs}_2$  [Fioretti et al., 1998],  $\text{K}_2$  [Nikolov et al., 1999], and  $\text{Rb}_2$  [Gabbanini et al., 2000].

**Cooling and trapping** Another tempting idea is the extension to cold molecules of the cooling and trapping techniques developed in the field of cold atoms and atom optics. However, due to the great variety of internal states in molecules and the resulting lack of cycling transitions laser cooling of molecules has not yet been demonstrated. It would require a large amount of laser frequencies to efficiently couple light to the molecule [Bahns et al., 1996]. Nevertheless, trapping of cold and ultracold molecules has been achieved: Using buffer-gas cooling, Weinstein *et al.* suc-

ceeded in magnetically trapping CaH molecules at 400 mK temperature [Weinstein et al., 1998]. Trapping of very few molecules in the ultracold regime was observed for the first time with Cs<sub>2</sub> dimers formed in a magneto-optic trap and stored in a QUEST [Takekoshi et al., 1998]. Very recently, simultaneous storage of Cs atoms and quasibound Cs<sub>2</sub> molecules was observed in a FORT [Chin et al., 2003]. In that experiment, the Cs<sub>2</sub> molecules were formed by Feshbach coupling in a sample of ultracold Cs atoms.

A very promising approach is the deceleration and trapping of polar molecules using time-varying electric fields. Using this technique, it was possible to slow and electrostatically trap ammonia molecules with mean energies below  $350 \text{ mK} \times k_B$  [Bethlem et al., 2000]. Trapping of polar molecules with using electrostatic fields has already been conjectured by [Sekatskii and Schmiedmayer, 1996]. Recently, Vanhaecke *et al.* were able to accumulate ultracold ( $\sim 30 \mu\text{K}$ ) Cs<sub>2</sub> molecules in a magnetic trap through PA of ultracold Cs atoms out of a magneto-optic trap [Vanhaecke et al., 2002]. The ultimate goal pursued in our group is the formation and trapping of LiCs in a (quasi-) electrostatic or magnetic trap.

**Cold collisions** The availability of ultracold molecules offers the opportunity to study a variety of atom-molecule and ultimately molecule-molecule collisions. Collisions between atoms  $A$  and molecules  $AB$  are particularly interesting in the context of sympathetic cooling of dimers  $AB$  with atoms  $A$ . In our LiCs case, particular interest lies on the collision properties of groundstate LiCs and Cs atoms, since Cs is well suited as a cooling agent for sympathetic cooling of LiCs. The efficiency of evaporative cooling of a molecular sample and the stability of a molecular Bose-Einstein condensate depends on the elastic scattering cross-section for  $AB$ - $AB$  collisions. Furthermore, one can think of collisions involving  $AB$  in the singlet or metastable triplet groundstate,  $AB$  prepared in a certain ro-vibrational state and even exchange reactions of the type  $A + AB \rightarrow B + A_2$ .

**Molecular BEC** Following the standard route to Bose-Einstein condensation with molecules poses additional complications. Due to the lacking electronic magnetic moment of alkali dimers in the singlet groundstate, magnetic trapping would rely on the coupling to the nuclear magnetic moment, which is roughly factor  $1/2000$  smaller than the electronic one. Triplet molecules, however, can collide inelastically and decay into the singlet state, which leads to trap loss. Moreover, the high degree of degeneracy of the nuclear spin state complicates BEC. For example, for  $^{133}\text{Cs}_2$  in the lowest electronic state, there are 28 nuclear spin states. Thus, one would require 28 times the total density

at a given temperature to achieve 28 simultaneous and degenerate BECs of  $\text{Cs}_2$ .

In addition, the intermolecular interactions will often be stronger than the interatomic. Especially the dipole-dipole interaction between polar molecules becomes roughly equal to the BEC transition temperature  $T_c$  even at nanokelvin temperatures [Bahns et al., 2000]. Such a condensate of strongly coupling particles would require a modified description in contrast to the near ideal BECs with atomic gases. In particular, interesting ordering effects are expected [Santos et al., 2000] similar to the observations in spinor condensates [Miesner et al., 1999]. The alternative approach to molecular BEC is the formation of molecules starting from an atomic BEC. Using coherent free-bound stimulated Raman transitions it was possible to create state-selected  $^{87}\text{Rb}_2$  molecules out of the atomic BEC. Due to the extremely narrow resonance in the transition rate (1.5 kHz), the mean-field interactions between the molecules and the atomic condensate could be detected [Wynar et al., 2000]. Two-photon molecular association has been employed to trigger the growth of a  $^6\text{Li}$  condensate for the investigation of the collapse in a Bose condensate with attractive interactions [Gerton et al., 2000].

As a recent highlight, Donley *et al.* were able to demonstrate coherent coupling between atoms and molecules in a BEC of  $^{85}\text{Rb}$ . By shifting the atomic BEC into resonance with a weakly bound molecular state using a time-varying magnetic field near a Feshbach resonance it was possible to prepare a coherent superposition of the atomic and molecular state and detect the interference [Donley et al., 2002]. Recently, the concept of an “atom laser”, describing a coherent state-selected atomic beam produced by an atomic BEC has been extended to molecules [Julienne et al., 2000]. The “molecule laser” is proposed to be a coherent molecular beam extracted from a molecular BEC by stimulated Raman transitions.

**Polar molecules** Heteronuclear dimers generally possess a permanent electric dipole moment according to the electro-negativity of the two constituents. A crude estimate of the electric dipole moment function of the  $\text{LiCs}$  dimer in the singlet groundstate is shown in Fig. 5.5 (a) [Saenz, 2002]. Fig. 5.5 (b) displays the expectation values  $\langle v | D(R) | v \rangle$  of the same dipole moment function for the various vibrational substates. Due to the difference in electro-negativity of  $\text{Li}$  (0.98) and  $\text{Cs}$  (0.79), the dipole moment is relatively large ( $\lesssim 8$  D compared with 1.85 D of  $\text{H}_2\text{O}$ )<sup>2</sup>. The dipole moment of a molecule can be used to couple it to external electric fields. As men-

---

<sup>2</sup>The conversion factor for the unit dipole moment is  $1 \text{ D} = 3.336 \times 10^{-30} \text{ Cm}$ , as compared to  $e a_0 = 8.47836 \times 10^{-30} \text{ Cm}$

tioned above, one can manipulate and even trap polar molecules using electric fields [Sekatskii and Schmiedmayer, 1996, Bethlem et al., 2000]. In particular if the coupling energy  $\mathbf{d} \cdot \mathbf{E}$  exceeds the rotational energy  $B_v$ , the molecules are expected to populate so called pendular states [Rost et al., 1992]. These are states in which the molecular axis rotates about the electric field vector. Thus, all molecules become orientated with respect to the external field.

The rotational constant  $B_v$  for LiCs can be computed from the ground-state potentials. The result is plotted in Fig. 5.4 for various vibrational states of the singlet potential. The condition for the existence of pendular states is fulfilled if the external electric field  $E$  is larger than  $\sim 2$  kV/cm. We conclude that LiCs is a particularly interesting model system for the investigation of the behavior of a polar gas at very low temperatures because of its large electric dipole moment. Moreover, the efficient coupling to the dipole moment using electric fields makes LiCs a favorable molecule for trapping and manipulation.

**Polarizability** Besides the permanent dipole moment in polar molecules, a dipole moment can be induced by strong laser fields proportional to the polarizability of the molecule. In the case of a quasi-electrostatic field such as the radiation of a CO<sub>2</sub>-laser ( $\lambda = 10.6 \mu\text{m}$ ), the induced dipole moment is given by the product of static polarizability and inducing electric field  $\mathbf{d} = \alpha_{\perp, \parallel} \mathbf{E}$ , as discussed in Sec. 2.2. For alkali dimers, the static polarizability is roughly given by the sum of the static polarizabilities of the two unbound atoms [Tarnovsky et al., 1993]. Again, coupling of the induced dipole moment to the electric field vector can give rise to pendular states and therefore orientation of the molecules [Friedrich and Herschbach, 1995].

For the alkali dimers Li<sub>2</sub>, Na<sub>2</sub> and K<sub>2</sub>, the static polarizabilities have been predicted theoretically [Müller and Meyer, 1986]. The resulting polarizabilities parallel and perpendicular to the molecular axis are plotted in Fig. 5.6 versus the internuclear distance. Note that at intermediate distance (5-15 $a_0$ ) the parallel polarizability function exceeds the perpendicular one by up to a factor of 2. This can be explained by the fact that the valence electrons are delocalized along the molecular axis on the range of roughly the bond length, whereas they are confined to the atomic charge diameter in perpendicular direction. Since the polarizability reflects the ability of the electrons to follow the external electric field, it is clear that the polarizabilities parallel to the molecular axis exceeds the perpendicular one. It is likely to find similar behavior with Cs<sub>2</sub> and LiCs. Such an anisotropy might be interesting in the context of self-aligning effects in an ultracold sample of alkali dimers.

**Fundamental interest** Precision spectroscopy with polar molecules is of even more fundamental interest. It has been realized a long time ago that polar molecules could be well suited for the search of the permanent dipole moment of the electron (EDM), which would give evidence of PT-violation [Sandars, 1967]. The large electric field along the molecular axis of a polar molecule can enhance the EDM of the unpaired electron. Up to now, the most stringent limit on EDM follows from an experiment with the heavy paramagnetic atom Tl rather than experiments with polar molecules. This is due to the difficulty of producing large numbers of state-selected molecules. However, first results of EDM measurements with polar molecules were recently published [Hudson et al., 2002, Kozlov and DeMille, 2002]. In this respect the investigation of photoassociation, trapping and state selection of LiCs dimers seems very interesting.

## 5.2 A feasibility study of LiCs

The following estimates concerning the photoassociation efficiency and the groundstate properties of LiCs are based on interaction potentials. In general, these internuclear potentials have two regions: the short-range interaction and the long-range Van-der-Waals interaction. The physics of these two regions is sufficiently different that separate theoretical techniques are required to study them. Obviously, the understanding of the core potential is the more complex theoretical task. For heavier atoms the inner shell electrons become relativistic and polarization of the core electrons must be accounted for, which requires sophisticated numerical methods. We rely on the end result of such calculations.

**Short-range potentials** The short-range potential curves for LiCs are published in [Korek et al., 2000]<sup>3</sup>. The short-range potential curves of Cs<sub>2</sub> are taken from [Spiess, 1989]. Figure 5.2 shows only the attractive LiCs-potential curves connected to the groundstate asymptote Cs(6s)+Li(2s) and to the relevant excited state asymptotes Cs(6p)+Li(2s) and Cs(6s)+Li(2p). They are given in the Hund's case (a) basis, which is the appropriate basis if the electronic interaction energy dominates over all other energy terms such as fine and hyperfine structure and rotational energy [Herzberg, 1989]. In this basis the total electronic spin  $S$ , the absolute value of the projection of the electronic orbital momentum  $L$  onto the molecular axis  $|\Lambda|$  and the parity with respect to reflection at a plane containing the molecular axis,

---

<sup>3</sup>The potential curves are accessible on the internet site <http://lasim.univ-lyon1.fr/allouche/pec.html>

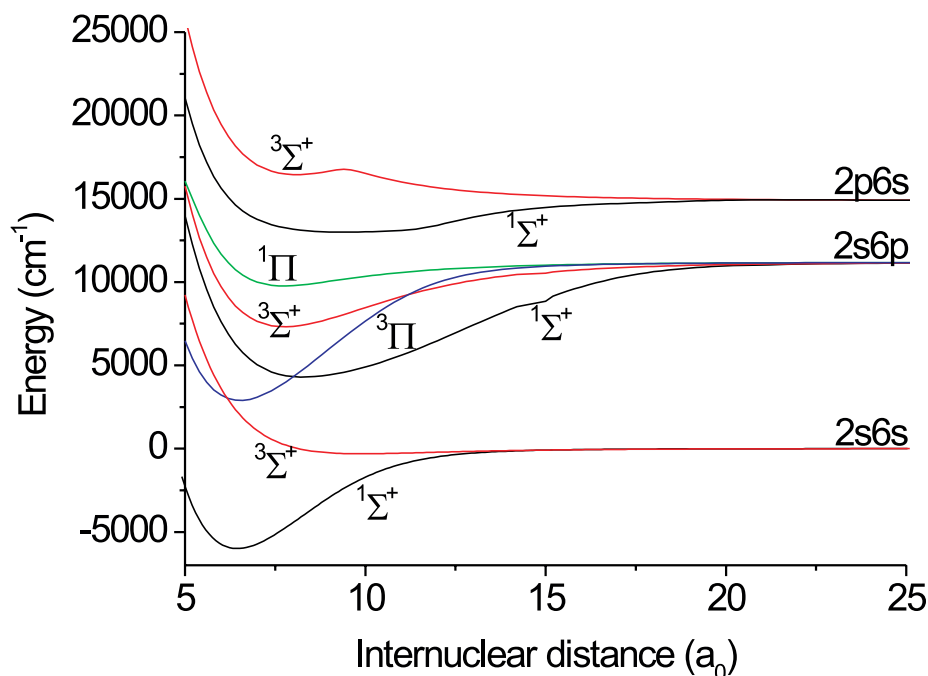


Figure 5.2: Selected LiCs potential curves from [Korek et al., 2000].

( $\pm$ ), are good quantum numbers. Thus, the notation of the Hund (a) states is:  $^{2S+1}|\Lambda|^{\pm}$ . In analogy to atomic physics,  $\Sigma$  stands for  $|\Lambda| = 0$  and  $\Pi$  stands for  $|\Lambda| = 1$ . In the case of homonuclear diatomic molecules there is the additional symmetry of reflection of the molecule about its center. The corresponding parity quantum numbers are  $g$  (*gerade*) and  $u$  (*ungerade*).

The groundstate is split into the singlet state ( $S = 0$ ) with the two valence electron spins being antiparallel and the triplet state ( $S = 1$ ) with electron spins coupled parallel. The exchange interaction at short distance leads to a large binding energy of the singlet groundstate  $^1\Sigma^+$ . The triplet state  $^3\Sigma^+$  has an attractive potential part only due to the much weaker Van-der-Waals interaction. The excited potential curves correlated to the Cs(6p)+Li(2s) asymptote as well as the ones correlated to the Cs(6s)+Li(2p) asymptote feature deep potential wells in the inner interaction region.

**Long-range potentials** The long-range interaction can be treated analytically by evaluating the different electric multipole interactions between

	$C_6$		$C_8$		$C_{10}$
	$1,3\Sigma$	$1,3\Pi$	$1,3\Sigma$	$1,3\Pi$	$1,3\Sigma$
LiCs( $2s6s$ )	2.9338[3]	-	3.1253[5]	-	3.7627[7]
LiCs( $2s6p$ )	2.2416[4]	8.9016[6]	3.6187[6]	1.8926[5]	-
LiCs( $2p6s$ )	-1.0349[4]	-7.4299[2]	-7.2314[6]	-2.6182[6]	-

Table 5.1: Dispersion coefficients from [Marinescu and Sadeghpour, 1999]. The numbers in square brackets denote powers of ten. The values are given in atomic units, i.e. hartree and  $a_0$ .

atoms correlated at large distances. Thus, for large internuclear distances, the potential curves may be expressed as

$$V(R) = -\frac{C_6}{R^6} - \frac{C_8}{R^8} - \frac{C_{10}}{R^{10}} - \dots, \quad (5.1)$$

where  $C_6$ ,  $C_8$ ,  $C_{10}$  are the so called dispersion coefficients. The exact values for the dispersion coefficients determining the long-range potentials are listed in table 5.1 in atomic units [Marinescu and Sadeghpour, 1999]. The corresponding values for  $\text{Cs}_2$  are found in [Amiot and Dulieu, 2002] for the groundstate and in [Marinescu and Dalgarno, 1995] for the excited states.

Note that already for the simple model of the two colliding atoms being represented by two-level systems, second-order perturbation theory predicts the right power-law dependence of the leading term describing the long-range interaction, including the correct sign of the corresponding coefficient [Weidemüller, 2000]. Thus, the interaction in the groundstate is characterized by strictly attractive Van-der-Waals-interaction, which scales as  $R^{-6}$  with the internuclear distance  $R$ . For the potentials correlated to the excited asymptote  $\text{Cs}(6p)+\text{Li}(2s)$ , the long-range potential is attractive as well. However, it is repulsive at the  $\text{Cs}(6s)+\text{Li}(2p)$  asymptote, in accordance with the two-level model. It is important to note the fundamental difference in the potential structure at large internuclear distance between homonuclear and heteronuclear dimers. In both cases, the dominating term of the groundstate potentials is the attractive Van-der-Waals interaction.

However, the long-range part of excited potentials in homonuclear dimers is characterized by the resonant dipole-dipole interaction in the leading order, which has a  $R^{-3}$ -dependence. This difference in the nature of the excited potential curves has important consequences as far as photoassociation is concerned. Due to the larger extension of the excited potential in homonuclear

dimers the bound states have large wave function amplitudes at large separation. Since the groundstate scattering wave function is also concentrated at large distance we expect more favorable conditions for photoassociative transitions to bound excited states in homonuclear dimers than in heteronuclear ones. The wave function overlap of bound excited states with bound levels in the groundstate, however, is expected to be more favorable for heteronuclear diatomic molecules. Therefore we are quite confident as far as the formation of stable groundstate LiCs is concerned, provided sufficiently high PA-rates.

**Combined potentials** In order to obtain the best curves at short range as well as in the outer region, the short-range potentials  $V_{short}(R)$  are merged with the asymptotic curves  $V_{long}(R)$  described by Eq. (5.1) with corresponding dispersion coefficients. This is done with an exponential crossover function of the form  $F(R) = \exp(-R/R_{crossover})$ , where  $R_{crossover} = 30 a_0$ . The combined potential has the general form

$$V_{combined}(R) = V_{short}(R) F(R) + V_{long}(R)(1 - F(R)). \quad (5.2)$$

**Inclusion of fine structure** In our PA-experiments the molecular transitions will mainly occur in the long-range part of the potentials, where fine and even hyperfine structure is of the same order or even larger than electronic energy. Therefore, we must convert the Hund (a) potential curves to potentials in the Hund's case (c) basis which is appropriate if fine structure is of the order or greater than the electronic interaction energy. In this case, the electronic orbital momentum  $L$  and spin  $S$  and their projections  $\Lambda$  and  $\Sigma$  are no longer good quantum numbers since they are coupled by spin-orbit coupling to the total angular momentum  $J$ . Therefore, the good quantum numbers defining Hund's case (c) states are the projection of the total angular momentum  $J$  onto the molecular axis  $\Omega$ , parity ( $\pm$ ) with respect to reflection about a plane containing the molecular axis and *gerade/ungerade* symmetry in the case of homonuclear dimers. The spectroscopic notation is  $\Omega_{g/u}^{\pm}$ . The conversion from Hund's case (a) to Hund's case (c) can be performed using standard perturbation theory [Spiegelmann et al., 1989]. The problem reduces to diagonalizing the following matrices:

$$0^- = \begin{pmatrix} V(^3\Pi) - \frac{A^{SO}}{2} & \frac{A^{SO}}{\sqrt{2}} \\ -\frac{A^{SO}}{\sqrt{2}} & V(^3\Sigma^+) \end{pmatrix}, \quad (5.3)$$

$$0^+ = \begin{pmatrix} V(^3\Pi) - \frac{A^{SO}}{2} & -\frac{A^{SO}}{\sqrt{2}} \\ -\frac{A^{SO}}{\sqrt{2}} & V(^1\Sigma^+) \end{pmatrix}, \quad (5.4)$$

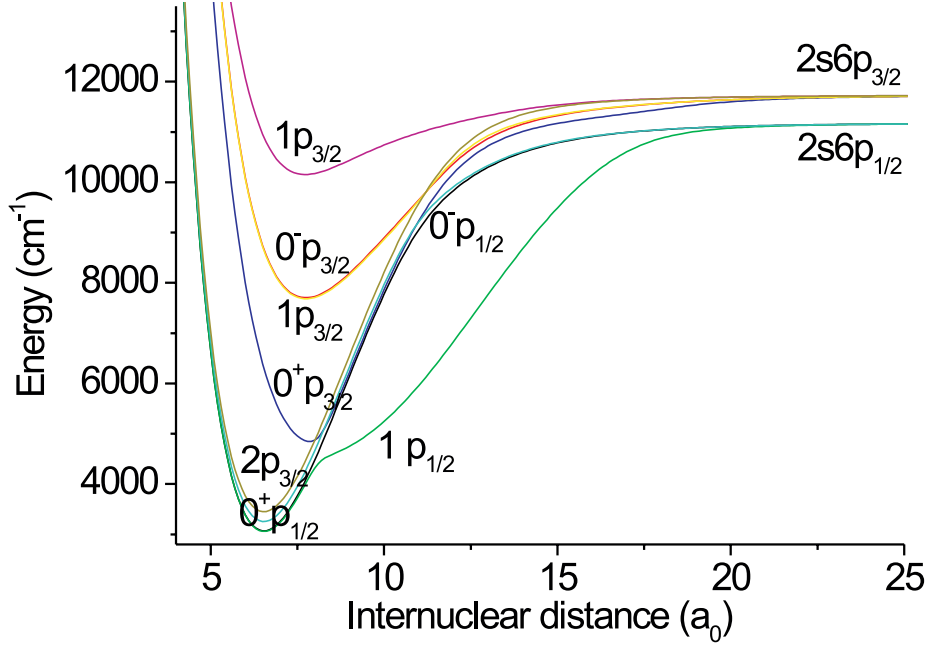


Figure 5.3: Hund's case (c) potential curves computed from the Hund's case (a) curves by matrix diagonalization.

$$1 = \begin{pmatrix} V(^3\Pi) & -\frac{A^{SO}}{2} & \frac{A^{SO}}{2} \\ -\frac{A^{SO}}{2} & V(^1\Pi) & \frac{A^{SO}}{2} \\ \frac{A^{SO}}{2} & \frac{A^{SO}}{2} & V(^3\Sigma^+) \end{pmatrix}, \quad (5.5)$$

where  $A^{SO}$  is taken to be  $(2/3) \times 554.0406(4) \text{ cm}^{-1}$ , the fine structure splitting of the  $^{133}\text{Cs}$  (6p) atomic state.  $V(\ )$  indicates the potential energy curves determined by Eq. (5.2). The diagonalization is carried out numerically at every internuclear separation  $R$ . The resulting Hund's case (c) potentials correlating to the Li(2s) Cs(6p) asymptote are depicted in Fig. 5.3. Due to the inclusion of spin-orbit coupling the Hund's case (c) states have less degeneracy than Hund's case (a) states. At long range, Hund's case (c) potentials merge with the atomic Cs(6p<sub>1/2</sub>) and Cs(6p<sub>3/2</sub>) fine structure states, whereas in the inner part each curve corresponds with different Hund's case (a) states.

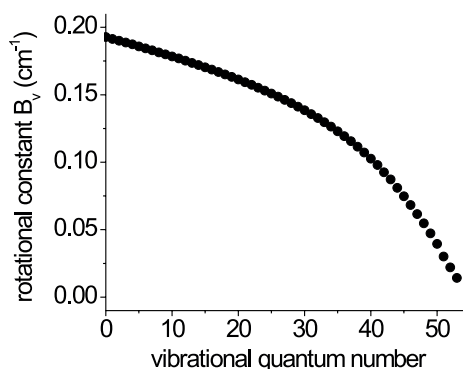


Figure 5.4: Predicted rotational constant for the vibrational levels of the singlet groundstate of LiCs.

### 5.2.1 Groundstate properties

Once the groundstate and relevant excited state potentials are determined, the next step is to calculate the energy eigenvalues and eigenstates. For this we solve the Schrödinger equation for the radial part of the total molecular wave function,

$$\left( -\frac{\hbar^2}{2\mu} \frac{d^2}{dR^2} + V_{el}(R) + \frac{l(l+1)\hbar^2}{2\mu R^2} \right) u_{v,J}(R) = E_{v,J} u_{v,J}(R). \quad (5.6)$$

The electronic Born-Oppenheimer potential  $V_{el}(R)$  is substituted by the computed above potential curves,  $v$  and  $J$  are the vibrational and rotational quantum numbers of a certain eigenstate and  $\mu = m_{\text{Li}}m_{\text{Cs}}/(m_{\text{Li}} + m_{\text{Cs}})$  is the reduced mass of LiCs. The numerical integration of the Schrödinger equation (5.6) is performed using the freely available fortran program LEVEL 7.5 distributed by R. J. Le Roy<sup>4</sup>. The program is based on the Numerov integration algorithm. The weakly bound states close to the dissociation limit are not found by the LEVEL program. For those states we use the program FGR developed at Laboratoire Aimé Cotton, which is based on a Fourier grid method [Dulieu, 2001].

The resulting energy levels found for the LiCs excited states correlated to the  $2s6p_{3/2}$ -asymptote are listed in appendix C. The LEVEL-program provides among other data the inertial rotation constant  $B_v =$

<sup>4</sup>The LEVEL 7.5 program is available from the internet site <http://scienide.uwaterloo.ca/~leroy/>

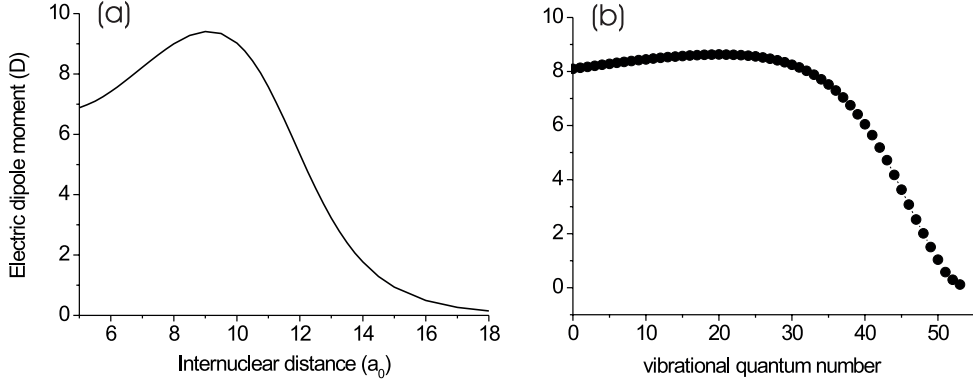


Figure 5.5: Electric dipole moment of the LiCs singlet groundstate; (a) as a function of the internuclear distance [Saenz, 2002]; (b) expected for the various vibrational substates.

$(-\hbar^2/2\mu) \langle v, J | 1/R^2 | v, J \rangle$  for a certain vibrational sublevel  $v$ . The resulting rotational constants  $B_v$  for the LiCs singlet electronic groundstate are depicted in Fig. 5.4 and have already been discussed in Sec. 5.1. Also, expectation values can be calculated, such as  $D_{v,J} = \langle v, J | D(R) | v, J \rangle$ , the expectation value for the singlet groundstate electronic dipole moment function of LiCs depicted in Fig. 5.5. For the vibrational groundstate ( $v = 0$ ), we find  $D \approx 8$  Debye, which is in rough agreement with the more precise calculation by [Igel-Mann et al., 1986],  $D = 5.48$  Debye.

Besides the electric dipole moment, the same paper calculates, bond lengths vibrational energies, dissociation energies, and ionization potentials for all dimers formed of alkali-atoms. Table 5.2 compares the relevant molecular constants for LiCs and Cs<sub>2</sub> in the vibrational groundstate  $v = 0$  found in [Igel-Mann et al., 1986] (slanted numbers) to the ones calculated in this work based on the groundstate potential curves from [Korek et al., 2000] and [Marinescu and Sadeghpour, 1999] for the short- and long-range potentials of LiCs, respectively, and from [Spiess, 1989] and [Patil and Tang, 1999] for the short- and long-range potentials of Cs<sub>2</sub>, respectively. The vibrational energy  $E_v$  denotes the difference in energy between vibrational levels  $v = 1$  and  $v = 0$ . The agreement between our results and the literature values is very good, which confirms the reliability of the potential curves.

The static polarizability of LiCs is thus far unknown, however, for the alkali dimers Li<sub>2</sub>, Na<sub>2</sub> and K<sub>2</sub>, the static polarizabilities have been predicted theoretically [Müller and Meyer, 1986]. The resulting polarizabilities

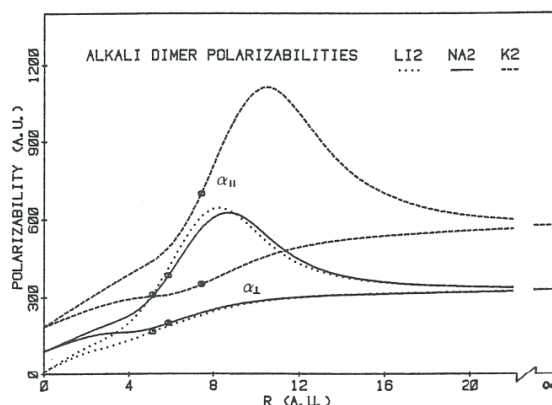


FIG. 1. Polarizability functions  $\alpha_{||}(R)$  and  $\alpha_{\perp}(R)$  for  $\text{Li}_2$ ,  $\text{Na}_2$ , and  $\text{K}_2$ . The circles mark the respective equilibrium separations.

Figure 5.6: From [Müller and Meyer, 1986].

are plotted in Fig. 5.6 versus the internuclear distance and discussed in Sec. 5.1. The values for  $\alpha_{stat}$  of  $\text{LiCs}$  and  $\text{Cs}_2$  listed in table 5.2 are calculated as the sum of the atomic polarizabilities, which is only valid for high vibrational excitation.

	$R_e$ ( $a_0$ )	$E_{diss}$ (eV)	$E_v$ ( $\text{cm}^{-1}$ )	$B_v$ (GHz)	$I.P.$ (eV)	$D$ (D)	$\alpha_{stat}$ ( $\text{Åsm}^2/\text{V}$ )
<b>LiCs</b>	6.864	0.7318	184.8	5.779			$0.933 \times 10^{-38}$
	<i>6.90</i>	<i>0.72</i>	<i>183</i>		<i>4.19</i>	<i>5.48</i>	
<b>Cs<sub>2</sub></b>	8.795	0.4499	41.76	0.3516		-	$1.33 \times 10^{-38}$
	<i>8.71</i>	<i>0.43</i>	<i>42</i>		<i>3.62</i>	-	

Table 5.2: Important molecular constants for  $\text{LiCs}$  and  $\text{Cs}_2$  in the vibrational groundstate  $v = 0$ , calculated from literature potentials (see text):  $R_e$  bond length;  $E_{diss}$  dissociation energy;  $E_v$  vibrational energy;  $B_v$  rotational constant;  $I.P.$  adiabatic ionization potential;  $D$  electric dipole moment;  $\alpha_{stat}$  static polarizability; The values printed in italic are taken from [Igel-Mann et al., 1986]. The static polarizability is calculated as the sum of the atomic polarizabilities.

### 5.2.2 Photoassociation rates

**Selection rules** Next we estimate the transition rates from the free collisional state to bound excited molecular states. The selection rules for *allowed* transitions between the states described by the Hund's case (a) are [Herzberg, 1989]:

- parity with respect to reflection  $+\leftrightarrow +$  and  $-\leftrightarrow -$
- For homonuclears:  $g\leftrightarrow u$  and  $g\leftrightarrow g$
- Projection of the orbital momentum onto the molecular axis  $\Delta\Lambda = 0, \pm 1$ <sup>1</sup>
- Electronic spin  $\Delta S = 0$
- Projection of the electronic spin onto the molecular axis  $\Delta\Sigma = 0$ <sup>2</sup>
- It follows from <sup>1,2</sup> for the projection of the total angular momentum  $\Delta\Omega = 0, \pm 1$
- If  $(\Omega = 0) \rightarrow (\Omega = 0)$ , then it follows for the rotation  $\Delta J \neq 0$

Transitions between Hund's case (c) states are governed by the selection rules

- $+\leftrightarrow +$  and  $-\leftrightarrow -$
- For homonuclears:  $g\leftrightarrow u$  and  $g\leftrightarrow g$
- Projection of the total angular momentum  $\Delta\Omega = 0, \pm 1$

Since the singlet and triplet groundstates are described by Hund's case (a) (no fine structure !) we have to decompose the excited Hund's (c) states with respect to the Hund's case (a) basis

$$|\Omega^\pm\rangle = \sum_i C_i |^{2S+1}\Lambda|\pm\rangle_i, \quad (5.7)$$

and then follow the selection rules for transitions between Hund's case (a) states. For example, we deduce from the expression (5.3) and from the selection rule for the electronic spin,  $\Delta S = 0$ , that transitions to the state  $|0^-\rangle$  may occur merely via the triplet groundstate. However, the  $|0^+\rangle$ -state can be reached via both singlet and triplet groundstates. The transition rate from either groundstate will then be modulated by the corresponding expansion coefficients given by Eq. (5.7). The expansion coefficients  $C_i$  are obtained from the Eigenvectors of matrices (5.3)-(5.5).

**Relative photoassociation rate** Our estimates of the rate of excitation of a bound molecular state are based on the formula for the photoassociation rate derived from a perturbative quantum approach [Pillet et al., 1997]. Thus, the total number of photoassociative transitions per unit time in a sample of  $N_1$  atoms (1) and  $N_2$  atoms (2) is given by

$$R \propto \frac{N_1 N_2}{V_{12}} \Lambda^3 e^{-E/(k_B T)} K^2 S^2, \quad (5.8)$$

where the effective two-particle volume  $V_{12}$  has already been introduced in Sec. 3.3.3. The thermal de Broglie wavelength  $\Lambda$  is defined as  $\Lambda = \sqrt{2\pi\hbar^2/(\mu k_B T)}$  with the reduced mass  $\mu$  and  $4K^2 = \frac{1}{2}(2\pi\Gamma)^2 I/I_0$  is the square of the Rabi frequency at the laser intensity  $I$ . The saturation intensity  $I_0$  is defined by  $I_0 = \pi\hbar c\Gamma/(3\lambda_L^3)$ , where  $\lambda_L$  is the wavelength of the PA-laser and  $\Gamma$  is the line width of the resonant transition which is on the order of the atomic natural line width ( $2\pi$  5.3 MHz). In expression (5.8) we neglect rotational excitation.

The prediction of absolute PA-rates is a difficult task due to the many experimental uncertainties. Therefore we will concentrate on estimating the relative PA-rate of LiCs with respect to Cs<sub>2</sub> in our QUEST. Since the actual PA-rate of Cs<sub>2</sub> is known from the experiment (Sec. 5.3), we obtain a realistic estimate for the PA-rate of LiCs. Thus, we investigate the ratio

$$\frac{R_{\text{LiCs}}}{R_{\text{Cs}_2}} = \left( \frac{m_{\text{Li}} + m_{\text{Cs}}}{2m_{\text{Li}}} \cdot \frac{\alpha_{\text{Li}}}{\alpha_{\text{Li}} + \alpha_{\text{Cs}}} \right)^{\frac{3}{2}} \cdot \frac{N_{\text{Li}}}{N_{\text{Cs}}} \cdot \frac{S_{\text{LiCs}}^2}{S_{\text{Cs}_2}^2}, \quad (5.9)$$

which results from Eq. (5.8) by substituting the expressions for the effective volumes, accounting for the relation between the trap frequencies for Li and Cs in the QUEST,  $\omega_{\text{Li}} = \sqrt{\alpha_{\text{Li}} m_{\text{Cs}} / (\alpha_{\text{Cs}} m_{\text{Li}})} \omega_{\text{Cs}}$ . We remind the static polarizabilities of Li and Cs,  $\alpha_{\text{Li}} = 2.70 \times 10^{-39}$  Fm<sup>2</sup> and  $\alpha_{\text{Cs}} = 6.63 \times 10^{-39}$  Fm<sup>2</sup>. The ratio of effective volumes for LiCs and Cs<sub>2</sub>  $V_{\text{LiCs}}/V_{\text{Cs}_2} = (\alpha_{\text{Li}}/(\alpha_{\text{Li}} + \alpha_{\text{Cs}}))^{3/2} = 0.16$  is smaller than unity as expected due to the reduced spatial overlap of the Li and Cs clouds trapped at different trap depth. However, the ratio of thermal wave lengths  $\Lambda_{\text{LiCs}}/\Lambda_{\text{Cs}_2} = ((m_{\text{Li}} + m_{\text{Cs}})/(2m_{\text{Li}}))^{3/2} = 31.5$  is much larger than unity so that the overall rate for LiCs exceeds the one for Cs<sub>2</sub> by a factor of 4.9. Unfortunately, due to the unfavorable relative number of Li atoms  $N_{\text{Li}}/N_{\text{Cs}} \approx 1/10$  the total PA-rate for LiCs will still stay behind the one for Cs<sub>2</sub>. Finally, we have to estimate the transition amplitudes  $S_{\text{LiCs}}^2$  and  $S_{\text{Cs}_2}^2$ , which will significantly alter the relative PA-rate.

**Transition amplitudes** The amplitude factors  $S_{\text{LiCs}}$  and  $S_{\text{Cs}_2}$  stand for the overlap integrals

$$\int_0^\infty dR u_{v'}^{exc}(R) C(R) u_{coll}(R) \quad (5.10)$$

of the radial wave functions of the free collisional state  $u_{coll}$  and excited molecular state  $u_{v'}^{exc}$ . This expression stems from the actual transition matrix element  $\langle v', J' | \mu_{v',coll,J',J''} | coll, J'' \rangle$  by neglecting angular factors and by expanding the transition dipole moment function to the lowest order. Here,  $\mu_{v',coll,J',J''}$  denotes the dipole moment operator and  $v', v'', J'$  and  $J''$  are the vibrational and rotational quantum numbers of the upper and lower state, respectively. The wave functions of the excited vibrational states of the  $0^+$  in LiCs are computed using the LEVEL and FGR programs mentioned above (wave function in the upper potential well in Fig. 5.1). The expansion coefficient  $C(R)$  from Eq. (5.7) accounts for the Hund's case (a) contribution with appropriate symmetry to the Hund's case (c) state  $u_{v'}^{exc}$ . Each bound wave function is normalized to unity,

$$\int_0^\infty dR u_{v'}^{exc}(R) u_{v''}^{exc}(R) = \delta_{v',v''}. \quad (5.11)$$

The free collisional wave function  $u_{coll}$  is calculated by integrating the Schrödinger equation (5.6) with  $E_{v,J} = 0$  from zero to some sufficiently large value of  $R$ .  $V_{el}(R)$  is taken either as the singlet or the triplet groundstate potential. The collisional wave functions  $u_{coll}$  are normalized to the asymptotic form

$$\sqrt{4\pi}(R - a), \quad (5.12)$$

where the constant  $a$  formally corresponds to the  $s$ -wave scattering length. The integration is performed numerically.

In the following we focus onto transitions to the excited state LiCs ( $2s6p_{3/2}$ )  $0^+$  correlating to the Li( $2s$ ) Cs( $6p_{3/2}$ ) asymptote. This frequency region is mainly chosen because it is easily accessible by our Ti:Sa laser. Moreover, photoassociation spectra of Cs<sub>2</sub> below the Cs( $6p_{3/2}$ ) asymptote have been extensively studied in the cold molecule group at Laboratoire Aimé Cotton in Orsay [Masnou-Seeuws and Pillet, 2001]. We pick the  $0^+$ -state because it has a similar radial structure at short range as the ( $6s6p_{3/2}$ )  $0_u^+$  of Cs<sub>2</sub>. Since for the Cs<sub>2</sub> ( $6s6p_{3/2}$ )  $0_u^+$  the PA-rates are known from the experiment (Sec. 5.3), we can obtain realistic estimates for PA-rates of LiCs in the ( $2s6p_{3/2}$ )  $0^+$ -state by comparing the computed amplitudes for LiCs and Cs<sub>2</sub>. Fig. 5.7 shows the expansion coefficients as a function of internuclear distance  $C_1$  and  $C_2$  in the expansion  $|0^+\rangle = C_1 |^1\Sigma^+\rangle + C_2 |^3\Pi\rangle$ .

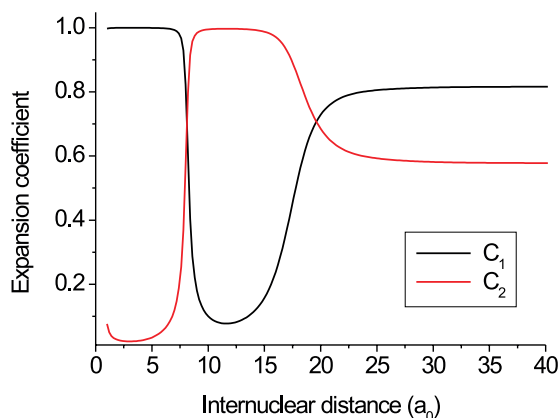


Figure 5.7: Expansion coefficients of the LiCs electronic state  $|0^+\rangle = C_1 |^1\Sigma^+\rangle + C_2 |^3\Pi\rangle$ .

Apparently, the excited LiCs  $0^+$ -state has purely  $^3\Pi$  character at very close internuclear distance ( $\lesssim 8a_0$ ) whereas in the intermediate range ( $8a_0 - 17a_0$ ) it is dominated by the  $^1\Sigma^+$ . Asymptotically, it becomes a mixture of both  $^3\Pi$  and  $^1\Sigma^+$ .

The resulting overlap integrals squared,  $S^2$ , are plotted in Fig. 5.8. In (a),  $S^2$  of the singlet zero-energy collisional wave function with the  $0^+$  ( $0_u^+$ ) excited state of LiCs ( $\text{Cs}_2$ ) is shown as a function of the frequency detuning from the atomic resonance  $\text{Cs}(6p_{3/2})$ . The pronounced modulation of  $S^2$  in the  $\text{Cs}_2$  case reflects the nodal structure of the Cs scattering wave function<sup>5</sup>. The amplitudes  $S^2$  for LiCs and  $\text{Cs}_2$  seem to be of the same order of magnitude over the plotted frequency range. This is a surprising result, since the different asymptotic behavior of the excited-state potentials for homo- and heteronuclear molecules was expected to favor PA of  $\text{Cs}_2$ . Fig. 5.8 (b) shows  $S^2$  of the triplet zero-energy collisional wave function with the  $0^-$  ( $0_g^-$ ) excited state of LiCs ( $\text{Cs}_2$ ). In this case free-bound transitions in LiCs appear less probable than in  $\text{Cs}_2$ , as expected. However, the absolute magnitudes are comparable with the ones involving the  $0^+$  ( $0_u^+$ )-state. The slow decrease with detuning  $\delta$  of  $S^2$  in the case of  $\text{Cs}_2$  is compatible with the approximate  $\delta^{-7/6}$  behavior discussed in [Pillet et al., 1997]. Similar calculations of the

<sup>5</sup>Since the amplitude of the bound state wave function is concentrated in a small region at the classical outer turning point integrating over the overlap with the scattering wave function effectively results in mapping it out (“delta approximation”, see [Comparat, 1999]).

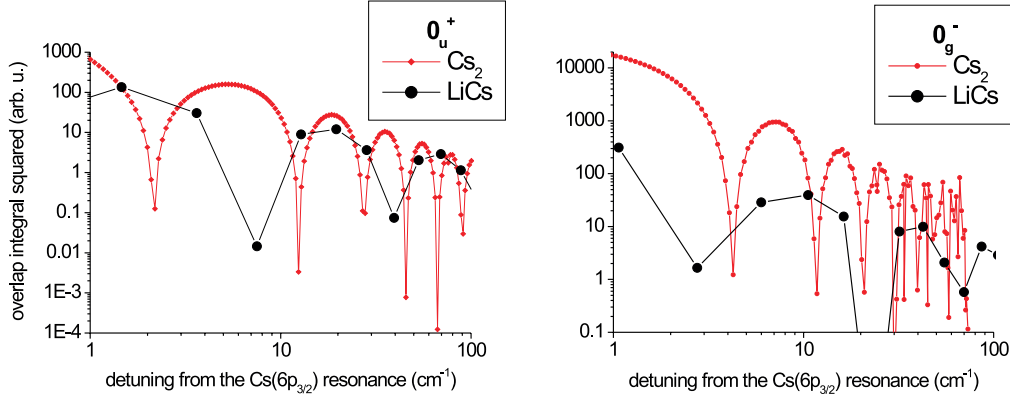


Figure 5.8: Square of the overlap integrals of zero-energy collisional wave functions with excited bound state wave functions. (a) Singlet scattering wave function and  $0^+$  ( $\text{Cs}_2 0_u^+$ ) excited state of LiCs ( $\text{Cs}_2$ ); (b) Triplet scattering wave function and  $0^-$  ( $\text{Cs}_2 0_g^-$ ) excited state of LiCs ( $\text{Cs}_2$ ).

free-bound Franck-Condon factors for different heteronuclear alkali dimers are performed in [Wang and Stwalley, 1998]. From these considerations together with the result of Eq. (5.9), we conclude that the LiCs PA-rates may be expected to be suppressed by roughly a factor 10-1000 compared with the PA-rates of  $\text{Cs}_2$ .

### 5.2.3 Formation of groundstate LiCs

In the following part we will try to anticipate the rate of formation of bound groundstate LiCs molecules. For this we need to estimate the overlap integrals from the excited state to bound states in the groundstate potentials,

$$\int_0^\infty dR u_{v'}^{exc}(R) C(R) u_{v''}^{ground}(R). \quad (5.13)$$

The square of this integral is called Franck-Condon-factor (FCF), modified by the expansion coefficient  $C(R)$ . Note that for the sake of feasibility we neglect transitions into the continuum above the groundstate asymptotes. The transition amplitudes involving the LiCs  $0^+$  excited and  $^1\Sigma^+$ -groundstate are plotted in Fig. 5.9 (a). Obviously, the overlap is best between vibrational wave functions close to the dissociation limit. This is due to the large period

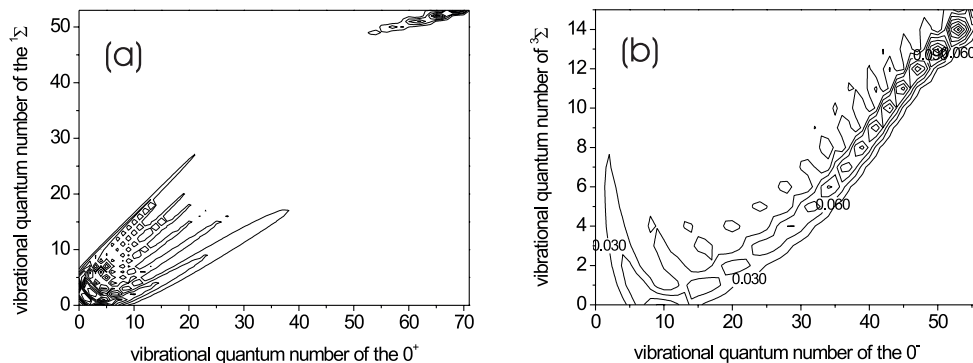


Figure 5.9: Transition amplitudes from the excited molecular states  $0^+$  to bound singlet states (a) and from  $0^-$  to bound triplet states of LiCs (b).

of the vibrationally highly excited wave function at the classical outer turning point (see Fig. 5.1, tip of the red arrow). Also, the overlap is favorable for deeply bound vibrational wave functions of similar vibrational quantum numbers. This results from the large period of deeply bound wave functions. For the vibrational number in between, the transition amplitude takes negligible values, mainly due to the expansion factor  $C_1(R)$  that nearly vanishes in the intermediate region (see Fig. 5.7).

Fig. 5.9 (b) displays the transition amplitudes involving the LiCs  $0^-$  and  ${}^3\Sigma^+$ -groundstate. Here,  $C(R) \equiv 1$  as discussed above. Again, the overlap is favorable for the high-lying vibrational states and even dominates over the one for deeply bound states.

By summing up the modified FCF over the vibrational quantum numbers of the groundstate we obtain the total probability that an excited state decays into a bound groundstate. These values are plotted in Fig. 5.10 (a) for the bound-bound transitions from the  $0^+$  ( $0_u^+$ ) to the  ${}^1\Sigma$ -groundstate of LiCs ( $\text{Cs}_2$ ). The main difference between the two curves is the fact that in the LiCs system there is a significant probability for high-lying vibrational states to undergo a transition into a bound vibrational groundstate. These high-lying states have an energy in the range  $10\text{-}100\text{ cm}^{-1}$  away from the atomic resonance. In this experimentally accessible frequency range we expect relatively high photoassociation rates (see Fig. 5.10 (a)), thus providing an efficient way of producing groundstate LiCs molecules. These favorable conditions originate from the fact that in the heteronuclear LiCs case both

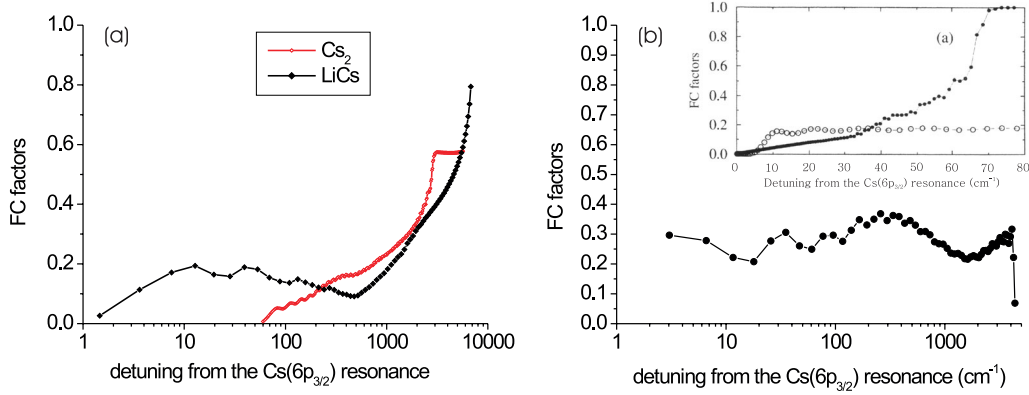


Figure 5.10: Sum of modified FCF over vibrational quantum numbers of the groundstate. (a) Comparison of the transitions LiCs  $0^+ \rightarrow {}^1\Sigma$  with Cs<sub>2</sub>  $0_u^+ \rightarrow {}^1\Sigma$ ; (b) Comparison of the transitions LiCs  $0^- \rightarrow {}^3\Sigma$  with Cs<sub>2</sub>  $0_g^- \rightarrow {}^3\Sigma$  (inset). The data displayed in the inset stems from [Drag et al., 2000].

excited and groundstate potentials are determined by the Van-der-Waals potential ( $\propto R^{-6}$ ) at large internuclear distance. This leads to an increased overlap of the excited and groundstate radial wave functions compared with the homonuclear case of Cs<sub>2</sub>.

The probability for bound-bound transitions from the  $0^-$  to the  ${}^3\Sigma$ -groundstate of LiCs (Fig. 5.10 (b)) is roughly unchanged for all excited bound states. In the interesting region of 10-100 cm<sup>-1</sup> detuning from the atomic resonance we find even more favorable conditions for bound-bound transitions than for the decay from the  $0^+$  into the  ${}^1\Sigma$  potential. For comparison, the inset of Fig. 5.10 (b) shows the computed sum of FCF for transition from the long-range part of the Cs<sub>2</sub>  $0_g^-$ -state taken from [Drag et al., 2000]. This particular potential curve features an second shallow potential well at about  $23 a_0$  which provides an additional Condon point at intermediate distance. The wave function overlap of the bound states in this outer well with bound groundstate wave functions is thereby strongly enhanced. The lowest vibrational states of the outer well (70-80 cm<sup>-1</sup> detuning) decay into bound groundstates with nearly unity probability.

We conclude that bound-bound transitions from high-lying states are generally facilitated in heteronuclear systems as LiCs due to the similar structure of the excited and groundstate potential curves. However, no double-well feature could be identified in any state correlating to the 2s6p asymptotes. Besides, there is further experimental indication for the possibility of

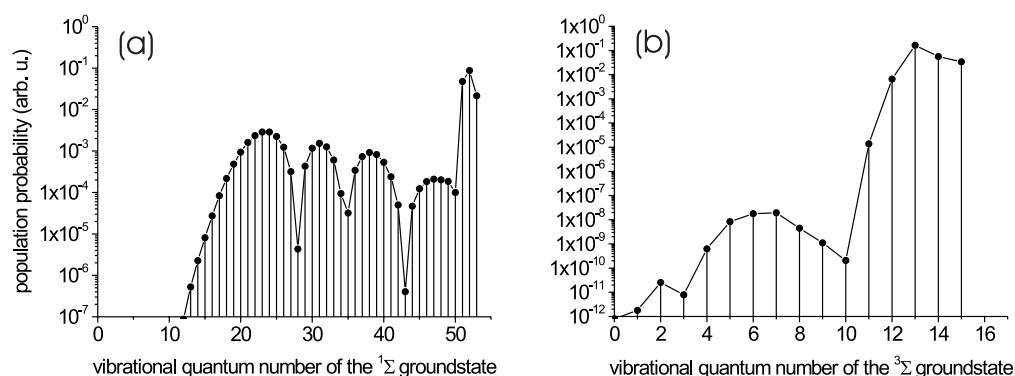


Figure 5.11: Expected populations of vibrational groundstates after spontaneous decay from the  $0^+$ ,  $v=64$  excited state to the  $^1\Sigma$ -groundstate (a) and from the  $0^-$ ,  $v=51$  excited state of LiCs (b).

forming groundstate molecules via an excited Van-der-Waals potential. In [Dion et al., 2001] colleagues from Laboratoire Aimé Cotton in Orsay have reported on the observation of groundstate  $\text{Cs}_2$  dimers created by PA via the  $\text{Cs}_2$  ( $6s6p_{1/2}$ )  $0_g^-$ -state. Due to coupling effects, this particular potential curve features an  $R^{-6}$ -dependence just as Van-der-Waals potentials in heteronuclear molecules.

**Final distribution of vibrational states** We can even go one step further and raise the question of what the distribution of population over the vibrational states after spontaneous decay would be like. For this purpose we plot the modified FCF depicted in Fig. 5.9 for a certain vibrational level of the excited state as a function of the vibrational quantum number in the groundstate. Fig. 5.11 (a) shows the expected distribution of  $^1\Sigma$ -states after spontaneous decay from the  $0^+$ ,  $v=64$  ( $E_v = -53 \text{ cm}^{-1}$  with respect to the atomic  $6p_{3/2}$ -resonance). Thus, we expect mainly the high-lying vibrational states  $v \gtrsim 50$  to be populated, although there is roughly 1% probability that a LiCs molecule is formed in the vibrational state around  $v = 23$ . Similarly, transition by spontaneous emission from the  $0^-$ ,  $v=51$  ( $E_v = -44 \text{ cm}^{-1}$  below resonance) nearly exclusively populate the 4 highest-lying vibrational states of the  $^3\Sigma$ -groundstate.

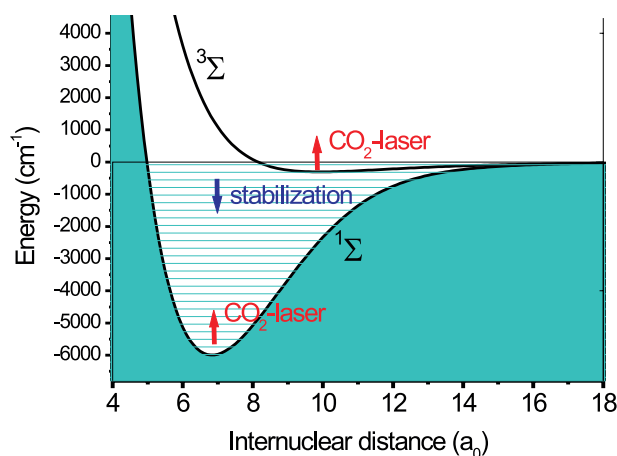


Figure 5.12: Schematic illustration of the possible processes with LiCs trapped in the QUEST formed by a CO<sub>2</sub>-laser beam.

#### 5.2.4 Storage of LiCs in a QUEST

The last question of more theoretical nature we want to address before discussing the experimental results is the possibility of storing LiCs-dimers in a QUEST. In general, molecules with a permanent electric dipole moment such as LiCs can undergo E1-transition between ro-vibrational states in the groundstate. The possible processes which may occur in optically stored LiCs are schematically illustrated in Fig. 5.12.

**Stabilization by spontaneous emission** First, groundstate LiCs, which is preferentially formed in high-lying vibrational states as discussed above, will eventually stabilize by successive spontaneous transitions into the  $v = 0$  lowest energy state (Fig. 5.12 blue arrow). This is the desired scenario since the ultimate goal is the achievement of ultracold LiCs molecules in all degrees of freedom. Second, the LiCs dimer can couple to the electric field of the trapping laser through its dipole moment and successively absorb photons (Fig. 5.12 red arrows <sup>6</sup>). This process leads to vibrational heating and eventually to the dissociation of the bound molecule into free atoms. Third, we can think of different types of multi-photon transitions such as stimulated Raman transitions, which we will neglect here.

---

<sup>6</sup> $\lambda_{\text{CO}_2}^{-1} = 943 \text{ cm}^{-1}$

The rate at which a spontaneous transition occurs from the ro-vibrational level  $v', J'$  to level  $v'', J''$  is given by the famous Einstein  $A$ -coefficient [Lefebvre-Brion and Field, 1989]

$$A_{v'J'v''J''} = |\mu_{v'J'v''J''}|^2 \nu_{v'J'v''J''}^3 \frac{8\pi^2}{3\hbar\varepsilon_0 c^3} \quad (5.14)$$

$$= 3.137 \times 10^{-7} |\mu_{v'J'v''J''}|^2 \nu_{v'J'v''J''}^3 \text{ s}^{-1} \quad (5.15)$$

where  $\nu_{v'J'v''J''}^3$  denotes the transition frequency and the transition dipole matrix element

$$\mu_{v'J'v''J''} = HL_{J'J''\Lambda} \int_0^\infty dR u_{v'J'}(R)D(R)u_{v''J''}(R) \quad (5.16)$$

has the unit Debye. The angular factor  $HL_{J'J''\Lambda}$  results from the angular momentum coupling of the initial state, the light field and the final state and is called Hönl-London factor. The explicit expressions for  $HL_{J'J''\Lambda}$  are given in [Amitay and Zajfman, 1994] and are automatically calculated by the LEVEL program. If we are interested in the lifetime  $\tau$  of one particular ro-vibrational level  $v', J'$  we have to sum up the transition rates from this level to all energetically lower-lying levels  $v'', J''$ ,

$$\tau_{v'} = \left( \sum_{v''=0}^{v'-1} \sum_{J''=J'\pm 1} A_{v'v''J'J''} \right)^{-1}. \quad (5.17)$$

We recall the selection rule  $\Delta J \neq 0$  if the projection of the electronic orbital momentum  $\Omega$  remains unchanged during a transition, which is the case for transitions within the electronic groundstate. The result of this sum is plotted in Fig. 5.17 (a) for the various vibrational states of the LiCs singlet groundstate.

The lifetime is longest ( $\gtrsim 10$  s) for the very high-lying and for the low-lying vibrational states. The decay of high-lying states is suppressed for the following reasons: On the one hand, transitions with small  $v' - v''$  are inhibited due to the small factor  $\nu_{v'v''}^3$  although the overlap of the radial wave functions and therefore the transition matrix element is large. On the other hand, transitions with large  $v' - v''$  are inhibited due to the weak overlap of the radial wave functions. The low-lying states feature long lifetimes because the number of decay channels goes to zero as  $v' \rightarrow 0$ .

**Absorption of trapping light** Next, we estimate the rate at which groundstate LiCs is vibrationally heated up by interacting with the trapping laser light. The rate of photon absorption is given by

$$R_{v'J'v''J''} = \int d\nu \rho(\nu - \nu_L) B_{v'J'v''J''}(\nu - \nu_{v'J'v''J''}), \quad (5.18)$$

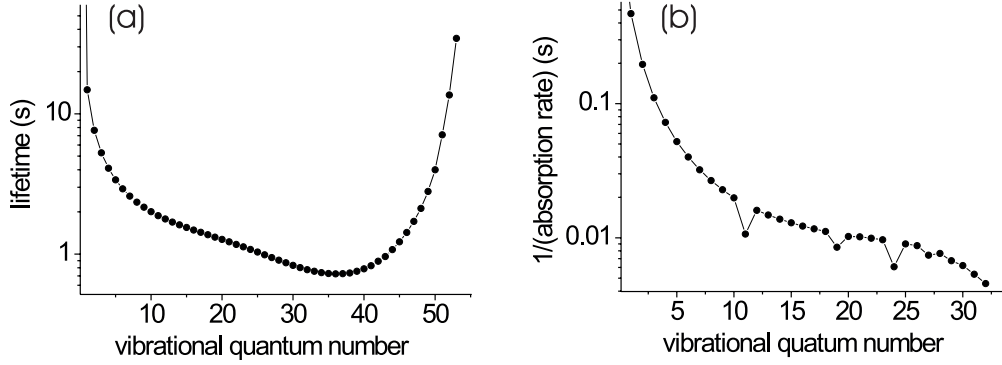


Figure 5.13: Lifetime of vibrational states of the LiCs groundstate with respect to spontaneous emission (a) and absorption of trapping light (b).

where  $\rho(\nu - \nu_L)$  denotes the spectral energy density of the trapping laser with laser frequency  $\nu_L$ . The frequency dependence is assumed to be a Gaussian function

$$\rho(\nu - \nu_L) = w \frac{\exp\left(-\frac{(\nu - \nu_L)^2}{2\sigma_L^2}\right)}{\sqrt{2\pi}\sigma_L}, \quad (5.19)$$

with Gaussian width  $\sigma_L$  and the spatial energy density

$$w = \frac{P}{\pi c w_0^2}. \quad (5.20)$$

Here, we assume a total laser power of our CO<sub>2</sub>-laser of  $P = 100$  W focused to a waist of  $w_0 = 70$   $\mu\text{m}$ . These values yield  $w = 21.7$   $\text{Jm}^{-3}$  spacial energy density. Since the detuning of the CO<sub>2</sub>-laser from any vibrational transition frequencies exceeds by far the laser line width,  $|\nu_L - \nu_{v'J'v''J''}| \gg \sigma_L$ , the Gaussian laser profile can be substituted by the delta function  $\delta(\nu - (\nu_L - \nu_{v'J'v''J''}))$ . Thus, Eq. (5.21) simplifies to

$$R_{v'J'v''J''} = w B_{v'J'v''J''}(\nu_L - \nu_{v'J'v''J''}). \quad (5.21)$$

The term  $B_{v'J'v''J''}$  denotes Einstein's famous  $B$ -coefficient including a frequency dependence to allow for off-resonant photon absorption. This frequency dependence is a Lorentzian function

$$B_{v'J'v''J''}(\nu_L - \nu_{v'J'v''J''}) = \frac{|\mu_{v'J'v''J''}|^2}{6\hbar^2\varepsilon_0} \frac{\gamma_{v'J'}}{\pi((\nu_L - \nu_{v'J'v''J''})^2 + \gamma_{v'J'}^2)}, \quad (5.22)$$

where  $\nu_{v'J'v''J''}$  denotes the resonance frequency of the transition from level  $v', J'$  to  $v'', J''$ . The width  $\gamma_{v'J'}$  of the homogeneously broadened levels  $v'J'$  is equal to the inverse natural lifetimes depicted in Fig. 5.13 (a). The total transition rate from the initial level  $v'', J''$  through absorption of trapping light is calculated by the sum

$$R_{v'',J''}^{tot} = \sum_{v'=v''}^{v_{max}} \sum_{J'=J''\pm 1} w B_{v'J'v''J''}(\nu_L - \nu_{v'J'v''J''}), \quad (5.23)$$

where  $v_{max} = 53$  denotes the last bound level. Fig. 5.13 (b) displays the inverse of the resulting total absorption rate  $1/R_{v'',J''}^{tot}$  for  $J'' = 0$ . Since transitions to the continuum are neglected, the abscissa is limited to the highest vibrational level  $v''$  with an energy  $E_{v''} < E_{CO_2}$ . It is interesting to note that the dominating terms in the sum 5.23 are the ones for  $v' = v''$  except for levels  $v'' = 11, 19$  and  $24$ . Those states are excited near-resonantly by the  $CO_2$ -laser. The high excitation probability of purely rotational transitions with  $\Delta J = \pm 1$  is due to the high similarity of the radial wave functions in the initial and final state. Besides, the Lorentzian dependence on the frequency detuning  $\nu_L - \nu_{v'J'v''J''}$  in Eq. (5.22) falls off as  $(\nu_L - \nu_{v'J'v''J''})^{-2}$  for large detunings, which still gives finite values.

**Absorption of black-body radiation** Unbound atoms are decoupled from the surrounding thermal radiation field due to their comparatively simple energetic structure. However, this is no longer true as soon as two atoms of different species bind together to form a molecule. Here, we estimate the influence of surrounding black-body radiation on the LiCs molecule.

Fig. 5.14 displays comparatively the spectral energy density of black-body radiation at 300 K, given by

$$\rho(\nu, T) = \frac{8\pi h\nu^3}{c^3} \frac{1}{\exp(h\nu/(k_B T)) - 1}, \quad (5.24)$$

over the energy range of transitions between rotational states. The horizontal line in Fig. 5.14 depicts the spectral energy density of the  $CO_2$ -laser field, assuming a Lorentzian profile for the absorption of off-resonant radiation,

$$\rho(\nu) = \frac{P}{\pi c w_0^2} \frac{1}{\pi(\nu - \nu_{CO_2})^2}. \quad (5.25)$$

In the considered frequency interval, the two lines intercept. Thus, we expect similar values for transition rates between rotational states as for the absorption of trap light. It might eventually be necessary to install a

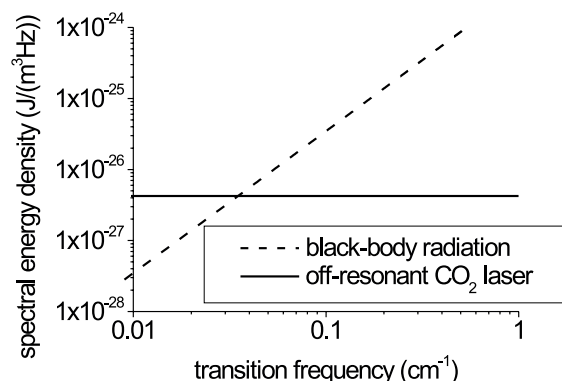


Figure 5.14: Comparison of the spectral energy density of black-body radiation at  $T = 300$  K with the one of the  $\text{CO}_2$ -laser assuming a Lorentzian absorption profile.

thermal shield around our apparatus to shield off background radiation. A more detailed analysis of rotational heating and the equilibrium distribution of rotational states will be performed in the near future.

**Conclusion** In conclusion, we have estimated the lifetimes of vibrational singlet groundstate levels due to spontaneous emission to be in the range 1-10 s. The inverse rates for the absorption of trap light, however, are found to be much shorter (0.1-0.01 s), mainly related to purely rotational transitions. In the frequency range associated with rotational transitions, we find that the spectral energy density of background radiation is of the same order of magnitude as the effective spectral density of the  $\text{CO}_2$  trapping laser. Thus, we may expect groundstate LiCs to be excited rotationally to high-energetic levels and eventually up to the dissociation limit on a faster time scale than stabilization occurs by spontaneous emission. Long storage times of the polar LiCs molecule in an optical dipole trap therefore appear unlikely. An alternative approach would be the storage of triplet groundstate LiCs in a magnetic trap as demonstrated with  $\text{Cs}_2$  [Vanhaecke et al., 2002]. Also, trapping in an electrostatic trap as suggested in [Xu, 2001] seems to be a promising perspective.

### 5.3 Photoassociation of Cs<sub>2</sub>

In this section, we outline our experimental results on PA-spectroscopy of Cs<sub>2</sub>. For a detailed description the reader is referred to [Lange, 2002]. In the first part, we briefly describe PA-experiments in a Cs-MOT using a Titanium-Sapphire (Ti:Sa) laser. In the second part we present first PA-measurements with Cs<sub>2</sub> performed in an optical dipole trap. We compare the results with the measurements in the Cs-MOT. In both setups, we measure the loss of Cs atoms from the traps.

#### 5.3.1 Photoassociation of Cs<sub>2</sub> in a MOT

In general, an excited molecule Cs<sub>2</sub><sup>\*</sup> formed by PA will decay either towards a bound state in the molecular groundstate, Cs<sub>2</sub>, as discussed above for LiCs, or it decays to give back two free Cs atoms with a certain amount of kinetic energy. Since the groundstate molecule Cs<sub>2</sub> can no longer be resonantly excited by the MOT laser beams, the PA-process leads to the loss of two Cs atoms out of the MOT. In the case that PA gives back two free atoms after spontaneous emission of a photon we observe trap loss of two atoms only if their velocity exceeds the recapture velocity of the MOT. The corresponding kinetic energy is on the order of  $1\text{ K} \times k_B$ . Since in our experiment we can only record the number of lost atoms from the MOT, we cannot distinguish between these two loss processes.

**Setup** The experimental setup for PA-experiments in the Cs-MOT is schematically shown in Fig. 5.15. The MOT laser detuning is chosen such that about  $10^7$ - $10^8$  atoms are loaded into the MOT at roughly 70  $\mu\text{K}$  temperature. For PA we use a Ti:Sa laser (MBR-110 from Coherent) pumped by an Argon-ion laser (Innova-90 from Coherent) operated at about 7.5 W output power. Thus, we reach 700 mW power at 852 nm out of the Ti:Sa laser. After coupling the light through an optical fiber we are left with 360 mW for PA-experiments. The PA-beam is directed four times through the MOT region in order to increase the effective power. Thereby it is focused to a waist of 150  $\mu\text{m}$  at the first two transitions through the main vacuum chamber and to about 500  $\mu\text{m}$  at the third and fourth transition. The foci are superimposed with the Cs-MOT by optimizing the PA-signal. The frequency of the PA-laser is slowly tuned at typically 36 GHz/h.

Trap loss due to PA is detected by recording the MOT fluorescence light as a function of the PA-laser detuning using a photodiode. In order to eliminate fluctuations in the MOT loading rate we use a lock-in amplifier for the detection of the PA-signal. The PA-laser beam is periodically switched on

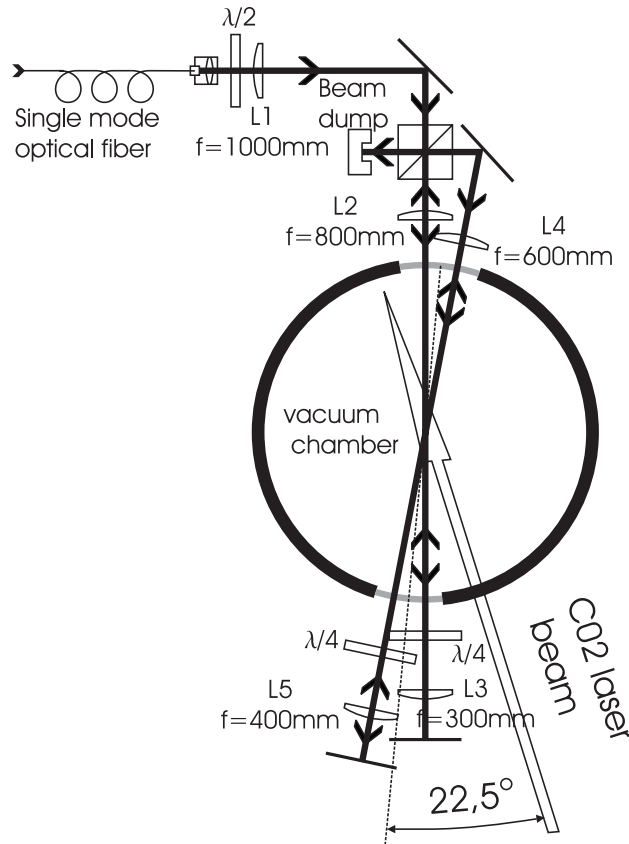


Figure 5.15: Sketch of the experimental setup.

and off at a rate of 0.5 Hz controlled by the internal oscillator of the lock-in amplifier. The latter is operated at a time constant of 10 s. The switching time  $1/(0.5 \text{ Hz})$  is long compared with the time constants of the MOT loading curve and the loss curve due to PA so that steady-state conditions are reached in each switching cycle. The Ti:Sa laser frequency is monitored by a wave meter (model WA-1000 from Burleigh Instruments) and by the transmission signal of a confocal Fabry-Perot-cavity.

**Results** Fig. 5.16 displays the  $\text{Cs}_2$  trap loss spectrum recorded in the range of 120-280 GHz detuning to lower frequencies with respect to the atomic transition  $6^2s_{1/2}(F=4) \rightarrow 6^2p_{3/2}(F'=5)$ . It is the result of several frequency scans. The zero level of the fluorescence signal detected with lock-in technique represents the MOT fluorescence level without shining in the PA-laser. The largest trap loss signal of about 200 mV corresponds to fluorescence reduc-

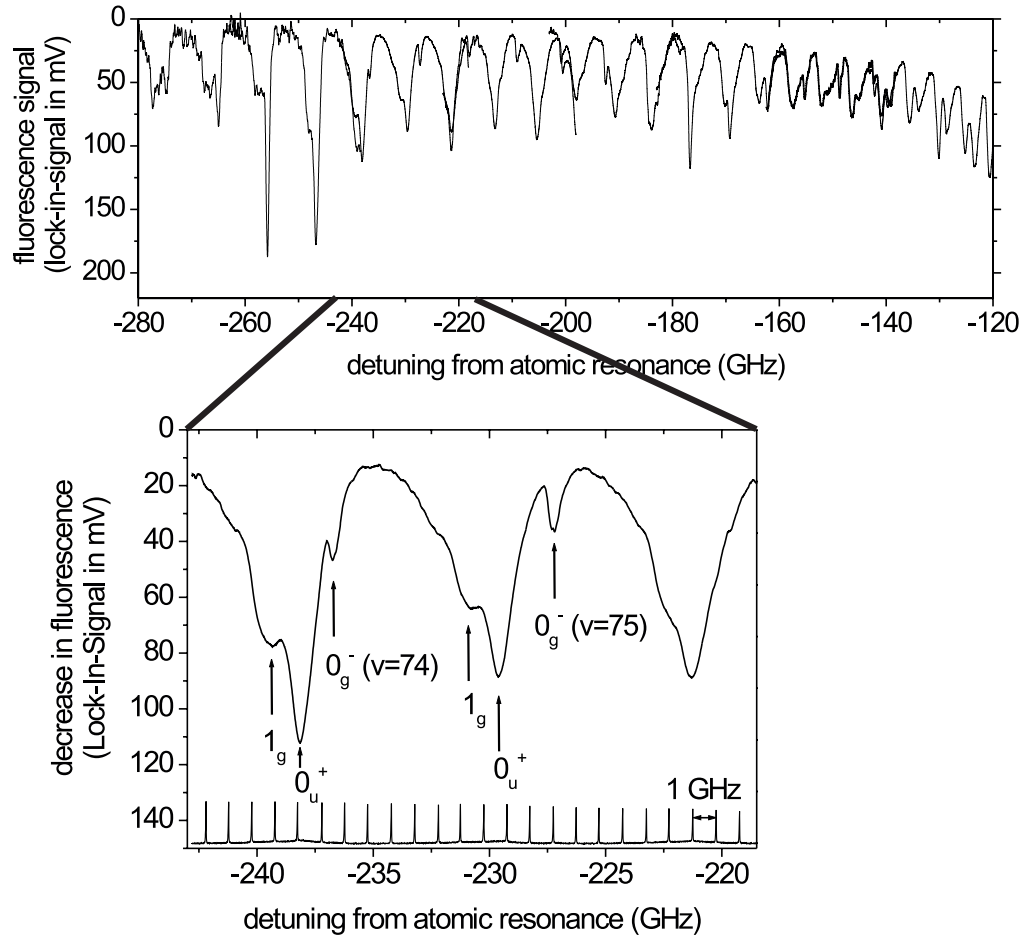


Figure 5.16:  $\text{Cs}_2$  trap loss spectrum as a function of detuning of the photoassociation laser from the  $6^2s_{1/2}(F=4) \rightarrow 6^2p_{3/2}(F'=5)$  atomic transition. The MOT fluorescence is recorded using lock-in technique.

tion of 50 %. The trap loss spectrum features discrete peaks which can be attributed to vibrational progressions associated to excited molecular states. The slow increase in the trap loss signal for detunings  $\gtrsim -150$  GHz can be attributed to overlapping ro-vibrational lines and to light-assisted inelastic collisions [Weiner et al., 1999].

By zooming into a smaller region of the PA-laser detuning we can identify a recurrent structure of three peaks (lower graph in Fig. 5.16). Thanks

to the detailed analysis of Cs<sub>2</sub> PA-spectra performed at Laboratoire Aimé Cotton in Orsay we were able to unambiguously identify all measured lines [Masnou-Seeuws and Pillet, 2001]. The agreement is on the  $\lesssim 300$  MHz level. Thus, all of the experimentally observed lines can be assigned to vibrational levels of the  $0_u^+$ ,  $0_g^-$  and  $1_g$  attractive long-range states of excited Cs<sub>2</sub><sup>\*</sup>. Expected lines associated to the  $1_u$ -state, however, are missing in our spectra. This could be explained by insufficient gain in kinetic energy of Cs atoms produced by spontaneous decay of the  $1_u$  state. Thus, the released Cs atoms remain trapped in the MOT and invisible to trap loss detection. The width of the observed lines resulting from broadening due to unresolved hyperfine structure and rotational sub-structure are also in good agreement with predictions [Fioretti et al., 1998]. The periodic pattern at the base line of the bottom graph in Fig. 5.16 is the transmission spectrum of our reference cavity with a free spectral range of 997.5 MHz.

### 5.3.2 Photoassociation of Cs<sub>2</sub> in a QUEST

Although a number of PA-experiments has been performed with MOTs, PA-measurements in an optical dipole trap have been reported only by one group [Miller et al., 1993, Cline et al., 1994]. Here, we present the first PA-measurements of Cs<sub>2</sub> performed in an optical trap, namely in our CO<sub>2</sub>-laser QUEST.

**Advantages** There are numerous advantages of the QUEST as opposed to the MOT as far as PA-measurements via trap loss is concerned. First, the atomic density in a QUEST is higher than in the MOT by a factor 10-100. Therefore we expect an increased total PA-rate by the same factor. Since continuous loading into the trap is absent, the trap loss signal due to PA can be improved by prolonging the PA-laser pulse. Ideally, the PA-duration is limited only by the finite storage time due to background gas collisions ( $\sim 100$  s). Another advantage is the higher sensitivity to photoassociative collisions in which the gain of kinetic energy of the outgoing atoms is small. All atoms with kinetic energy  $\gtrsim 740 \mu\text{K} \times k_B$  are lost from the QUEST compared with  $\sim 1 \text{ K} \times k_B$  needed to escape from the MOT.

Furthermore, the QUEST is the more suitable environment for precise PA-studies due to the fact that the trapped Cs atoms can be prepared in specific internal states such as hyperfine and magnetic sub-states prior to PA. Indeed, this feature of the QUEST is taken advantage of in the experiments discussed below. The QUEST not only provides improved conditions for PA-spectroscopy, it additionally offers the possibility of storing groundstate Cs<sub>2</sub> molecules formed via PA [Takekoshi et al., 1998]. Moreover, there is one

further advantage related to PA of LiCs. In the combined Li and Cs-MOT it is particularly difficult to identify PA-lines of LiCs because of the cross-talk of Li and Cs as a result of inelastic collisions [Schlöder et al., 1999]. Trap loss of Cs due to PA of Cs<sub>2</sub> influences the Li atom number and fluorescence signal, and vice versa. In the QUEST, however, Li and Cs atoms do not interact inelastically, thereby suppressing this perturbing effect.

**Difficulties** However, there are a few complications to take care of when choosing an optical dipole trap for PA-experiments. Since a dipole trap forms a conservative potential, heating of the atomic sample due to off-resonant scattering of photons from the PA-laser leads to decreasing density and eventually to trap loss. This difficulty can be met by repeatedly applying optical cooling pulses which does not significantly affect the atomic sample (see Section 2.5.3). The low trap depth of an optical trap implicates that inelastic atomic collisions such as spin-exchange or dipolar collisions (see Section 4.3) lead to trap loss. If the atom loss resulting from inelastic collisions is much faster than the PA-rate, then one has to suppress these collisions by optically pumping into the lowest-energy state, as discussed below.

**Setup** The experimental setup is identical to the one used for PA-experiments in the Cs-MOT. However, particular attention has to be concentrated to the adjustment of the PA-laser beam with respect to the CO<sub>2</sub>-laser trapping beam. The PA-laser beam propagates at a small angle of 22.5° with respect to the beam axis of the trapping beam which ensures good spatial overlap with the trapped Cs sample. For further optimization we take advantage of the fact that the focus of the red-detuned PA-laser beam acts as an optical dipole trap. Using absorption pictures, we are able to image the Cs atomic cloud trapped in the “far-off-resonance trap” (FORT) formed by the PA-laser focus. In particular, we find a position in which Cs atoms released from the QUEST remained trapped in the FORT. By optimizing the atomic density in the FORT we obtain the best starting conditions for PA in the QUEST.

The experimental sequence is the following. Cs atoms are loaded from the Cs-MOT into the QUEST as described in Sec. 2.5.3. Typically 10<sup>6</sup> Cs atoms are prepared in the lowest hyperfine groundstate ( $F = 3$ ) at a temperature of  $\sim 40 \mu\text{K}$ . Then we shine in the PA-laser during 0.1 to 5 seconds and recapture the remaining Cs atoms into the Cs-MOT. From the fluorescence image of the recaptured MOT cloud we infer the number of Cs atoms surviving the PA-phase (see Sec. 2.6.1). Since this detection method is destructive the sequence is repeated for every value of the PA-laser frequency. One cycle takes roughly

2 s plus the PA-phase, so that typical scan rates are in the range of 30 GHz per 30 min. It is important to note that we need to apply an additional “PA-repumping” laser simultaneously with the PA-laser. Off-resonant scattering of photons from the PA-laser at a rate of 10-1000 s<sup>-1</sup> effectively pumps the atoms into ( $F = 3$ ) and ( $F = 4$ ) to roughly equal shares. Since the fraction in ( $F = 3$ ) escapes from the QUEST in about 0.1 s (see Sec. 4.4.1) due to spin exchange collisions we observe constant trap loss. This effect can be suppressed by switching on the attenuated MOT “cooling” laser shifted to resonance with the atomic transition ( $F = 4 \rightarrow F' = 4$ ) during the entire PA-phase.

**Results** Fig. 5.17 compares two PA-spectra recorded in the MOT with lock-in technique (a) and measured by trap-loss from the QUEST (b). The two spectra result from four respectively five individual frequency scans. The PA-duration is 1 s. The value unity on the ordinate axis in graph (b) corresponds to about  $8 \times 10^5$  Cs atoms recaptured into the MOT. This is the case when the PA-laser is absent. The maximum PA-signal of 40 mV in graph (a) corresponds to a drop in MOT fluorescence of roughly 50%. The Cs atoms were stored in the QUEST in the lowest-energy state ( $F = 3$ ) whereas in the MOT preferentially the upper hyperfine groundstate ( $F = 4$ ) is populated. This results in a frequency shift of the two PA-spectra by  $2 \times \Delta E_{HFS} \approx 18.4$  GHz. For better comparison this frequency shift is compensated by shifting the frequency axes by the same value.

First of all, we notice the lower noise level in the QUEST spectrum compared to the MOT spectrum although each data point results from an individual loading and PA-sequence. PA-resonances manifest themselves by trap loss of up to 70%. The off-resonance trap loss level caused by scattering of light from the PA-laser and the PA-repumper, however, is negligible. As in the MOT spectrum, we identify three vibrational progressions that can be assigned to the electronic states  $1_g$ ,  $0_g^-$  and  $0_u^+$ . In contrast to the MOT spectrum, the  $1_g$ -progression is hardly visible in the QUEST spectrum, however the  $0_g^-$  and  $0_u^+$  progressions are more pronounced. The reason for the different line amplitudes is the modulation of the transition amplitudes as displayed in Fig. 5.8. The  $1_g$ -progression features a minimum in transition amplitude in the displayed frequency range. This effect is also nicely visible at the line amplitudes of the  $0_u^+$ -progression which fall off with increasing detuning. Different line amplitudes in MOT and QUEST spectra are mainly caused by the lower frequency resolution of the lock-in technique which leads to averaging over the substructure of the lines. Besides, we expect differences resulting from the different initial hyperfine states and from the fact

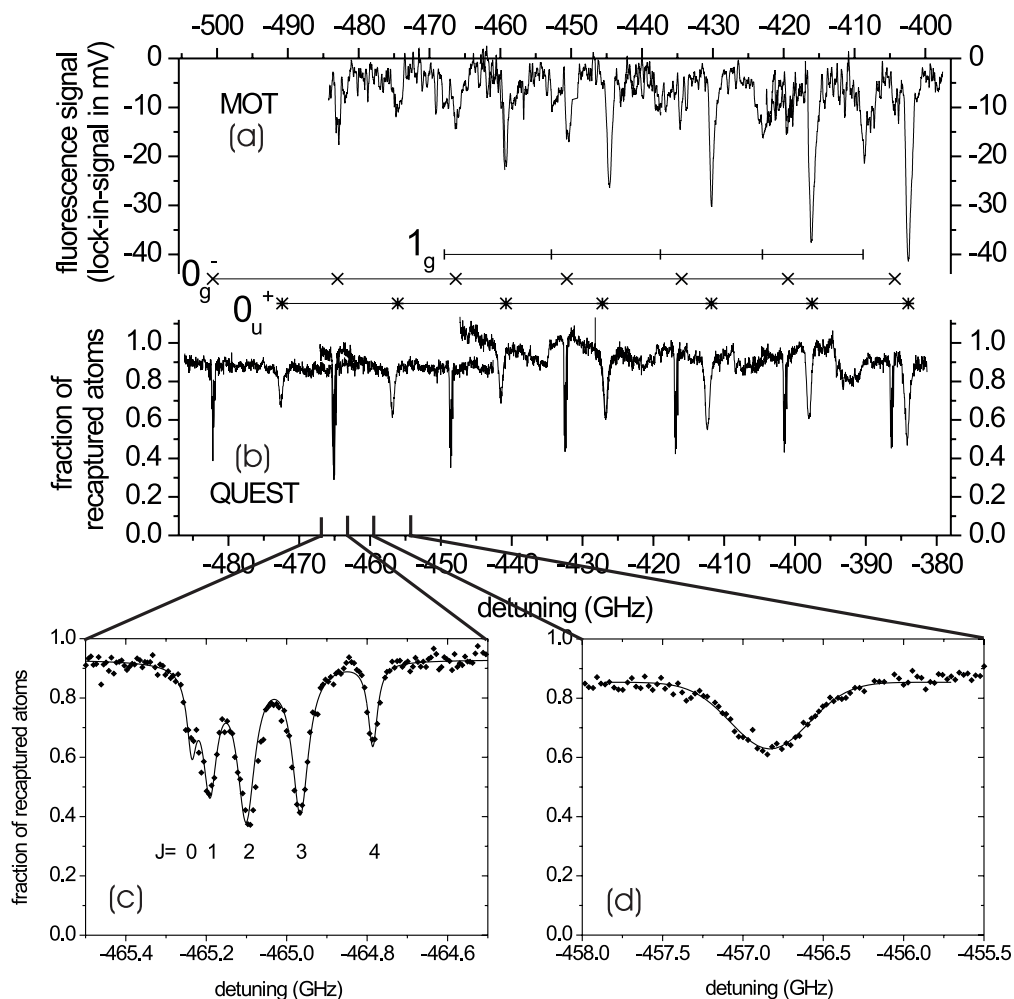


Figure 5.17: Comparison of  $\text{Cs}_2$  photoassociation spectra recorded in the MOT (a) and in the QUEST (b). The frequency axis in graph (b) is shifted by 18.4 GHz with respect to graph (a) because of the different initial states of Cs atoms (see text). Graph (c) and (d) are magnifications of vibrational lines attributed to the  $0_g^-$  ( $v = 55$ ) and the  $0_u^+$  electronic state.

that trap loss resolution is higher with the shallower QUEST.

Fig. 5.17 (c) and (d) show magnified representations of PA-lines attributed to the vibrational state  $v = 55$  in the outer potential well of the  $0_g^-$  and to the  $0_u^+$  electronic states, respectively. The  $0_u^+$  vibrational line

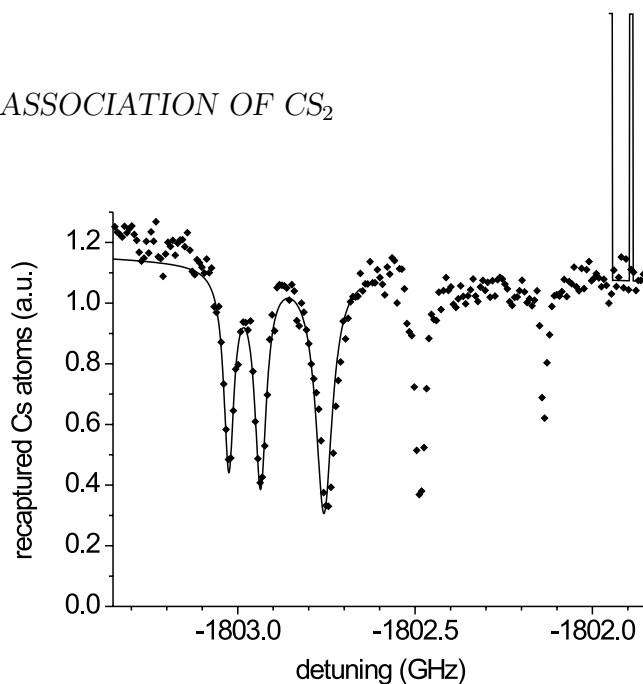


Figure 5.18: Zoom into the rotational structure of the vibrational line  $v = 10$  of the  $0_g^-$ -state.

(Fig. 5.17 (d)) shows no resolved substructure. The width of the fitted Gaussian function (solid line) amounts to about 220 MHz. We attribute this line broadening to complex coupling between hyperfine and rotational structure. In addition, one expects line broadening due to predissociation as a result of the coupling to the  $0_u^+$ -state correlated to the  $6p_{1/2}$ -asymptote [Dion et al., 2001]. The vibrational line ( $v = 55$ ) of the  $0_g^-$ -state, however, features several rotational lines (Fig. 5.17 (c)). Surprisingly, the rotational levels are clearly visible up to  $J = 4$ . If we consider only  $s$ -wave collisions to play a role, this can only be explained by complete recoupling of the orbital and spin angular momenta during the PA-process, which is rather improbable<sup>7</sup>. Alternatively, the high rotational excitation could be explained by assuming more photons to be involved in the PA-process, as observed in [Fioretti et al., 1999b]. The solid line in Fig. 5.17 (c) results from the fit of the sum of 5 Lorentzian functions whose positions are determined by the energy relation for the rigid rotator

<sup>7</sup>Before photon absorption, the collisional state of triplet symmetry has spin  $S = 1$  and the photon carries angular momentum  $L = 1$ , which gives a maximum total angular momentum  $J = 2$  if both spins are parallel ( $\rightarrow\rightarrow$ ). After photon absorption, there is additional rotation of the molecular axis  $\mathbf{l} = \mathbf{J} - \mathbf{L} - \mathbf{S}$ . If both orbital and spin angular momentum flip, conservation of total angular momentum  $\mathbf{J}$  implies  $l = 4$  ( $\leftarrow\leftarrow$ ).

$$E_{rot}(v, J) = hB_v J(J + 1). \quad (5.26)$$

Besides the vibrational line ( $v = 55$ ), we have measured rotational progressions for the vibrational lines  $v = 2, 6, 7$  and  $10$  in the outer well of the  $0_g^-$ -state. For the first time, we were able to perform PA-spectroscopy by trap loss measurements in the range of large detunings  $-1.8$  to  $-2.2$  THz from the  $6p_{3/2}$  ( $F' = 5$ ) asymptote. Fig. 5.18 shows exemplarily the rotational structure of the vibrational line  $v = 10$ . The line positions with respect to  $J = 0$  and rotational constants  $B_v$  obtained from the Lorentzian fits for a total of 5 fitted rotational progressions of the  $0_g^-$  are listed in table 5.3.2. Considering the specified precision of our wave meter of  $\pm 0.5$  GHz, the agreement of our data with literature values is excellent.

Interestingly, in all the recorded rotational progressions we have observed a larger width of the  $J = 2$  rotational lines as compared to the other lines of one rotational progression. The measured full-width at half-maximum (FWHM) for  $J = 2$  amounts to roughly 1.5 MHz, whereas all other lines feature a FWHM of roughly 0.5 MHz. The origin of this behavior is not yet understood. One reason for the global broadening of rotational lines recorded with trapped Cs atoms in the QUEST is the anisotropic polarizability of the Cs molecules (see Sec. 5.2.1). Since the rotating molecule constitutes a superposition of parallel and perpendicular states, both polarizabilities contribute to the AC-Stark shift of the resonance frequencies of trapped molecules, thereby leading to line-broadening. This effect will be further investigated.

In [Drag et al., 2000], an enhanced bound-bound transition probability from the deeply bound states ( $v \lesssim 10$ ) of the outer potential well to bound states of the  $^3\Sigma$ -groundstate are found (see Fig. 5.10). By assuming 100% efficiency of the production of bound groundstate Cs<sub>2</sub> from via PA of these particular excited states, we estimate a production rate of the order of  $10^6$ /s. Since our QUEST is well suited for trapping homonuclear molecules, we are confident to be able to store large numbers of groundstate Cs<sub>2</sub> molecules. These could be observed by detecting the interaction with Cs or Li atoms. Since the groundstate molecules are preferentially formed in high-lying ro-vibrational states, inelastic collisions in which the molecules undergo transitions to more deeply bound states may reveal the presence of the molecules in the trap. In addition, trap loss rates would give information about inelastic atom-molecule interactions in the micro Kelvin range, which have not been observed so far. For collisions between Na atoms and Na<sub>2</sub> molecules, it was recently found theoretically that vibrational relaxation collisions dominate over elastic processes in the ultracold regime [Soldán et al., 2002].

$v$	55	10	7	6	2
$\delta(\text{GHz})$ *	-465.236	-1803.025	-1942.036	-1989.59	-2189.1
$\delta(\text{GHz})$ **	-465.24	-1803.2	-1942.0	-1989.8	-2189.3
$B_v$ (MHz) *	22.5	44.7	47.5	-	-
$B_v$ (MHz) **	23.68	44.97	46.47	46.77	48.87

Table 5.3: Comparison of line positions and rotational constants: \* this work; \*\* [Fioretti et al., 1999a].

## 5.4 Conclusion and outlook

In conclusion, we have performed comparative PA- studies with Cs atoms stored in a MOT and in an optical dipole trap (QUEST). The advantages of our QUEST as an environment for performing PA- studies have enabled us to nicely resolve the ro-vibronic structure of excited  $\text{Cs}_2^*$  even at large detunings from the atomic resonance frequency. The resulting spectroscopic data is in excellent agreement with literature.

Our spectroscopic measurements on  $\text{Cs}_2$  could be continued in order to provide complementary data to the existing one. However, in the near future we will pursue two different goals. First, PA- spectroscopy of the heteronuclear LiCs system in our QUEST seems to be within reach. Second, the formation and storage of ultracold  $\text{Cs}_2$ -groundstate molecules in our QUEST opens the way to studying atom-molecule interactions with perfect control of the external and internal degrees of freedom.



# Chapter 6

## Conclusion and outlook

### 6.1 Conclusion

The present work addressed three main topics, all related to interactions in an optically stored mixture of ultracold Li and Cs atoms: Thermalization between Li and lasercooled Cs, homo- and heteronuclear spin-exchange collisions and photoassociation of LiCs and Cs<sub>2</sub>.

**Combined transfer** The pre-condition for the presented experiments with simultaneously stored Li and Cs atoms in the QUEST is an efficient strategy for the combined transfer of Li and Cs atoms from two individual MOTs into the QUEST. Optimum transfer conditions are achieved when the transfer sequences for Li and Cs are shifted in time, thereby suppressing inelastic light-assisted collisions involving optically excited Cs atoms [Schlöder et al., 1999, Mosk et al., 2001b]. We observe both largest transfer efficiency and low temperatures of Cs when the atoms are cooled by blue detuned optical molasses [Boiron et al., 1998]. The number of transferred Li atoms is enhanced by attenuating the MOT lasers and simultaneously shifting the laser frequencies close to the atomic resonance before switching off the magnetic quadrupole field. In addition, we observe an increase in the number of transferred Li atoms by a factor of 3 when compressing the atomic cloud by ramping up the quadrupole field in the last stage of magneto-optic trapping. In order to suppress collisions between excited Li and optically stored Cs atoms in the groundstate, the Li-MOT is loaded spatially separated from the QUEST by applying a homogeneous magnetic offset field. Under optimum conditions, we achieve the following initial values for the number and temperature of transferred atoms:  $N_{\text{Li}} = 10^5$ ,  $N_{\text{Cs}} = 10^6$ ,  $T_{\text{Li}} \sim 150 \mu\text{K}$ ,  $T_{\text{Cs}} = 30 \mu\text{K}$ .

**Thermalization** Starting from a gas mixture of Li and Cs atoms optically pumped into the lowest hyperfine groundstate, we were able to observe sympathetic cooling of Li through thermal contact with lasercooled Cs in the QUEST [Mudrich et al., 2002]. For the first time, we present a nearly loss-free approach to cooling of atoms below the temperature limitation of optical cooling methods. A reduction of the Li temperature from  $\sim 150 \mu\text{K}$  to  $30 \mu\text{K}$  within 5 s is observed. Due to the small mass of Li, this leads to an increase in phase-space density by about a factor 100. From the timescale of thermalization, we infer the previously unknown scattering cross section for elastic Li-Cs collisions,

$$\sigma_{\text{LiCs}} = 8(4) \times 10^{-12} \text{ cm}^2.$$

Furthermore, we observe evaporation of Li induced by elastic Li-Cs collisions (sympathetic evaporation) [Mosk et al., 2001b]. Contrary to intuition, this effect can lead to cooling of the coolant gas through evaporation of the hot Li gas out of the trap.

**Spin-exchange collisions** When the stored atoms are optically pumped into the upper hyperfine groundstate ( $F = 4$  (Cs),  $F = 2$  (Li)), we observe non-exponential loss of atoms from the QUEST accompanied by rising temperature. This effect can be attributed to exoergic spin-exchange collisions. Since trap-loss collisions preferentially take place at the bottom of the trapping potential, the mean potential energy of the escaping atoms falls below the mean potential energy of the entire ensemble. Elimination of the latter atoms therefore leads to increasing mean energy of the remaining sample, e.g. relaxation heating. By fitting the density evolution as a function of storage time after optically pumping into the upper hyperfine groundstate, we precisely determine the rate coefficients for homonuclear collisions involving two Cs atoms in  $F = 4$  on the one hand, and one Cs atom in  $F = 4$  and one in  $F = 3$  on the other hand. The resulting values,

$$\begin{aligned} G_{(4,4)} &= 1.1(3) \times 10^{-11} \text{ cm}^3/\text{s} , \\ G_{(3,4)} &= 1.5(4) \times 10^{-12} \text{ cm}^3/\text{s} \end{aligned}$$

are in excellent agreement with theoretical predictions [Tiesinga, 2002]. In analogous experiments with a mixture of Li and Cs, one of which is prepared in the upper hyperfine state, we observe inelastic inter-species collisions leading to trap-loss of an equal number of Li and Cs atoms. The corresponding rate coefficients are found to be on the order of  $10^{-10} \text{ cm}^3/\text{s}$ .

**Photoassociation** In the last part, the feasibility of forming LiCs dimers through photoassociation is studied theoretically. On the basis of molecular potential curves taken from literature [Korek et al., 2000], the LiCs spectrum is calculated in the relevant frequency range. Photoassociation rates of LiCs are expected to fall below the ones of Cs<sub>2</sub> by one to three orders of magnitude due to the structure of the molecular potentials. From the measured formation rates of groundstate Cs<sub>2</sub> molecules [Drag et al., 2000], we estimate a total rate for the formation of LiCs dimers in the groundstate of up to 10<sup>5</sup>/s.

The prominent feature of the LiCs dimer is the extremely large electric dipole moment of 5.48 Debye [Igel-Mann et al., 1986]. We find that coupling of the large dipole moment to the trapping laser field and to Black-Body radiation may pose limitations as far as storage in the QUEST is concerned.

Besides these theoretical considerations, we present photoassociation experiments of Cs<sub>2</sub> both in the MOT and in the QUEST. The advantages of the QUEST as an environment for performing photoassociation spectroscopy have enabled us to nicely resolve the ro-vibronic structure of excited Cs<sub>2</sub> even at large detunings from the atomic resonance frequency. The resulting spectroscopic data is in excellent agreement with literature. At these large detunings, the probability for transitions to stable groundstate molecules tends to unity [Drag et al., 2000]. Therefore, we estimate production rates of groundstate Cs<sub>2</sub> molecules in the range of 10<sup>6</sup>/s, most of which are assumed to remain trapped in the QUEST.

## 6.2 Outlook

**Detection of groundstate molecules through collisions** In the near future, we will explore the possibility of detecting stored Cs<sub>2</sub> dimers in the QUEST through inelastic collisions with atomic Cs or Li. For collisions between spin-polarized Na and vibrationally excited Na<sub>2</sub>, the rate coefficient for inelastic vibrational relaxation collisions ( $v = 1 \rightarrow v = 0$ ) is predicted to be on the order of 10<sup>-10</sup> cm<sup>3</sup>/s at 10 μK temperature [Soldán et al., 2002]. If the rate coefficients for inelastic collisions Cs + Cs<sub>2</sub> or Li + Cs<sub>2</sub> were in the same range, the presence of Cs<sub>2</sub> molecules in the QUEST should be detectable through the loss of the atomic component within a fraction of a second.

**Saturation effects** Saturation of a transition occurs, when the driving field is sufficiently strong for the Rabi-frequency to become comparable or even greater than the natural decay rate of the excited state. In this regime, the system undergoes coherent transitions between ground and excited states.

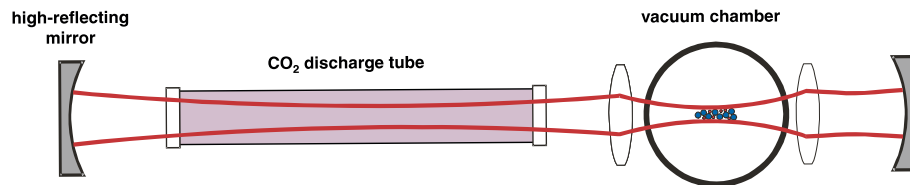


Figure 6.1: Schematic illustration of the novel intra-cavity quasi-electrostatic trap (ICET).

In the case of photoassociation transitions, saturation implies coherent coupling of a bound molecular state to a free collisional state, which is a peculiar thought. However, the theory of photoassociation at large laser power is not yet fully understood. Only recently, a clear signature of saturation of the rate of photoassociation of  ${}^6\text{Li}{}^7\text{Li}$  was observed in a MOT [Schlöder et al., 2002]. A cold and dense sample of Cs atoms in the QUEST would provide excellent initial conditions for the investigation of saturation effects. Besides, additional effects related to the trap dynamics such as relaxation heating as a result of trap loss are comparatively simple in a conservative trapping potential. It is therefore easier to unambiguously identify saturation effects. We will try to contribute to this field by measuring  $\text{Cs}_2$  photoassociation rates in the QUEST at different laser intensities and photoassociation pulse durations.

**Photoassociation of LiCs** The principal goal for future experiments is photoassociation spectroscopy of the heteronuclear LiCs dimer. In first measurements, no indications for trap-loss of Li as a consequence of photoassociation of LiCs was found. However, the noise level was in the range of 20%, mainly due to fluctuations in the transfer efficiency of Li. Therefore, we are currently improving the stability of the system in order to be more sensitive to weak resonances in the trap loss signal. Furthermore, the initial conditions for LiCs photoassociation have to be improved. For this purpose, Raman sideband cooling of Cs will be implemented [Kerman et al., 2000]. By reducing the Cs temperature to  $\sim 1 \mu\text{K}$ , which appears realistic, the mixed density  $N_{\text{Li}}N_{\text{Cs}}/V_{\text{LiCs}}$  in expression (5.8) of Chapter 5 would rise by roughly a factor of 150, assuming the current trap geometry and fast thermalization.

Another approach we intend to pursue is the modification of trap geometry. In a crossed-beam QUEST [Grimm et al., 2000], the density of both Li and Cs is expected to increase by at least one order of magnitude [Barrett et al., 2001]. Besides, we are currently setting up an apparatus with the objective of exploring a new type of trap, the intra-cavity quasi-electrostatic trap (ICET). The basic idea is to insert the experimen-

tal environment including the MOT chamber into a CO<sub>2</sub>-laser resonator, as illustrated in Fig. 6.1. Both cavity mirrors are high-reflecting, which leads to maximum power build-up inside the resonator. We expect an effective intra-cavity power of up to 1 kW. We are currently characterizing the trap parameters and the transfer scheme of Cs atoms into the ICET.

**Groundstate LiCs** For the detection of groundstate LiCs molecules, an ionization scheme in combination with standard time-of-flight mass spectrometry will be implemented in the apparatus. The possibility of enhancing the formation rate of groundstate LiCs through two-color photoassociation will be investigated. As a next step, the possibility of optically storing LiCs molecules in the QUEST will be investigated. Once groundstate dimers are trapped, we will demonstrate the possibility of manipulating LiCs molecules with external fields by deflecting the formed sample of LiCs in an electric field gradient. The observation of pendular states with LiCs in strong electric fields as proposed in [Rost et al., 1992], is a tantalizing prospect.

**Spin polarization** The capability of selectively populating well-defined magnetic sub-states of groundstate Li and Cs atoms is important in many respects. Inelastic trap-loss collisions are expected to be suppressed for atoms prepared in the upper hyperfine state, if only the outermost magnetic sub-states ( $m_F = \pm F$ ) are populated (Section (4.2.2)). Besides, the photoassociation spectra are altered when the atomic sample is doubly polarized prior to photoassociation. In particular, more efficient excitation of molecular states of pure triplet symmetry, such as the  $0_g^-$  state in Cs<sub>2</sub>, is expected. Furthermore, the elastic scattering cross-section between polarized atoms is enhanced by a factor of two compared with unpolarized atoms. This may be important to accelerate evaporative cooling of Cs atoms. Spin-polarization of Li is crucial for achieving quantum degeneracy of Li through sympathetic cooling by Cs.

In order to be able to monitor the efficiency of spin-polarization we will implement a double-resonance scheme. This method is based on a tunable RF or microwave emitter in combination with absorption imaging. In a weak homogeneous magnetic field the magnetic sub-levels of the ground-state are shifted in energy. Thus, particular RF (microwave) transitions between Zeeman levels of the two hyperfine groundstates can be addressed by choosing the appropriate RF (microwave) frequency. From subsequent absorption imaging of the population of one of the two hyperfine states, one infers the population of the initial magnetic sub-state of interest. For eventually performing double-resonance detection with Li, a 800 MHz RF-source

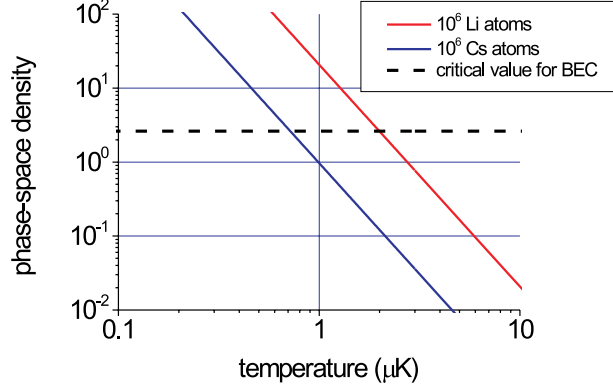


Figure 6.2: Phase-space densities of Li and Cs as a function of temperature for the current QUEST configuration.

including a Yagi-antenna has already been set up during this work. For Cs, a microwave-generator was acquired and tested in the frame of this work.

**Sympathetic cooling towards quantum degeneracy** Besides our main objective, the formation of LiCs through photoassociation, we will explore different scenarios of optimized sympathetic cooling of Li. In Fig. 6.2, the phase-space densities  $n\Lambda^3$  of Li and Cs are plotted for the current QUEST configuration and assuming  $10^6$  atoms of each species to be trapped in the QUEST. Due to the small mass of Li, the critical value for reaching Bose-Einstein condensation of Li is reached at a higher temperature than with Cs. Fig. 6.2 demonstrates, that cooling Cs to a realistic temperature of  $2\mu\text{K}$  would be sufficient to attain the degenerate regime with Li through sympathetic cooling. Bose-Einstein condensation with  $^7\text{Li}$  in a magnetic trap has already been demonstrated [Bradley et al., 1997]. Due to attractive interaction in the magnetic trappable state, however, the number of atoms in the condensate was limited to a few thousand. In the dipole trap, there is no limitation on the spin states. Therefore appropriate states with repulsive interaction, necessary to achieve large numbers of condensed atoms, can be chosen. Moreover, the fermionic isotope  $^6\text{Li}$  is interesting because of its large negative triplet scattering length [Abraham et al., 1997] and a Feshbach resonance in the elastic scattering cross section at 530 G [Jochim et al., 2002]. This gives rise to a comparatively large temperature for the BCS transition and for the formation of Cooper pairs [Baranov and Petrov, 1998].

# Appendix A

## Release-and-recapture thermometry

In the case of Li, the density of the trapped atomic cloud in the QUEST is too low for absorption imaging (see Sec. 2.6.1). Therefore, the Li temperature is measured by a different technique, so-called release-and-recapture thermometry. We consider a cold atomic gas confined in an optical dipole trap. The trap potential is suddenly turned off for a variable ballistic expansion time of order 1 ms. After this time, the dipole trap is turned on again for  $\sim 500$  ms to recapture the remaining fraction of atoms. The number of recaptured atoms is then measured by the fluorescence in the MOT. The drop in number of recaptured atoms as a function of expansion time is related to the temperature of the trapped sample. In the following, we essentially reproduce the derivations of [Mosk, 2002].

We derive an analytical approximation of the number of recaptured atoms for a gas at low temperature ( $k_{\text{B}}T \ll U_0$ ) in an extremely elongated Gaussian trap ( $\omega_{\text{ax}} \ll \omega_{\text{rad}}$ ):

$$N_{\text{r}}(t) = \frac{N_0}{1 - e^{-\eta}} [1 - \exp(-\eta W(\tilde{t}^2)/\tilde{t}^2)]. \quad (\text{A.1})$$

Here,  $w_0$  is the Gaussian beam waist,  $\eta = U_0/(k_{\text{B}}T)$ ,  $\tilde{t}^2 = mw_0^2t^2/4U_0$ , and  $W(z)$  is the product logarithm function, satisfying  $W(z)\exp(W(z)) = z$ . The analytical approximation of Eq. (A.1) agrees with numerical simulation for temperatures up to  $k_{\text{B}}T \sim 0.15 U_0$ . Full numerical calculation of  $N_{\text{r}}(t)$  is possible for any  $T$  and shows that for  $k_{\text{B}}T > 0.2 U_0$  ( $75 \mu\text{K}$  for Li) the width of the recapture curve becomes essentially independent of temperature, i.e., release-recapture measurements no longer provide reliable temperature data. Hence Eq. (A.1) can be used over the entire range of useful parameters. For the temperature range of interest, we estimate the accuracy of this method

to be better than 20%. The release-recapture curve of the pure Li in Fig. 3.6 in Chapter 3 can be reproduced by assuming a thermal distribution at  $T_{\text{Li}} = 71 \pm 15 \mu\text{K}$ . The sympathetically cooled Li ensemble is well-described by  $T_{\text{Li}} = 30 \pm 6 \mu\text{K}$ , which is equal to the Cs temperature within the uncertainty margins, indicating that the gases have fully thermalized.

We consider a thermal ensemble of atoms expanding from a small cloud at  $(0, 0, 0)$  that are recaptured after a time  $t$  into a trap which is very elongated along the  $z$  axis and tight along the  $x, y$  axis. The influence of gravity and collisions between the atoms is neglected as well as motion along the  $z$  axis.

The potential is given by

$$U(x, y) = U(r) = -U_0 e^{-2r^2/w_0^2}.$$

If an atom manages to fly a radial distance  $r$  in a time  $t$  it has kinetic energy  $(r/t)^2 m/2$ , and it will be recaptured only if

$$\frac{m}{2}(r/t)^2 \leq U_0 e^{-2r^2/w_0^2}.$$

Here,  $r_{\text{max}}$  is the distance for which this becomes an equality. Let us simplify this expression using the product logarithm function defined by

$$W(z)e^{W(z)} = z,$$

and define the dimensionless quantity  $R^2 = 2r^2/w_0^2$ . We obtain

$$e^{R_{\text{max}}^2} R_{\text{max}}^2 = 4U_0 t^2 / (mw_0^2),$$

which we rewrite using the product logarithm function

$$R_{\text{max}}^2 = W(4U_0 t^2 / mw_0^2) \equiv W(\tilde{t}^2).$$

Now we know the maximum distance, therefore the maximum initial velocity of the atoms, and we simply integrate over the Boltzmann distribution.

The fraction of recaptured atoms is

$$\begin{aligned} F_r &= \int_0^{v_{\text{max}}(t)} v e^{-mv^2/2k_{\text{B}}T} dv / \int_0^{(2U_0/m)^{1/2}} v e^{-mv^2/2k_{\text{B}}T} dv \\ &= \frac{1}{1 - e^{-\eta}} (1 - e^{-mv_{\text{max}}^2/2k_{\text{B}}T}) \end{aligned}$$

We insert  $v_{\text{max}}^2 = r_{\text{max}}^2/t^2 = (w_0^2/2)R_{\text{max}}^2/t^2 = (w_0^2/2t^2)W(\tilde{t}^2)$ , and are left with

$$F_r = \frac{1}{1 - e^{-\eta}} (1 - e^{-\eta(mw_0^2/4U_0 t^2)W(\tilde{t}^2)}).$$

By substituting the dimensionless quantity  $\tilde{t} = 4U_0t^2/(mw_0^2)$ , we obtain the final expression (see Eq. (1) in [Mudrich et al., 2002])

$$F_r = \frac{1}{1 - e^{-\eta}}(1 - e^{-\eta W(\tilde{t}^2)/\tilde{t}^2}).$$

The influence of gravity is neglected in this derivation, which is a valid approximation for the rapidly expanding Li sample. In the case of cold and heavy Cs, however, the influence of gravity can no longer be neglected, and fitting the experimental data with Eq. A.1 leads to an error  $\gtrsim 100\%$ .



# Appendix B

## Vacuum and lasers

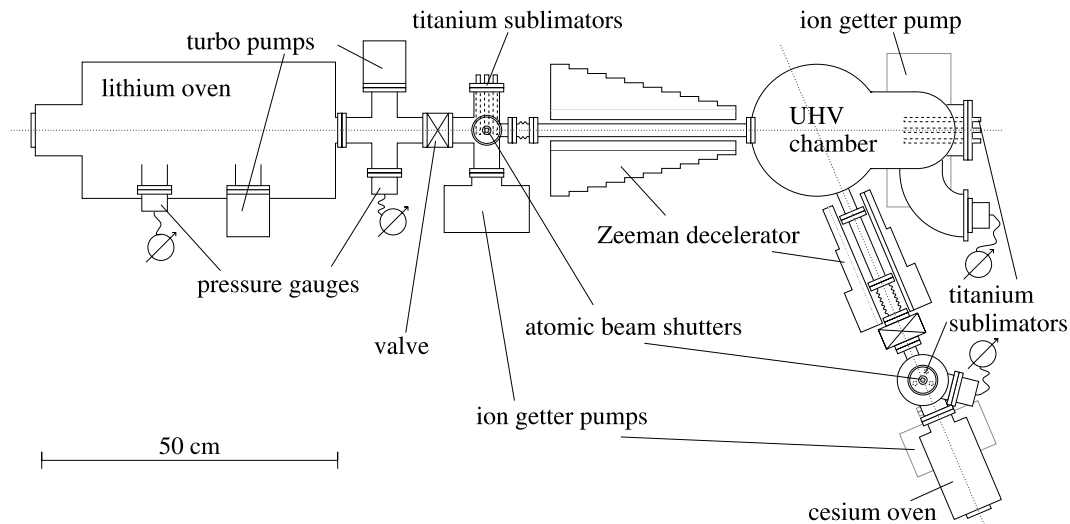


Figure B.1: Top view of the vacuum system.

**Vacuum system** The central part of the experiment is the main vacuum chamber, shown in Fig. B.1. The chamber is fabricated out of stainless steel (type 316LN). On the upper part, a total of 24 CF-flanges with windows of different diameter provide excellent optical access to the trapping region in the center of the chamber. Titanium sublimation pumps in addition to a 60 l/s ion-getter-pump mounted in the lower part of the chamber sustain an ultra-high vacuum of  $5 \times 10^{-11}$  mbar.

The main chamber is connected to two oven chambers containing Cs dispensers and metallic Li. The pressure in the oven sections is on the order of  $10^{-6}$  mbar. Both the effusive Li and Cs atomic beams are Zeeman slowed

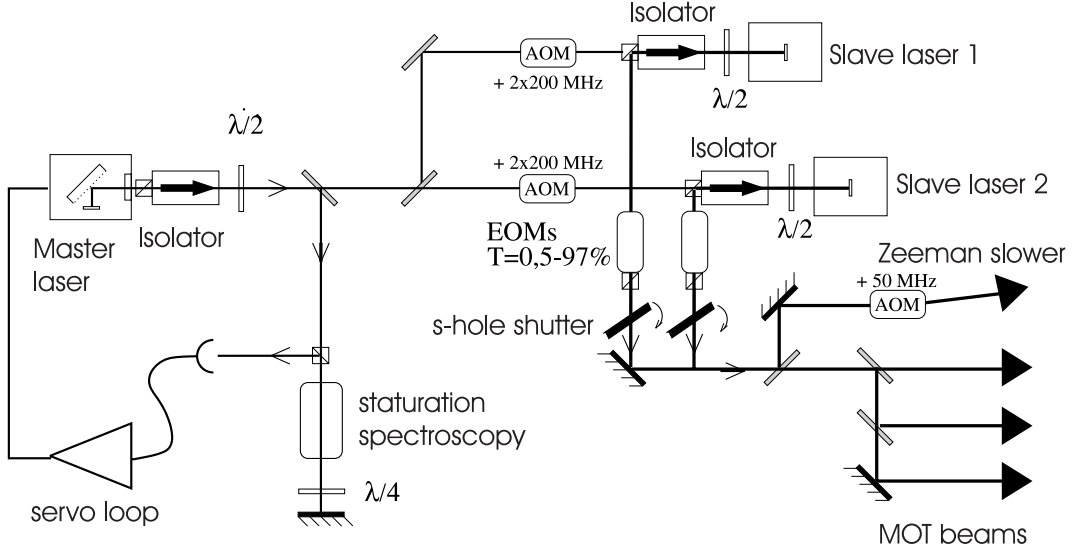


Figure B.2: Schematic overview over the Li laser system.

and can be blocked individually by means of mechanical paddles. For details on the vacuum system the reader is referred to [Engler, 2000].

**Laser system** The laser system required for the Li-MOT is sketched in Fig. B.2. The grating stabilized master laser is locked by radio-frequency spectroscopy to the Doppler-free cross-over line halfway in between the required frequencies for MOT operation. The laser light is then split into two beams of equal intensity. Using two acousto-optic modulators (AOM), the beams are shifted in frequency to the red and to the blue, respectively, to match the frequencies of the  $2S_{1/2}(F=2) \rightarrow 2P_{3/2}$  and  $2S_{1/2}(F=1) \rightarrow 2P_{3/2}$  transitions of the lithium  $D_2$  line at 671 nm. The two frequencies are amplified by injection locking two slave-laser diodes. The latter are operated at 12 and 16 mW output power. One electro-optic modulator (EOM) in combination with a polarizing beam splitter in each beam are used for intensity modulation. The two slave-laser beams are then superimposed and the resulting beam is divided into three MOT beams plus one beam for Zeeman slowing. The latter beam is frequency shifted by about 60 MHz through an AOM. All beams are guided to the experiment without optical fibers lest losing laser power.

Fig. B.3 displays schematically the Cs laser system, which is set up on an individual optical table. The cooling and repumping light is provided by distributed-Bragg-reflection (DBR) diode lasers. Both lasers are frequency-stabilized relative to absorption lines from cesium vapor cells at room tem-

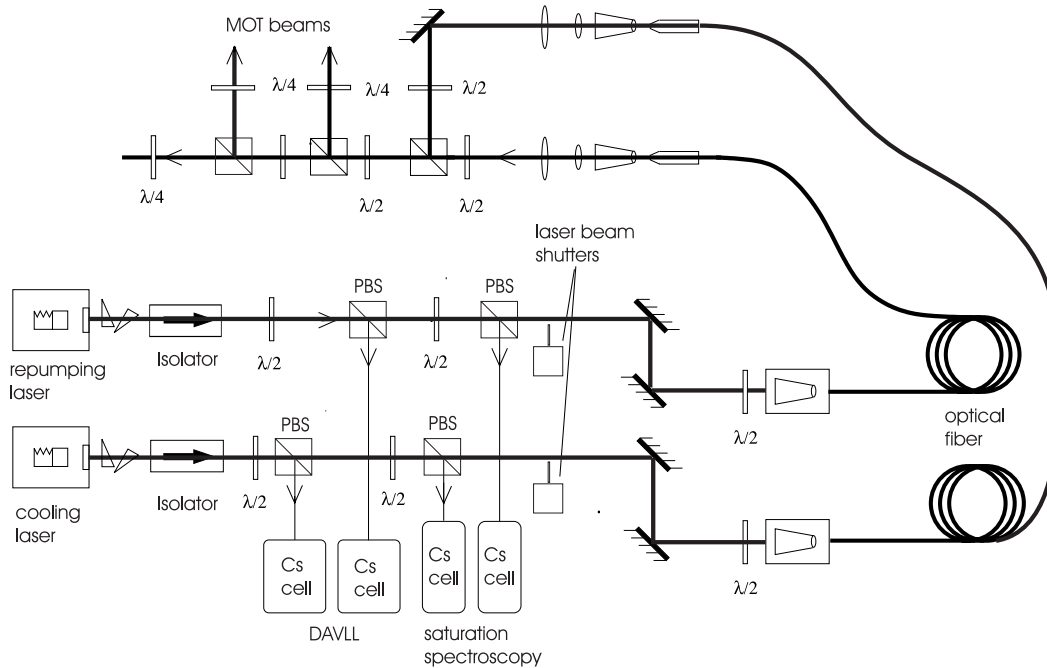


Figure B.3: Cs-MOT laser system.

perature. The error signal of the servo loops is provided by the frequency-dependent circular dichroism of cesium vapor in a glass cell, to which a longitudinal magnetic field of some tens of Gauss is applied (dichroic-atomic-vapor laser lock (DAVLL)) [Corwin et al., 1998]. The dichroism is measured as the difference in absorption between the left- and right-circular components of a linearly polarized beam. Since the dichroism signal is Doppler-broadened, the capture range is typically on the order of 300 MHz. Thus, the laser frequency can be adjusted by applying an offset voltage over a comparatively wide range. The two beams are guided to the experiments using individual single-mode polarization maintaining optical fibers. Behind the output couplers, the two beams are merged using polarizing beam splitters. This way, fluctuations of the polarization due to the imperfectness of the optical fibers are eliminated. Besides the shown laser setup, there is one more DBR laser diode for the Zeeman slower beam.

For absorption imaging of Cs, a stable laser with a very narrow line width is required. For this purpose, we have set up a grating-stabilized diode laser, frequency-locked to a Cs vapor cell using Doppler-free DAVLL. The setup is sketched in Fig. B.4. A few percent of the laser power is separated from the main beam using a simple glass plate for saturation spectroscopy. As in the case of Doppler-broadened DAVLL, the dichroism is measured as the

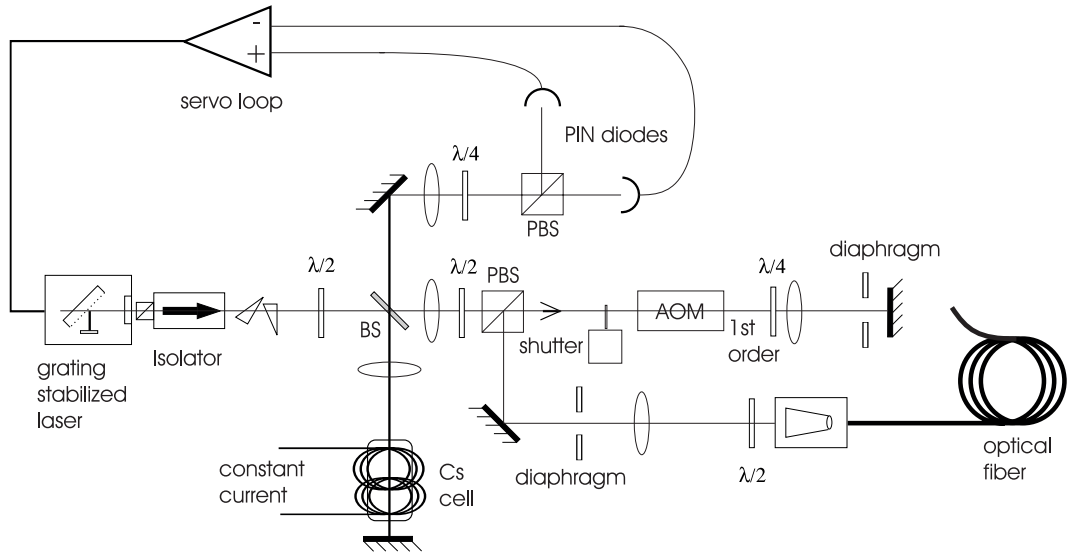


Figure B.4: Laser setup for absorption imaging.

difference in absorption between the left- and right-circular components of a linearly polarized beam. The weak axial magnetic field ( $\sim 5$  G) is generated by a pair of coils, allowing optimization of the field amplitude.

Both the saturation spectrum and Doppler-free DAVLL signal are shown in Fig. B.5. At the cross-over frequency between transitions  $F = 4 \rightarrow F' = 4$  and  $F = 4 \rightarrow F' = 5$  the DAVLL signal features a pronounced dispersive curve which is perfectly suited for locking the laser frequency. In addition to the step edge of the DAVLL signal which allows tight locking, the DAVLL signal is completely independent of temperature fluctuations. In contrast to the Doppler-broadened DAVLL setup, the spectroscopy cell does not have to be temperature stabilized. The beam is subsequently guided through an AOM in double pass which shifts the frequency to the  $F = 4 \rightarrow F' = 5$  resonance frequency.

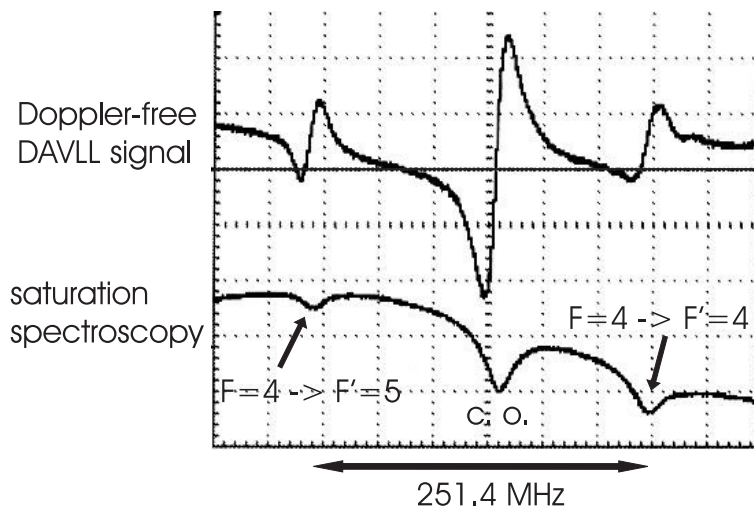


Figure B.5: Doppler-free DAVLL signal and saturation spectrum. The horizontal line intersecting the DAVLL signal represents the zero-line. The latter signal is perfectly suited as a lock-signal for laser stabilization.



# Appendix C

## Calculated LiCs levels

$v$	$0^-$	$0^+$	$1_1$	$1_2$	$2$
0	-118854.53126	-203467.37565	-45731.75189	-119498.97313	-245526.91613
1	-115088.93688	-197615.82854	-42692.13982	-115745.26551	-239958.15682
2	-111374.60993	-191819.27227	-39787.38318	-112043.70371	-234428.66126
3	-107711.39452	-186127.2115	-37018.4593	-108394.08386	-228940.12929
4	-104098.51119	-180540.54861	-34381.10513	-104795.68948	-223489.0803
5	-100536.03789	-175048.98873	-31878.15672	-101248.4546	-218080.11012
6	-97024.25641	-169647.28251	-29505.0632	-97752.83492	-212712.00759
7	-93562.27339	-164330.06068	-27259.17443	-94307.57129	-207383.94228
8	-90149.27338	-159092.85633	-25136.47919	-90911.67441	-202096.56174
9	-86784.68078	-153932.65355	-23131.56323	-87564.04704	-196849.75805
10	-83467.09257	-148846.53237	-21238.13991	-84262.55467	-191643.88795
11	-80194.58408	-143832.78099	-19449.27205	-81004.12441	-186479.53006
12	-76965.42252	-138890.03234	-17758.86788	-77785.51253	-181357.31692
13	-73778.4327	-134016.95535	-16158.97391	-74603.42131	-176277.14062
14	-70631.74392	-129212.32087	-14641.16599	-71453.44981	-171238.95619
15	-67523.23964	-124475.50534	-13198.93863	-68330.81334	-166243.75893
16	-64450.46758	-119805.88219	-11827.59109	-65230.81716	-161291.62679
17	-61412.07866	-115203.2026	-10524.46421	-62150.78713	-156382.74264
18	-58407.98294	-110667.35863	-9287.61236	-59090.4984	-151517.35232
19	-55438.63312	-106198.52118	-8119.68568	-56051.63281	-146696.13035
20	-52505.21337	-101797.09195	-7024.46456	-53037.54203	-141919.64935
21	-49610.79655	-97463.5896	-6005.2707	-50053.74223	-137188.68875
22	-46759.37591	-93198.85653	-5067.44937	-47106.87381	-132503.89913
23	-43955.14852	-89004.31377	-4214.31029	-44203.44825	-127866.04194
24	-41203.67554	-84881.1125	-3448.87836	-41350.83444	-123275.63283
25	-38510.9288	-80830.19109	-2773.00329	-38556.68606	-118733.43627
26	-35883.50974	-76853.04549	-2185.27007	-35829.10949	-114240.12979
27	-33327.63904	-72952.43679	-1684.97118	-33176.11817	-109796.41491
28	-30849.96609	-69130.84127	-1266.16476	-30605.55167	-105403.23596
29	-28458.07262	-65390.08166	-924.74364	-28126.53864	-101061.54928
30	-26158.47611	-61733.25782	-651.55518	-25748.33667	-96772.40116
31	-23957.35528	-58164.44691	-437.6296	-23479.37891	-92536.88881
32	-21860.32823	-54686.96164	-275.85884	-21328.16145	-88356.30137
33	-19872.45544	-51304.45647	-153.68761	-19301.78039	-84231.98488

$v$	$0^-$	$0^+$	$1_1$	$1_2$	$2$
34	-17997.83508	-48021.72508	-64.14274	-17406.60928	-80165.74709
35	-16238.9824	-44844.05879		-15645.95485	-76159.3328
36	-14595.81945	-41776.89283		-14019.41537	-72214.12704
37	-13068.14237	-38825.50654		-12522.92865	-68331.69173
38	-11654.11944	-35995.82981		-11151.12543	-64514.56311
39	-10349.24179	-33295.11161		-9894.0586	-60765.80505
40	-9147.54354	-30729.4557		-8742.04788	-57087.71396
41	-8043.92825	-28305.25065		-7686.52222	-53482.75114
42	-7031.89941	-26027.92269		-6719.02448	-49954.72693
43	-6105.23634	-23902.35244		-5832.56352	-46507.65556
44	-5259.65202	-21932.10143		-5022.69042	-43144.93666
45	-4489.5853	-20118.05404		-4283.72113	-39870.76433
46	-3790.64723	-18456.98752		-3611.81831	-36690.26501
47	-3158.84758	-16945.67009		-3004.3108	-33608.93388
48	-2592.46555	-15571.56147		-2459.18702	-30632.37106
49	-2090.86257	-14316.96492		-1977.51121	-27766.09872
50	-1650.73493	-13159.72883		-1554.81948	-25016.74826
51	-1273.54563	-12076.10966		-1194.25065	-22391.90441
52	-957.01924	-11044.71426		-892.16824	-19898.16561
53	-697.27046	-10050.88279		-645.89811	-17542.88573
54	-486.96637	-9087.22539		-445.47516	-15332.48934
55	-315.89007	-8149.9227		-282.71808	-13273.7727
56	-179.30483	-7241.29812		-154.04736	-11372.45587
57	-82.51399	-6363.21935		-67.87215	-9632.65197
58		-5521.7062			-8056.56748
59		-4722.03202			-6648.39349
60		-3970.98111			-5405.35093
61		-3276.8697			-4323.29368
62		-2645.33687			-3397.77881
63		-2080.70262			-2618.05879
64		-1591.8348			-1975.59254
65		-1180.85295			-1455.96607
66		-848.33865			-1044.50455
67		-587.16885			-726.67406
68		-382.73769			-483.93548
69		-224.23166			-304.42003
70		-108.18518			-172.4366
71		-42.76457			-75.13011
72					-19.56067

Table C.1: Calculated vibrational spectrum of the electronic states of LiCs correlated to the  $2s6p_{3/2}$ -asymptote. The listed energy values of bound states with  $J = 0$  are given in GHz-detuning with respect to the atomic transition  $\text{Cs } 6s \rightarrow 6p_{3/2}$ . Hyperfine splitting is neglected.

# Bibliography

[Gre, ]

[Abraham et al., 1997] Abraham, E. R. I., McAlexander, W. I., Gerton, J. M., Hulet, R. G., Côté, R., and Dalgarno, A. (1997). Triplet s-wave resonance in  ${}^6\text{Li}$  collisions and scattering lengths of  ${}^6\text{Li}$  and  ${}^7\text{Li}$ . *Phys. Rev. A* **55**, R3299.

[Adams et al., 1995] Adams, C. S., Lee, H., Davidson, N., Kasevich, M., and Chu, S. (1995). Evaporative Cooling in a Crossed Dipole Trap. *Phys. Rev. Lett.* **74**, 3577.

[Amiot and Dulieu, 2002] Amiot, C. and Dulieu, O. (2002). The  $\text{Cs}_2$  ground electronic state by Fourier transform spectroscopy: Dispersion coefficients. *J. Chem. Phys.* **117**, 5155.

[Amitay and Zajfman, 1994] Amitay, Z. and Zajfman, D. (1994). Rotational and vibrational lifetime of isotopically asymmetric homonuclear diatomic molecular ions. *Phys. Rev. A* **50**, 2304.

[Arndt et al., 1997] Arndt, M., Dahan, M. B., Guéry-Odelin, D., Reynolds, M. W., and Dalibard, J. (1997). Observation of a Zero-Energy Resonance in Cs-Cs Collisions. *Phys. Rev. Lett.* **79**, 625.

[Ashkin, 1978] Ashkin, A. (1978). Trapping of atoms by resonance radiation pressure. *Phys. Rev. Lett.* **40**, 729.

[Bahns et al., 2000] Bahns, J. T., Gould, P. L., and Stwalley, W. C. (2000). Formation of cold ( $T \leq 1$  K) molecules. *Adv. Atomic Mol. Opt. Phys.* **42**, 171.

[Bahns et al., 1996] Bahns, J. T., Stwalley, W. C., and Gould, P. L. (1996). Laser cooling of molecules: A sequential scheme for rotation, translation, and vibration. *J. Chem. Phys.* **104**, 9689.

- [Baranov and Petrov, 1998] Baranov, M. A. and Petrov, D. S. (1998). Critical temperature and Ginzburg-Landau equation for a trapped Fermi gas. *Phys. Rev. A* **58**, R801.
- [Barrett et al., 2001] Barrett, M. D., Sauer, J. A., and Chapman, M. S. (2001). All-Optical Formation of an Atomic Bose-Einstein Condensate. *Phys. Rev. Lett.* **87**, 010404.
- [Bedaque et al., 2000] Bedaque, P. F., Braaten, E., and Hammer, H.-W. (2000). Three-body Recombination in Bose Gases with Large Scattering Length. *Phys. Rev. Lett.* **85**, 908.
- [Beijerinck, 2000] Beijerinck, H. C. W. (2000). Heating rates in collisionally opaque alkali-metal atom traps: Role of secondary collisions. *Phys. Rev. A* **62**, 063614.
- [Bethlem et al., 2000] Bethlem, H. L., Berden, G., Cromptoets, F. M. H., Jongma, R. T., van Roij, A. J. A., and Meijer, G. (2000). Electrostatic trapping of ammonia molecules. *Nature* **406**, 491.
- [Bloch et al., 2001] Bloch, I., Greiner, M., Mandel, O., Hänsch, T., and Esslinger, T. (2001). Sympathetic Cooling of  $^{85}\text{Rb}$  and  $^{87}\text{Rb}$ . *Phys. Rev. A* **64**, R021402.
- [Boiron et al., 1998] Boiron, D., Michaud, A., Fournier, J. M., Simard, L., Sprenger, Grynberg, G., and Salomon, C. (1998). Laser cooling of cesium atoms in gray optical molasses down to  $1.1 \mu\text{K}$ . *Phys. Rev. A* **57**, 4106.
- [Bradley et al., 1997] Bradley, C. C., Sackett, C. A., and Hulet, R. G. (1997). Analysis of *in situ* images of Bose-Einstein condensates of Lithium. *Phys. Rev. A* **55**, 3951.
- [Burnett et al., 2002] Burnett, K., Julienne, P., Lett, P., Tiesinga, E., and Williams, C. (2002). Quantum encounters of the cold kind. *Nature* **416**, 225.
- [Chin et al., 2003] Chin, C., Kerman, A. J., Vuletić, V., and Chu, S. (2003). Sensitive Detection of Cold Cesium Molecules Formed on Feshbach Resonances. *Phys. Rev. Lett.* **90**, 033201.
- [Chin et al., 2000] Chin, C., Vuletić, V., Kerman, A. J., and Chu, S. (2000). High-resolution Feshbach Spectroscopy of Cesium. *Phys. Rev. Lett.* **85**, 2717.

- [Cline et al., 1994] Cline, R. A., Miller, J. D., and Heinzen, D. J. (1994). Study of  $\text{Rb}_2$  Long-Range States by High-Resolution Photoassociation Spectroscopy. *Phys. Rev. Lett.* **73**, 632.
- [Cohen-Tannoudji et al., 1988] Cohen-Tannoudji, C., Dupont-Roc, J., and Grynberg, G. (1988). *Processus d'interaction entre photons et atomes*. InterEdition. Paris.
- [Comparat, 1999] Comparat, D. (1999). *Molécules froides*. Dissertation Université Paris XI, U.F.R. scientifique d'Orsay.
- [Corwin et al., 1998] Corwin, K. L., Lu, Z., Hand, C. F., Epstein, R. J., and Wieman, C. E. (1998). Frequency-stabilized diode laser with the Zeeman shift of an atomic vapor. *Appl. Opt.* **37**, 3295.
- [Dalibard and Cohen-Tannoudji, 1989] Dalibard, J. and Cohen-Tannoudji, C. (1989). Laser cooling below the Doppler limit by polarization gradients: simple theoretical models. *J. Opt. Soc. Am. B* **6**, 2023.
- [deCarvalho et al., 1999] deCarvalho, R., Doyle, J., Friedrich, B., Guillet, T., Kim, J., Patterson, D., and Weinstein, J. (1999). Buffer-gas loaded magnetic traps for atoms and molecules: A primer. *Eur. Phys. J. D* **7**, 289.
- [Delannoy et al., 2001] Delannoy, G., Murdoch, S. G., Boyer, V., Josse, V., Bouyer, P., and Aspect, A. (2001). Understanding the production of dual Bose-Einstein condensation with sympathetic cooling. *Phys. Rev. A* **63**, R051602.
- [Dion et al., 2001] Dion, C. M., Drag, C., Dulieu, O., Tolra, B. L., Masnou-Seeuws, F., and Pillet, P. (2001). Resonant Coupling in the Formation of Ultracold Ground State Molecules via Photoassociation. *Phys. Rev. Lett.* **86**, 2253.
- [Donley et al., 2002] Donley, E. A., Claussen, N. R., Thompson, S. T., and Wieman, C. E. (2002). Atom-molecule coherence in a Bose-Einstein condensate. *Nature* **417**, 529.
- [Drag et al., 2000] Drag, C., Tolra, B. L., Dulieu, O., Comparat, D., Vatasescu, M., Boussen, S., Guibal, S., Crubellier, A., and Pillet, P. (2000). Experimental versus theoretical rates for photoassociation and for formation of ultracold molecules. *IEEE Journal of Quantum Electronics* **36**, 1378.

- [Dulieu, 2001] Dulieu, O. (2001). Schrödinger equation solver using Fourier grid method. private communication.
- [Dulieu et al., 1994] Dulieu, O., Julienne, P., and Weiner, J. (1994). Accuracy of molecular data in the understanding of ultracold collisions. *Phys. Rev. A* **49**, 607.
- [Engler, 2000] Engler, H. (2000). *A quasi-electrostatic trap for neutral atoms*. Dissertation Universität Heidelberg.
- [Engler et al., 2000] Engler, H., Weber, T., Mudrich, M., Grimm, R., and Weidemüller, M. (2000). Very long storage times and evaporative cooling of cesium atoms in a quasi-electrostatic trap. *Phys. Rev. A* **62**, R031402.
- [Ferrari et al., 2002] Ferrari, G., Inguscio, M., Jastrzebski, W., Modugno, G., and Roati, G. (2002). Collisional Properties of Ultracold K-Rb Mixtures. *Phys. Rev. Lett.* **89**, 053202.
- [Fioretti et al., 1998] Fioretti, A., Comparat, D., Crubellier, A., Dulieu, O., Masnou-Seeuws, F., and Pillet, P. (1998). Formation of Cold Cs<sub>2</sub> Molecules through Photoassociation. *Phys. Rev Lett.* **80**, 4402.
- [Fioretti et al., 1999a] Fioretti, A., Comparat, D., Drag, C., Amiot, C., Dulieu, O., Masnou-Seeuws, F., and Pillet, P. (1999a). Photoassociative spectroscopy of the Cs<sub>2</sub> 0<sub>g</sub><sup>-</sup> long-range state. *Eur. Phys. J. D* **5**, 1839.
- [Fioretti et al., 1999b] Fioretti, A., Comparat, D., Drag, C., Gallagher, T. F., and Pillet, P. (1999b). Long-Range Forces between Cold Atoms. *Phys. Rev. Lett* **82**, 1839.
- [Friedrich and Herschbach, 1995] Friedrich, B. and Herschbach, D. (1995). Alignment and Trapping of Molecules in Intense Laser Fields. *Phys. Rev. Lett.* **74**, 4623.
- [Gabbanini et al., 2000] Gabbanini, C., Fioretti, A., Lucchesini, A., Gozzini, S., and Mazzoni, M. (2000). Cold Rubidium Molecules Formed in a Magneto-Optical Trap. *Phys. Rev. Lett.* **84**, 2814.
- [Gensemer et al., 2000] Gensemer, S. D., Gould, P. L., Leo, P. J., Tiesinga, E., and Williams, C. J. (2000). Ultracold <sup>87</sup>Rb Ground-State Hyperfine-Changing Collisions in the Presence and Absence of Laser Light. *Phys. Rev. A* **62**, R030702.

- [Gerton et al., 1999] Gerton, J. M., Sackett, C. A., Frew, B. J., and Hulet, R. G. (1999). Dipolar relaxation collisions in magnetically trapped  ${}^7\text{Li}$ . *Phys. Rev. A* **59**, 1514.
- [Gerton et al., 2000] Gerton, J. M., Strekalov, D., Prodan, I., and Hulet, R. G. (2000). Direct observation of growth and collapse of a Bose-Einstein condensate with attractive interactions. *Nature* **408**, 692.
- [Granade et al., 2002] Granade, S. R., Gehm, M. E., O'Hara, K. M., and Thomas, J. E. (2002). All-Optical Production of a Degenerate Fermi Gas. *Phys. Rev. Lett.* **88**, 120405.
- [Grimm, 2002] Grimm, R. (2002). Towards BEC of cesium in an optical trap. Talk at the Conference "Interactions in Ultracold Gases: From Atoms to Molecules" in Heidelberg.
- [Grimm et al., 2000] Grimm, R., Weidemüller, M., and Ovchinnikov, Y. B. (2000). Optical dipole traps for neutral atoms. In: Bederson, B. and Walther, H. (Eds.), *Advances in Atomic Molecular and Optical Physics* Vol. 42, p. 95. Academic Press. San Diego.
- [Guéry-Odelin, 1998] Guéry-Odelin, D. (1998). *Dynamique collisionnelle des gaz d'alcalins lourds: Du refroidissement évaporatif à la condensation de Bose-Einstein*. Dissertation Département de physique de l'école normale supérieure.
- [Guéry-Odelin et al., 1998] Guéry-Odelin, D., Söding, J., Desbiolles, P., and Dalibard, J. (1998). Is Bose-Einstein condensation of atomic cesium possible? *Europhys. Lett.* **44**, 25.
- [Hadzibabic et al., 2002] Hadzibabic, Z., Stan, C. A., Dieckmann, K., Gupta, S., Zwierlein, M. W., Görlitz, A., and Ketterle, W. (2002). Two-Species Mixture of Quantum Degenerate Bose and Fermi Gases. *Phys. Rev. Lett.* **88**, 160401.
- [Heinzen, 1999] Heinzen, D. J. (1999). Ultracold atomic interactions. In: M. Inguscio, S. S. and Wieman, C. E. (Eds.), *Bose-Einstein Condensation in Atomic Gases, Proceedings of the International School of Physics "Enrico Fermi"*, p. 351. IOS Press. Amsterdam.
- [Herzberg, 1989] Herzberg, G. (1989). *Spectra of Diatomic Molecules*. Krieger Publishing Company, Malabar, Florida.

- [Hess et al., 1987] Hess, H. F., Kochanski, G. P., Doyle, J. M., Masuhara, N., Kleppner, D., and Greytak, T. J. (1987). Magnetic Trapping of Spin Polarized Atomic Hydrogen. *Phys. Rev. Lett.* **59**, 672.
- [Hudson et al., 2002] Hudson, J. J., Sauer, B. E., Tarbutt, M. R., and Hinds, E. A. (2002). Measurement of the Electron Electric Dipole Moment Using YbF Molecules. *Phys. Rev. Lett.* **89**, 023003.
- [Igel-Mann et al., 1986] Igel-Mann, Wedig, U., Fuentealba, P., and Stoll, H. (1986). Ground-state properties of alkali dimers XY (X,Y=Li to Cs). *J. Chem. Phys.* **84**, 5007.
- [Jochim et al., 2002] Jochim, S., Bartenstein, M., Hendl, G., Denschlag, J. H., Grimm, R., Mosk, A., and Weidemüller, M. (2002). Magnetic field control of elastic scattering in a cold gas of fermionic lithium atoms. submitted to *Phys. Rev. Lett.*; [arXiv:physics/0207098](https://arxiv.org/abs/physics/0207098).
- [Julienne et al., 2000] Julienne, P. S., Burnett, K., Band, Y. B., and Stwalley, W. C. (2000). Stimulated Raman molecule production in Bose-Einstein condensates. *Phys. Rev. A* **58**, R797.
- [Kerman et al., 2001] Kerman, A. J., Chin, C., Vuletic, V., Chu, S., Leo, P., Williams, C. J., and Julienne, P. S. (2001). *C. R. Acad. Sci. Paris IV* **2**, 633.
- [Kerman et al., 2000] Kerman, A. J., Vuletić, V., Chin, C., and Chu, S. (2000). Beyond Optical Molasses: 3D Raman Sideband Cooling of Atomic Cesium to High Phase-Space Density. *Phys. Rev. Lett.* **84**, 439.
- [Ketterle et al., 1993] Ketterle, W., Davis, K. B., Joffe, M. A., Martin, A., and Pritchard, D. E. (1993). High densities of cold atoms in a dark spontaneous-force optical trap. *Phys. Rev. Lett.* **70**, 2253.
- [Ketterle and van Druten, 1996] Ketterle, W. and van Druten, N. J. (1996). Evaporative Cooling of Trapped Atoms. *Adv. At. Mol. Opt. Phys.* **37**, 181.
- [Korek et al., 2000] Korek, M., Allouche, A. R., Fakhreddine, K., and Chaalan, A. (2000). Theoretical study of the electronic structure of LiCs, NaCs, and KCs molecules. *Can. J. Phys.* **78**, 977.
- [Kozlov and DeMille, 2002] Kozlov, M. G. and DeMille, D. (2002). Enhancement of the Electric Dipole Moment of the Electron in PbO. *Phys. Rev. Lett.* **89**, 133001.

- [Kraft, 2001] Kraft, S. (2001). Sympathetische Kühlung in einem Gemisch aus ultrakaltem Lithium und Cäsium. Diplomarbeit Universität Heidelberg und Max-Planck-Institut für Kernphysik.
- [Kuppens et al., 2000] Kuppens, S. J. M., Corwin, K. L., Miller, K. W., Chupp, T. E., and Wieman, C. E. (2000). Loading an optical dipole trap. *Phys. Rev. A* **62**, 013406.
- [Lagendijk et al., 1986] Lagendijk, A., Silvera, I. F., and Verhaar, B. J. (1986). Spin exchange and dipolar relaxation rates in atomic hydrogen: Lifetimes in magnetic traps. *Phys. Rev. B* **33**, R626.
- [Landau and Lifshitz, 1977] Landau, L. D. and Lifshitz, E. M. (1977). *Quantum Mechanics*. Pergamon Press. Oxford. Sect. 142 - 143.
- [Lange, 2002] Lange, J. (2002). Photoassoziation von Cs<sub>2</sub> in einer optischen Dipolfalle. Diplomarbeit Universität Heidelberg und Max-Planck-Institut für Kernphysik.
- [Larson et al., 1986] Larson, D. J., Bergquist, J. C., Bollinger, J. J., Itano, W. M., and Wineland, D. J. (1986). Sympathetic cooling of trapped ions: A laser-cooled two-species nonneutral ion plasma. *Phys. Rev. Lett.* **57**, 70.
- [Lefebvre-Brion and Field, 1989] Lefebvre-Brion, H. and Field, R. W. (1989). *Perturbations in the spectra of diatomic molecules*. Academic Press Inc. London.
- [Lemonde et al., 1995] Lemonde, P., Morice, O., Peik, E., Reichel, J., Perrin, H., Hänsel, W., and Salomon, C. (1995). An Opto-electric Trap for Cold Atoms. *Europhys. Lett.* **32**, 555.
- [Leo et al., 2000] Leo, P. J., Williams, C. J., and Julienne, P. S. (2000). Collision properties of ultracold <sup>133</sup>Cs atoms. *Phys. Rev. Lett.* **85**, 2721.
- [Le Roy, 1973] Le Roy, R. J. (1973). , p. 113. R. F. Barrow *et al.* (Eds.) *Molecular spectroscopy 1*. Chem. Soc. London.
- [Luiten et al., 1996] Luiten, O. J., Reynolds, M. W., and Walraven, J. T. M. (1996). Kinetic theory of the evaporative cooling of a trapped gas. *Phys. Rev. A* **53**, 381.
- [Marinescu and Dalgarno, 1995] Marinescu, M. and Dalgarno, A. (1995). Dispersion forces and long-range electronic transition dipole moments of alkali-metal dimer excited states. *Phys. Rev. A* **52**, 311.

- [Marinescu and Sadeghpour, 1999] Marinescu, M. and Sadeghpour, H. R. (1999). Long-range potentials for two-species alkali-metal atoms. *Phys. Rev. A* **59**, 390.
- [Masnou-Seeuws and Pillet, 2001] Masnou-Seeuws, F. and Pillet, P. (2001). Formation of ultracold molecules ( $T \leq 200 \mu\text{K}$ ) via photoassociation in a gas of laser-cooled atoms. *Adv. Atomic Mol. Opt. Phys.* **47**, 53.
- [Metcalf and van der Straten, 1999] Metcalf, H. and van der Straten, P. (1999). *Laser Cooling and Trapping*. Springer Verlag, New York.
- [Mewes et al., 1996] Mewes, M.-O., Andrews, M. R., van Druten, N. J., Kurn, D. M., Durfee, D. S., and Ketterle, W. (1996). Bose-Einstein Condensation in a Tightly Confining dc Magnetic Trap. *Phys. Rev. Lett.* **77**, 416.
- [Miesner et al., 1999] Miesner, H.-J., Stamper-Kurn, D. M., Stenger, J., Inouye, S., Chikkatur, A. P., and Ketterle, W. (1999). Observation of Metastable States in Spinor Bose-Einstein Condensates. *Phys. Rev. Lett.* **82**.
- [Miller et al., 1993] Miller, J. D., Cline, R. A., and Heizen, D. J. (1993). Photoassociation Spectrum of Ultracold Rb Atoms. *Phys. Rev. Lett.* **71**, 2204.
- [Modugno et al., 2001] Modugno, G., Ferrari, G., Roati, G., Brecha, R. J., Simoni, A., and Inguscio, M. (2001). Bose-Einstein Condensation of Potassium Atoms by Sympathetic Cooling. *Science* **7294**, 1320.
- [Modugno et al., 2002] Modugno, G., Roati, G., Ferlaino, F. R. F., Brecha, R. J., and Inguscio, M. (2002). Collaps of a degenerate Fermi gas. *Science* **297**, 2240.
- [Moerdijk and Verhaar, 1996] Moerdijk, A. J. and Verhaar, B. J. (1996). Collisional two- and three-body decay rates of dilute quantum gases at ultralow temperatures. *Phys. Rev. A* **53**, R19.
- [Mosk, 2000a] Mosk, A. (2000a). Analytic model for the thermalization process in trapped gas mixtures. private communication.
- [Mosk, 2000b] Mosk, A. (2000b). Numerical simulation of the thermalization process in trapped gas mixtures. private communication.
- [Mosk, 2002] Mosk, A. (2002). Analytic model for release-and-recapture thermometry. private communication.

- [Mosk et al., 2001a] Mosk, A., Jochim, S., Moritz, H., Elsässer, T., Weidemüller, M., and Grimm, R. (2001a). Resonator-enhanced optical dipole trap for fermionic lithium atoms. *Optics Letters* **26**, 1837.
- [Mosk et al., 2001b] Mosk, A., Kraft, S., Mudrich, M., Singer, K., Wohlleben, W., Grimm, R., and Weidemüller, M. (2001b). Mixture of ultracold lithium and cesium atoms in an optical trap. *Appl. Phys. B* **73**, 791.
- [Mudrich et al., 2002] Mudrich, M., Kraft, S., Singer, K., Grimm, R., Mosk, A., and Weidemüller, M. (2002). Sympathetic cooling with two atomic species in an optical trap. *Phys. Rev. Lett.* **88**, 253001.
- [Müller and Meyer, 1986] Müller, W. and Meyer, W. (1986). Static dipole polarizabilities of  $\text{Li}_2$ ,  $\text{Na}_2$ , and  $\text{K}_2$ . *J. Chem. Phys.* **85**, 953.
- [Myatt et al., 1997] Myatt, C. J., Burt, E. A., Ghrist, R. W., Cornell, E. A., and Wieman, C. E. (1997). Production of Two Overlapping Bose-Einstein Condensates by Sympathetic Cooling. *Phys. Rev. Lett.* **78**, 586.
- [Nesnidal and Walker, 2000] Nesnidal, R. C. and Walker, T. G. (2000). Light-induced ultracold spin-exchange collisions. *Phys. Rev. A* **62**, R030701.
- [Nikolov et al., 1999] Nikolov, A. N., Eyler, E. E., Wang, X., Li, J., Wang, H., Stwalley, W. C., and Gould, P. L. (1999). Observation of translationally ultracold ground state potassium molecules. *Phys. Rev. Lett.* **82**, 703.
- [O'Hara et al., 2001] O'Hara, K. M., Gehm, M. E., Granade, S. R., and Thomas, J. E. (2001). Scaling laws for evaporative cooling in time-dependent optical traps. *Phys. Rev. A* **64**, 051403.
- [O'Hara et al., 2002] O'Hara, K. M., Hemmer, S. L., Gehm, M. E., Granade, S. R., and Thomas, J. E. (2002). Observation of a Strongly Interacting Degenerate Fermi Gas of Atoms. *Science* **298**, 2179.
- [Patil and Tang, 1999] Patil, S. H. and Tang, K. T. (1999). Polarizabilities and dispersion coefficients for alkali systems in second- and third-order perturbation. *Chem. Phys. Lett.* **301**, 64.
- [Pethick and Smith, 2002] Pethick, C. J. and Smith, H. (2002). *Bose-Einstein Condensation in Dilute Gases*. Cambridge University Press.

- [Petrich et al., 1994a] Petrich, W., Anderson, M. H., Ensher, J. R., and Cornell, E. A. (1994a). Behavior of atoms in a compressed magneto-optical trap. *J. Opt. Soc. Am. B* **11**, 1332.
- [Petrich et al., 1994b] Petrich, W., Anderson, M. H., Ensher, J. R., and Cornell, E. A. (1994b). Evaporative cooling of rubidium atoms in a magnetic trap. In: *Fourteenth International Conference on Atomic Physics (ICAP XIV)*, p. 7.
- [Pillet et al., 1997] Pillet, P., Crubellier, A., Bleton, A., Dulieu, O., Nosbaum, P., Mourachko, I., and Masnou-Seeuws, F. (1997). Photoassociation in a gas of cold alkali atoms: I. Perturbative quantum approach. *J. Phys. B: At. Mol. Opt. Phys.* **30**, 2801.
- [Pinkse et al., 2000] Pinkse, P. W. H., Fischer, T., Maunz, P., and Rempe, G. (2000). Trapping an atom with single photons. *Nature* **404**, 365.
- [Raab et al., 1987] Raab, E. L., Prentiss, M., Cable, A., Chu, S., and Pritchard, D. E. (1987). Trapping neutral sodium atoms with radiation pressure. *Phys. Rev. Lett.* **59**, 2631.
- [Roati et al., 2001] Roati, G., Jastrzebski, W., Simoni, A., Modugno, G., and Inguscio, M. (2001). An optical trap for collisional studies on cold fermionic potassium. *Phys. Rev. A* **63**, 052709.
- [Roati et al., 2002] Roati, G., Riboli, F., Modugno, G., and Inguscio, M. (2002). Fermi-Bose Quantum Degenerate K - Rb Mixture with Attractive Interaction. *Phys. Rev. Lett.* **89**, 150403.
- [Rost et al., 1992] Rost, J. M., Griffin, J. C., Friedrich, B., and Herschbach, D. R. (1992). Pendular states and spectra of oriented linear molecules. *Phys. Rev. Lett.* **68**, 1299.
- [Saenz, 2002] Saenz, A. (2002). Dipole moment function of the singlet groundstate of LiCs. private communication.
- [Sandars, 1967] Sandars, P. G. H. (1967). Measurability of the Proton Electric Dipole Moment. *Phys. Rev. Lett.* **19**, 1396.
- [Santarelli et al., 1999] Santarelli, G., Laurent, P., Lemonde, P., Clairon, A., Mann, A. G., Chang, S., Luiten, A. N., and Salomon, C. (1999). Quantum Projection Noise in an Atomic Fountain: A High Stability Cesium Frequency Standard. *Phys. Rev. Lett.* **82**, 4619.

- [Santos et al., 2000] Santos, L., Shlyapnikov, G. V., Zoller, P., and Lewenstein, M. (2000). Bose-Einstein Condensation in Trapped Dipolar Gases. *Phys. Rev. Lett.* **85**, 1791.
- [Santos et al., 1999] Santos, M. S., Nussenzeig, P., Antunes, A., Cardona, P. S. P., and Bagnato, V. S. (1999). Hyperfine-changing collision measurements in trap loss for mixed species in a magneto-optical trap. *Phys. Rev. A* **60**, 3892.
- [Schlöder et al., 2002] Schlöder, D., Silber, C., Deuschle, T., and Zimmermann, C. (2002). Saturation in heteronuclear photoassociation of  ${}^6\text{Li}{}^7\text{Li}$ . to appear in *Phys. Rev. A* (Rapid Communication).
- [Schlöder, 1998] Schlöder, U. (1998). Ultrakalte Stöße zwischen Lithium- und Cäsiumatomen in einer kombinierten magneto-optischen Falle. Diplomarbeit Universität Heidelberg und Max-Planck-Institut für Kernphysik.
- [Schlöder et al., 1999] Schlöder, U., Engler, H., Schünemann, U., Grimm, R., and Weidemüller, M. (1999). Cold inelastic collisions between lithium and cesium in a two-species magneto-optical trap. *Eur. Phys. J. D* **7**, 331.
- [Schlöder et al., 2001] Schlöder, U., Silber, C., and Zimmermann, C. (2001). Photoassociation of heteronuclear lithium. *Appl. Phys. B* **73**, 802.
- [Schreck et al., 2001a] Schreck, F., Ferrari, G., Corwin, K. L., Cubizolles, J., Khaykovich, L., Mewes, M.-O., and Salomon, C. (2001a). Sympathetic cooling of bosonic and fermionic Lithium gases towards quantum degeneracy. *Phys. Rev. A*. **64**, R011402.
- [Schreck et al., 2001b] Schreck, F., Khaykovich, L., Corwin, K. L., Ferrari, G., Bourdel, T., Cubizolles, J., and Salomon, C. (2001b). Quasipure Bose-Einstein Condensate Immersed in a Fermi Sea. *Phys. Rev. Lett.* **87**, 080403.
- [Schünemann et al., 1998] Schünemann, U., Engler, H., Zielonkowski, M., Weidemüller, M., and Grimm, R. (1998). Magneto-optic trapping of lithium using semiconductor lasers. *Opt. Commun.* **158**, 263.
- [Sekatskii and Schmiedmayer, 1996] Sekatskii, S. K. and Schmiedmayer, J. (1996). Trapping polar molecules with a charged wire. *Europhys. Lett.* **36**, 407.
- [Sesko et al., 1989] Sesko, D., Walker, T., Monroe, C., Gallagher, A., and Wieman, C. (1989). Collisional losses from a light-force atom trap. *Phys. Rev. Lett.* **63**, 961.

- [Shaffer et al., 1999] Shaffer, J. P., Chalupczak, W., and Bigelow, N. P. (1999). Photoassociative Ionization of Heteronuclear Molecules in a Novel Two-Species Magneto-optical Trap. *Phys. Rev. Lett.* **82**, 1124.
- [Singer et al., 2002] Singer, K., Jochim, S., Mudrich, M., Mosk, A., and Weidemüller, M. (2002). Low-cost mechanic. *Rev. Sci. Instrum.* **73**, 4402.
- [Söding et al., 1998] Söding, J., Guéry-Odelin, D., Desbiolles, P., Ferrari, G., and Dalibard, J. (1998). Giant Spin Relaxation of an Ultracold Cesium Gas. *Phys. Rev. Lett.* **80**, 1869.
- [Soldán et al., 2002] Soldán, P., Cvita, M. T., Hutson, J. M., Honvault, P., and Launay, J.-M. (2002). Quantum Dynamics of Ultracold Na + Na<sub>2</sub> Collisions. *Phys. Rev. Lett.* **89**, 153201.
- [Spiegelmann et al., 1989] Spiegelmann, F., Pavolini, D., and Daudey, J. P. (1989). Theoretical study of the excited states of the heavier alkali dimers. II. The Rb<sub>2</sub> molecule. *J. Phys. B* **22**, 2465. and references therein.
- [Spiess, 1989] Spiess, N. (1989). Dissertation Universität Kaiserslautern.
- [Steck, 1998] Steck, D. A. (1998). Cesium D Line Data. Available online: <http://george.ph.utexas.edu/~dsteck/alkalidata>.
- [Stwalley and Uang, 1978] Stwalley, W. C. and Uang, Y.-H. (1978). Pure Long-Range Molecules. *Phys. Rev. Lett.* **41**, 1164.
- [Stwalley and Wang, 1999] Stwalley, W. C. and Wang, H. (1999). Photoassociation of ultracold atoms: a new spectroscopic technique. *J. Mol. Spectrosc.* **195**, 194.
- [Takekoshi and Knize, 1996] Takekoshi, T. and Knize, R. J. (1996). CO<sub>2</sub> laser trap for cesium atoms. *Opt. Lett.* **21**, 77.
- [Takekoshi et al., 1998] Takekoshi, T., Patterson, B. M., and Knize, R. J. (1998). Observation of Optically Trapped Cold Cesium Molecules. *Phys. Rev. Lett.* **81**, 5105.
- [Takekoshi et al., 1995] Takekoshi, T., Yeh, J. R., and Knize, R. J. (1995). Quasi-electrostatic trap for neutral atoms. *Opt. Commun.* **114**, 421.
- [Tarnovsky et al., 1993] Tarnovsky, V., Bunimovich, M., Vušković, L., Stumpf, B., and Bederson, B. (1993). Measurement of the dc electric dipole polarizabilities of the alkali dimer molecules, homonuclear and heteronuclear. *J. Chem. Phys.* **98**, 3894.

- [Telles et al., 2001a] Telles, G. D., Bagnato, V. S., and Marcassa, L. G. (2001a). Alternative to the Hyperfine-Change-Collision Interpretation for the Behavior of Magneto-optical-Trap Losses at Low Light Intensity. *Phys. Rev. Lett.* **86**, 4496.
- [Telles et al., 2001b] Telles, G. D., Garcia, W., Marcassa, L. G., and Bagnato, V. S. (2001b). Trap-loss in a two-species Rb-Cs magneto-optical trap. *Phys. Rev. A.* **63**, 033406.
- [Thorsheim et al., 1987] Thorsheim, H. R., Weiner, J., and Julienne, P. S. (1987). Laser-induced photoassociation of ultracold sodium atoms. *Phys. Rev. Lett.* **58**, 2420.
- [Tiesinga, 2002] Tiesinga, E. (2002). Rate coefficients for spin-exchange and dipolar collisions of Cs. private communication.
- [Truscott et al., 2001] Truscott, A. G., Strecker, K. E., McAlexander, W. I., Patridge, G. B., and Hulet, R. G. (2001). Observation of Fermi Pressure in a Gas of Trapped Atoms. *Science* **291**, 2570.
- [Vanhaecke et al., 2002] Vanhaecke, N., Melo, W. S., Tolra, B. L., Comparat, D., and Pillet, P. (2002). Accumulation of Cold Cesium Molecules via Photoassociation in a Mixed Atomic and Molecular Trap. *Phys. Rev. Lett.* **89**, 063001.
- [Vuletić et al., 1998] Vuletić, V., Chin, C., Kerman, A. J., and Chu, S. (1998). Degenerate Raman Sideband Cooling of Trapped Cesium Atoms at Very High Atomic Densities. *Phys. Rev. Lett.* **81**, 5768.
- [Wang and Stwalley, 1998] Wang, H. and Stwalley, W. C. (1998). Ultracold photoassociative spectroscopy of heteronuclear alkali-metal diatomic molecules. *J. Chem. Phys.* **108**, 5767.
- [Weber et al., 2002] Weber, T., Herbig, J., Mark, M., Nägerl, H.-C., and Grimm, R. (2002). Bose-Einstein Condensation of Cesium. *Science* **0**, 10796991.
- [Weidemüller, 2000] Weidemüller, M. (2000). *Mixtures of ultracold atoms and the quest for ultracold molecules*. Habilitationsschrift, Max-Planck-Institut für Kernphysik und Universität Heidelberg.
- [Weiner et al., 1999] Weiner, J., Bagnato, V. S., Zilio, S., and Julienne, P. (1999). Experiments and theory in cold and ultracold collisions. *Rev. Mod. Phys.* **71**, 1.

- [Weinstein et al., 1998] Weinstein, J. D., deCarvalho, R., Guillet, T., Friedrich, B., and Doyle, J. M. (1998). Magnetic trapping of calcium monohydride molecules at millikelvin temperatures. *Nature* **395**, 148.
- [Witteman, 1987] Witteman, W. J. (1987). *The CO<sub>2</sub> [CO] Laser*. Springer-Verlag. Berlin, Heidelberg, New York.
- [Wohlleben, 2000] Wohlleben, W. (2000). Simultane Speicherung von Lithium und Cäsium in einer quasi-elektrostatischen Dipolfalle. Spinändernde Stöße und sympathetische Evaporation. Diplomarbeit Universität Heidelberg und Max-Planck-Institut für Kernphysik.
- [Wynar et al., 2000] Wynar, R., Freeland, R. S., Han, D. J., Ryu, C., and Heinzen, D. J. (2000). Atom-molecule coherence in a Bose-Einstein condensate. *Science* **287**, 1016.
- [Xu, 2001] Xu, G. (2001). *Manipulation and Quantum Control of Ultracold Atoms and Molecules for Precision Measurements*. Dissertation The University of Texas at Austin.
- [Young et al., 2000] Young, Y. E., Ejnisman, R., Shaffer, J. P., and Bigelow, N. P. (2000). Heteronuclear hyperfine-state-changing cold collisions. *Phys. Rev. A* **62**, 055403.

# Danksagung

Ich danke all denjenigen, die dazu beigetragen haben, dass die letzten drei Jahre am Max-Planck-Institut für Kernphysik und die drei Monate am Laboratoire Aimé Cotton zwar eine harte, aber lehrreiche und letztendlich auch schöne Zeit waren:

...Matthias Weidemüller, für den unermüdlichen freundschaftlichen Ansporn, für anregende Ideen und Hilfestellung in den entscheidenden Momenten,

...Dirk Schwalm, für die wohlwollende Atmosphäre des gegenseitigen Interesses und Mitdenkens in einer so grossen und bunten Truppe. Ich kann mir nur wünschen, in Zukunft in einem ähnlichen Arbeitsklima tätig zu sein,

...Allard Mosk, für seinen “peace-of-mind”, durch den auch die paradoxesten Beobachtungen enträtselt werden. Vielen Dank für die grosse Hilfe gerade in der heissen Phase des Zusammenschreibens (und des Verstehens),

...der LiCs-crew: Stephan Kraft, Marc Eichhorn, Jörg Lange und Matthias Staudt, für die enge, konstruktive Team-Arbeit, für viele unterhaltsame Stunden im Labor und für die Unterstützung in den letzten Wochen,

...den Rydbergs: Kilian Singer, Michaela Tscherneck, Markus Reetz-Lamour und Simon Fölling, für die nette Zusammenarbeit und die Hilfsbereitschaft bei jeder Art von Problemen,

...der TSR-Fraktion: Björn Eike und Achim Dahlbokum für das unkomplizierte gegenseitige Aushelfen und die gute Stimmung im Team,

...Helga, für die vielen kleinen und grossen Hilfen von der Laserjustage bis zum Weihnachtsschmaus,

...den Ehemaligen: Rudi Grimm, Altmeister Hengler, Wendel Wohlleben, Udo Eisenbarth, Patrick Friedmann, Sandro Hannemann, Tino Weber, Selim Jochim, Markus Hammes und David Rychtarik, für die handfeste Unterstützung in der Einarbeitungsphase und den weiterhin regen Austausch von Tipps & Tricks,

...meinen Eltern, für ihre materielle und moralische Unterstützung und die stete Anteilnahme an meinen Fortschritten in Sachen Dr. rer. nat.

...Viola Droujinina, für die geduldige und liebevolle Unterstützung bei allem rund um das Projekt Doktorarbeit.

*Un grand merci à l'équipe des molécules froides du Laboratoire Aimé Cotton, Pierre Pillet, Daniel Comparat, Nicolas VanHaecke et Christian Lisdat, de m'avoir reçu si amablement et surtout pour toutes les heures de discussions auprès du tableau dans la salle de manipe !*

I gratefully acknowledge the financial support by the ESF Scientific Programme "BEC2000+", which made possible my research stay at Laboratoire Aimé Cotton.